NASA-CR-201482

JOINT INSTITUTE FOR AERONAUTICS AND ACOUSTICS

National Aeronautics and
Space Administration
Ames Research Center

JIAA TR 116

Stanford University

EXPERIMENTAL AND COMPUTATIONAL INVESTIGATION OF LIFT-ENHANCING TABS ON A MULTI-ELEMENT AIRFOIL

Dale Ashby

Stanford University
Department of
Aeronautics and Astronautics
Stanford, CA 94305

June 1996

ABSTRACT

An experimental and computational investigation of the effect of lift-enhancing tabs on a two-element airfoil has been conducted. The objective of the study was to develop an understanding of the flow physics associated with lift-enhancing tabs on a multi-element airfoil. An NACA 63_2-215 ModB airfoil with a 30% chord fowler flap was tested in the NASA Ames 7- by 10-Foot Wind Tunnel. Lift-enhancing tabs of various heights were tested on both the main element and the flap for a variety of flap riggings. Computations of the flow over the two-element airfoil were performed using the two-dimensional incompressible Navier-Stokes code INS2D-UP. The computed results predicted all of the trends observed in the experimental data quite well.

When the flow over the flap upper surface is attached, tabs mounted at the main element trailing edge (cove tabs) produce very little change in lift. At high flap deflections, however, the flow over the flap is separated and cove tabs produce large increases in lift and corresponding reductions in drag by eliminating the separated flow. Cove tabs permit higher flap deflection angles to be achieved and reduce the sensitivity of the airfoil lift to the size of the flap gap. Tabs attached to the flap trailing edge (flap tabs) are effective at increasing lift without significantly increasing drag. A combination of a cove tab and a flap tab increased the airfoil lift coefficient by 11% relative to the highest lift coefficient achieved by any baseline configuration at an angle of attack of 0° and C_{lmax} was increased by 3%.

A simple analytic model based on potential flow was developed to provide a more detailed understanding of how lift-enhancing tabs work. The tabs were modeled by a point vortex at the trailing edge. Sensitivity relationships were derived which provide a mathematical basis for explaining the effects of lift-enhancing tabs on a multi-element airfoil. Results of the modeling effort indicate that the dominant effects of the tabs on the pressure distribution of each element of the airfoil can be captured with a potential flow model for cases with no flow separation.

ACKNOWLEDGMENTS

I would like to thank Dr. Brian Cantwell for his guidance and support in preparation of this dissertation. I also want to express my appreciation to Dr. James C. Ross at NASA Ames Research Center for his contributions in obtaining the time, funds, and support necessary to conduct this research. Finally I want to thank my wife and son for their support, encouragement, and understanding during the long process of completing this research. Without them, I would not have made it to the finish line.

TABLE OF CONTENTS

LIST OF TABLES

LIST OF FIGURES

NOMENCLATURE

A	Jacobian matrix of convective flux vector in the x direction
B	Jacobian matrix of convective flux vector in the z direction
b	Wing span
B_{ij}	Source influence coefficient matrix
c	Airfoil chord
C_d	Wind-axis drag coefficient
C_{ij}	Doublet influence coefficient matrix
C_f	Skin friction coefficient
C_l	Wind-axis lift coefficient
C_{lmax}	Maximum lift coefficient
C_m	Wind-axis pitching moment coefficient
C_p	Pressure coefficient
D	Drag
e	Internal energy per unit mass
E_t	Total energy per unit volume
F	Convective flux vector in the x direction
f_i	Components of body force per unit volume
F_v	Viscous flux vector in the x direction
g	Acceleration due to gravity
G	Convective flux vector in the z direction
G_v	Viscous flux vector in the z direction
h	Height
i, j, k	Dummy indices or grid point indices
J	Jacobian of the generalized coordinate transformation
k_F	Fourier's coefficient of heat conduction
K	Turbulent kinetic energy
l	Length of wake rake
L	Lift
n_j	Normal vector for panel j
p	Pressure
P_{swr}	Static pressure measured at wake rake
P_{Twr}	Total pressure measured at wake rake
$P_{T\infty}$	Freestream total pressure
Q	State vector

q_c	Corrected test section dynamic pressure
Q_h	Rate of heat produced per unit volume
q_u	Uncorrected test section dynamic pressure
q_∞	Freestream dynamic pressure
R	Residual vector
$R_1 - R_8$	Vectors between point vortices and control points
T	Temperature
t	Time
t/c	Airfoil thickness-to-chord ratio
U_1, U_2	Contravariant components of velocity
u_i, u_j, or u_k	Components of the velocity vector
u_∞	Component of freestream velocity in x direction
$V_1 - V_8$	Component of velocity normal to airfoil chord induced by point vortices
V_∞	Magnitude of freestream velocity
w_∞	Component of freestream velocity in z direction
X	Eigenvector matrix of the convective flux Jacobian
x, y, z	Cartesian coordinates
x_i, x_j, or x_k	Components of the position vector
x_{ol}	Flap overlap
z_{ct}	Cove tab height
z_{ft}	Flap tab height
z_g	Flap gap
z_t	Lift-enhancing tab height
α	Angle of attack
α_{7h}	Flow angle in horizontal plane measured by 7-hole probe
β	Artificial compressibility factor
β_{7h}	Flow angle in vertical plane measured by 7-hole probe
δ_f	Flap deflection angle
Δq_η	Change in dynamic pressure due to compressibility effects
ε	Rate of turbulence dissipation
γ_{ct}	Strength of the point vortex representing the cove tab
γ_f	Strength of the point vortex representing the circulation of the flap
γ_{ft}	Strength of the point vortex representing the flap tab
γ_m	Strength of the point vortex representing the circulation of the main element
Λ	Diagonal matrix of eigenvalues of the convective flux Jacobian
μ	Dynamic viscosity

μ_j	Strength of doublet distribution on panel j
μ_t	Turbulent dynamic viscosity
μ_w	Strength of doublet distribution on wake panel
ν	Kinematic viscosity
ν_t	Turbulent kinematic viscosity
ρ	Density
σ_j	Strength of source distribution on panel j
τ	Pseudo-time
ω	Vorticity
ξ, η	Generalized coordinates

CHAPTER I
INTRODUCTION

The high-lift capability of an aircraft is an important design parameter that affects takeoff and landing performance and low-speed maneuverability. The high-lift system has a direct impact on maximum allowable takeoff and landing weights for a given runway length. Alternatively, for a given payload weight, the required takeoff and landing distances are fixed by the high-lift characteristics of the aircraft. Approach speed and attitude are also determined by the high-lift system performance. This can have implications for such factors as community noise created by the aircraft during approach. Meredith [1] has highlighted the importance of the high-lift system on commercial jet transport aircraft with three examples from a design study for a generic large twin-engine transport. An increase in lift coefficient of 0.10 at a constant angle of attack allows the approach attitude to be reduced by about one degree, which can lead to shorter landing gear and reduced aircraft weight. A 1.5% increase in maximum lift coefficient would allow a 6600 lb increase in payload at a fixed approach speed. Increasing the take-off lift-to-drag ratio (L/D) by 1% permits a 2800 lb increase in payload or a 150 nautical mile increase in range.

Because the high-lift system has such a strong impact on the low-speed performance of an aircraft, a significant amount of effort goes into its design. The high-lift capability is only required in the low-speed flight regime characteristic of takeoff and landing. Most aircraft, particularly commercial transport aircraft, spend the majority of their flight time in the high-speed cruise flight regime. Thus transport aircraft wings are generally optimized for the cruise condition where maintaining low drag is a prime consideration. Airfoil shapes that are efficient for high-speed cruise (Mach 0.8 or higher) are usually not optimum for the low-speed high-lift flight regime. This leads to the requirement for a high-lift system that can be stowed during cruise and deployed during low-speed flight. A deployable high-lift system, however, increases the mechanical complexity and weight of the wing.

Most modern high-lift systems are composed of a basic wing with a deployable leading-edge slat and at least one, and sometimes more, deployable trailing-edge flap elements as shown in Figure 1. It was recognized as early as 1921 by Handley Page and others [2] that the high-lift performance of a multi-element airfoil can be improved by increasing the number of trailing-edge flap elements. The trend in transport aircraft design in the 1960s and 1970s was to achieve better high-lift performance, required for the larger

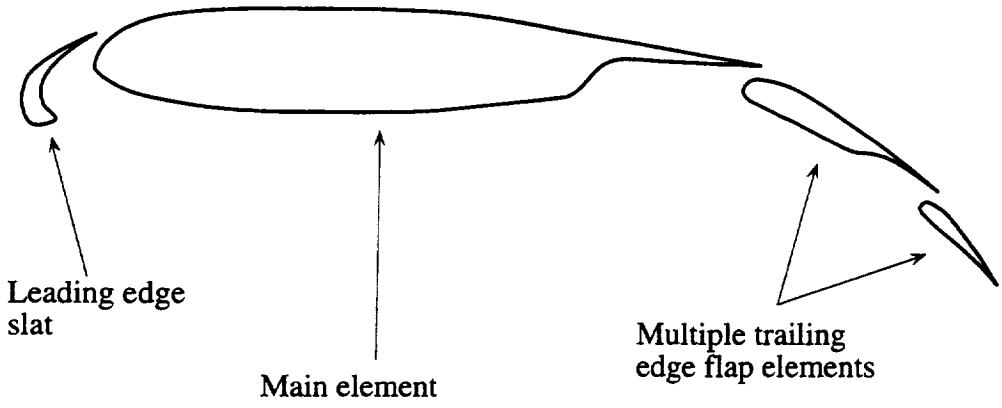

Figure 1: Typical high-lift system for current transport aircraft.

transports being designed, by increasing the number of trailing-edge flap elements. Designs of that era seemed to reach a practical limit of three on the number of trailing-edge flap elements. The Boeing 737, for example, has a three-element trailing-edge flap system which is highly efficient aerodynamically, but very complicated and costly to design and maintain. The benefits from the increased high-lift performance gained by using more than three trailing-edge flap elements are outweighed by the weight and cost penalties.

The current trend in high-lift system design for transport aircraft is to return to simpler two-element or even one-element trailing-edge flap systems and improve the performance of these systems to meet design requirements. Aircraft such as the Boeing 767 with its single-element outboard and two-element inboard trailing-edge flaps and the Airbus 340 with its single-element trailing-edge flaps reflect this philosophy. One way of accomplishing the necessary improvements in high-lift performance of simpler high-lift systems is through application of new computational and experimental tools which permit a better understanding of associated flow physics. The flow field associated with high-lift multi-element two-dimensional airfoils or three-dimensional wings is extremely complex. Such flow fields are governed by viscous phenomena such as transition of boundary layers from laminar to turbulent, laminar boundary layer separation and reattachment, confluent wakes and boundary layers, viscous wake interactions, and separated flow. Advances in computer technology over the past 20 years now make possible numerical simulations of the flow fields associated with multi-element airfoils and wings using the full Navier-Stokes equations or appropriate subsets of the full equations. New experimental techniques have also been developed such as Laser Velocimetry (LV), Doppler Global Velocimetry (DGV), and Pressure Sensitive Paint (PSP), which permit much greater detail about the flow fields associated with high-lift systems to be obtained experimentally.

These advances in computational and experimental capabilities have provided high-lift system designers with new tools to use for improving the design of multi-element airfoils and wings. These tools can provide designers with a better understanding of the flow physics governing high-lift systems, allowing them to tailor the pressure distribution over individual elements of the high-lift system and to optimize the geometric positioning of the various elements, leading to better high-lift performance.

Attention is also being focused on the use of miniature flow-enhancement devices such as vortex generators, trailing-edge wedges, and lift-enhancing tabs to improve the performance of high-lift systems. Examples of these devices are shown in Figure 2. The

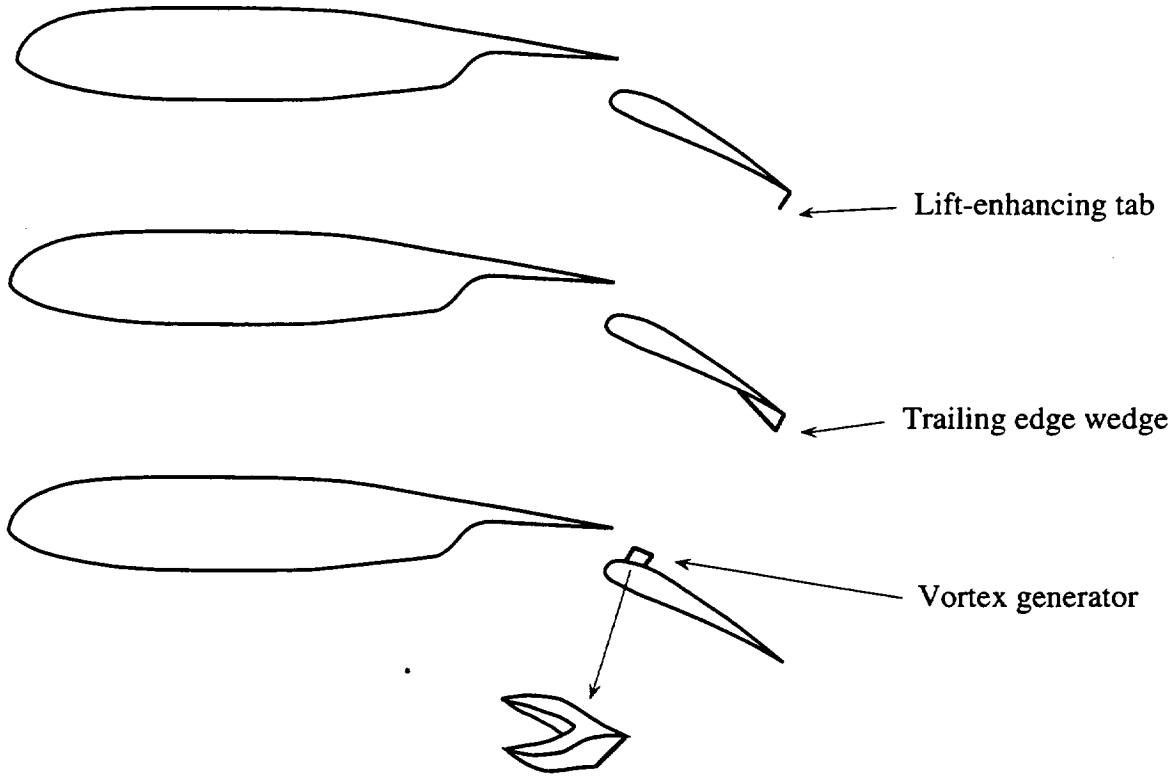

Figure 2: Examples of miniature flow-enhancement devices.

size of the devices has been exaggerated for illustration purposes. These devices have the advantage of being simple, lightweight, and cheap. The size of the devices is generally of the order of the local boundary layer height. Appropriately positioned on the airfoil or wing, these devices can have a significant impact of the performance of the high-lift system.

Storms and Jang [3] conducted an experimental investigation of the use of vortex generators to delay separation on the upper surface of a single-element airfoil. They found

that Wheeler wishbone type vortex generators with a height of 0.5% chord mounted at a location 12% chord back from the leading edge on the upper surface of a NACA 4412 airfoil were effective in delaying flow separation. The vortex generators delayed the onset of flow separation on the upper surface from an angle of attack of 12° to an angle of attack of 19°. This increased the value of C_{lmax} by 23%. The vortex generators produce the same type of effect on the plot of lift coefficient versus angle of attack that a leading edge slat does. At lift coefficients below C_{lmax}, the lift coefficient remains unchanged when vortex generators are added. The vortex generators also had the effect of increasing the drag of the airfoil substantially. Thus they would need to be retracted for efficient cruise performance.

Trailing-edge wedges, or divergent trailing edges, have been investigated by a number of researchers, including Valarezo, et. al. [4]. Valarezo conducted an experimental investigation of trailing-edge wedges placed on the lower surface of the flap at the trailing edge on a three-element airfoil (slat, main element, flap). Wedges with angles of 15°, 30°, 45°, and 60° were tested. The wedges had a length of 3% chord and height was determined by the wedge angle. The wedges produced an increase in lift coefficient that was largest at an angle of attack of 0° and diminished as the angle of attack was increased. The 60° wedge produced an increase of 0.2 in C_{lmax} at a Reynolds number of 5×10^6. When Reynolds number was increased to 9×10^6, the change in C_{lmax} due to the 60° wedge was only 0.07. The baseline lift data for the three-element airfoil also indicated a strong dependence on Reynolds number, with C_{lmax} increasing by 0.1 as Reynolds number was increased from 5×10^6 to 9×10^6. Flow over the upper surface of the baseline flap separated at approximately the 70% flap chord location when angle of attack was 8°. Valarezo hypothesizes that the sensitivity to Reynolds number for the baseline flap could be due to the presence of flow separation on the upper surface of the flap. The same could be true for the sensitivity of the performance of the trailing edge wedges to Reynolds number.

Lift-enhancing tabs have received considerable attention over the last few years and appear to be one of the more promising means of improving high-lift performance. A lift-enhancing tab is a flat plate with a height of between 0.25% and 5% of the main wing chord. It is attached to the lower surface of the airfoil at the trailing edge as shown in Figure 2. One of the advantages of lift-enhancing tabs over the devices discussed above is that the tabs can be retracted or stowed when not in use. This means that lift-enhancing tabs can be attached to the trailing edge of any or all elements of a multi-element airfoil as shown in Figure 3. Gurney flaps, named after the race car driver Dan Gurney, are an example of a lift-enhancing tab. The Gurney flap was placed at the trailing edge of the wing on an Indianapolis race car and was found to provide increased downforce on the

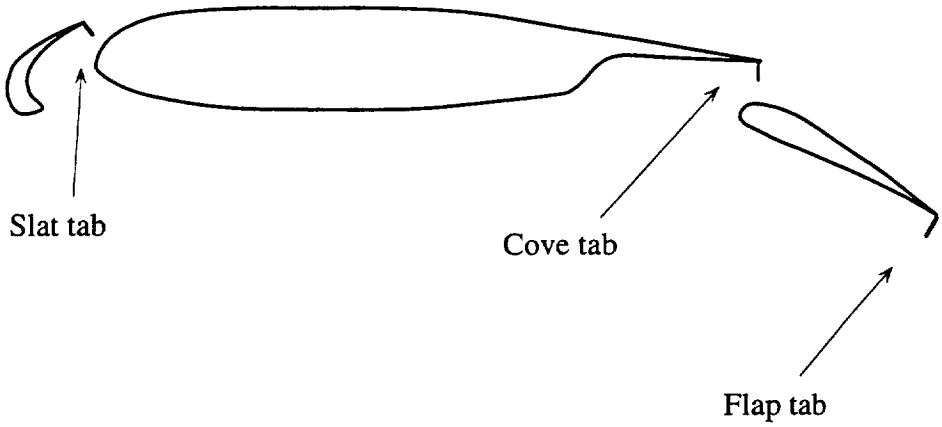

Figure 3: Lift-enhancing tabs on a 3-element airfoil.

wing (note that race car wings are inverted so that lift is toward the race track) resulting in better cornering performance.

Leibeck [5] provides some of the earliest wind tunnel data documenting the effects of a Gurney flap on a single-element airfoil. Leibeck tested a 1.25% chord Gurney flap on a Newman airfoil. Lift coefficient increased by approximately 0.35 at all angles of attack and drag coefficient was reduced by roughly 50 drag counts for all values of lift coefficient. The reduction in drag coefficient was a surprising result to Leibeck. A hypothesized flow field in the vicinity of the Gurney flap, shown in Figure 4, is proposed by Leibeck in an attempt to explain the drag reduction observed in the experiment. However, he lacked sufficient data to verify his hypothesis.

Katz and Largman [6] experimentally investigated the performance of a Gurney flap attached to the flap trailing edge of a two-element race car wing. The Gurney flap had a height of 5% chord. In this case, the Gurney flap was found to provide increases in lift coefficient on the order of 0.5 at a normal operating angle of attack. However, the large size of the Gurney flap used created a significant increase in drag as well. The lift-to-drag ratio for the wing dropped from approximately 8.0 to 6.0 when the Gurney flap was installed.

Roesch and Vuillet conducted tests of lift-enhancing tabs at the trailing edge of single element horizontal stabilizers and vertical tails on helicopters [7]. Tab heights of 1.25% chord and 5% chord were used. The 1.25% chord tab increased lift coefficient by 0.25 to 0.4 at a given angle of attack, with the larger increase occurring at the angle of attack for C_{lmax}. Drag coefficient for this case was essentially the same as the baseline case at the same lift coefficient. The 5% chord tab produced increases in lift coefficient of 0.35 to 0.65 at a given angle of attack, with the larger increase again occurring at the angle of

a) Trailing-edge flow conditions of a conventional airfoil at a moderate lift coefficient.

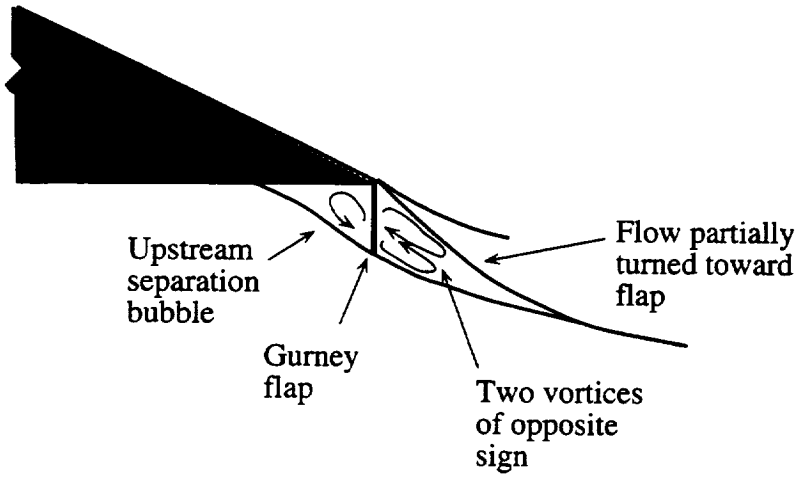

b) Hypothesized trailing-edge flow conditions of the airfoil of (a) with a Gurney flap.

Figure 4: Hypothesized flow field around a Gurney flap [5].

attack for C_{lmax}. In this case, however, the drag coefficient at moderate lift coefficient was nearly doubled. Plots of pressure coefficient distribution on the stabilizer, with and without the tabs, indicates that the tab increases the aft loading of the airfoil as shown in Figure 5. Note that the lift coefficient was held constant at $C_l = 1.07$ for the comparison.

Lift-enhancing tabs mounted at the trailing edge of a two-dimensional wing with a NACA 4412 airfoil section were tested in an experiment performed in the NASA Ames Research Center 7- by 10-Foot Wind Tunnel by Storms [3]. Tab height was varied from 0.5% to 2.0% chord in 0.5% chord increments. The lift coefficient was increased by as much as 0.5 over the baseline using a 2.0% chord tab. The increment in lift coefficient obtained for each increment in tab height grew successively smaller. This implies the existence of an optimal tab height which yields the maximum increment in lift coefficient

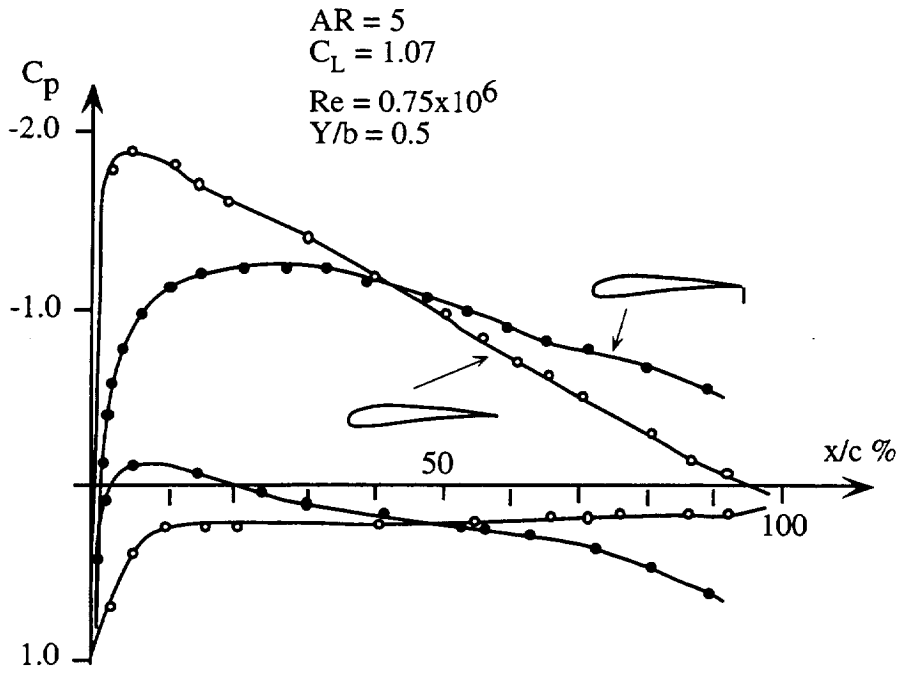

Figure 5: Effect of trailing edge strips on chordwise pressure distribution [7].

for a given airfoil. Drag coefficient at moderate lift coefficients remained unchanged for the smallest tab height and increased by as much as 100% for the largest tab height. The pitching moment coefficient became increasingly negative as tab height was increased. Plots of the pressure distribution on the airfoil indicate that this is a result of the increased loading on the aft portion of the airfoil caused by the tab, as shown in Figure 6. These plots also indicate that the tabs increase the circulation of the airfoil. The tabs were also tested at locations 1.25% and 2.37% chord forward of the trailing edge. Moving the tabs forward approximately 1 to 2 tab heights did not change the effectiveness of the tabs.

In a more recent experiment conducted by Storms [8, 9] in the NASA Ames Research Center 7- by 10-Foot Wind Tunnel, lift-enhancing tabs mounted at the trailing edge of the main element and the flap of a two-element airfoil model were tested. This is the first known experimental data available on the effect of placing lift-enhancing tabs at the trailing edge of the main element on a two-element airfoil. The airfoil was an NACA 63_2–215 ModB airfoil with a 30% chord slotted flap. The flap deployment did not include significant fowler motion. The model was tested at four combinations of flap angle, gap, and overlap. Tab heights of 0.5% and 1.0% chord were tested at the main element trailing edge and a tab height of 0.5% chord was tested at the flap trailing edge. For a flap angle of 22°, lift-enhancing tabs mounted at the trailing edge of the main element reduced the lift coefficient for all angles of attack and drag was substantially increased. When the flap

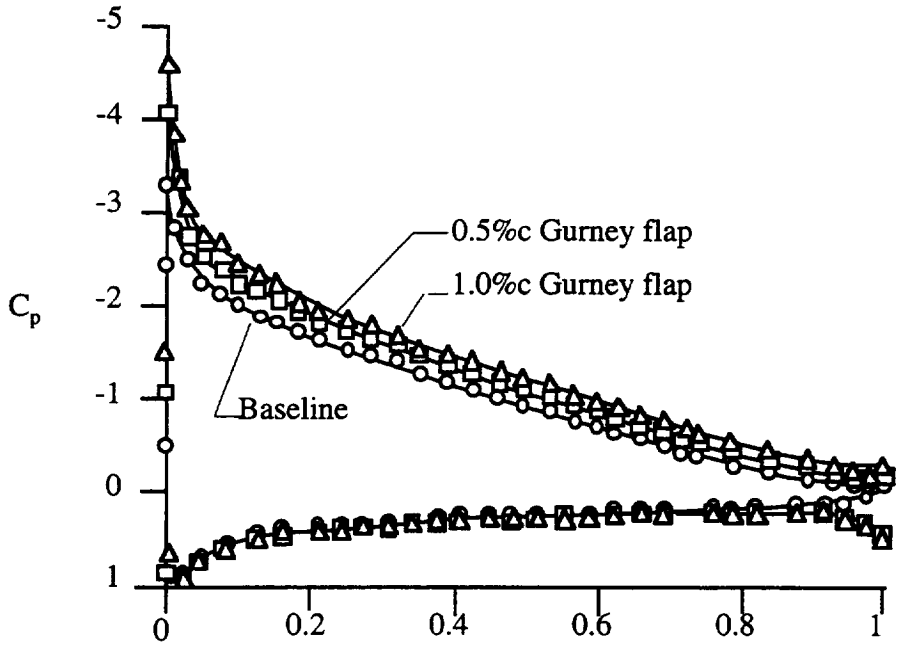

Figure 6: Effect of Gurney flap height on chordwise pressure distribution of a NACA 4412 airfoil at $\alpha = 9°$ [3].

angle was increased to 32°, the flow was separated over the majority of the upper surface of the flap for the baseline case. Addition of a lift-enhancing tab at the trailing edge of the main element caused the flow over the upper surface of the flap to reattach, significantly increasing the lift coefficient and reducing the drag coefficient. A similar result was observed when the flap angle was increased to 42° and the flap gap was made large (5% chord). Unfortunately, this two-element airfoil is not very representative of current transport high-lift systems, due to the lack of significant fowler motion in the flap deployment.

Very little work on formulating an understanding of the flow physics associated with lift-enhancing tabs has been reported in the literature. As mentioned earlier, Leibeck [5] proposed a hypothetical flow field generated by the lift-enhancing tab, but his hypothesis has not yet been rigorously verified. Water tunnel tests of a rectangular wing with NACA 0012 airfoil and a lift-enhancing tab at the wing trailing edge provide some qualitative information on the flow structure behind the tab at low Reynolds number [10]. Dye injected into the flow near the trailing edge indicates the presence of two counter-rotating recirculation regions behind the lift-enhancing tab.

A two-dimensional computational investigation of the lift-enhancing tabs tested on the 4412 airfoil of reference [3] was conducted by Jang [11] which provided some insight

into the flow physics associated with tabs as applied to the trailing edge of a single-element airfoil. The computations were performed using the incompressible Navier-Stokes code INS2D-UP. The outer boundary of the C-grid used to represent the airfoil in these computations was only about 6 chord lengths away from the airfoil surface and the grid was relatively coarse (250x69). Comparisons of the computational and experimental results [3] indicate that the general trends observed in the experimental lift and drag coefficient data when a tab is added to the wing trailing edge are reproduced by the computational results. However, the magnitude of the change in the lift and drag coefficients due to adding a tab of given size to the wing trailing edge is not accurately reproduced by the computations.

A similar computational investigation of the multi-element airfoil described in references [8] and [9] was conducted by Carrannanto [12]. The two-element airfoil was represented with a composite structured grid created using a chimera scheme. The C-grid for the main element consisted of 307 x 98 grid points and the C-grid for the flap consisted of 155 x 42 grid points. The boundary layer along the tab surface was not resolved by the grids used in this study. The outer boundary of the composite grid was located 10 chord lengths from the airfoil surface. A comparison of the experimental and computational results indicates that the magnitude of the change in lift and drag coefficients due to the addition of a tab at the trailing edge of the main element is predicted well by the computations. However, the slope of the lift coefficient versus angle of attack curve predicted by the computations did not match the experimental results very well. One of the interesting results of this computational study is that when a tab is added to the main element, the separated flow over the upper surface of the flap is replaced with a flow reversal in the wake of the main element above the trailing edge of the flap, as shown in Figure 7. This reversal of the flow away from the flap surface appears to be due to the inability of the main element wake to negotiate the adverse pressure gradient encountered over the upper surface of the flap.

In the present research, a detailed parametric experimental and computational investigation of the effect of lift-enhancing tabs on a multi-element airfoil is conducted. The objective of the investigation is to develop an understanding of the flow physics associated with lift-enhancing tabs on a multi-element airfoil configuration which is representative of current transport high-lift systems. It is anticipated that an understanding of the flow physics will lead to the development of a model which can be used to explain how lift-enhancing tabs work on multi-element airfoils. To accomplish the objective of this study, a two-element high-lift airfoil was tested in the NASA Ames 7- by 10-Foot Wind Tunnel [13]. The airfoil tested was the two-element airfoil described in references [8]

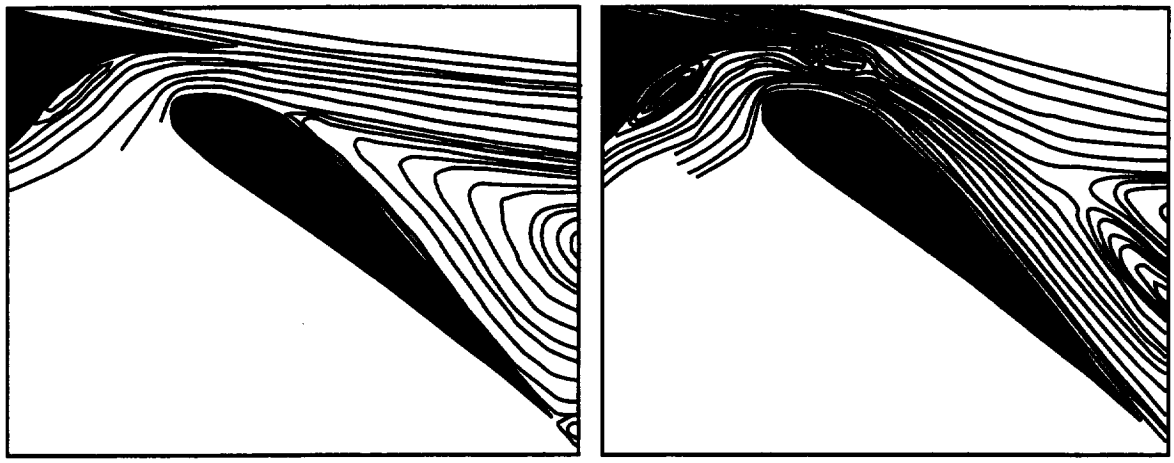

a) Baseline airfoil with no tab, $\alpha = 8.43°$ b) Airfoil with 1%c tab at 1%c from trailing edge, $\alpha = 8.5°$

Figure 7: Computed streamline patterns around NACA 63_2-215 ModB airfoil with a slotted flap. Recreated from reference [12].

and [9], but with the slotted flap replaced by a 30% chord fowler flap. The parameters that were systematically varied in the test are flap angle, flap gap, tab height, and the element to which the tab was attached. Data acquired during the test includes detailed surface pressure measurements and seven-hole probe flow surveys behind selected configurations.

A companion set of computations was performed using the incompressible Navier-Stokes code INS2D-UP. Some of the computations were performed prior to the experiment and were used to guide the experimental work. Computational solutions were obtained for a large number of the configurations tested in the experiment. After validating the Navier-Stokes computations with experimental results, the experimental and computational databases are used to develop an understanding of how lift-enhancing tabs function on a multi-element airfoil.

This report describes the results of the aforementioned experimental and computational investigation. Details of the experimental setup and the model are given. The test procedures used for the experiment are discussed. The governing fluid dynamics equations are derived and the specific numerical scheme used by INS2D-UP to solve them is described. The grid generation process used and the composite grids used for the computations are covered in detail, along with the boundary conditions employed. A comparison of the experimental and computational results is presented and differences

between the two sets of data are discussed. Finally, a theoretical model which describes how lift-enhancing tabs work on a multi-element airfoil is developed.

CHAPTER II
EXPERIMENTAL SET-UP

A two-dimensional two-element high-lift airfoil was tested in the NASA Ames Research Center 7- by 10-Foot Wind Tunnel. Baseline configurations and configurations which included lift-enhancing tabs were tested for a variety of different flap riggings. This chapter describes the experimental set-up which was used. First, a description of the test facility will be given. The model installation will be outlined, followed by a description of the model itself. Finally, the model instrumentation and the data acquisition system will be described.

Facility Description

The NASA Ames 7- by 10-Foot Wind Tunnel is a closed-circuit, single-return wind tunnel with the return passage at atmospheric pressure. A diagram of the tunnel is shown in Figure 8. The tunnel is capable of a dynamic pressure range of 5 to 200 psf. The free

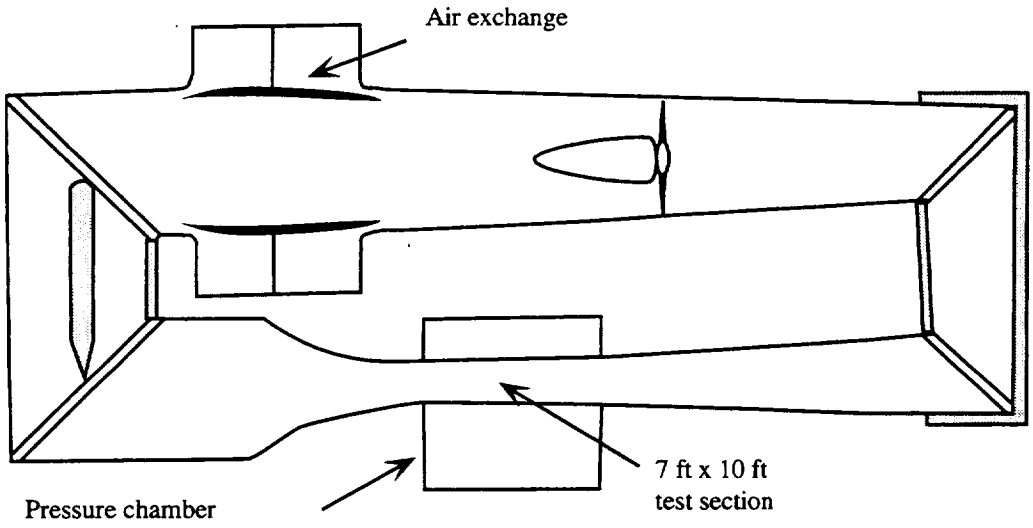

Figure 8: Schematic diagram of the NASA Ames 7- by 10-Foot Wind Tunnel.

stream turbulence intensity level in the test section is 1.0% at a free stream velocity of 225 ft/sec. The test section is 15 ft long, with a constant height of 7 ft and a width at the beginning of the test section of 10 ft. The width of the test section includes a one percent divergence to account for the test section boundary layer growth. The maximum boundary layer thickness in the test section is approximately 6 - 9 in. The side walls of the test section are removable and a variety of side wall options are available, including acoustically

treated side walls and side walls with large windows made of high quality optical glass. The side walls with windows allow flow visualization techniques and non-intrusive flow measurement techniques such as laser doppler velocimetry (LDV) to be used. The 7- by 10-Foot Wind Tunnel is used primarily for small-scale exploratory investigations in the areas of basic fluid mechanics and acoustics.

A traversing rig capable of linearly traversing probes vertically, horizontally, and longitudinally is mounted in the tunnel ceiling. The traverse rig can be run manually or operated by computer in a closed-loop fashion for automated traverses. Many different types of probes can be accommodated on the traverse, including hot wire probes, seven-hole probes, and pitot-static probes. All of the instrumentation wiring and pressure tubing required for a particular probe can be routed out of the test section internally in the traverse rig. The entire volume of the test section can be surveyed using the traverse rig.

Model forces and moments are generally measured using the tunnel's external balance system. Sting mounted models with an internal balance can also be accommodated. A turntable in the tunnel floor allows the model angle-of-attack to be varied. A second turntable can be mounted in the tunnel ceiling for two-dimensional testing. When two-dimensional models are mounted in the tunnel using both turntables, the tunnel external balance system cannot be used for direct measurement of forces and moments. In this situation, model loads must be obtained by integrating surface pressures on the model. Model drag for a two-dimensional model can be obtained using wake survey techniques.

Two pressurized air systems are available for use in the 7- by 10-Foot Wind Tunnel. The high-pressure air system has a supply pressure of 3000 psig and can deliver mass flow rates of 10.0 lb_m/sec. Heaters installed in the system allow the air temperature to be controlled. The low-pressure air system has a supply pressure of 140 psig and can deliver mass flow rates of 30.0 lb_m/sec. The low-pressure system is convenient to use in applications where high air pressures are not required, such as for boundary layer control (BLC) applications.

Model Installation

The two-element airfoil model used for this study was mounted vertically in the Ames 7- by 10-Foot Wind Tunnel as shown in Figure 9. The model is attached at the top and bottom to pedestals, which in turn are attached to the tunnel upper and lower tunnel turntables. The model is aligned in the tunnel so that at an angle of attack of 0° the model chord line is parallel to the tunnel centerline. This was accomplished using a laser transit. Wall-to-wall image planes are mounted to the tunnel ceiling and floor as shown in Figure 9

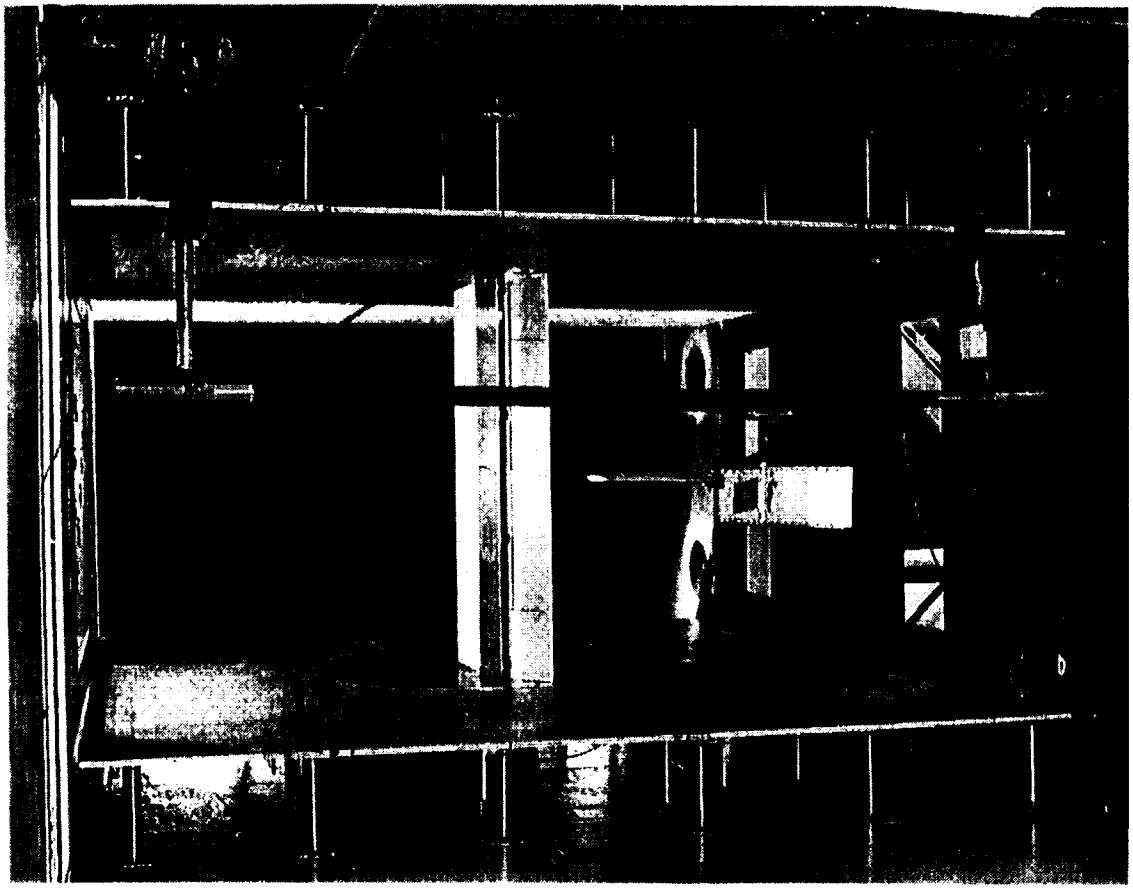

Figure 9: Installation of the NACA 63_2-215 ModB airfoil in the NASA Ames 7- by 10-Foot Wind Tunnel.

to keep the model out of the tunnel boundary layer and to serve as end walls for the airfoil model. The image planes are located at a distance of one foot from the floor and ceiling and extend approximately 2.5 airfoil chord lengths upstream and downstream from the center of rotation of the model.

Auxiliary turntables are mounted between the model and the pedestals, coplanar with the ground planes, to accommodate the model Boundary Layer Control (BLC) system. The BLC system is used to ensure the flow over the wing is two-dimensional. The BLC system, shown in Figure 10, is composed of 4 tangential blowing slots mounted

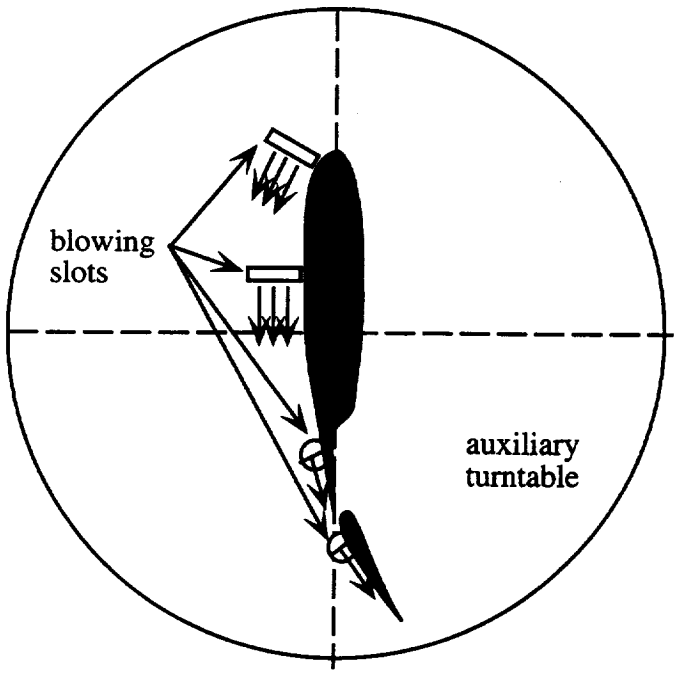

Figure 10: Schematic diagram of the Boundary Layer Control (BLC) system.

on each auxiliary turntable. The blowing slots are located on the upper side of the airfoil at the leading edge, the mid-chord, and the trailing edge of the main element and the mid-chord of the flap. The slots for the trailing edge of the main element and for the flap are mounted in circular plugs. This permits the direction of the flow from the slots to be adjusted for different flap angle settings. Air for the BLC system is provided by the tunnel low-pressure air system. A single supply line is manifolded to three pairs of gate valves as indicated in Figure 11. One pair of valves controls the upper and lower main-element leading-edge slots. The second pair of valves controls the upper and lower main-element mid-chord slots. The final pair of valves controls the upper and lower main-element

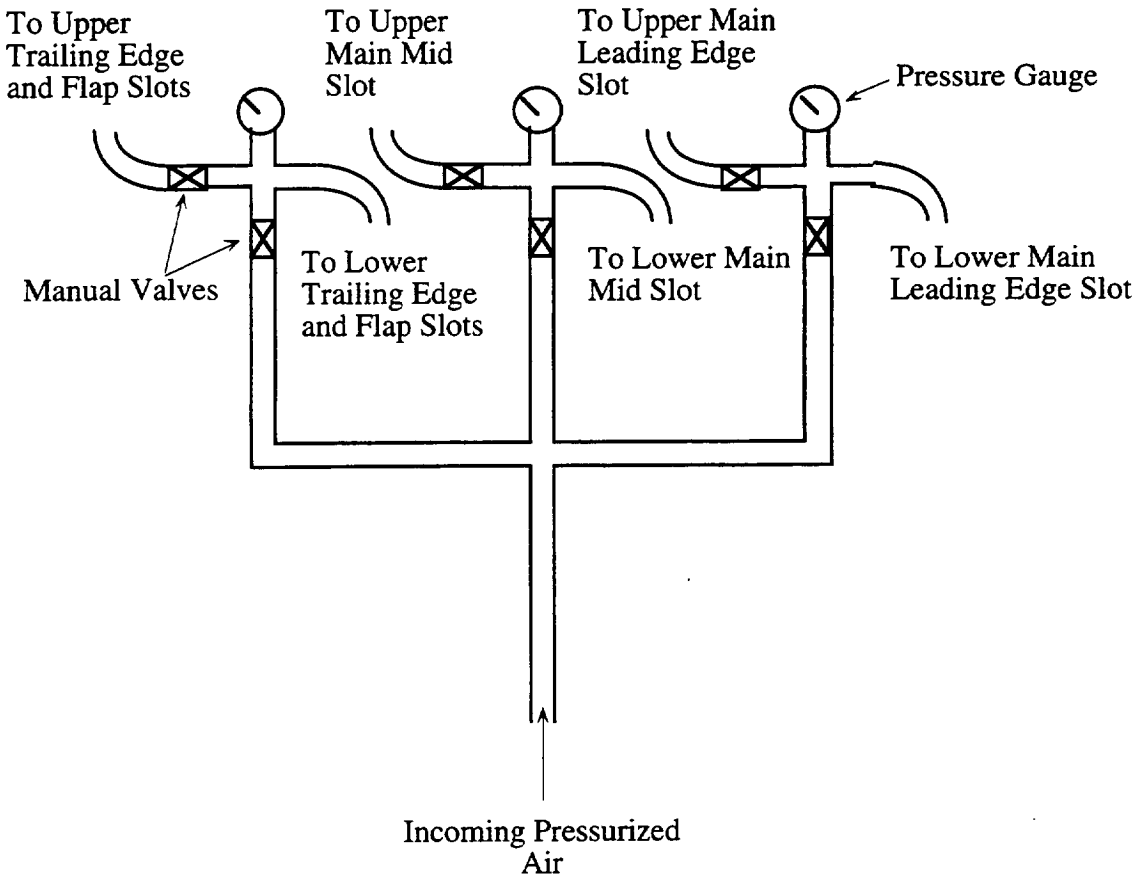

Figure 11: Manifold setup for the Boundary Layer Control (BLC) system.

trailing-edge and flap slots. This allows the plenum pressure for each pair of upper and lower blowing slots to be matched to one another.

Model Description

The model used for this test is a rectangular wing with an NACA 63_2-215 ModB airfoil. The ModB designation refers to slight modifications that were made to the upper surface of the original NACA airfoil by Hicks [14] to improve cruise performance. Coordinates for the main element and the flap are given in Appendix A. The span of the wing is 60 in. and the chord for the clean airfoil is 30 in. The trailing edge of the wing from x/c=0.62 to x/c=1.0 is removable and can be replaced with a trailing edge that has a flap cove incorporated as shown in Figure 12. For this test, a trailing edge that extended from x/c=0.62 to x/c=0.95 was used along with a 30% chord fowler flap.

The fowler flap is attached to the wing trailing edge by flap brackets at span locations of y/b = 0.033, 0.346, 0.654, and 0.967. The brackets are a two piece

arrangement as shown in Figure 13, with holes drilled to allow nominal flap deflection angles of δ_f = 10°, 20°, 30°, and 40°. Flap overlap is continuously adjustable between x_{ol}/c = 0.002 and x_{ol}/c = 0.041. Flap gap can be set in increments of 1% chord starting at z_g/c = 0.02 using a series of spacer blocks and/or a second set of brackets for larger gaps. Flap deflection, gap, and overlap were measured as shown in Figure 14.

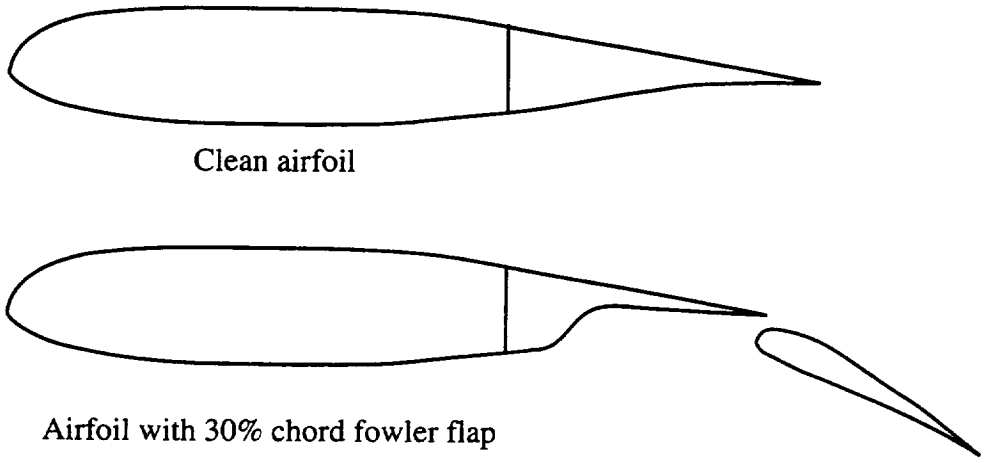

Figure 12: Diagram of the NACA 63_2-215 ModB airfoil.

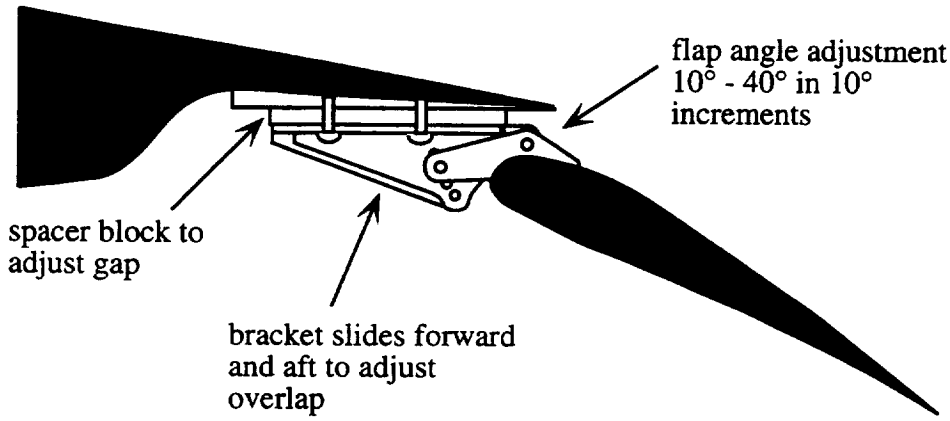

Figure 13: Sketch of flap brackets.

Instrumentation

Instrumentation on the model consisted of 9 rows of static pressure taps on the main element and 3 rows of static pressure taps on the trailing edge and the flap. The locations of the rows of pressure taps are shown in Figure 15. The position of the flap brackets is shown for reference. A total of 392 pressure taps were installed on the model. The coordinate locations of all the pressure taps on the row at the mid-span of the model are

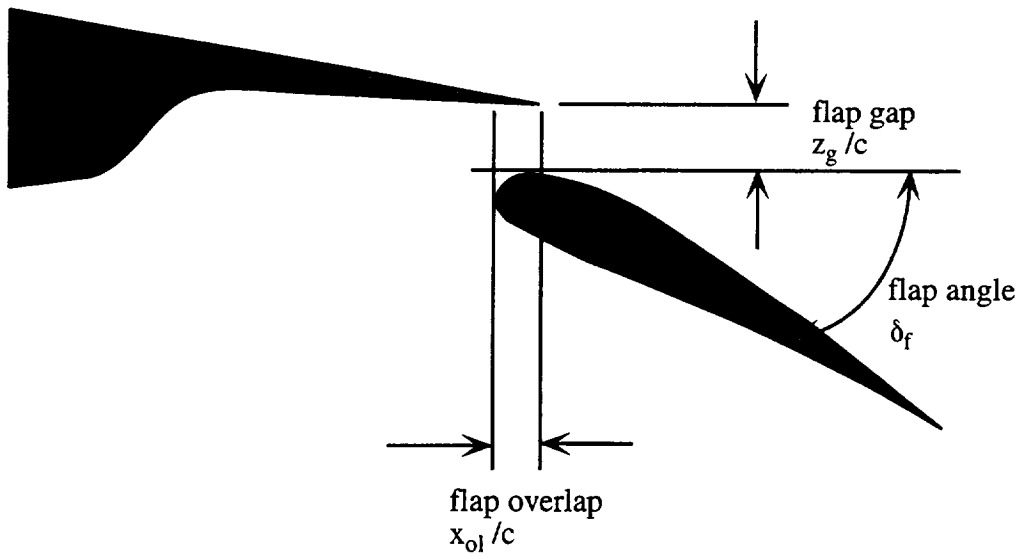

Figure 14: Definition of flap rigging parameters.

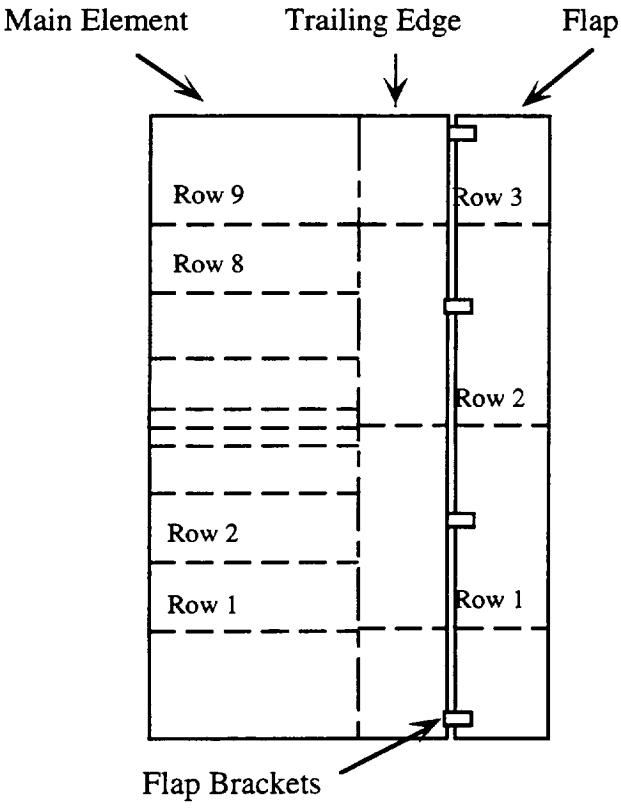

Figure 15: Location of static pressure tap rows on main element, trailing edge, and flap.

given in Appendix B. Static pressure taps were also installed on both image planes. A row of 10 taps spanning the width of the tunnel was installed parallel to the leading edge of each of the image planes. These taps were used to obtain a reference dynamic and static pressure for the model. All of the static pressure taps were connected to Pressure Systems Incorporated (PSI) electronic pressure sensing modules (either 48 or 64 port modules). The modules were stored in a thermal chamber designed to keep the temperature constant at approximately 110°F in order to reduce thermal drift of the transducers to a negligible value.

A wake rake was used to obtain the airfoil viscous drag. The wake rake can be seen mounted to the tunnel traverse rig in Figure 9. It is composed of a rectangular wing with a symmetric airfoil which holds all the pressure probes making up the rake and a main body which houses the drive mechanism for pivoting the rake as well as the electronic pressure sensing modules. The rake has 91 total pressure tubes, 9 static pressure tubes, and 5 three-hole directional probes. The spacing of the total pressure tubes is denser (0.25 in.) in the middle of the rake and sparser (1 in.) at the ends. The static pressure tubes and three-hole directional probes were spaced equally along the length of the rake. The total wake rake width is 36 in. The static pressure tubes were vertically offset from the plane of the total pressure tubes by 1.0 in. to minimize interference effects on the static pressure measurement. The three-hole directional probes are used to line up the wake rake with the local two-dimensional flow field. All of the pressure probes from the wake rake are connected to PSI electronic pressure sensing modules contained in the main body of the wake rake. The modules were mounted to a hot-plate designed to keep the temperature of the modules constant at 110°F in order to reduce thermal drift of the transducers to a negligible value.

A sting with three seven-hole probes was also mounted to the tunnel traverse rig in place of the wake rake for part of the test [15]. The seven-hole probes were used to conduct flow surveys behind the model. A diagram of the three seven-hole probes mounted on the sting is shown in Figure 16. All three seven-hole probes were connected to a PSI module stored in the pod at the back end of the sting mount. This PSI module was also mounted on a hot-plate to keep the temperature of the module constant.

Test section conditions were recorded for every data point during the test. The parameters defining the test section conditions are test section relative humidity, test section temperature, reference static pressure, reference dynamic pressure, atmospheric pressure, and model angle of attack. The reference static and dynamic pressures were measured using the two rows of static pressure taps on the images planes, as mentioned earlier. The

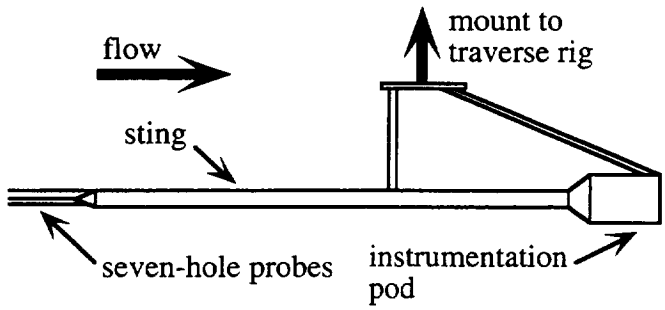

a) Side view

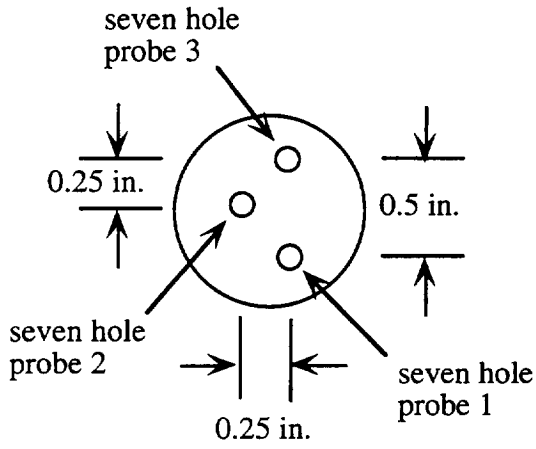

b) View of sting tip and probes looking downstream

Figure 16: Schematic of three seven-hole probes mounted on a sting.

rationale for obtaining the reference static and dynamic pressures in this manner and the actual procedure used will be discussed in the next chapter.

The majority of the experimental measurements were made using the PSI 8400 system and PSI electronic pressure sensing modules. The accuracy of measurements made using this system is 0.25% of the full-scale range of the individual modules. Modules with ranges of 10 in. H_2O, 1 psid, 2.5 psid, 5 psid, and 10 psid were used to measure the static pressures on the model, as well as the pressures from the wake rake, the seven-hole probe, and static pressures on the image planes. The criteria used for assigning pressure measurements to different modules was that the measurements should utilize the majority of the range of the module. This criteria minimizes the error in a given pressure measurement. The tunnel temperature measurement was accurate to ±0.3° F. The relative humidity measurement was accurate to ±0.5%. The barocell used to measure atmospheric pressure

was accurate to ±0.002 psi. The model angle of attack measurement was accurate to ±0.05°. There is a hysteresis in the mechanism for changing model angle of attack of approximately 0.25° if the direction of the turntable is reversed. Thus during this test, model angle of attack was always increased from 0° to the angle of attack for stall. The procedure for returning the model to 0° was to bring the model to -2° first and then return it to 0°.

Data Acquisition System

The data acquisition system used for this experiment consisted of a Macintosh Quadra 650 computer running Labview version 2.2 software by National Instruments. In addition, a PSI 8400 system was used to calibrate and acquire data from the PSI electronic pressure sensing modules. Communication between the PSI 8400 and the Macintosh Quadra was handled by means of a GPIB interface. The Labview software allowed complete control of the data acquisition process. For example, instructions could be issued in Labview via a graphical user interface to have the PSI 8400 system calibrate the PSI electronic pressure sensing modules or to take a data point. The data acquired by the PSI 8400 system was passed via the GPIB interface to Labview for display and storage. Analog signals such as test section temperature were acquired using an A/D converter card from National Instruments in the Macintosh Quadra. This was also controlled using Labview. The Labview data acquisition routines were based on the routines originally written by Storms for the experiment of references [8] and [9].

Data reduction was handled within the Labview program as well. Labview routines were written to convert all the measured pressures to pressure coefficients and to numerically integrate the pressure distributions at each row of pressure taps on the model to obtain force and moment coefficients. A routine was written to convert data acquired by the wake rake to a drag coefficient. The data acquired using the seven-hole probes was converted to velocity components and static and dynamic pressure. All of the measured and reduced data was written to an ASCII file which was compressed and appended to an indexed, binary database file after each run.

An important aspect of the Labview data acquisition program was the capability to graphically display selected subsets of the data during a run. The Labview program could be switched to a real-time mode during a run and plots of pressure coefficient on the wing and flap displayed. The plots were updated about once every two seconds. This allowed the pressure distribution on the wing to be checked for two-dimensionality and also permited easy identification of static pressure taps that were leaking or plugged. Plots of the wake rake pressures allowed the wake rake to be centered on the wake at each angle of

attack and permited alignment of the wake rake with the local streamlines. The pressure at each of the blowing slots in the BLC system was also monitored to ensure that the BLC system was functioning properly. Test section parameters were displayed in a table that was continuously updated during a run. After each data point was taken, a running plot of lift coefficient versus angle of attack was updated with the latest point, permitting easy identification of the angle of attack for C_{lmax}. The ability to display data graphically during a run greatly increased the efficiency of the test and helped ensure the quality of the data.

CHAPTER III
TEST PROCEDURES

The test of the NACA 63_2-215 ModB airfoil in the NASA Ames 7- by 10-Foot Wind Tunnel was divided into several phases. First, the seven-hole probes were calibrated in the empty tunnel. Next a dynamic pressure calibration between the image planes was performed. Finally, the model was installed and tested. This chapter describes the various calibrations that were performed prior to installing the model. The basic test procedures used during the test are then discussed. The chapter concludes with a discussion of data quality and repeatability.

Empty Tunnel Calibrations

The first part of the test was dedicated to calibrating the seven-hole probes in the empty wind tunnel. The seven-hole probe sting assembly was mounted to a calibration rig which in turn was mounted to the traverse rig in the tunnel. The sting could then be set at any arbitrary angle α_{7h} in the vertical plane, and β_{7h} in the horizontal plane. This setup permitted a range of $\pm 45°$ for both α_{7h} and β_{7h}. A pitot-static probe mounted in the test section was used to monitor test section dynamic pressure. The tunnel dynamic pressure was set to approximately 50 psf. The probe was run through the full range of α_{7h} and β_{7h} angle combinations in 5° increments. At each known geometric angle, the seven pressures on each probe were recorded and converted to nondimensional coefficient form. All of the data was used to form calibration tables employing the technique described by Zilliac [16].

Once the seven-hole probe calibration was complete, the image planes were installed in the tunnel. A dynamic pressure calibration was performed to obtain the dynamic pressure between the image planes with no model installed as a function of the dynamic pressure measured using a static pressure ring upstream of the test section. A pitot-static probe was mounted to the traverse rig and was positioned at the center of the test section. Dynamic pressure, as measured by the static pressure ring upstream of the test section, was varied from 10 psf to 70 psf in 5 psf increments and the corresponding dynamic pressure measured using the pitot-static probe was recorded. The dynamic pressure measured by the pitot-static probe was corrected for compressibility effects using equation (1) below, which was taken from reference [17].

$$\Delta q_\eta = \mathbf{0.0089} + \mathbf{0.0033} * q_u + \mathbf{1.319E-4} * q_u^2 + \mathbf{1.24E-7} * q_u^3$$
$$q_c = q_u + \Delta q_\eta \qquad (1)$$

The calibration was performed with the BLC system off and repeated with the BLC system on. The difference between the calibration curves obtained with the BLC system on and off was negligible. The dynamic pressure based on this calibration was recorded for all data points taken during the test to try to assess the change in dynamic pressure due to changes in model blockage.

The reference dynamic and static pressures used to nondimensionalize the pressure data on the airfoil were obtained from a numerical integration of the static pressure tap measurements on the image planes. As mentioned previously, static pressure taps were installed on both the upper and lower image planes, providing a redundant set of static pressures with which to compute the reference static pressure. The number of static taps required to accurately compute the reference static pressure was determined by examining the pressure distribution on the image plane predicted by a Navier-Stokes computation of the two-element airfoil in the tunnel.

Basic Test Procedure

Once the empty tunnel calibrations were complete, the model was installed between the image planes. Boundary layer trip strips were installed on the upper and lower surface of the main element at x/c = 0.05 and x/c = 0.10 respectively. The trip strips consisted of 0.015 in. diameter glass beads attached to the wing surface with Polaroid film fixer. The required diameter of the glass beads for the present test conditions was determined using the method of reference [18]. Trip strips were not used on the flap in this test. The number of changes to the flap configuration required during the test made it too difficult to maintain a consistent trip strip on the flap.

The supply pressure required for each of the blowing slots of the BLC system was determined as follows. The tunnel dynamic pressure was set to 50 psf at the upstream static pressure ring, yielding the required reference dynamic pressure of 66 psf between the image planes. The model surface pressures for rows 1, 5, and 9 on the main element and rows 1, 2, and 3 on the trailing edge and flap were plotted on a real-time display to monitor variations in pressure across the span of the wing. The supply pressure for each of the blowing slots was set to minimize variations across the span of the wing. The real-time display was monitored throughout the test and the supply pressures needed to maintain two-dimensional flow were found to be independent of model configuration. The pressure in the plenum immediately upstream of each blowing slot was recorded throughout the entire test to ensure that the BLC system was functioning properly for all data points.

The test matrix included parametric variations of flap deflection angle δ_f, flap gap z_g/c, tab height z_t/c, and element to which the tabs were attached. Flap overlap was not

varied for this test. A previous test of the baseline airfoil indicated that a flap overlap of $x_{ol}/c = 0.015$ was near optimum for most flap riggings. Thus, this value of flap overlap was used for the present test. All data was taken at a Reynolds number based on wing chord of 3.5 million. Table 1 summarizes all the parameters varied in this test.

Table 1: Summary of test parameters.

δ_f	z_g/c	x_{ol}/c	z_t/c	element with tab
19°	0.02	0.015	0	none
29°	0.03		0.0025	main
39°	0.04		0.005	flap
	0.05		0.01	both

For each configuration tested, the model was rotated through an angle-of-attack range starting at 0° and increasing until the airfoil stalled. The lift coefficient and pitching moment coefficient were computed by numerically integrating the center row (y/b = 0.5) of surface static pressures on the main element, trailing edge, and flap. The drag coefficient was computed by applying Betz's formula [19] to the wake rake data, which was taken at a position one chord length behind the flap trailing edge. Betz's formula can be written as shown in equation (2).

$$C_d = \int \frac{P_{T\infty} - P_{swr}}{q_\infty} d\left(\frac{y}{l}\right) + \int \left(\sqrt{\frac{P_{T\infty} - P_{swr}}{q_\infty}} - \sqrt{\frac{P_{Twr} - P_{swr}}{q_\infty}}\right)\left(\sqrt{\frac{P_{T\infty} - P_{swr}}{q_\infty}} + \sqrt{\frac{P_{Twr} - P_{swr}}{q_\infty}} - 2\right) d\left(\frac{y}{l}\right) \quad (2)$$

The NACA 63_2-215 ModB multi-element airfoil has a very abrupt stall. The flow over the entire upper surface of the airfoil separates when the angle of attack exceeds that for C_{lmax}. This creates a very turbulent wake downstream of the airfoil which causes heavy buffeting of the wake rake and the traverse system. The wake rake had to be tethered to the tunnel ceiling with a steel cable during each run so that the buffeting from the turbulent wake would not cause damage to the traverse system. The lateral position of the wake rake was not changed during a run. An investigation was made at the beginning of the test to determine how much the wake shifted laterally for a given flap deflection angle as angle of attack was increased from 0° up to the angle of attack for stall. The lateral shift in the wake position, as measured by the wake rake, over the angle of attack range studied

was small enough that the complete wake total pressure deficit could be contained within the region of densely spaced total pressure tubes on the wake rake with the wake rake in a fixed position. The wake rake was rotated as model angle of attack was changed, to keep the wake rake lined up with the local flow direction as determined by the directional probes on the rake. The lateral position of the wake rake did have to be changed, however, when the flap deflection angle was changed on the model.

As mentioned previously, the majority of the measurements for the test were made with the PSI 8400 system and PSI electronic pressure sensing modules. A calibration was performed on all the pressure sensing modules prior to each run. The calibration lines and the reference pressure line were leak-checked every day prior to any testing. For every data point, the PSI 8400 system was used to acquire 6 measurement sets of 100 samples each. The data in each measurement set was averaged and then the 6 measurement sets were ensemble averaged. Each data point took approximately 30 seconds to acquire with the PSI 8400 system. The total time to acquire and process each data point, including data reduction and writing the data to the database file, using the Labview data acquisition system was just over one minute. A typical run, including a model change and PSI system calibration, took between 30 and 45 minutes to complete.

Data Quality

Because the data from this test is to be used as a database for validating two-dimensional computational results, time was spent ensuring that the flow over the model was two-dimensional. One particular concern was the effect of the flap brackets on the flow over the flap. Tufts were applied to the upper and lower surface of the flap to determine if the flap brackets were causing any three dimensional flow. At a flap deflection of 29° and a flap gap of $z_g/c = 0.03$, wedge-shaped regions of flow separation were observed on the upper surface of the flap behind each flap bracket as illustrated in Figure 17. The cause of the flow separation was traced to the cutouts in the flap where the bracket was mounted. When these cutouts were filled in with clay, the regions of flow separation disappeared. The separated flow on the flap was not evident in the pressure distributions measured on rows 1, 2, and 3 on the flap because the pressure tap rows happened to lie between the regions of separated flow. A comparison of lift coefficient versus angle of attack curves for the open and the filled cutouts is shown in Figure 18. Filling in the flap bracket cutouts shifts the lift coefficient curve up by $\Delta C_l = 0.1$. All the data for this test was taken with the flap bracket cutouts filled in.

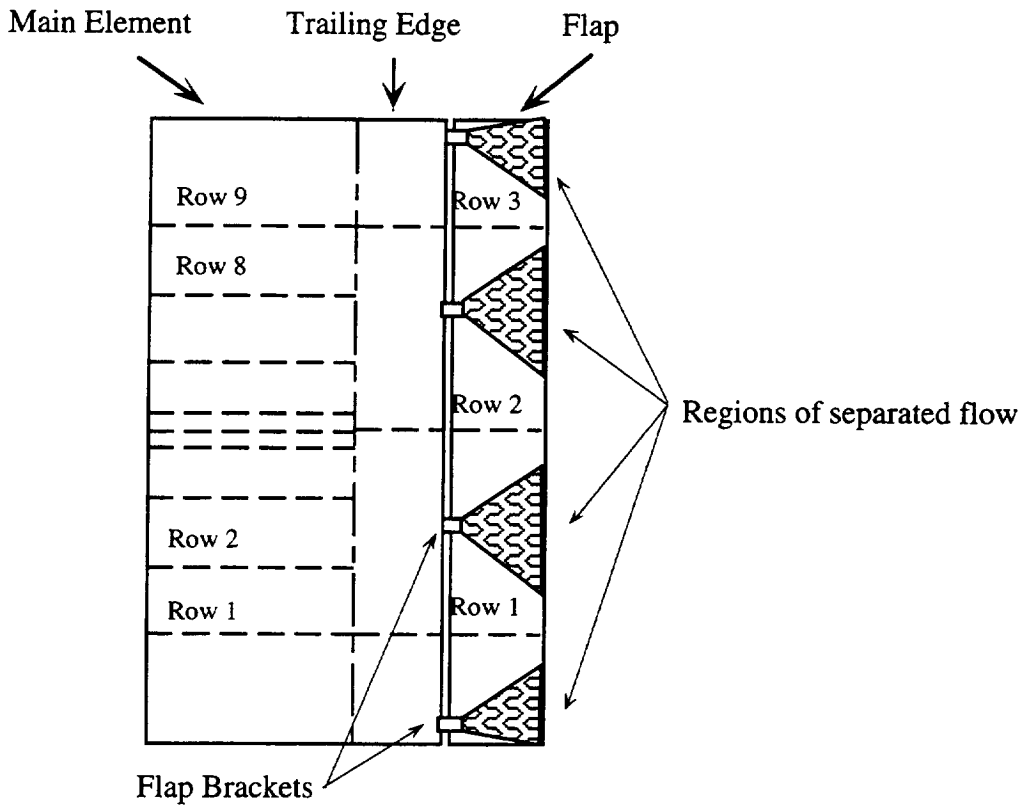

Figure 17: Regions of separated flow on flap upper surface indicated by tufts.

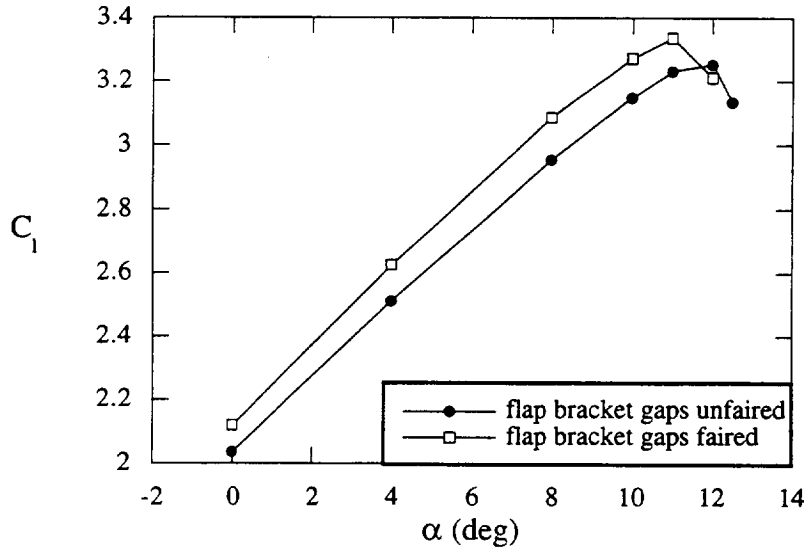

Figure 18: Comparison of lift coefficient versus angle of attack curves for the open and the filled-in flap bracket cutouts. ($\delta_f = 29°$, $z_g/c = 0.03$, $x_{ol}/c = 0.015$)

Data repeatability was assessed by comparing force and moment coefficient curves for different runs of the same configuration. The lift coefficient was repeatable to within $\Delta C_l = \pm 0.005$ for lift coefficients below C_{lmax}. C_{lmax} was repeatable to within $\Delta C_l = \pm 0.01$. The larger uncertainty in lift coefficient at C_{lmax} is due to unsteadiness in the onset of stall. Stall for this airfoil occurred when the flow over the upper surface of the main element separated near the leading edge, causing a rapid decrease in lift coefficient with increasing angle of attack. At C_{lmax}, flow over the upper surface of the main element intermittently separated and reattached. Because the turbulent flow from the stalled airfoil buffeted the wake rake severely, the angle of attack polars only extended far enough into stall to define the maximum lift coefficient. When no flow separation was present on either the flap or the main element, the drag coefficient was repeatable to within $\Delta C_d = \pm 0.001$ or ± 10 drag counts. If flow separation was present over either the main element or the flap, the drag coefficient was repeatable to within $\Delta C_d = \pm 0.003$ or ± 30 drag counts. The pitching moment coefficient was repeatable to within $\Delta C_m = \pm 0.0004$ for lift coefficients below C_{lmax}. At C_{lmax} the pitching moment coefficient was repeatable to within $\Delta C_m = \pm 0.001$.

Wake profiles were also measured behind selected configurations using the set of three seven-hole probes mounted on the traverse rig. The seven-hole probe data was used to obtain an independent check on the accuracy of the drag coefficients computed with the wake rake data. The measurements with the seven-hole probes were made at the same location behind the model as the wake rake measurements. Profiles were obtained for an entire angle-of-attack polar and drag coefficients were computed from the measured profiles using Betz's formula. Additional profiles were measured with the seven-hole probes at a position 0.067 chords aft of the flap trailing edge with the airfoil at 0° angle of attack.

Figure 19 shows a comparison of drag coefficient versus angle of attack curve computed using wake rake data with a similar curve computed using seven-hole probe data. At an angle of attack of 0°, there is a difference of 30 drag counts between the drag coefficient computed from wake rake data and the drag coefficient computed from seven-hole probe data. The difference in drag coefficient computed from seven-hole probe data taken one chord behind the airfoil and data taken 0.067 chords behind the airfoil is about 10 drag counts. The drag coefficients obtained from the wake rake data and the seven-hole probe data agree to within 10 drag counts for angles of attack greater than 0°.

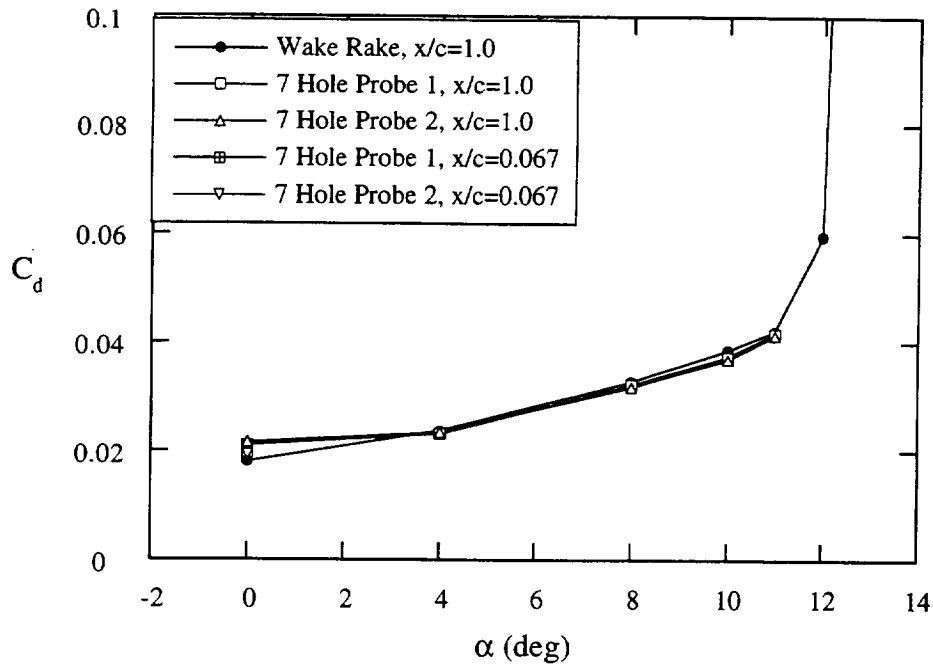

Figure 19: Comparison of drag coefficient versus angle of attack curves computed using wake rake data and seven-hole probe data.

CHAPTER IV
GOVERNING FLUID DYNAMICS EQUATIONS

The most general set of governing equations for problems in fluid dynamics are the Navier-Stokes equations. Although the Navier-Stokes equations, as originally derived, are a mathematical expression of the law of conservation of momentum in a fluid flow, it is common practice to include the equations for conservation of mass and energy as part of the Navier-Stokes equation set. The equations account for both spatial and temporal variations in mass, momentum, and energy of a fluid acting under the influence of forces such as gravity and the forces generated due to the viscosity of the fluid. The Navier-Stokes equations can be expressed in either integral or differential form. Exact, closed form solutions to the Navier-Stokes equations do not exist except for special, simplified cases. The Navier-Stokes equations are generally solved using numerical methods which require the flow domain to be discretized into a computational grid. Numerical solutions of the full three-dimensional, time accurate Navier-Stokes equations can be very costly to compute.

Subsets of the Navier-Stokes equations can be obtained by making simplifying assumptions appropriate to the type of fluid dynamics problem being analyzed. Common examples of subsets of the Navier-Stokes equations include the Reynolds-averaged Navier-Stokes equations, the incompressible Navier-Stokes equations, the Thin-Layer Navier-Stokes equations, and the Parabolized Navier-Stokes equations. The Navier-Stokes equations can also be simplified by assuming that the fluid flow problem being analyzed is two-dimensional in nature. Further simplification of the governing equations for fluid dynamics can be made by neglecting the effects of viscosity and heat transfer. The particular fluid dynamics problem being analyzed will generally dictate what simplifying assumptions can be made.

The form of the Navier-Stokes equations chosen to represent the fluid dynamics problem being examined in this research is the two-dimensional Reynolds-averaged Incompressible Navier-Stokes equations. The simplifying assumptions applied to the full Navier-Stokes equations and their impact on the computed solutions will be discussed in the following sections. A brief overview of the turbulence model used in the computations will be given. Finally, the scaling of the governing equations and the generalized non-orthogonal coordinate transformation applied to the equations will be covered.

Derivation of Governing Equations

The three-dimensional Navier-Stokes equations can be written as a set of five partial differential equations expressing the conservation of mass, momentum, and energy. Using tensor notation, they can be written as

$$\frac{\partial \rho}{\partial t} + \frac{\partial (\rho u_i)}{\partial x_i} = 0 \tag{3a}$$

$$\frac{\partial (\rho u_i)}{\partial t} + \frac{\partial (\rho u_i u_j)}{\partial x_j} = \rho f_i - \frac{\partial p}{\partial x_i} + \frac{\partial}{\partial x_j}\left\{\mu\left[\left(\frac{\partial u_i}{\partial x_j} + \frac{\partial u_j}{\partial x_i}\right) - \frac{2}{3}\delta_{ij}\frac{\partial u_k}{\partial x_k}\right]\right\} \tag{3b}$$

$$\frac{\partial E_t}{\partial t} - \frac{\partial Q_h}{\partial t} + \frac{\partial}{\partial x_i}\left(E_t u_i + p u_i - u_j \mu\left[\left(\frac{\partial u_i}{\partial x_j} + \frac{\partial u_j}{\partial x_i}\right) - \frac{2}{3}\delta_{ij}\frac{\partial u_k}{\partial x_k}\right] - k_F \frac{\partial T}{\partial x_i}\right) = 0 \tag{3c}$$

where $i, j, k = 1,2,3$, f_i represents the body force per unit volume acting on the fluid, Q_h is the rate of heat produced per unit volume by external agencies, and Fourier's law for heat transfer by conduction has been assumed. The term δ_{ij} is known as the Kronecker delta function. It has a value of 1 when $i = j$, and is zero otherwise. The term E_t is the total energy per unit volume and is given by

$$E_t = \rho\left(e + \frac{u_i u_i}{2} + gh\right) \tag{4}$$

where e is the internal energy per unit mass. The second term in equation (4) represents the kinetic energy of the fluid. The third term on the right hand side of equation (4) represents the potential energy of the fluid due to the gravitational field.

An examination of the fluid dynamics problem being investigated in this research leads to several assumptions which simplify equations (3a), (3b), (3c), and (4). For the flow over the two-element airfoil being studied, there are no external heat sources so Q_h can be set to zero. The only energy terms which are significant in equation (4) are the internal energy and the kinetic energy of the fluid. The experimental portion of this investigation was set up to simulate a two-dimensional flow over the airfoil, as discussed in the section on experimental setup. Thus, the governing equations can be simplified by writing them in two-dimensional form. Applying these simplifying assumptions to equations (3) and (4)

and substituting equation (4) into equation (3) yields the following set of equations

$$\frac{\partial \rho}{\partial t} + \frac{\partial (\rho u_i)}{\partial x_i} = 0 \tag{5a}$$

$$\frac{\partial (\rho u_i)}{\partial t} + \frac{\partial (\rho u_i u_j)}{\partial x_j} = -\frac{\partial p}{\partial x_i} + \frac{\partial}{\partial x_j}\left\{\mu\left[\left(\frac{\partial u_i}{\partial x_j} + \frac{\partial u_j}{\partial x_i}\right) - \frac{2}{3}\delta_{ij}\frac{\partial u_k}{\partial x_k}\right]\right\} \tag{5b}$$

$$\frac{\partial}{\partial t}\left(\rho e + \frac{\rho u_i u_i}{2}\right) + \frac{\partial}{\partial x_i}\left(\left(\rho e + \frac{\rho u_i u_i}{2}\right)u_i + p u_i - u_j \mu\left[\left(\frac{\partial u_i}{\partial x_j} + \frac{\partial u_j}{\partial x_i}\right) - \frac{2}{3}\delta_{ij}\frac{\partial u_k}{\partial x_k}\right] - k_F \frac{\partial T}{\partial x_i}\right) = 0 \tag{5c}$$

where $i, j, k = 1, 2$.

Note that writing the governing equations in two-dimensional form strictly enforces the two-dimensionality of the computed solution. In the experiment, however, the two-dimensionality of the flow cannot be strictly enforced. Asymmetries in the model geometry along the span, hardware such as flap brackets, and local surface irregularities can all lead to locally three-dimensional flows. When flow separation occurs on the upper surface of the main element or flap in the experiment, the flow field becomes more three-dimensional since the separation point typically varies somewhat along the span of the airfoil. The turbulence in the experimental flow can have components in all three dimensions, whereas in the computed solution, the turbulence is strictly two-dimensional. This can lead to differences in the boundary layer profiles between experimental and computed results, which can result in differences in the flow through the flap gap and thus the overall performance of the airfoil.

Using the two-dimensional form of the governing equations, however, still makes sense, despite the potential differences between the experimental results and the computed results. Careful attention to detail in the experimental setup can minimize many of the potential differences. A two-dimensional numerical solution can be obtained considerably faster than a three-dimensional solution, allowing more cases to be run and compared with experimental results. Finally, the overall objective of this research must be remembered. The goal is to use the experimental and computational results together to try to develop an understanding of the flow physics associated with lift-enhancing tabs. This goal does not require an absolute match between experimental and computational results. As long as the lift-enhancing tabs produce the same trends and increments in the experimental and

computational results, both sets of results can be used together to determine how lift-enhancing tabs work.

Another considerable simplification of the governing equations can be made by assuming that the flow can be treated as incompressible. High-lift multi-element airfoil configurations are used in low speed applications such as takeoff or landing, where the free stream Mach number is generally below 0.3. At flow speeds less than Mach 0.3 in air, the effects of compressibility are very small. At a positive angle of attack, multi-element airfoils will have local regions where the flow velocity is higher than Mach 0.3 and compressibility may be important, but these regions are generally confined to the leading edge area of the first element (slat or main element). Other researchers have obtained good agreement between experimental results and computational results using an incompressible set of governing equations [20, 21, 22]. The assumption of incompressible flow reduces the Navier-Stokes equations to a set of mixed elliptic-parabolic partial differential equations which can be numerically solved more efficiently than the compressible Navier Stokes equations for problems where the free stream Mach number is low. The size of the time step that can be used in a numerical solution to the compressible Navier-Stokes equations becomes very small when the free-stream Mach number is less than 0.3, due to stability criteria. This limitation on time step size is removed for numerical solutions to the incompressible Navier-Stokes equations.

In an incompressible flow, density ρ can be treated as a constant. This means the equation for conservation of mass (1a) can be written as

$$\frac{\partial u_i}{\partial x_i} = 0 \tag{6}$$

where $i = 1,2$. Equation (6) simply states that the divergence of the velocity field is zero in an incompressible flow. If equation (6) is substituted into equation (5b) and the constant density ρ is factored out, the following equation for conservation of momentum in an incompressible flow is obtained.

$$\frac{\partial u_i}{\partial t} + \frac{\partial (u_i u_j)}{\partial x_j} = -\frac{1}{\rho}\frac{\partial p}{\partial x_i} + \frac{1}{\rho}\frac{\partial}{\partial x_j}\mu\left(\frac{\partial u_i}{\partial x_j} + \frac{\partial u_j}{\partial x_i}\right) \qquad i, j = 1, 2 \tag{7}$$

An examination of equations (6) and (7) reveals another important benefit of the incompressible flow assumption. Equations (6) and (7) form a closed set of equations for

the unknowns p and u_i if the viscosity is considered a constant. The equation for conservation of energy is no longer required to close the set of equations. This is true even if viscosity cannot be considered constant, as in the case of turbulent flows. However, another equation must then be introduced to define the viscosity as discussed below.

The aerodynamic performance of high-lift multi-element airfoil configurations is usually sensitive to Reynolds number. The flight Reynolds number associated with these configurations can range from approximately 2×10^6 to over 20×10^6. Computational or experimental simulations of high-lift configurations must match the flight Reynolds number in order to accurately predict aerodynamic performance. At these Reynolds numbers, the flow over much of the configuration is turbulent. The numerical grid required to fully resolve all the turbulent eddies in the flow would have to be extremely fine, imposing unacceptable requirements for computer memory, disk space, and computation time. The current approach for computing high Reynolds number turbulent flows is to perform a Reynolds averaging of the Navier-Stokes equations by decomposing the dependent variables in the equations into mean and fluctuating components and then time averaging the entire set of equations. This process introduces new terms called Reynolds stresses into the equation set which are associated with the turbulent motion. A turbulence model must be introduced to relate the Reynolds stresses to mean flow variables and close the equation set.

In the standard Reynolds time-averaging approach [23], a time-averaged flow variable $\overline{f}$ is defined as

$$\overline{f} \equiv \frac{1}{\Delta t} \int_{t_0}^{t_0 + \Delta t} f \, dt \tag{8}$$

The Δt used for the time-averaging process must be selected so that it is large compared to the fluctuations in the flow variable due to turbulence, but small compared to the time period of any unsteadiness in the mean flow field. This is generally not a problem, since the period of the turbulent fluctuations is several orders of magnitude smaller than the period of any unsteadiness in the mean flow. In this manner the high frequency fluctuations due to turbulence are averaged out, but the relatively lower frequency variations in the mean flow are retained.

The dependent variables u_i and p in equations (6) and (7) are replaced by the sum of a time-averaged mean value and a fluctuating component.

$$u_i = \overline{u_i} + u_i'$$
$$p_i = \overline{p_i} + p_i' \tag{9}$$

Equations (6) and (7) are then time-averaged to yield the Reynolds Averaged Incompressible Navier-Stokes equations. Note that the time average of a fluctuating component is by definition zero, but the time average of the product of two fluctuating components is, in general, not zero. The equations for the two-dimensional Reynolds-Averaged Incompressible Navier-Stokes equations can be written as follows

$$\frac{\partial \overline{u_i}}{\partial x_i} = 0 \tag{10}$$

$$\frac{\partial \overline{u_i}}{\partial t} + \frac{\partial(\overline{u_i}\,\overline{u_j})}{\partial x_j} + \frac{\partial(\overline{u_i'u_j'})}{\partial x_j} = -\frac{1}{\rho}\frac{\partial \overline{p}}{\partial x_i} + \frac{1}{\rho}\frac{\partial}{\partial x_j}\mu\left(\frac{\partial \overline{u_i}}{\partial x_j} + \frac{\partial \overline{u_j}}{\partial x_i}\right) \tag{11}$$

Equation (11) can be rearranged to yield

$$\frac{\partial \overline{u_i}}{\partial t} + \frac{\partial(\overline{u_i}\,\overline{u_j})}{\partial x_j} = -\frac{1}{\rho}\frac{\partial \overline{p}}{\partial x_i} + \frac{1}{\rho}\frac{\partial}{\partial x_j}\left(\mu\left(\frac{\partial \overline{u_i}}{\partial x_j} + \frac{\partial \overline{u_j}}{\partial x_i}\right) - \rho\overline{u_i'u_j'}\right) \tag{12}$$

which is a more traditional form of expressing the momentum equation. The last term on the right hand side of equation (12) is known as the Reynolds stress term. The Reynolds stress terms represent an apparent stress due to the transport of momentum by turbulent fluctuations.

Turbulence model

Equations (10) and (12) do not form a closed set of equations due to the addition of the unknown Reynolds stress terms. Additional equations must be introduced to close the system. This is accomplished by means of a turbulence model. Most of the turbulence models in common engineering use today rely on an assumption known as the Boussinesq assumption. The Boussinesq assumption relates the general Reynolds stress tensor to the rate of mean strain by means of a scalar turbulent or eddy viscosity as shown in the following equation.

$$-\rho\overline{u_i'u_j'} = \mu_T\left(\frac{\partial \overline{u_i}}{\partial x_j} + \frac{\partial \overline{u_j}}{\partial x_i}\right) - \frac{2}{3}\delta_{ij}\left(\mu_T\frac{\partial \overline{u_k}}{\partial x_k}\right) \tag{13}$$

The term μ_T is the turbulent viscosity For incompressible flows, equation (13) reduces to the following form.

$$-\rho\overline{u_i'u_j'} = \mu_T\left(\frac{\partial\overline{u_i}}{\partial x_j} + \frac{\partial\overline{u_j}}{\partial x_i}\right) \tag{14}$$

If equation (14) is substituted into equation (12), the momentum equation, after simplification, becomes

$$\frac{\partial u_i}{\partial t} + \frac{\partial(u_i u_j)}{\partial x_j} = -\frac{1}{\rho}\frac{\partial p}{\partial x_i} + \frac{\partial}{\partial x_j}\left[(\nu + \nu_T)\left(\frac{\partial u_i}{\partial x_j} + \frac{\partial u_j}{\partial x_i}\right)\right] \tag{15}$$

where the overbars on all the mean flow variables have been dropped for convenience. The unknown Reynolds stress tensor has been replaced with a single unknown scalar quantity, the turbulent viscosity. The turbulence model is then used to determine the value of this unknown quantity.

Turbulence models can be classified by the number of partial differential equations that must be solved to yield the parameters necessary to compute the turbulent viscosity coefficient. The simplest turbulence models are the zero-equation models. These models utilize algebraic relationships to compute length and velocity scales of turbulence, from which the turbulent viscosity may be computed. These models have the advantage of being simple to implement and computationally inexpensive to use. However, they are limited in their generality. The models, or at least the coefficients used in the model, have to be modified to be applicable to different types of flow problems.

Turbulence models utilizing one or more partial differential equations to determine the parameters needed to compute the turbulent viscosity have been formulated in an attempt to create a more general model. The partial differential equations are generally in the form of transport equations for parameters related to turbulence such as turbulent kinetic energy K or the turbulence dissipation rate ε. The transport equations for a turbulence parameter can be derived from the Navier-Stokes equations. The advantage of using one or more partial differential equations in a turbulence model is that the parameters computed using a partial differential equation become functions of the global flow field, rather than being functions only of the local flow field as is the case for zero-equation models. Once the partial differential equations are solved, the dependent variables are used in empirical relationships to compute the turbulent viscosity. The disadvantage of turbulence models

that utilize partial differential equations is that they are computationally more expensive to use than the zero-equation models.

The turbulence model selected for this research work was the Spalart-Allmaras one-equation model [24]. The Spalart-Allmaras model has been successfully used by other researchers to compute flow fields associated with high-lift multi-element airfoils [21,22,25]. One advantage of the Spalart-Allmaras turbulence model is that it does not require as fine a grid point spacing near the surface as two-equation models like the K-ε or the K-ω models do [21]. Navier-Stokes solution algorithms coupled with the Spalart-Allmaras model also seem to converge much faster than when they are coupled with a two-equation model. A second one-equation model, the Baldwin-Barth model [26], was also used for comparison purposes and the results of the comparison are discussed later in this report. Only the Spalart-Allmaras model will be discussed here. The development of the Baldwin-Barth model is very similar.

In the Spalart-Allmaras turbulence model, the turbulent viscosity is defined by the following relationships.

$$\nu_t = \tilde{\nu} f_{v1} \tag{16}$$

$$f_{v1} = \frac{\chi^3}{\chi^3 + c_{v1}^3} \tag{17}$$

$$\chi = \frac{\tilde{\nu}}{\nu} \tag{18}$$

The variable $\tilde{\nu}$ is chosen to satisfy the transport equation given by

$$\frac{D\tilde{\nu}}{Dt} = c_{b1}\left[1 - f_{t2}\right]\tilde{S}\tilde{\nu} + \frac{1}{\sigma}\left[\nabla\cdot\left(\left(\nu+\tilde{\nu}\right)\nabla\tilde{\nu}\right) + c_{b2}\left(\nabla\tilde{\nu}\right)^2\right] - \left[c_{w1}f_w - \frac{c_{b1}}{\kappa^2}f_{t2}\right]\left[\frac{\tilde{\nu}}{d}\right]^2 + f_{t1}\Delta U^2 \tag{19}$$

The term $\tilde{S}$ is defined as

$$\tilde{S} \equiv S + \frac{\tilde{\nu}}{\kappa^2 d^2} f_{v2} \tag{20}$$

where the function f_{v2} is given by

$$f_{v2} = 1 - \frac{\chi}{1 + \chi f_{v1}} \tag{21}$$

the variable S in equation (20) is the magnitude of the vorticity and d is the distance to the closest wall. The function f_w is given by the equation

$$f_w = g\left[\frac{1 + c_{w3}^6}{g^6 + c_{w3}^6}\right]^{1/6} \tag{22}$$

where

$$g = r + c_{w2}\left(r^6 - r\right) \tag{23}$$

and

$$r \equiv \frac{\tilde{\nu}}{\tilde{S}\kappa^2 d^2} \tag{24}$$

The Spalart-Allmaras turbulence model has a transition model built in which gives a smooth transition from laminar flow to turbulent flow at a user-defined transition location. The terms f_{t1} and f_{t2} in equation (19) are transition functions and are given by the following equations.

$$f_{t1} = c_{t1} g_t \exp\left(-c_{t2} \frac{\omega_t}{\Delta U^2}\left[d^2 + g_t^2 d_t^2\right]\right) \tag{25}$$

$$f_{t2} = c_{t3} \exp\left(-c_{t4} \chi^2\right) \tag{26}$$

$$g_t \equiv \min\left(0.1, \frac{\Delta U}{\omega_t \Delta x_t}\right) \tag{27}$$

The term d_t is the distance from a field point to a user-defined transition point on a wall. The ω_t term is the wall vorticity at the transition point. ΔU is the difference between the velocity at a field point and the velocity at the transition point. Δx_t is the grid spacing along the wall at the transition location.

Empirically derived relationships and direct numerical simulations (using the non-Reynolds-averaged Navier Stokes equations) of a variety of different shear flows are used to calibrate the turbulence model. The various functions and constants used in the Spalart-Allmaras formulation were chosen to yield a model which best simulates the available data

on turbulent shear flows. The values of the constants used in equations (16) through (27) are listed below.

$$\sigma = \frac{2}{3}$$
$$\kappa = 0.41$$
$$c_{b1} = 0.1355$$
$$c_{b2} = 0.622$$
$$c_{w1} = \frac{c_{b1}}{\kappa^2} + \frac{(1 + c_{b2})}{\sigma}$$
$$c_{w2} = 0.3$$
$$c_{w3} = 2.0$$
$$c_{v1} = 7.1$$
$$c_{t1} = 1.0 \qquad (28)$$
$$c_{t2} = 2.0$$
$$c_{t3} = 1.2$$
$$c_{t4} = 0.5$$

Boundary conditions and initial values for $\tilde{\nu}$ must be set before equation (19) can be numerically solved. At no-slip wall boundaries, $\tilde{\nu}$ is set to zero. At outflow and slip wall boundaries, the normal derivative of $\tilde{\nu}$ is set to zero. The ideal value of $\tilde{\nu}$ in the free stream (away from shear layers) is zero. The initial value of $\tilde{\nu}$ at all field points is typically set equal to the free stream value. The solution to equation (19) is advanced to the next iteration level using an implicit solution procedure. The updates of the velocity field from the Navier-Stokes solution algorithm and turbulent viscosity from the turbulence model are computed in an uncoupled fashion at each time step or iteration.

Scaling and Transformation of the Governing Equations

It is common practice to scale the dependent and independent variables in the Navier-Stokes equations so that all variables are in a non dimensional form. The scaling process gives rise to several non dimensional parameters which can be used to characterize the flow field being modeled. These include the Reynolds number, the Mach number, and the Prandtl number. When the Navier-Stokes equations are solved in their non dimensional form, the Reynolds number, Mach number, and Prandtl number can be used to set the scale of the flow being simulated. A typical scaling of the governing equations is given by the set of equations listed below.

$$\hat{u}_i = \frac{u_i}{u_{ref}}$$

$$\hat{x}_i = \frac{x_i}{x_{ref}}$$

$$\hat{t} = \frac{t}{\left(x_{ref} / u_{ref} \right)}$$

$$\hat{p} = \frac{p - p_{ref}}{\rho u_{ref}^2} \qquad (29)$$

$$\hat{\nu} = \frac{\nu}{(x_{ref}\, u_{ref})}$$

If the scaling given in equations (29) are applied to the governing equations (10) and (15), the following set of non dimensional governing equations are obtained.

$$\frac{\partial \hat{u}_i}{\partial \hat{x}_i} = \mathbf{0} \qquad i = 1, 2 \qquad (30)$$

$$\frac{\partial \hat{u}_i}{\partial \hat{t}} + \frac{\partial (\hat{u}_i \hat{u}_j)}{\partial \hat{x}_j} = -\frac{\partial \hat{p}}{\partial \hat{x}_i} + \frac{\partial}{\partial \hat{x}_j}\left[\left(\hat{\nu} + \hat{\nu}_T \right) \left(\frac{\partial \hat{u}_i}{\partial \hat{x}_j} + \frac{\partial \hat{u}_j}{\partial \hat{x}_i} \right) \right] \qquad i, j = 1, 2 \qquad (31)$$

Equations (30) and (31) represent the non dimensional form of the two-dimensional Reynolds-averaged Incompressible Navier-Stokes equations in a Cartesian coordinate system. The overbars on the mean variables resulting from the Reynolds averaging have been dropped for convenience. From this point on, all variables will be treated as non dimensional and the hats will also be dropped.

The governing equations are generally written in conservation law form for computational fluid dynamics (CFD) applications. A partial differential equation written in conservation law form has the property that the coefficients of the derivative terms are either constant or, if variable, their derivatives do not appear in the equation. The main advantage of the conservation law form of the equations is that numerical difficulties are avoided in situations where the coefficients may be discontinuous, such as flows containing shock waves. Equations (30) and (31) can be combined into a single vector

equation and expressed in conservation law form as shown below.

$$\frac{\partial Q}{\partial t}+\frac{\partial}{\partial x}(F-F_v)+\frac{\partial}{\partial y}(G-G_v)=\mathbf{0} \tag{32}$$

where

$$Q=\begin{bmatrix}\mathbf{0}\\ u_1\\ u_2\end{bmatrix} \qquad F=\begin{bmatrix}u_1\\ u_1^2+p\\ u_1u_2\end{bmatrix} \qquad G=\begin{bmatrix}u_2\\ u_1u_2\\ u_2^2+p\end{bmatrix}$$

$$F_v=\begin{bmatrix}\mathbf{0}\\ 2(\nu+\nu_T)\dfrac{\partial u_1}{\partial x}\\ (\nu+\nu_T)\left(\dfrac{\partial u_1}{\partial y}+\dfrac{\partial u_2}{\partial x}\right)\end{bmatrix} \qquad G_v=\begin{bmatrix}\mathbf{0}\\ (\nu+\nu_T)\left(\dfrac{\partial u_1}{\partial y}+\dfrac{\partial u_2}{\partial x}\right)\\ 2(\nu+\nu_T)\dfrac{\partial u_2}{\partial y}\end{bmatrix} \tag{33}$$

In equation (32), F and G are the convective flux vectors and F_v and G_v are the viscous flux vectors.

Equation (32) is an expression of the Navier-Stokes equations for a Cartesian coordinate system. However, for most applications a Cartesian coordinate system is not a suitable choice of coordinate systems on which to apply a finite difference scheme for numerically solving the governing equations. The finite difference scheme becomes quite complicated and application of boundary conditions becomes difficult because the values of x and y are generally not constant along grid lines. This problem is resolved by applying a general non orthogonal transformation process to the governing equations. The transformation process maps a physical domain in Cartesian coordinates to a computational domain in generalized coordinates ξ and η. If the computational domain is represented with a finite difference grid, the values of ξ and η are constant along grid lines and the grid lines are uniformly spaced. The resulting transformed governing equations are then valid in the computational domain. Application of a finite difference scheme to numerically solve the transformed governing equations in the computational domain is greatly simplified.

Using the method given in reference [23], the general non orthogonal transformation process is accomplished by assuming generalized coordinates of the form

$$\xi = \xi(x,y)$$
$$\eta = \eta(x,y) \tag{34}$$

The chain rule of partial differentiation is used to express partial derivatives with respect to x and y in terms of derivatives with respect to ξ and η.

$$\frac{\partial}{\partial x} = \xi_x \frac{\partial}{\partial \xi} + \eta_x \frac{\partial}{\partial \eta}$$
$$\frac{\partial}{\partial y} = \xi_y \frac{\partial}{\partial \xi} + \eta_y \frac{\partial}{\partial \eta} \tag{35}$$

In equation (35) abbreviated partial derivative notation has been used (i.e. $\xi_x \equiv \frac{\partial \xi}{\partial x}$). The terms ξ_x, ξ_y, η_x, and η_y are known as the metric terms of the transformation. In order to complete the transformation, the metric terms must be defined. This can be done by writing expressions for the total derivative of ξ and η.

$$d\xi = \xi_x dx + \xi_y dy$$
$$d\eta = \eta_x dx + \eta_y dy \tag{36}$$

Equation (36) can be expressed in matrix form as follows.

$$\begin{bmatrix} d\xi \\ d\eta \end{bmatrix} = \begin{bmatrix} \xi_x & \xi_y \\ \eta_x & \eta_y \end{bmatrix} \begin{bmatrix} dx \\ dy \end{bmatrix} \tag{37}$$

Expressions for the total derivatives of x and y can also be written in matrix form.

$$\begin{bmatrix} dx \\ dy \end{bmatrix} = \begin{bmatrix} x_\xi & x_\eta \\ y_\xi & y_\eta \end{bmatrix} \begin{bmatrix} d\xi \\ d\eta \end{bmatrix} \tag{38}$$

Comparing equations (37) and (38), the following relationship can easily be derived.

$$\begin{bmatrix} \xi_x & \xi_y \\ \eta_x & \eta_y \end{bmatrix} = \begin{bmatrix} x_\xi & x_\eta \\ y_\xi & y_\eta \end{bmatrix}^{-1} \tag{39}$$

Evaluating the right hand side of equation (39) leads to the following expressions for the metric terms.

$$\begin{aligned} \xi_x &= J\, y_\eta \\ \xi_y &= -J\, x_\eta \\ \eta_x &= -J\, y_\xi \\ \eta_y &= J\, x_\xi \end{aligned} \tag{40}$$

The term J in equation (40) is the Jacobian of the transformation and is given by

$$J = \frac{1}{\begin{vmatrix} x_\xi & x_\eta \\ y_\xi & y_\eta \end{vmatrix}} = \frac{1}{\left(x_\xi y_\eta - x_\eta y_\xi\right)} \tag{41}$$

The metric terms can be easily evaluated using equation (40) if analytical expressions for the inverse of the transformation exist (i.e. $x = x(\xi, \eta)$, $y = y(\xi, \eta)$). For complex finite difference grids, analytical expressions for the inverse of the transformation generally do not exist and the metric terms must be evaluated by using finite difference approximations in equation (40). If the grid varies with time, then additional constraints on the evaluation of the metric terms using finite difference approximations are imposed by the geometric conservation law of Thomas and Lombard [27]. Since the grids used in this research are not varying with time, this is not a concern here and will not be covered further. The specific differencing schemes used to evaluate the metric terms will be discussed in the next chapter.

The expressions given in equation (35) for the partial derivatives with respect to x and y can be substituted into equation (32) to transform the governing equations into the computational domain.

$$\frac{\partial Q}{\partial t} + \xi_x \frac{\partial}{\partial \xi}\left(F - F_v\right) + \eta_x \frac{\partial}{\partial \eta}\left(F - F_v\right) + \xi_y \frac{\partial}{\partial \xi}\left(G - G_v\right) + \eta_y \frac{\partial}{\partial \eta}\left(G - G_v\right) = \mathbf{0} \tag{42}$$

If equation (42) is multiplied by J^{-1} and the chain rule for differentiation is used, equation (42) can be rewritten as follows.

$$\frac{\partial}{\partial t}(J^{-1}Q)+\frac{\partial}{\partial \xi}\left[J^{-1}\xi_x(F-F_v)\right]+\frac{\partial}{\partial \eta}\left[J^{-1}\eta_x(F-F_v)\right]+\frac{\partial}{\partial \xi}\left[J^{-1}\xi_y(G-G_v)\right]+$$
$$\frac{\partial}{\partial \eta}\left[J^{-1}\eta_y(G-G_v)\right]-Q\frac{\partial J^{-1}}{\partial t}-(F-F_v)\frac{\partial}{\partial \xi}(J^{-1}\xi_x)-(F-F_v)\frac{\partial}{\partial \eta}(J^{-1}\eta_x)- \qquad (43)$$
$$(G-G_v)\frac{\partial}{\partial \xi}(J^{-1}\xi_y)-(G-G_v)\frac{\partial}{\partial \eta}(J^{-1}\eta_y)=\mathbf{0}$$

If the relations defined in equation (40) are substituted into the last four terms of equation (43), the last four terms cancel each other out. As mentioned earlier, the grids used in this research do not vary with time, so that the term involving the derivative of J^{-1} with respect to time is zero. Thus equation (43) can be reduced to

$$\frac{\partial}{\partial t}(J^{-1}Q)+\frac{\partial}{\partial \xi}\left[J^{-1}\left(\xi_x(F-F_v)+\xi_y(G-G_v)\right)\right]+$$
$$\frac{\partial}{\partial \eta}\left[J^{-1}\left(\eta_x(F-F_v)+\eta_y(G-G_v)\right)\right]=\mathbf{0} \qquad (44)$$

In order to simplify equation (44) further, the following definitions are made.

$$\hat{Q}=\frac{\mathbf{1}}{J}Q$$
$$\hat{F}=\frac{\mathbf{1}}{J}\left(\xi_x F+\xi_y G\right) \qquad \hat{F}_v=\frac{\mathbf{1}}{J}\left(\xi_x F_v+\xi_y G_v\right) \qquad (45)$$
$$\hat{G}=\frac{\mathbf{1}}{J}\left(\eta_x F+\eta_y G\right) \qquad \hat{G}_v=\frac{\mathbf{1}}{J}\left(\eta_x F_v+\eta_y G_v\right)$$

Substituting the relationships in equation (45) into equation (44) results in the following vector equation for the conservation form of the two-dimensional Reynolds-averaged incompressible Navier-Stokes equations expressed in a generalized non orthogonal coordinate system.

$$\frac{\partial \hat{Q}}{\partial t}+\frac{\partial}{\partial \xi}\left(\hat{F}-\hat{F}_v\right)+\frac{\partial}{\partial \eta}\left(\hat{G}-\hat{G}_v\right)=\mathbf{0} \qquad (46)$$

The viscous flux vectors in equation (46) contain derivatives with respect to x and y that must also be transformed to the computational domain. The individual vectors in equation (46) are defined below.

$$\hat{Q} = \frac{1}{J}\begin{bmatrix} 0 \\ u_1 \\ u_2 \end{bmatrix}$$

$$\hat{F} = \frac{1}{J}\begin{bmatrix} \xi_x u_1 + \xi_y u_2 \\ \xi_x(u_1^2 + p) + \xi_y u_1 u_2 \\ \xi_x u_1 u_2 + \xi_y(u_2^2 + p) \end{bmatrix} \qquad \hat{G} = \frac{1}{J}\begin{bmatrix} \eta_x u_1 + \eta_y u_2 \\ \eta_x(u_1^2 + p) + \eta_y u_1 u_2 \\ \eta_x u_1 u_2 + \eta_y(u_2^2 + p) \end{bmatrix}$$

$$\hat{F}_v = \frac{(\nu + \nu_t)}{J}\begin{bmatrix} 0 \\ \left(2\xi_x^2 + \xi_y^2\right)\frac{\partial u_1}{\partial \xi} + \left(2\xi_x\eta_x + \xi_y\eta_y\right)\frac{\partial u_1}{\partial \eta} + \xi_x\xi_y\frac{\partial u_2}{\partial \xi} + \xi_y\eta_x\frac{\partial u_2}{\partial \eta} \\ \left(\xi_x^2 + 2\xi_y^2\right)\frac{\partial u_2}{\partial \xi} + \left(\xi_x\eta_x + 2\xi_y\eta_y\right)\frac{\partial u_2}{\partial \eta} + \xi_x\xi_y\frac{\partial u_1}{\partial \xi} + \xi_x\eta_y\frac{\partial u_1}{\partial \eta} \end{bmatrix}$$

$$\hat{G}_v = \frac{(\nu + \nu_t)}{J}\begin{bmatrix} 0 \\ \left(2\xi_x\eta_x + \xi_y\eta_y\right)\frac{\partial u_1}{\partial \xi} + \left(2\eta_x^2 + \eta_y^2\right)\frac{\partial u_1}{\partial \eta} + \xi_x\eta_y\frac{\partial u_2}{\partial \xi} + \eta_x\eta_y\frac{\partial u_2}{\partial \eta} \\ \left(\xi_x\eta_x + 2\xi_y\eta_y\right)\frac{\partial u_2}{\partial \xi} + \left(\eta_x^2 + 2\eta_y^2\right)\frac{\partial u_2}{\partial \eta} + \xi_y\eta_x\frac{\partial u_1}{\partial \xi} + \eta_x\eta_y\frac{\partial u_1}{\partial \eta} \end{bmatrix} \tag{47}$$

The vector equation (46) represents the set of equations governing the fluid dynamics of the two-dimensional flow field to be studied in this research. The numerical scheme used to solve the set of equations (46) will be discussed in the next chapter.

CHAPTER V
NUMERICAL SOLUTION OF GOVERNING EQUATIONS

The computer code chosen to perform all the computations presented in this research was INS2D-UP. INS2D-UP was developed at NASA Ames Research Center by Rogers and Kwak [28,29,30,31]. The code numerically solves the two-dimensional Reynolds-averaged Incompressible Navier-Stokes equations developed in the previous chapter by making use of the method of artificial compressibility, first introduced by Chorin [32]. INS2D can be used to compute time-accurate solutions to unsteady flow problems, as well as steady-state solutions. All of the computations presented in this report were performed using the steady-state flow option. A number of turbulence models are available in INS2D, including the Baldwin-Lomax algebraic model, the one-equation Baldwin-Barth model, the one-equation Spalart-Allmaras model, and the two-equation k-ω model. In addition, INS2D includes several different schemes for solving the linear system of equations that result from the implicit finite difference algorithm.

In this chapter, a brief description of the method of artificial compressibility will be given, followed by a development of the finite difference equations used to approximate the governing equations. A description of the flux-difference splitting scheme used to compute the convective terms will also be given. The linear system of equations that result from the implicit finite difference algorithm will be derived. Finally, the characteristic relations used to update boundary conditions will be covered.

Method of Artificial Compressibility

The two-dimensional incompressible Navier-Stokes equations are a set of mixed elliptic-parabolic partial differential equations. This means that disturbances must propagate to all points in the flow field in a single time step. The elliptic nature of the equations requires an iterative solution scheme to solve the equations at each time step. One approach to solving the two-dimensional incompressible Navier-Stokes equations is to recast the equations into a parabolic transport equation for vorticity and an elliptic Poisson equation for stream function. These equations are solved using a time-marching scheme. Initial conditions for vorticity and stream function are specified at all grid points. The vorticity transport equation is then solved at all grid points to advance the values of vorticity to the next time step. An iterative scheme is used to solve the Poisson equation for new values of stream function at all grid points using the new values of vorticity. The new values of stream function can be used to compute the components of velocity at each grid point. A second Poisson equation must be solved to determine the pressure at each grid

point for each step. The boundary conditions are updated based on values of vorticity and stream function at interior grid points and the process is repeated for the next time step. This same procedure can be used to compute steady flows also. In this case, the solution is marched in pseudo-time until steady-state values for vorticity and stream function are achieved. The Poisson equation for pressure in a steady flow is only solved once, after vorticity and stream function have reached their steady-state values.

There are several disadvantages of using the vorticity-stream function formulation to solve the two-dimensional incompressible Navier-Stokes equations. The solution of one or two Poisson equations at each time step is computationally expensive. Because the pressure is computed at the end of each iteration, it is only indirectly coupled to the velocity field as the solution is advanced in time. However, the biggest drawback of the vorticity-stream function formulation is the difficulty in extending the method to solving the three-dimensional incompressible Navier-Stokes equations. A dual stream function, which is the three-dimensional analog to the two-dimensional stream function, must be used to extend the technique to three dimensions.

In the artificial compressibility method, the continuity equation is modified by adding an artificial compressibility term which vanishes when the steady-state solution is reached. Thus the steady-state solution still satisfies the requirement of a divergence-free velocity field as required by the incompressible continuity equation. The modified continuity equation can be written as

$$\frac{\partial \tilde{\rho}}{\partial \tau} + \frac{\partial u_1}{\partial x} + \frac{\partial u_2}{\partial y} = 0 \tag{48}$$

where $\tilde{\rho}$ is the artificial density and τ is a pseudo-time which is analogous to real time in a compressible flow. Equation (48), together with the conservation of momentum equation, is marched in pseudo-time until a steady-state solution is achieved. For unsteady flow fields requiring time-accurate solutions to the incompressible Navier-Stokes equations, the solution is advanced in physical time by iterating in pseudo-time until a divergence-free velocity field is obtained at each new physical time level. As mentioned earlier, INS2D-UP can be used to perform either steady-state or time accurate computations. All of the computations performed for this research were steady-state in nature. Thus only the steady-state formulation of INS2D-UP will be covered here. The differences between the steady-state and the time accurate formulations are minor and the reader is referred to reference [30] for details on the time-accurate formulation.

The addition of the artificial compressibility term to the continuity equation changes the incompressible Navier-Stokes equations from a mixed set of elliptic-parabolic partial differential equations to a mixed set of hyperbolic-parabolic partial differential equations. This allows the equations to be solved using a marching scheme and avoids the need for solving a Poisson equation at each step. The hyperbolic nature of the equations also permits the convective fluxes to be upwind differenced rather than central differenced. Schemes employing central differencing of the convective fluxes require artificial dissipation to be explicitly added in order to damp out numerical oscillations resulting from the non linearity of the convective fluxes. The amount of dissipation added has a direct effect on the final solution and must be adjusted to fit the specific application being simulated. Use of an upwind differencing scheme for the convective fluxes avoids the difficulties associated with central differencing. The upwind differencing of the convective fluxes is a way of following the propagation of the artificial waves generated by the artificial compressibility. Upwind differencing is a naturally dissipative scheme which damps out the numerical oscillations caused by the nonlinear convective fluxes. An additional benefit of using upwind differencing of the convective fluxes is that the scheme contributes to terms on the diagonal of the Jacobian of the residual, making the scheme nearly diagonally dominant. This helps improve the convergence rate of the algorithm used to solve the system of linear equations.

The artificial density can be related to the pressure by an artificial equation of state as shown below.

$$p = \beta\tilde{\rho} \tag{49}$$

The term β in equation (49) is the artificial compressibility factor and is analogous to the square of the speed of sound in the physical domain. The value of β governs the rate at which waves propagate throughout the domain. If equation (49) is substituted into equation (48), the following modified continuity equation is obtained.

$$\frac{\partial p}{\partial \tau} + \beta\left(\frac{\partial u_1}{\partial x} + \frac{\partial u_2}{\partial y}\right) = \mathbf{0} \tag{50}$$

The direct coupling of the pressure field and the velocity field provided by the artificial compressibility method is evident from equation (50). Replacing the standard incompressible continuity equation in the vector equation (46) with equation (50) yields the following vector equation.

$$\frac{\partial \hat{Q}}{\partial \tau}+\frac{\partial}{\partial \xi}\left(\hat{F}-\hat{F}_v\right)+\frac{\partial}{\partial \eta}\left(\hat{G}-\hat{G}_v\right)=\mathbf{0}$$

$$\hat{Q}=\frac{1}{J}\begin{bmatrix} p \\ u_1 \\ u_2 \end{bmatrix}$$

$$\hat{F}=\frac{1}{J}\begin{bmatrix} \beta\left(\xi_x u_1+\xi_y u_2\right) \\ \xi_x(u_1^2+p)+\xi_y u_1 u_2 \\ \xi_x u_1 u_2+\xi_y(u_2^2+p) \end{bmatrix} \qquad \hat{G}=\frac{1}{J}\begin{bmatrix} \beta\left(\eta_x u_1+\eta_y u_2\right) \\ \eta_x(u_1^2+p)+\eta_y u_1 u_2 \\ \eta_x u_1 u_2+\eta_y(u_2^2+p) \end{bmatrix}$$

$$\hat{F}_v=\frac{(\nu+\nu_t)}{J}\begin{bmatrix} \mathbf{0} \\ \left(2\xi_x^2+\xi_y^2\right)\frac{\partial u_1}{\partial \xi}+\left(2\xi_x\eta_x+\xi_y\eta_y\right)\frac{\partial u_1}{\partial \eta}+\xi_x\xi_y\frac{\partial u_2}{\partial \xi}+\xi_y\eta_x\frac{\partial u_2}{\partial \eta} \\ \left(\xi_x^2+2\xi_y^2\right)\frac{\partial u_2}{\partial \xi}+\left(\xi_x\eta_x+2\xi_y\eta_y\right)\frac{\partial u_2}{\partial \eta}+\xi_x\xi_y\frac{\partial u_1}{\partial \xi}+\xi_x\eta_y\frac{\partial u_1}{\partial \eta} \end{bmatrix}$$

$$\hat{G}_v=\frac{(\nu+\nu_t)}{J}\begin{bmatrix} \mathbf{0} \\ \left(2\xi_x\eta_x+\xi_y\eta_y\right)\frac{\partial u_1}{\partial \xi}+\left(2\eta_x^2+\eta_y^2\right)\frac{\partial u_1}{\partial \eta}+\xi_x\eta_y\frac{\partial u_2}{\partial \xi}+\eta_x\eta_y\frac{\partial u_2}{\partial \eta} \\ \left(\xi_x\eta_x+2\xi_y\eta_y\right)\frac{\partial u_2}{\partial \xi}+\left(\eta_x^2+2\eta_y^2\right)\frac{\partial u_2}{\partial \eta}+\xi_y\eta_x\frac{\partial u_1}{\partial \xi}+\eta_x\eta_y\frac{\partial u_1}{\partial \eta} \end{bmatrix} \qquad (51)$$

Finite Difference Approximations

In order to numerically solve the set of governing equations expressed in equation (51), all of the partial derivatives must be replaced by finite difference approximations. A finite difference approximation is an algebraic expression based on a Taylor series expansion about a point, which approximates the value of the partial derivative at that point. A wide variety of finite difference approximations of differing orders of accuracy can be derived for a given partial derivative. The finite difference approximations used in the INS2D-UP code will be discussed in the following sections. The approach outlined here follows the development by Rogers [31].

Metric Terms. All of the metric terms that resulted from the transformation of the governing equations to a generalized non orthogonal coordinate system must be represented with finite difference approximations. The metric terms appearing in equation (51) are not evaluated directly using finite difference approximations. Rather, the quantities x_ξ, x_η, y_ξ,

and y_η are evaluated using finite difference approximations. The results are then averaged and substituted into equations (40) and (41) to obtain values for the metric terms in equation (51). This method of computing the metric terms ensures free-stream preservation on a stationary grid. A second-order accurate central difference approximation can be used to represent the partial derivatives as shown in the example below.

$$\left(x_\xi\right)_{i,j} = \left(\frac{\partial x}{\partial \xi}\right)_{i,j} = \frac{1}{2\Delta\xi}\left(x_{i+1,j} - x_{i-1,j}\right) \tag{52}$$

Similar expressions can be written for the remaining partial derivatives. These expressions are evaluated for the entire finite difference grid. The metric terms are then defined as illustrated using the following averaging procedure.

$$\left(\eta_y\right)_{i,j} = \frac{J}{2}\left[\left(x_\xi\right)_{i+1,j} + \left(x_\xi\right)_{i-1,j}\right] \tag{53}$$

Since the grids do not vary with time, this process only needs to be done once to define the metric terms for the entire computation.

Convective flux terms. The convective flux terms are represented by the vectors $\hat{F}$ and $\hat{G}$ in equation (51). If the contravariant velocity components U_1 and U_2, defined as

$$\begin{aligned} U_1 &= \xi_x u_1 + \xi_y u_2 \\ U_2 &= \eta_x u_1 + \eta_y u_2 \end{aligned} \tag{54}$$

are used in the convective flux vectors, then $\hat{F}$ and $\hat{G}$ can be written as follows.

$$\hat{F} = \frac{1}{J}\begin{bmatrix} \beta U_1 \\ u_1 U_1 + \xi_x p \\ u_2 U_1 + \xi_y p \end{bmatrix} \qquad \hat{G} = \frac{1}{J}\begin{bmatrix} \beta U_2 \\ u_1 U_2 + \eta_x p \\ u_2 U_2 + \eta_y p \end{bmatrix} \tag{55}$$

The Jacobian matrix of the convective flux vector $\hat{F}$ is then given by

$$A = \frac{\partial \hat{F}}{\partial Q} = \frac{1}{J}\begin{bmatrix} 0 & \beta\xi_x & \beta\xi_y \\ \xi_x & \xi_x u_1 + U_1 & \xi_y u_1 \\ \xi_y & \xi_x u_2 & \xi_y u_2 + U_1 \end{bmatrix} \tag{56}$$

A similar expression can be written for the Jacobian matrix B of $\hat{G}$. The Jacobian matrices A and B can be diagonalized by applying a similarity transformation of the form

$$A = X_A \Lambda_A X_A^{-1} \tag{57}$$

where X_A is the matrix of eigenvectors of A and Λ_A is the diagonal matrix of eigenvalues of A. A similar process is followed for matrix B. The matrices Λ_A and Λ_B are defined as

$$\Lambda_A = \frac{1}{J}\begin{bmatrix} U_1 & 0 & 0 \\ 0 & U_1 + c_A & 0 \\ 0 & 0 & U_1 - c_A \end{bmatrix} \qquad \Lambda_B = \frac{1}{J}\begin{bmatrix} U_2 & 0 & 0 \\ 0 & U_2 + c_B & 0 \\ 0 & 0 & U_2 - c_B \end{bmatrix} \tag{58}$$

where

$$\begin{aligned} C_A &= \frac{1}{J}\left[U_1^2 + \beta\left(\xi_x^2 + \xi_y^2\right)\right]^{0.5} \\ C_B &= \frac{1}{J}\left[U_2^2 + \beta\left(\eta_x^2 + \eta_y^2\right)\right]^{0.5} \end{aligned} \tag{59}$$

Note that C_A and C_B are always positive and will always be larger in magnitude than U_1 and U_2 respectively. Thus the second eigenvalue for A and B will always be positive and the third eigenvalue will always be negative. This fact will be used to bias the differencing of the convective flux vectors based on the eigenvalues of the convective flux Jacobians.

The upwind differencing scheme will be developed for one coordinate direction and then applied to each coordinate direction separately. The derivative of the convective flux vector $\hat{F}$ with respect to ξ can be approximated by

$$\left(\frac{\partial \hat{F}}{\partial \xi}\right)_{i,j} \approx \frac{\left(\hat{F}_{i+1/2,j} - \hat{F}_{i-1/2,j}\right)}{\Delta\xi} \tag{60}$$

where

$$\begin{aligned} \hat{F}_{i+1/2,j} &= \frac{1}{2}\left[\hat{F}\left(\hat{Q}_{i+1,j}\right) + \hat{F}\left(\hat{Q}_{i,j}\right) - \phi_{i+1/2,j}\right] \\ \hat{F}_{i-1/2,j} &= \frac{1}{2}\left[\hat{F}\left(\hat{Q}_{i,j}\right) + \hat{F}\left(\hat{Q}_{i-1,j}\right) - \phi_{i-1/2,j}\right] \end{aligned} \tag{61}$$

The terms $\phi_{i+1/2,j}$ and $\phi_{i-1/2,j}$ are dissipation terms. If $\phi_{i+1/2,j}$ and $\phi_{i-1/2,j}$ are set to zero, then equations (60) and (61) represent a second-order central-difference scheme. If the terms $\phi_{i+1/2,j}$ and $\phi_{i-1/2,j}$ are defined as

$$\begin{aligned}\phi_{i+1/2,j} &= \Delta\hat{F}^{+}_{i+1/2,j} - \Delta\hat{F}^{-}_{i+1/2,j} \\ \phi_{i-1/2,j} &= \Delta\hat{F}^{+}_{i-1/2,j} - \Delta\hat{F}^{-}_{i-1/2,j}\end{aligned} \tag{62}$$

then a first-order upwind scheme results. The terms $\Delta\hat{F}^{\pm}$ represent the flux difference across positive or negative traveling waves. These terms are defined as

$$\begin{aligned}\Delta\hat{F}^{\pm}_{i+1/2,j} &= A^{\pm}\left(\overline{\hat{Q}}_{i+1/2,j}\right)\Delta\hat{Q}_{i+1/2,j} \\ \Delta\hat{F}^{\pm}_{i-1/2,j} &= A^{\pm}\left(\overline{\hat{Q}}_{i-1/2,j}\right)\Delta\hat{Q}_{i-1/2,j}\end{aligned} \tag{63}$$

where

$$\begin{aligned}\Delta\hat{Q}_{i+1/2,j} &= \hat{Q}_{i+1,j} - \hat{Q}_{i,j} \\ \Delta\hat{Q}_{i-1/2,j} &= \hat{Q}_{i,j} - \hat{Q}_{i-1,j}\end{aligned} \tag{64}$$

and

$$\begin{aligned}\overline{\hat{Q}}_{i+1/2,j} &= \frac{1}{2}\left(\hat{Q}_{i+1,j} + \hat{Q}_{i,j}\right) \\ \overline{\hat{Q}}_{i-1/2,j} &= \frac{1}{2}\left(\hat{Q}_{i,j} + \hat{Q}_{i-1,j}\right)\end{aligned} \tag{65}$$

The splitting of the Jacobian matrix A is accomplished by using equation (57) together with the following equation.

$$\Lambda^{\pm}_{A} = \frac{1}{2}\left(\Lambda_{A} \pm |\Lambda_{A}|\right) \tag{66}$$

The Λ^{+}_{A} diagonal matrix contains only positive eigenvalues and the Λ^{-}_{A} diagonal matrix contains only negative eigenvalues.

Higher order upwind difference schemes can be created by making suitable choices for the $\phi_{i+1/2,j}$ and $\phi_{i-1/2,j}$ terms. INS2D-UP includes a third-order and a fifth-order

accurate upwind difference scheme and allows the user to designate which scheme should be used by means of a parameter in the input file. Implementation of the higher-order schemes does not significantly increase the computation time because all the flux differences $\Delta \hat{F}^{\pm}$ are computed for an entire grid line at a time. The main difficulty with using upwind schemes of greater than first order accuracy is that a reduction of order is required at the boundaries. This problem is handled in INS2D-UP by using the following for the $\phi_{i+1/2,j}$ and $\phi_{i-1/2,j}$ terms adjacent to boundaries.

$$\begin{aligned} \phi_{i+1/2,j} &= \epsilon \left[\Delta \hat{F}^{+}_{i+1/2,j} - \Delta \hat{F}^{-}_{i+1/2,j} \right] \\ \phi_{i-1/2,j} &= \epsilon \left[\Delta \hat{F}^{+}_{i-1/2,j} - \Delta \hat{F}^{-}_{i-1/2,j} \right] \end{aligned} \tag{67}$$

For $\epsilon = \mathbf{0}$, the scheme degenerates to a second-order central-difference approximation at the boundary. If $\epsilon = \mathbf{1}$, the scheme becomes the first-order upwind difference scheme given by equation (62). By using a small value for ϵ, dissipation is added to the central difference scheme, suppressing numerical oscillations at the boundary and maintaining near second-order accuracy. The default value recommended in INS2D-UP is $\epsilon = \mathbf{0.01}$.

Viscous Flux Terms. The partial derivatives of the viscous flux terms $\hat{F}_v$ and $\hat{G}_v$ in equation (51) must also be approximated using finite difference approximations. A second-order accurate central difference scheme is used in INS2D-UP to approximate the partial derivatives of the viscous flux terms. The finite difference expressions for the partial derivatives of $\hat{F}_v$ with respect to ξ and $\hat{G}_v$ with respect to η can be written as

$$\begin{aligned} \left(\frac{\partial \hat{F}_v}{\partial \xi} \right)_{i,j} &\approx \frac{\left(\left(\hat{F}_v \right)_{i+1,j} - \left(\hat{F}_v \right)_{i-1,j} \right)}{2\Delta\xi} \\ \left(\frac{\partial \hat{G}_v}{\partial \eta} \right)_{i,j} &\approx \frac{\left(\left(\hat{G}_v \right)_{i,j+1} - \left(\hat{G}_v \right)_{i,j-1} \right)}{2\Delta\eta} \end{aligned} \tag{68}$$

Note that the turbulent viscosity appearing in the viscous flux vectors must be computed for the entire grid at each step in pseudo-time using the turbulence model.

Pseudo-Time Derivatives. Since equation (51) is solved by using a marching scheme in pseudo-time until a steady-state solution is obtained, accuracy in pseudo-time is not required and a first-order implicit Euler differencing scheme can be used to represent

the partial derivative of $\hat{Q}$ with respect to pseudo-time τ. The use of an implicit differencing scheme eliminates the restriction on step size in pseudo-time that exists for an explicit scheme due to stability criteria. Equation (51) is first rewritten as

$$\frac{\partial \hat{Q}}{\partial \tau} = -R \tag{69}$$

where

$$R = \frac{\partial}{\partial \xi}\left(\hat{F} - \hat{F}_v\right) + \frac{\partial}{\partial \eta}\left(\hat{G} - \hat{G}_v\right) \tag{70}$$

is referred to as the residual vector. Applying the implicit Euler scheme to equation (69) yields

$$\frac{Q^{n+1} - Q^n}{J\Delta\tau} = -R^{n+1} \tag{71}$$

where

$$Q = J\hat{Q} \tag{72}$$

The right hand side of equation (71) can be written as a Taylor series expansion in time and truncated after the first two terms to linearize it. If the chain rule for partial differentiation is also used, then the right hand side of equation (71) can be expressed as

$$\begin{aligned} R^{n+1} &\approx R^n + \Delta\tau\left(\frac{\partial R}{\partial \tau}\right)^n = R^n + \Delta\tau\left(\frac{\partial R}{\partial Q}\right)^n\left(\frac{\partial Q}{\partial \tau}\right) \\ R^{n+1} &\approx R^n + \left(\frac{\partial R}{\partial Q}\right)^n \left(Q^{n+1} - Q^n\right) \end{aligned} \tag{73}$$

If equation (73) is substituted back into equation (71) and the terms are rearranged, the following linear system of equations results

$$\left[\frac{\mathbf{1}}{J\Delta\tau} I + \left(\frac{\partial R}{\partial Q}\right)^n\right]\left(Q^{n+1} - Q^n\right) = -R^n \tag{74}$$

Equation (74) represents the linear system of equations that must be solved to obtain the steady-state flow field on the computational domain. The Jacobian of the residual vector R on the right hand side of equation (74) can be very expensive to form for each iteration. Therefore, INS2D-UP utilizes approximate Jacobians of the flux differences to form the banded matrix represented by the Jacobian of the residual vector. The detailed expressions for the elements of the approximate Jacobian of the residual vector can be found in reference [31].

As mentioned previously, INS2D-UP provides a number of different schemes for solving the linear system of equations represented by equation (74). The method used for the present research is the Generalized Minimal Residual or GMRES method, which is described by Rogers [33]. Rogers notes that the convergence of the GMRES method is dependent on the eigenvalue distribution of the matrix being solved. Rapid convergence requires the system of equations to be preconditioned. The preconditioner used INS2D-UP is an Incomplete Lower-Upper (ILU) factorization scheme with zero additional fill. In the study conducted by Rogers [33], the GMRES with ILU preconditioner outperformed point relaxation and line relaxation solution schemes by a factor of between 2 and 9 for a variety of different cases. Typical solution times for the grids used in this research are given in Chapter 7.

Characteristic Relations for Updating Inflow/Outflow Boundary Conditions

Boundary conditions are required at all boundaries of the computational domain in order to obtain a solution to the governing equations on the computational domain. Boundary conditions at no-slip surfaces, slip surfaces, and at the interfaces between grids of a composite grid will be discussed in the next chapter. The boundary conditions used for inflow and outflow boundaries in INS2D-UP are based on the method of characteristics. The use of the artificial compressibility formulation introduces finite-speed waves in the computational domain which are governed by the equations

$$\frac{\partial \hat{Q}}{\partial \tau} = -\frac{\partial \hat{F}}{\partial \xi} \tag{75}$$

for waves traveling in the ξ direction and

$$\frac{\partial \hat{Q}}{\partial \tau} = -\frac{\partial \hat{G}}{\partial \eta} \tag{76}$$

for waves traveling in the η direction. The characteristic relations will be developed here for the ξ direction, noting that similar results are obtained for the η direction. Using equations (54) and (55), equation (75) can be rewritten as

$$\frac{\partial \hat{Q}}{\partial \tau} = -\frac{\partial \hat{F}}{\partial Q}\frac{\partial Q}{\partial \xi} = -A\frac{\partial Q}{\partial \xi} = -X_A \Lambda_A X_A^{-1}\frac{\partial Q}{\partial \xi} \tag{77}$$

Multiplying both sides of equation (77) by X_A^{-1} yields

$$X_A^{-1}\frac{\partial \hat{Q}}{\partial \tau} = -\Lambda_A X_A^{-1}\frac{\partial Q}{\partial \xi} \tag{78}$$

If the X_A^{-1} matrix were moved inside the spatial and time derivatives, the result would be a system of independent scalar equations known as the characteristic equations, each having the form of a wave equation. The sign of the eigenvalues determine the direction of travel of each of the characteristic waves. Information is propagated by the characteristic waves in the direction dictated by the sign of the eigenvalues. For example, at an inflow boundary in a subsonic flow, there are two characteristic waves traveling in the positive direction and one traveling in the negative direction, corresponding to the two positive and one negative eigenvalues (see equation 56). The characteristic wave traveling in the negative direction brings flow field information from the interior of the computational domain to the boundary. Thus at an inflow boundary in a subsonic flow, two elements of the $\hat{Q}$ vector can be specified and the third is computed using a characteristic relation.

For an outflow boundary in a subsonic flow, there are again two characteristic waves traveling in the positive direction and one in the negative direction. In this case the two characteristic waves traveling in the positive direction bring flow field information from the interior of the computational domain to the boundary. Thus, at an outflow boundary in a subsonic flow, one element of the $\hat{Q}$ vector can be specified and the other two are computed using the characteristic relations.

Equation (78) can be generalized to apply to either inflow or outflow boundaries by multiplying both sides of the equation by a diagonal selection matrix L which has an entry of 1 in the position of the eigenvalues to be selected for a given boundary and zeros elsewhere. Thus equation (78) becomes

$$LX_A^{-1}\frac{\partial \hat{Q}}{\partial \tau} = -L\Lambda_A X_A^{-1}\frac{\partial Q}{\partial \xi} \tag{79}$$

If the psuedotime derivative in equation (79) is replaced with an implicit Euler differencing scheme, equation (79) can be written as

$$\left(\frac{LX_A^{-1}}{J\Delta\tau} + L\Lambda_A X_A^{-1}\frac{\partial}{\partial \xi}\right)\left(Q^{n+1} - Q^n\right) = -LX_A^{-1}\frac{\partial Q^n}{\partial \xi} \tag{80}$$

Equation (80) provides an implicit means of updating boundary conditions at inflow and outflow boundaries. However, boundary conditions must be supplied for all the diagonal elements of the L matrix which have a value of zero. This can be incorporated into equation (80) by defining a vector Ω which contains a boundary condition corresponding to each diagonal element of the L matrix which has a value of zero. The remaining elements of the Ω vector are zero. Note that since the elements of the Ω vector are held constant in time, the following relationship holds true.

$$\mathbf{0} = \frac{\partial \Omega}{\partial \tau} = \frac{\partial \Omega}{\partial Q}\frac{\partial Q}{\partial \tau} = \frac{\partial \Omega}{\partial Q} = \mathbf{0} \tag{81}$$

Substituting equation (81) into equation (80) yields

$$\left(\frac{LX_A^{-1}}{J\Delta\tau} + L\Lambda_A X_A^{-1}\frac{\partial}{\partial \xi} + \frac{\partial \Omega}{\partial Q}\right)\left(Q^{n+1} - Q^n\right) = -LX_A^{-1}\frac{\partial Q^n}{\partial \xi} \tag{82}$$

which can be used to implicitly update the elements of the $\hat{Q}$ vector at any inflow or outflow boundary with the proper choice of L and Ω.. The specific choices used for the L and Ω. elements in the present study will be discussed in the next chapter.

CHAPTER VI
COMPUTATIONAL GRID GENERATION AND BOUNDARY CONDITIONS

Generating the two-dimensional computational grid for a multi-element airfoil can be a difficult process. The goal is to generate a computational grid which has sufficient resolution to capture the pertinent flow features. In the flow field around a multi-element airfoil, the important features include the wake regions from the main element, the flap elements, and the slat, the cove regions on the main element or the flaps where recirculating flow may exist, and the gap region between elements where confluent boundary layers are usually present. The grid density should be such that further increases in grid density do not change the solution.

There are two main types of finite-difference grids in general use for performing numerical solutions to the Navier-Stokes equations: unstructured grids and structured grids. Unstructured two-dimensional grids are essentially made up of clouds of grid points in space. Typically, every grid point is joined to neighboring grid points to form triangular cells. There are several advantages to using unstructured grids. Grid points can be easily clustered in regions of the computational domain where detailed flow features need to be resolved. Multiple independent closed surfaces can be easily represented within the computational domain using a single grid. There are also some disadvantages to using unstructured grids. A large number of grid points are required to adequately resolve boundary layer flows, due to constraints on the aspect ratio of the triangular elements. Most algorithms for numerically solving the Navier-Stokes equations are written for structured grids and must be modified to work with unstructured grids. Solution algorithms for the Navier-Stokes equations on unstructured grids are slower and require more memory than corresponding algorithms for structured grids.

An example of a structured two-dimensional grid for a cylinder is shown in Figure 20. It is composed of i radial grid lines and j circumferential grid lines, forming an ixj mesh. If the i grid lines are perpendicular to the j grid lines everywhere within the grid, the grid is classified as an orthogonal grid. C grids, O grids, and H grids are common examples of structured grids. Two-dimensional structured grids around a single body, such as an airfoil, are easy to generate. Their regular structure simplifies the numerical algorithms used to solve the Navier-Stokes equations, leading to lower memory requirements and faster solution speeds. One of the disadvantages of structured grids is that it is difficult, and in many cases impossible, to represent two or more closely spaced independent closed surfaces, such as a multi-element airfoil, within the computational

domain using a single grid. There are, however, several ways to combine multiple individual structured grids into a single composite computational grid.

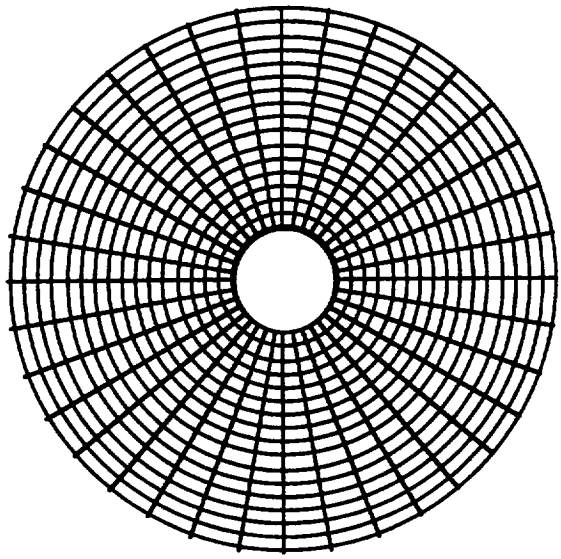

Figure 20: Example of a two-dimensional structured O grid around a cylinder.

One way to patch grids together is by means of the chimera scheme [34]. In the chimera scheme, one grid can be imbedded within another, as shown in Figure 21. A hole boundary is defined in the outer or parent grid to allow the inner grid to be imbedded. The grid points from the outer grid contained within the hole boundary can be 'blanked out' so that they are ignored in the Navier-Stokes solution algorithm. The hole boundary becomes a physical boundary for the outer grid. The hole boundary must be completely contained within the outer boundary of the imbedded grid so that boundary conditions can be interpolated from the inner grid to the hole boundary grid points. Likewise boundary conditions for the outer boundary grid points of the imbedded grid are interpolated from the outer grid. In this manner, several relatively simple structured grids can be combined to create a complex composite grid.

The choice of grid type to be used for this investigation was dictated by a number of factors. The large number of configurations to be computed to generate the computational database made solution speed an important consideration. The need to parametrically vary flap position relative to the main element also had an impact on the choice of grid type. If an unstructured grid were used, it would have to be completely regenerated every time the flap position was changed. By using the chimera scheme with structured grids, the individual grids can be generated once and the flap grid can then be imbedded in the main

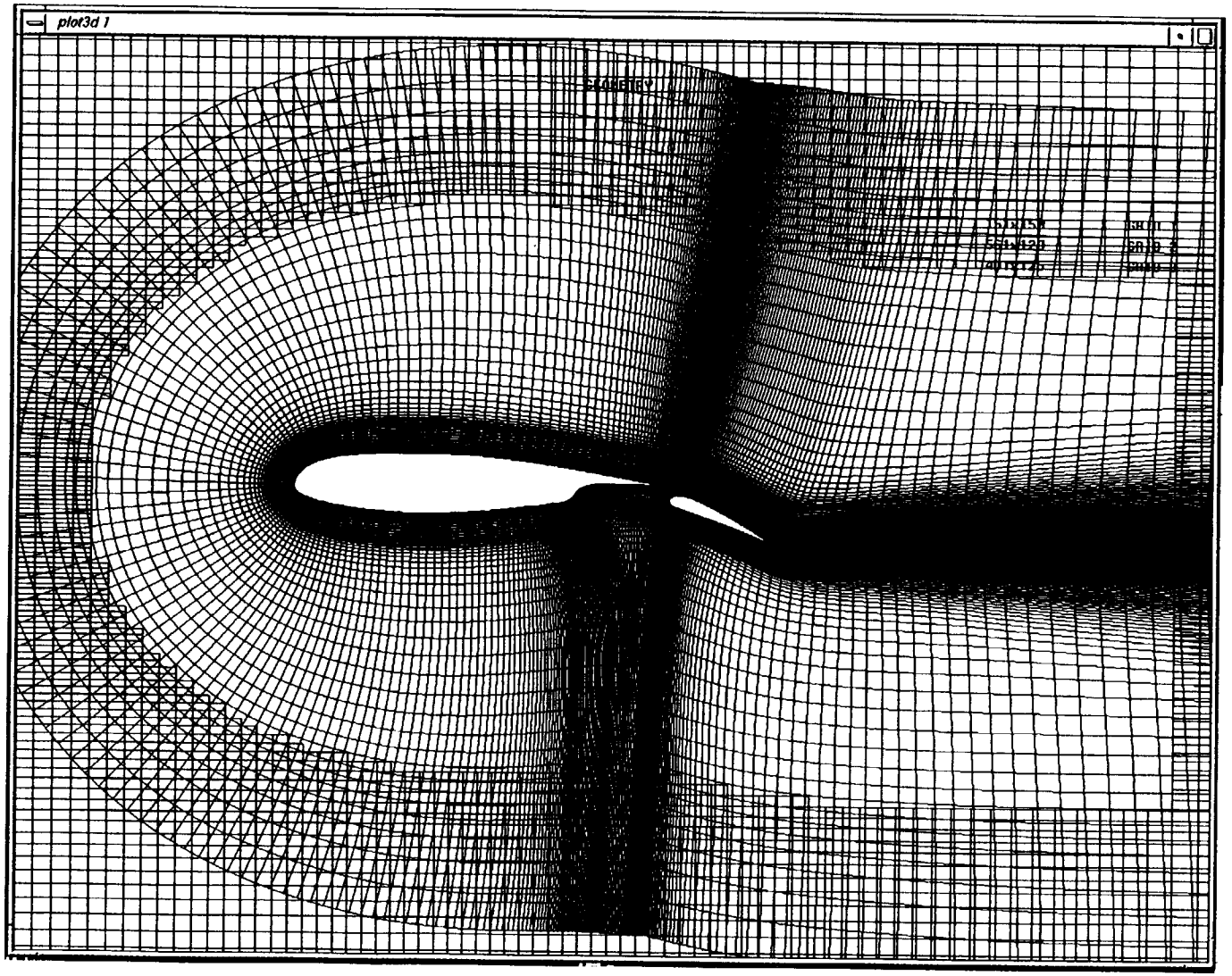

Figure 21: Example of airfoil grid imbedded in outer tunnel grid using the Chimera scheme.

element grid in different positions. These factors dictated the use of the chimera scheme to combine several simple structured grids into a composite grid representing the NACA 63_2-215 ModB airfoil in the NASA Ames 7- by 10-Foot Wind Tunnel. In the following sections, the programs used to generate and combine the grids are discussed briefly and the grids used for the present computations are described in detail. The boundary conditions used for each grid and in particular the boundary conditions used to model the lift-enhancing tabs are also discussed. Finally, the results of a grid sensitivity study are presented.

Surface Grid Generation

The first step in the grid generation process is to create the surface grids. A program called SURFGEN2D was written to generate surface grids for the main element and the flap element. SURFGEN2D is based on the surface grid generation routines used in the potential flow panel code PMARC [35]. A set of (x,z) coordinates representing the surface are read in from a file and cubic splines are fit through the data. Nodes or break points can be specified at any of the points in the original set of coordinates. A break point is always required at the end of the coordinate set. At each break point the user must specify the number of grid points and the spacing of the grid points between the current break point and the previous one, or the beginning of the coordinate set if there is no previous break point. In addition, the slope of the cubic spline fit must be specified as continuous or discontinuous across each break point. The grid point spacing options available within SURFGEN2D include equal spacing, half cosine spacing with the smallest spacing at current break point, half cosine spacing with the smallest spacing at the previous break point, full cosine spacing, and a spacing algorithm developed by Vinokur [36] with the grid point spacing specified at both ends of the region between the current break point and the previous break point. The output from SURFGEN2D is a surface grid file which is then used to generate a two-dimensional finite difference grid.

Two-Dimensional Finite Difference Grid Generation

The grid generation program HYPGEN [37] was used to generate the main element and flap grids. HYPGEN is a hyperbolic grid generation program which requires a surface grid as input. Both two-dimensional and three dimensional grids can be generated with HYPGEN. The finite difference grid is generated in a direction normal to the surface using the solution to a set of hyperbolic partial differential equations. The program allows multiple zones to be defined in the grid generation process, with the number of points, the size of the region, and the stretching options identified for each zone. The stretching

options include exponential stretching with initial spacing at the beginning of the region specified, hyperbolic tangent stretching with grid spacing specified at one or both ends of the region, exponential stretching with variable grid spacing at the beginning of the region, hyperbolic stretching with variable grid spacing at one or both ends of the region, and user-defined stretching. HYPGEN also allows many different types of boundary conditions to be imposed at the boundary of the grid. The boundary of the generated grid can be free-floating (i.e. no constraint is applied), constrained to a constant x, y, or z plane, constrained in two coordinates and free in the third, or periodic with the first and last grid point in the periodic direction coincident. Several other types of boundary conditions can be imposed at the boundary of the grid to handle special cases such as a singular axis point. HYPGEN also has several input parameters that are used to control the smoothness and orthogonality of the generated grid. Guidelines for setting these parameters are given in the HYPGEN users manual, but the optimum settings for a particular grid are problem-dependent and must be determined on a trial-and-error basis.

Composite Grid Generation

Once the individual two-dimensional finite difference grids have been generated, they must be combined into a single composite computational grid using the chimera scheme. This is accomplished by using a program called PEGSUS [38]. PEGSUS reads in the individual grids to be combined and a file of user inputs which tell PEGSUS how to combine the grids. In the simplest case of combining two grids, the user must identify which grid is the imbedded grid and which grid is the outer grid. The scale, position and orientation of the imbedded grid within the outer grid is then defined in that order. The imbedded grid is then positioned within the outer grid by PEGSUS as shown in Figure 22.

The next step performed by PEGSUS is to identify the holes and interpolation boundary points within the various grids. PEGSUS provides three ways to define holes within grids. Two of these methods are indirect means of defining holes and the third is a direct specification of the grid points that define the hole. The indirect means of defining holes in a grid are the more commonly used methods, since the desired hole is generally irregular in shape and the grid points within the hole are not generally known beforehand.

The first method of defining holes in a grid is to define a surface or set of surfaces within the imbedded grid which cut a hole in the outer grid. For the case illustrated in Figure 23, the $j = 10$ grid line (where $j = 1$ is the surface grid and $j = 17$ is the outer boundary of the grid) is defined as the surface in the imbedded grid which makes a hole in the outer grid. The grid points in the outer grid are then checked to see if they lie inside or outside the hole boundary defined by the $j = 10$ surface in the imbedded grid. Grid points

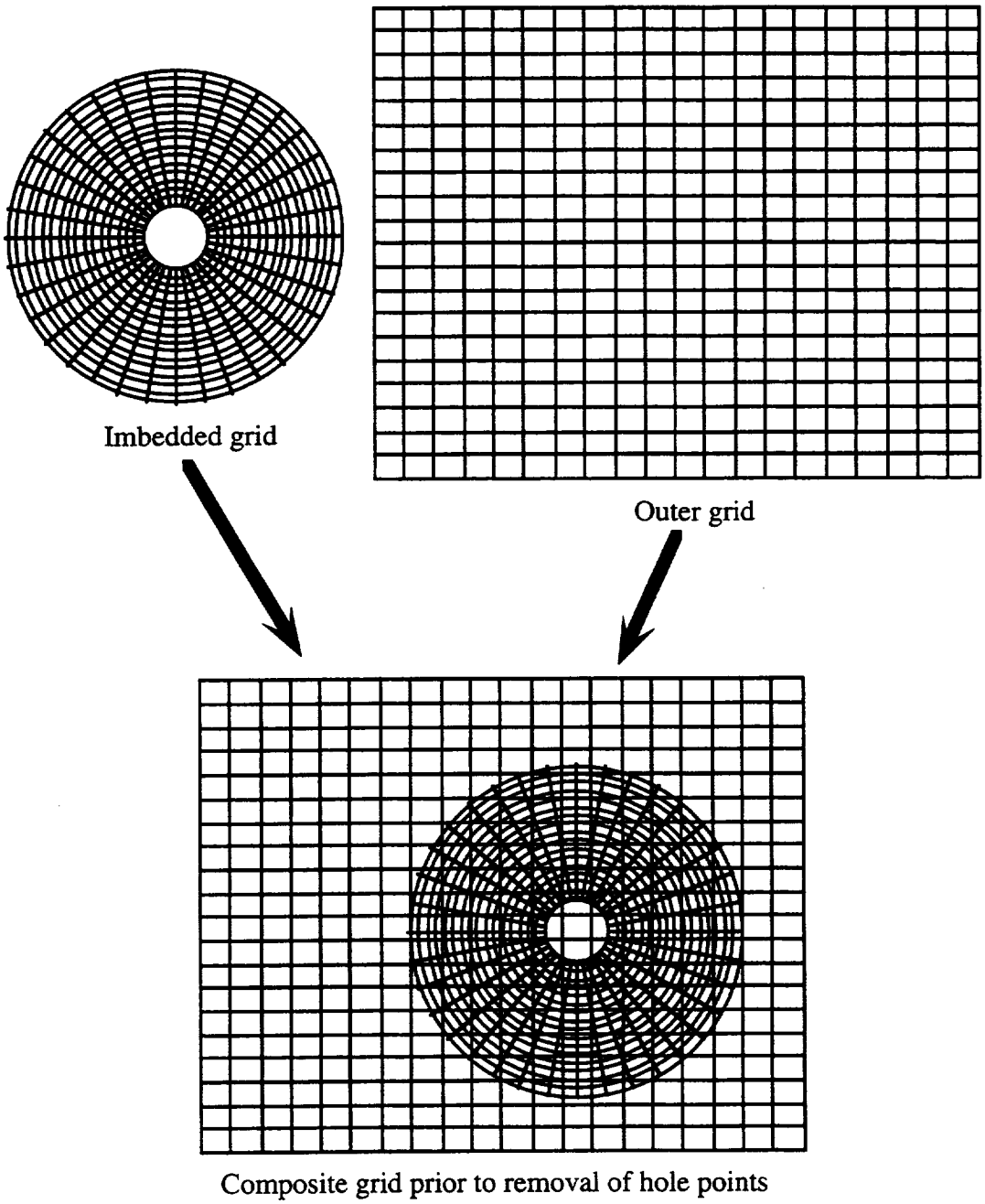

Figure 22: Example of imbedding one grid within another.

from the outer grid lying inside the surface defining the hole boundary are identified as hole points. The set of grid points from the outer grid that are immediately outside the surface defining the hole boundary are identified as interpolation boundary points. The outer boundary points of the imbedded grid are also identified as interpolation boundary points. Communication of the solution to the Navier-Stokes equations between the two grids is

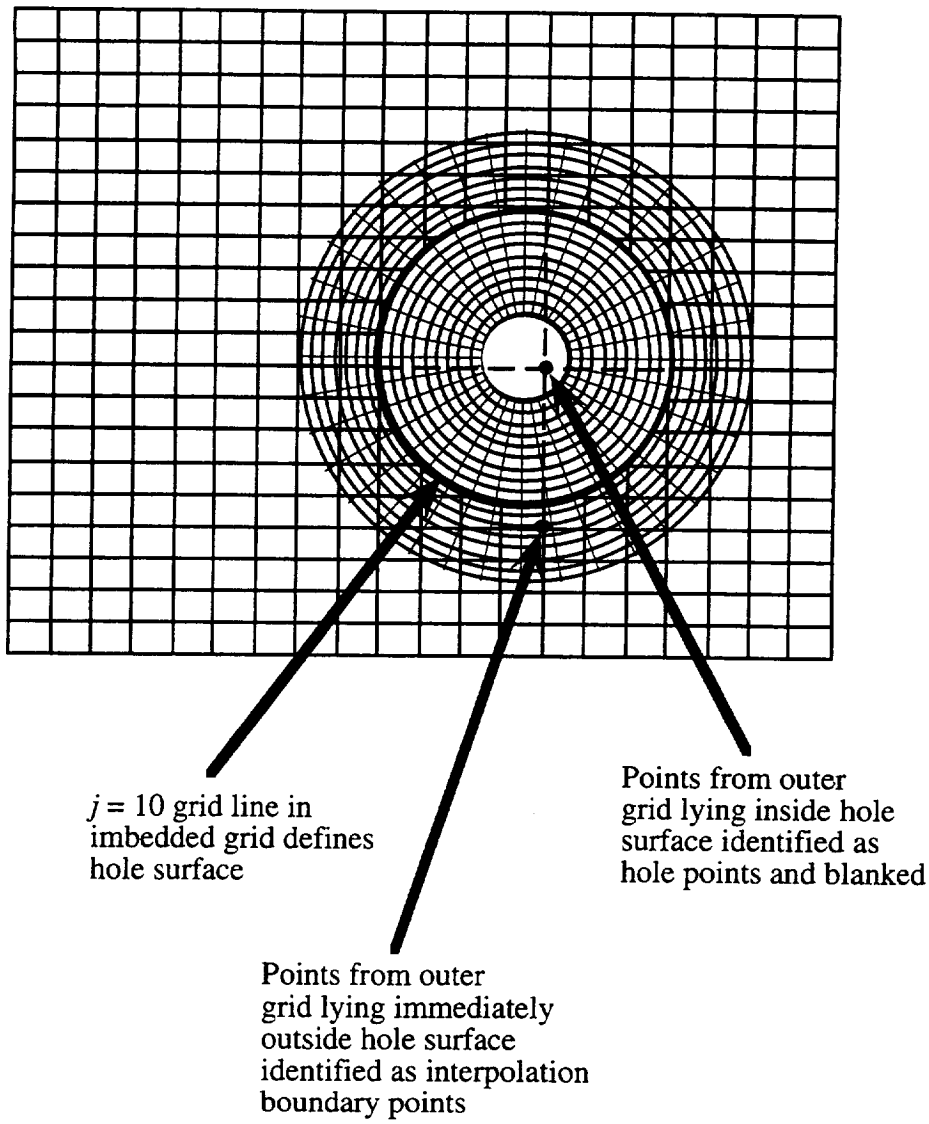

Figure 23: Example of defining hole in outer grid using surface from imbedded grid.

achieved by interpolating the boundary conditions for the interpolation boundary points in one grid from the field points in the other grid. Thus care must be taken to define the surface in the imbedded grid which makes a hole in the outer grid such that there is a minimum overlap of at least one grid cell between the grids around the entire hole boundary.

The second method of creating holes in a grid is to specify a box or set of boxes in the outer grid which define hole boundaries. For the simple case of two grids, the imbedded grid is positioned within the box and must have its entire outer boundary outside the box as shown in Figure 24. For more complex cases, multiple boxes can be used to

define the hole boundary. Boxes can also be used in conjunction with the surface method described above to generate a complex hole boundary. Each box is defined by inputting minimum and maximum values for each of the x, and y coordinates. Hole points and interpolation boundary points are then identified as described above.

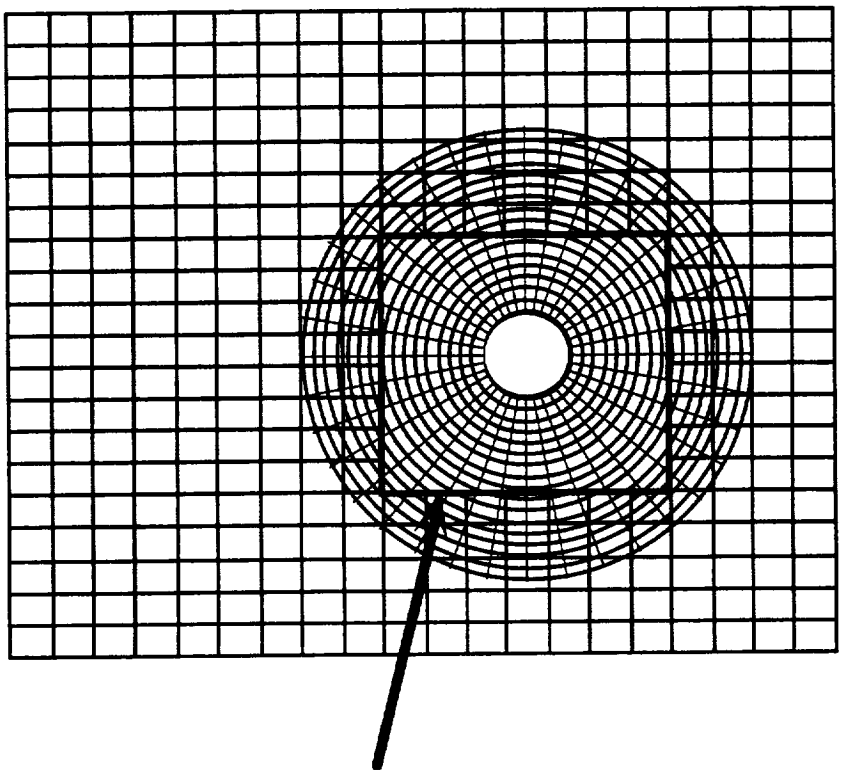

Figure 24: Example of defining hole in outer grid using a box.

The direct method for defining a hole in a mesh involves specifying the i, j indices of the grid points that are to be identified as hole points. The interpolation boundary points are defined as the set of grid points immediately adjacent to the user-specified hole points. Again, care must be taken to allow the imbedded grid and the outer grid to overlap by at least one grid cell around the entire hole boundary to allow interpolation stencils to be set up for each of the interpolation boundary points. The direct method of defining holes in a mesh can be combined with the indirect methods described above to provide considerable flexibility in creating complex hole boundaries.

Once the individual grids have all been positioned within the composite grid and all the hole points and interpolation boundary points have been identified, PEGSUS must

identify each grid point in the composite grid as either a field point, a hole point, or an interpolation boundary point so that the algorithm used for solving the Navier-Stokes equations on the composite grid can treat all the grid points properly. This is accomplished by means of an array called IBLANK. Every grid point in the composite grid has an IBLANK value which is stored in the IBLANK array. Hole points and interpolation boundary points are assigned an IBLANK value of zero (IBLANK = 0). These points are either ignored by the flow solution algorithm if they are a hole point or have the solution updated by interpolation if they are an interpolation boundary point. Field points have an IBLANK value of one (IBLANK = 1) and the solution at these points is updated by the flow solution algorithm and the associated boundary conditions. The IBLANK array is written to an interpolation file which can be read in by the flow solution algorithm.

In addition to setting up the IBLANK array, PEGSUS must determine an interpolation stencil or set of grid points that can be used to supply information to a given interpolation boundary point and the corresponding interpolation coefficients for that stencil. The interpolation stencil for a given interpolation boundary point will depend on how the hole boundary is defined. PEGSUS provides a choice of two different types of hole boundaries: a single fringe boundary and double fringe boundary. A fringe point is another name for an interpolation boundary point. A single fringe boundary is defined as the set of grid points immediately adjacent to a hole in a grid. For a single fringe boundary, there is only one interpolation boundary point or fringe point between a hole point and a field point. If two interpolation boundary points are defined between a hole point and a field point, a double fringe boundary results. A double fringe boundary generally provides more accurate interpolation between grids than a single fringe boundary because it allows the use of a higher order interpolation stencil. However, a double fringe boundary can be more difficult to implement when creating a composite grid because it requires a larger overlap region between the hole boundary in the outer grid and the outer boundary of the imbedded grid.

Grid Generation Process

The two-dimensional computational grid used to represent the two-element NACA 63_2-215 ModB airfoil in the Ames 7- by 10-Foot Wind Tunnel was composed of three individual structured grids which were combined into a single composite computational grid using the chimera scheme. The three individual grids used were the main element grid, the flap grid, and the wind tunnel test section grid. The computational grid included the wind tunnel test section so that direct comparisons could be made between the computational results and the experimental results without having to make any wind tunnel wall corrections to the experimental data.

The coordinate data used to generate the surface grids representing the main element and the flap was obtained from a digital validation of the model. A Brown and Sharpe validator was used to digitize the main element and the flap. Approximate section coordinate data for the main element and flap was used to determine surface normal vectors so that the validator could make its measurements by coming in normal to the surface. This greatly improves the accuracy of the measurements in regions of high surface curvature such as in the leading edge regions. The Brown and Sharpe validator has a nominal accuracy of better than ±0.001 inch. For the computational grids, all coordinate data was nondimensionalized by the chord of the airfoil with the flap retracted, yielding a reference chord of 1.0 for the computational model. All grid point spacings and distances in the following discussion should be understood as nondimensional fractions of chord.

The main element of the airfoil and the flap were each represented with a single two-dimensional C grid. The surface grid used for the main element and its wake is shown in Figure 25. Note that the upper and lower wake lines are coincident and the full length of the wake is not shown. The actual grid points are omitted for clarity. A similar surface

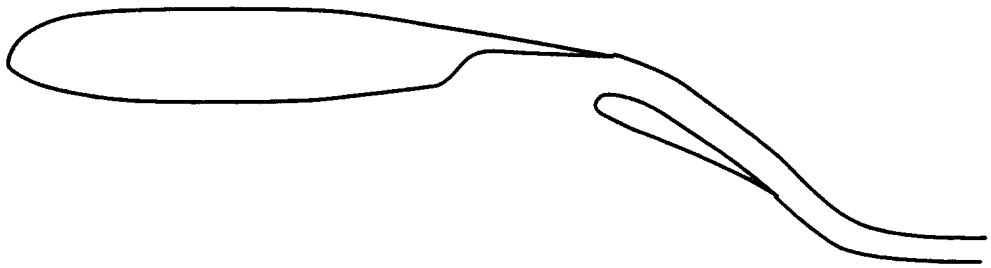

Figure 25: Surface grids used to generate main element and flap grids.

grid was used for the flap. The shape of the main element wake line was based in part on previous computational work done on two-element airfoils by Carrananto [12]. The main element wake line follows the contour of the upper surface of the deflected flap, maintaining a constant height above the flap equal to the size of the flap gap between the main element and the flap. Beyond the trailing edge of the flap, the main element wake line is then deflected gradually until it lines up with the free stream flow. The main element wake line extends 2.5 chord lengths downstream from the flap trailing edge. The wake line is represented with 130 grid points. Vinokur stretching is used with a grid spacing of 0.08 at the downstream end of the wake and a grid spacing of 1.0E-05 at the main element trailing edge. A high density of grid points along the main element wake line was desired in order to resolve flow field details over the upper surface of the flap.

The flap wake line leaves tangent to the lower surface of the flap at the trailing edge and gradually deflects until it lines up with the free stream flow. The flap wake line extends 1.25 chord lengths downstream from the flap trailing edge and is represented with 110 grid points. Vinokur stretching is used with a grid spacing of 0.025 at the downstream end of the wake line and a grid spacing of 1.0E-05 at the flap trailing edge. The shape of the wake lines for each element were determined on a trial-and-error basis with the objective of keeping the computed velocity defect from each wake more or less centered on the wake lines.

The trailing edges of the main element and the flap required special attention in the surface grid generation process. The NACA 63_2-215 ModB airfoil has blunt trailing edges on the main element and flap, with a thickness of t/c = 0.0013 and t/c = 0.001 respectively. The blunt trailing edges were modeled as shown in Figure 26. The actual

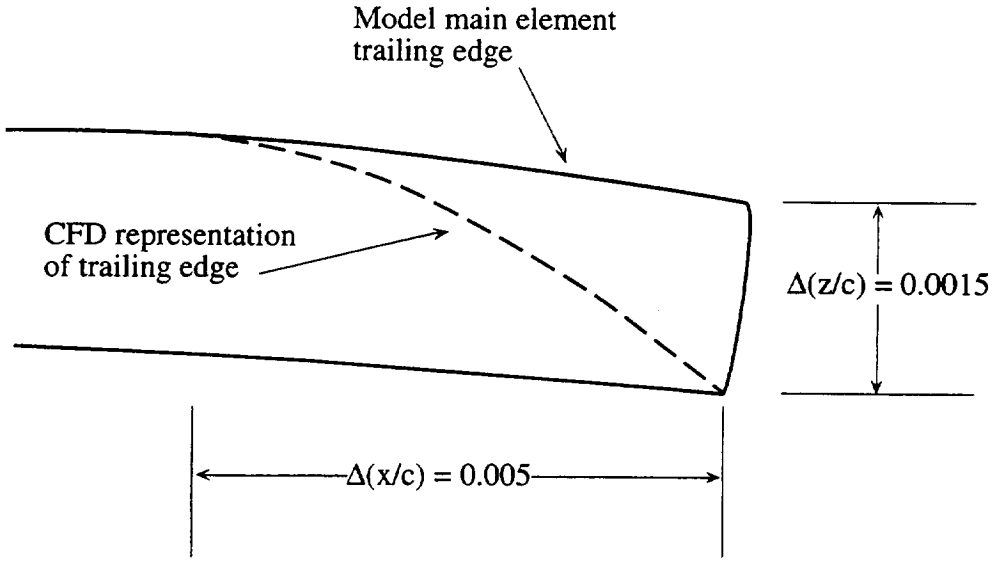

Figure 26: Model used to represent blunt trailing edges in the computational grid.

trailing edge thickness was maintained up to a point 0.005 from the trailing edge. Then the upper surface was transitioned down to the lower surface using a quadratic curve fit which matched the slope of the upper surface at the point 0.005 from the trailing edge. This model allowed the flow physics associated with a blunt trailing edge, namely a recirculation bubble aft of the blunt trailing edge and a base pressure load, to be captured while permitting the main element and flap to each be represented with a single conventional C grid. This model also simplified the task of creating the composite grid using the chimera scheme. The wake region behind the blunt trailing edges of the main element and

flap did not have to be represented with separate grids. This reduced the number of individual grids required to represent the two-element airfoil from four to two and made it easier to parametrically vary the flap gap and flap angle with respect to the main element.

The surface grids for the main element and flap were divided into several regions. Vinokur stretching with grid point spacing specified at the beginning and end of the region was used to control the spacing of grid points in all regions. The first region extended from the trailing edge to a point 0.001 forward of the trailing edge on the lower surface on each element. This region was represented using 25 grid points with a beginning and ending grid spacing of 1.0E-05. This region was created to allow the lift-enhancing tabs to be modeled as shown in Figure 27. In the boundary conditions file for the Navier-Stokes solution algorithm, no slip boundary conditions are specified for a set of grid points representing the surface of the tab, as depicted by the outline in Figure 27. The points within the outline representing the tab have their IBLANK value set to zero in the IBLANK array, so that these points are ignored by the solution algorithm. The beginning and ending grid spacings in this region were chosen to resolve the boundary layer along the surface of the tabs. The number of grid points used in the tab region was chosen such that the grid lines leaving normal to the lower surface at the trailing edge remained relatively parallel to each other at least through a distance equal to the height of the tab. When no tab is desired on either the main element or the flap, the corresponding boundary conditions are simply commented out in the boundary condition file and the grid points at the tab location are treated as normal field points.

The next region of the surface grid for the main element is the cove region. This region extends from a point 0.001 forward of the main element trailing edge to the beginning of the cove on the lower surface. On the NACA 63_2-215 ModB airfoil used in the experiment, the lower surface of the airfoil transitions smoothly into the cove region as shown in Figure 28a. This geometry does not produce a well-defined flow separation point, as would be the case for the cove region shown in Figure 28b. Thus, the grid spacing at the beginning of the cove region was made fine to try and accurately resolve the point at which the flow separates as it enters the cove region. The cove region was represented using 80 grid points with a grid spacing of 0.0005 at the upstream end of the cove and a grid spacing of 1.0E-05 at the downstream end of the cove.

The remainder of the surface grids for the main element and the flap are divided into two regions: the lower surface region and the upper surface region. This allowed grid points to be clustered at the leading edge of each element. The lower surface of the main element, from the leading edge to the beginning of the cove, is represented using 80 grid points with a grid spacing of 0.002 at the leading edge and 0.0005 at the beginning of the

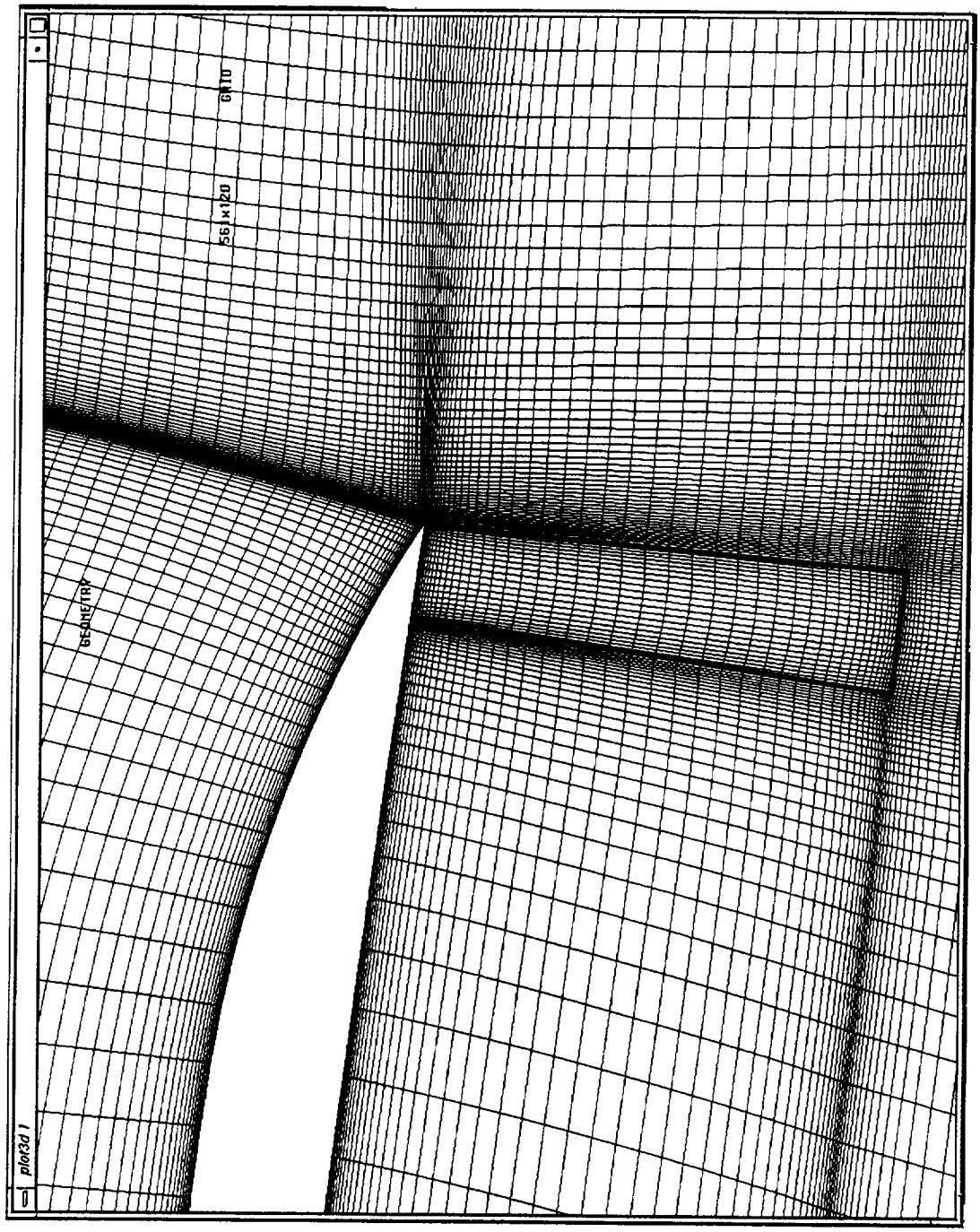

Figure 27: Cove tab region of main element grid.

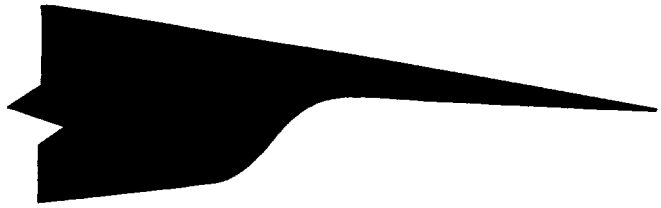

a) Main element cove for ModB airfoil

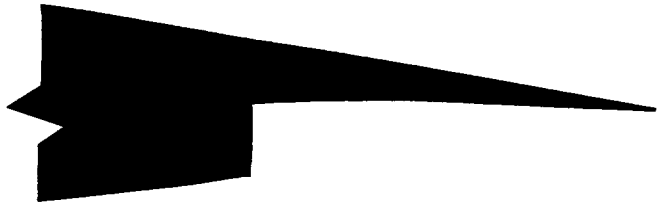

b) Main element cove typical of current transport aircraft

Figure 28: Cove regions on main element for ModB model and for typical transport aircraft.

cove. The upper surface of the main element is represented using 115 grid points with a grid spacing of 0.002 at the leading edge and 1.0E-05 at the trailing edge. The flap lower surface, from the leading edge to the beginning of the tab region, is represented with 65 grid points with a grid spacing of 0.001 at the leading edge and 1.0E-05 at the beginning of the tab region. The flap upper surface is represented with 90 grid points with the same initial and ending grid point spacing as the lower surface. The main element surface grid, including the upper and lower wake lines, utilizes 561 grid points. The flap surface grid, including the wake lines, is made up of 401 grid points.

The C grids for the main element and flap were generated with HYPGEN, using the surface grids for the main element and the flap as input. Both C grids were divided into several zones in order to capture key flow field features. Hyperbolic tangent stretching with initial and final grid point spacing specified was used to control the spacing of grid points in each zone. The first zone extended from the surface to a distance, measured normal to the surface, equal to the height of the lift-enhancing tab being modeled. For example, if the tab height being simulated was 0.005, the first zone extended a distance of

0.005 from the surface. This allowed the grid spacing in the *j* direction (normal to the surface grid) to be controlled at the tip of the tab. The grid spacing at the surface in this zone was 1.0E-05, which yielded a $y^+ \approx 3.0$ at the first grid point above the surface. This value was chosen based on work done by Rogers in which the effect of the grid spacing at the surface on the accuracy of various turbulence models was studied [21]. The grid point spacing at the outer edge of this zone was 2.0E-05. A total of 45 grid points in the *j* direction were used for this zone.

The remaining zones in the main element grid were used to control grid point spacing in the *j* direction in the flap gap region of the grid, as well as in the vicinity of the hole boundary created by the flap grid. The grid point spacing at the inner edge of each zone matched the spacing at the outer edge of the previous zone, thus providing a smooth transition in grid point spacing from one zone to the next. The second zone in the main element grid had a width in the *j* direction of 0.07 and a total of 45 points were used in this zone. The grid point spacing at the outer edge of this zone was 2.0E-03. The third zone had a width of 0.5 and the grid point spacing at the outer edge of this zone was 5.0E-02. This zone contained 20 grid points in the *j* direction. The final outer zone in the main element grid was 0.5 wide, contained 10 grid points in the *j* direction, and a grid point spacing at the outer edge of the zone of 1.0E-01. The total number of grid points in the *j* direction used for the main element grid was 120. The outer boundary of the main element grid was located 1.075 chord lengths from the surface.

The remaining zones in the flap grid were used to control grid point spacing in the *j* direction in the region where the flap grid crosses the wake line of the main element grid. Previous work by Rogers [21] has shown the importance of providing sufficient resolution in the flap grid at the interface between the flap grid and the main element grid where the flap grid crosses the main element wake cut. This is necessary so that flow field information from the main element wake is properly communicated to the flap grid. Since the main element wake line maintains a distance above the flap upper surface equal to the flap gap size, the width of the second zone in the flap grid is set equal to the flap gap size minus the width of the first zone in the flap grid. This allows *j* grid lines in the flap grid to be clustered around the wake line of the main element. The second zone in the flap grid contains 45 points in the *j* direction and the spacing at the outer edge of the zone is 2.0E-04. The final zone in the flap grid has a width of 0.045, contains 35 grid points in the *j* direction, and has a grid spacing of 2.0E-03 at the outer edge. A total of 125 grid points in the *j* direction were used in the flap grid. The outer boundary of the flap grid was located 0.07 to 0.10 chord lengths from the surface, depending on the size of the flap gap.

Once the basic main element and flap grids were constructed, further refinement was required in the wake regions of each grid. For a C grid around an airfoil, the grid spacing in the direction normal to the wake line tends to be very fine, with a large number of grid points near the wake line. This is a result of the fine grid spacing used normal to the airfoil surface to resolve the boundary layer. The clustering of grid lines around the wake line can lead to convergence problems if the airfoil grid is imbedded in an outer, coarser grid, due to inaccuracies in the interpolation between the very fine grid and the coarse grid. It can also make resolving the wake velocity defect more difficult as the distance from the trailing edge increases. The wake from an airfoil spreads as it moves away from the airfoil trailing edge. If grid lines are tightly clustered around the wake line, the wake velocity defect is not resolved very well. However, if the grid lines are spread away from the wake line in a fashion similar to the wake spreading, it is easier to resolve the wake accurately over a greater distance downstream from the airfoil trailing edge. Spreading the grid lines away from the wake line can also improve convergence for an airfoil grid imbedded in a coarse outer grid because it provides a better matching of grid spacing at the interface between the two grids. The grid lines around the wake line can be made to spread with increasing distance from the airfoil trailing edge by applying an elliptic smoothing algorithm to the wake region of the grid.

The individual grid files were read into an elliptic smoothing program along with an input file identifying the grid point index corresponding to the lower surface trailing edge grid point. The grid point index corresponding to the upper surface trailing edge grid point can be computed based on the fact that the upper and lower wake lines of a C grid have the same number of grid points. The elliptic smoothing algorithm only affects grid points that are downstream of the trailing edge.

The algorithm works by utilizing the elliptic grid generation equations given below.

$$\begin{aligned} \xi_{xx} + \xi_{yy} &= P(\xi, \eta) \\ \eta_{xx} + \eta_{yy} &= Q(\xi, \eta) \end{aligned} \tag{83}$$

The grid spacing control parameters P and Q are set to zero, reducing equations (83) to a pair of Laplace's equations. Transforming equations (83) to computational space with P and Q set to zero yields

$$\begin{aligned} \alpha\, x_{\xi\xi} - 2\beta\, x_{\xi\eta} + \gamma\, x_{\eta\eta} &= 0 \\ \alpha\, y_{\xi\xi} - 2\beta\, y_{\xi\eta} + \gamma\, y_{\eta\eta} &= 0 \end{aligned} \tag{84}$$

Finite difference expressions for the partial derivatives are then substituted into equations (84). The resulting finite difference equations are solved by using an ADI method, but

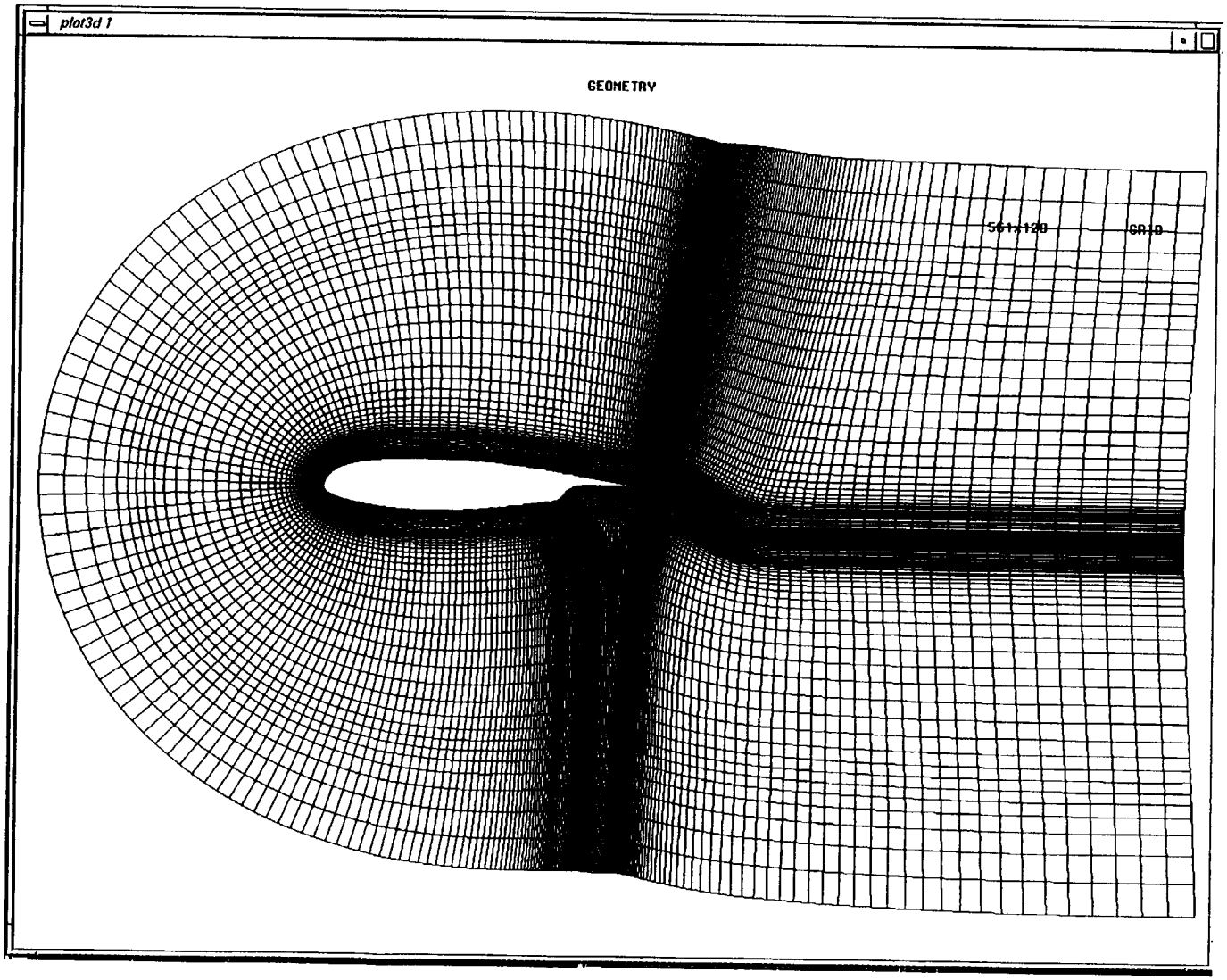

a) Prior to smoothing

Figure 29: Elliptic smoothing of grid in region of main element wake.

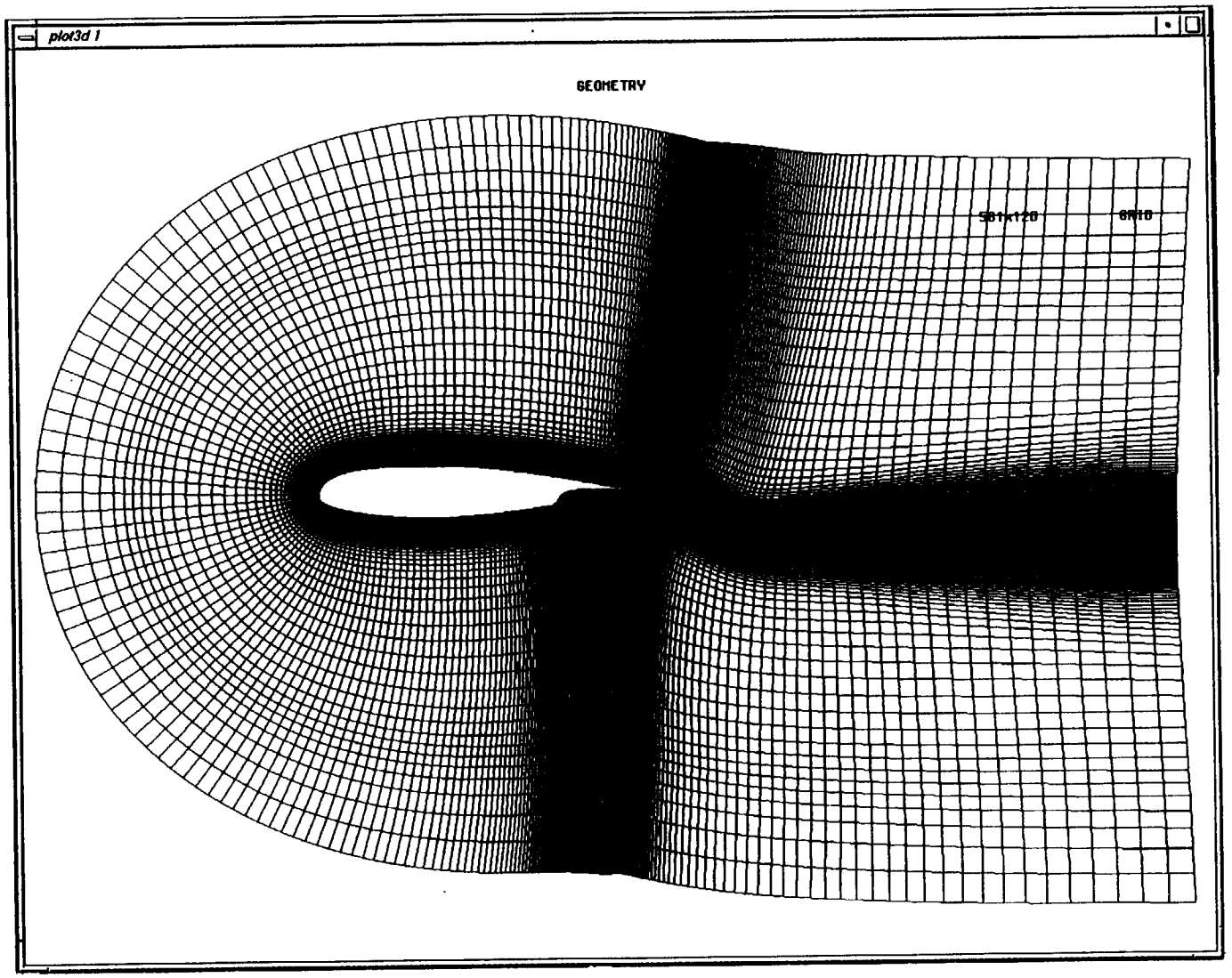

b) After smoothing

Figure 29, concluded: Elliptic smoothing of grid in region of main element wake.

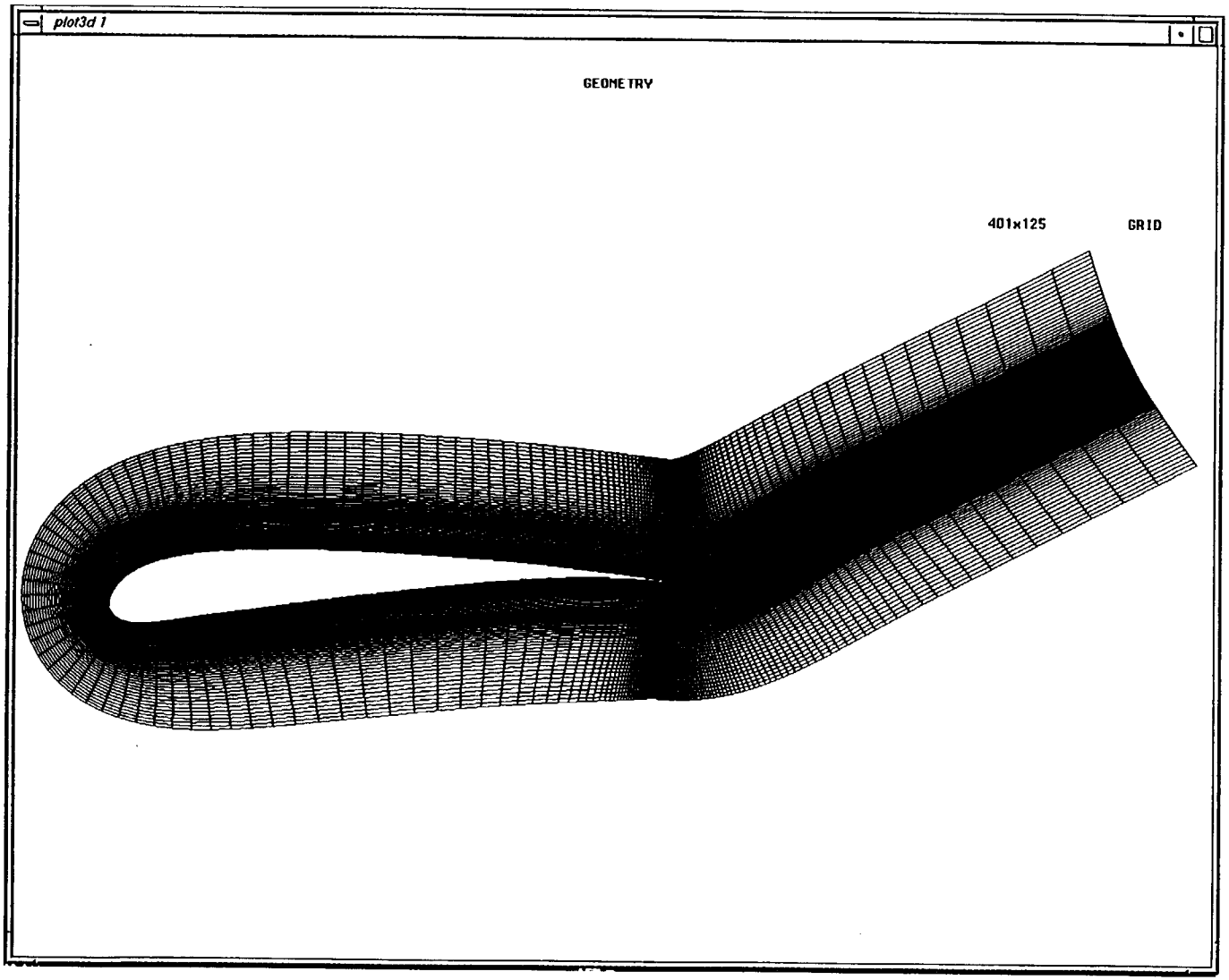

a) Prior to smoothing

Figure 30: Elliptic smoothing of grid in region of flap wake.

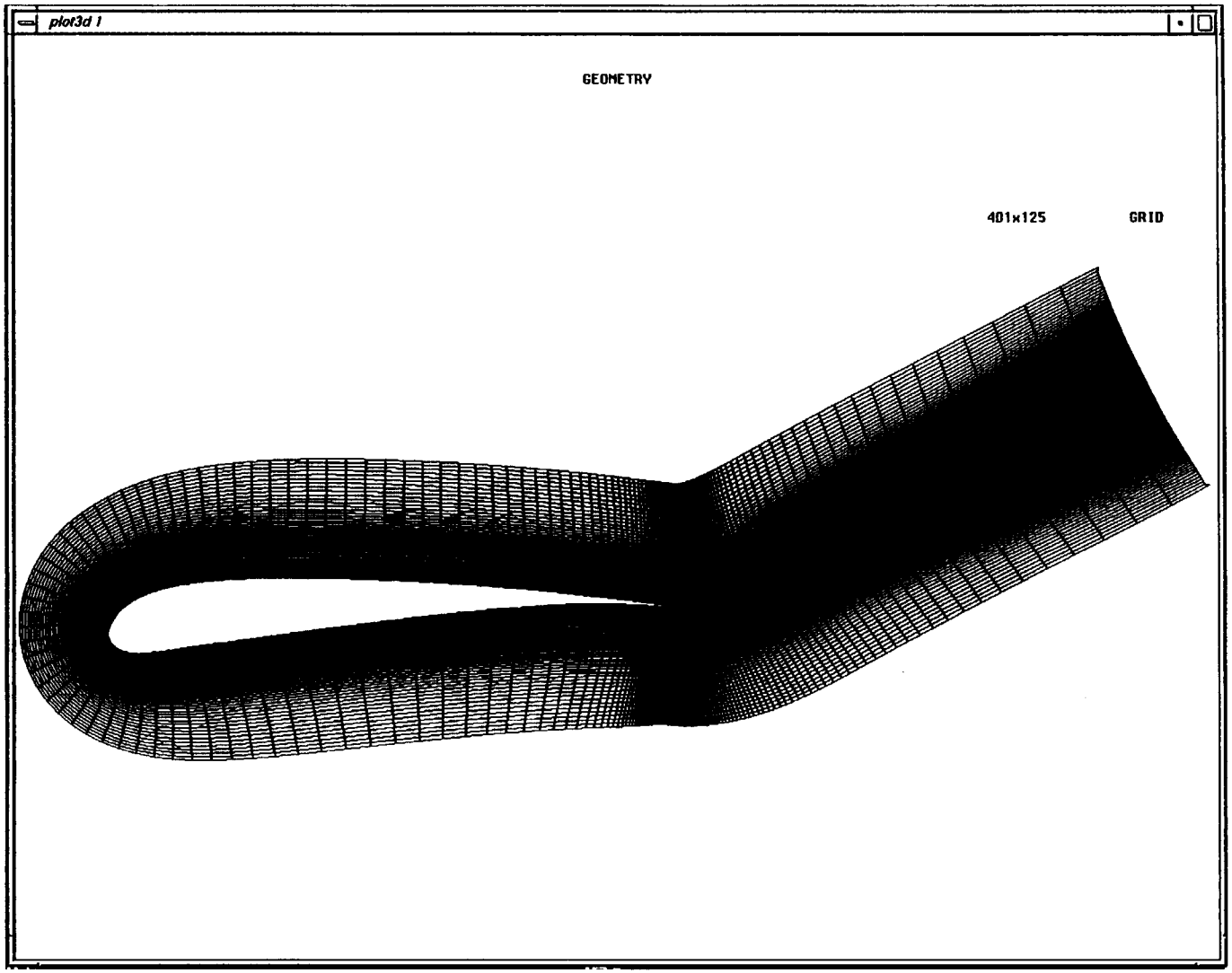

b) After smoothing

Figure 30, concluded: Elliptic smoothing of grid in region of flap wake.

only sweeping through the grid in the *i* direction (along the wake line). This has the effect of making the grid point spacing in the direction normal to the wake line more uniform with increasing distance downstream from the trailing edge, while preserving the grid point spacing along the wake line. Two to four iterations are sufficient to produce a smoothly spreading grid in the wake region. The resulting refined grid is compared to the original grid in Figure 29. A similar comparison is shown in Figure 30 for the flap grid.

The area bounded by the wind tunnel test section walls was represented using an H grid as shown in Figure 31. A close up of the test section region of the grid is given in Figure 32. The test section walls in the NASA Ames 7- by 10-Foot Wind Tunnel diverge at a small angle to account for the growth in the displacement thickness of the wall boundary layer. Thus, the effective width between the side walls in the 7- by 10-Foot Wind Tunnel is a constant 10 ft down the length of the test section. The walls in the computational grid were modeled as parallel walls set 10 ft apart. A "slip" boundary condition was specified at the wall, so that a uniform velocity profile was obtained across the entire width of the test section grid. The test section grid was extended 10 chord lengths upstream and 11 chord lengths downstream of the center of rotation for the airfoil. Increasing the length of the test section grid further in either the upstream or the downstream direction did not affect the solution in the imbedded multi-element airfoil grid. Vinokur stretching was used to space the grid points in both the downstream and cross-stream directions in the test section grid. A total of 151 grid points were used in the downstream direction with the initial and final grid point spacing set to 1.0. In the cross-stream direction, 150 grid points were used with the initial and final grid point spacing set to 0.1. This resulted in a clustering of grid lines in the central portion of the test section grid, which made defining the interface between the test section grid and the imbedded airfoil grid simpler.

Once the three individual grids were constructed and refined, the final step in the grid generation process was to combine the three grids in the proper positions and orientations using PEGSUS to create the composite grid. The flap grid was imbedded entirely within the main element grid. The input parameters in PEGSUS used to define the position and orientation of the flap grid in the main element grid were determined using a utility program called GAPME, originally written by Storms [8,9] and modified for the present study. The GAPME program reads in the surface grid files for the main element and the flap, along with the desired settings for flap angle, gap, and overlap. GAPME has several algorithms for setting flap gap. The one used in this case was consistent with the experimental definition of flap gap described earlier and shown in Figure 14. The GAPME program rotates the flap about its leading edge to the desired flap angle. The flap is then

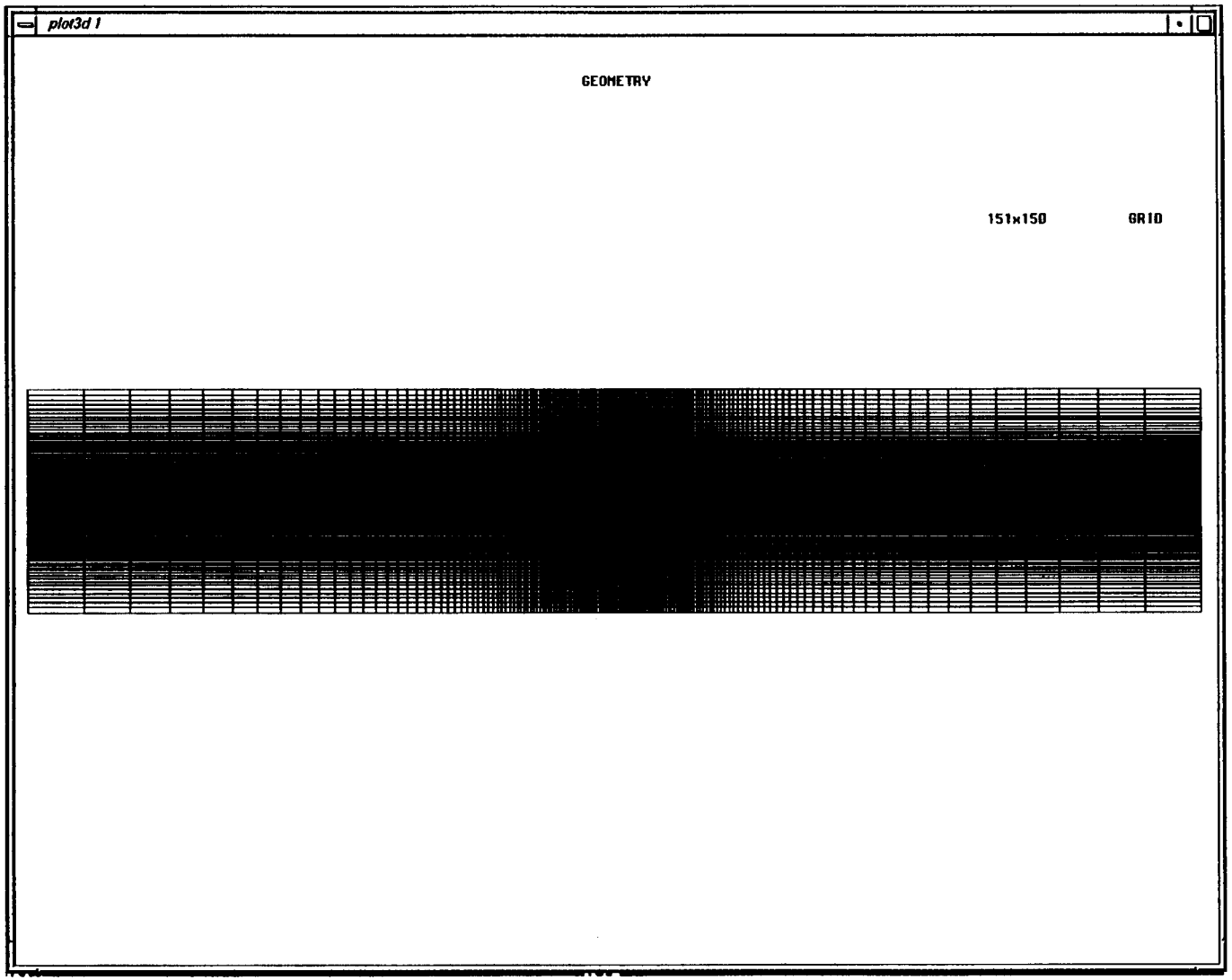

Figure 31: H grid used to model tunnel.

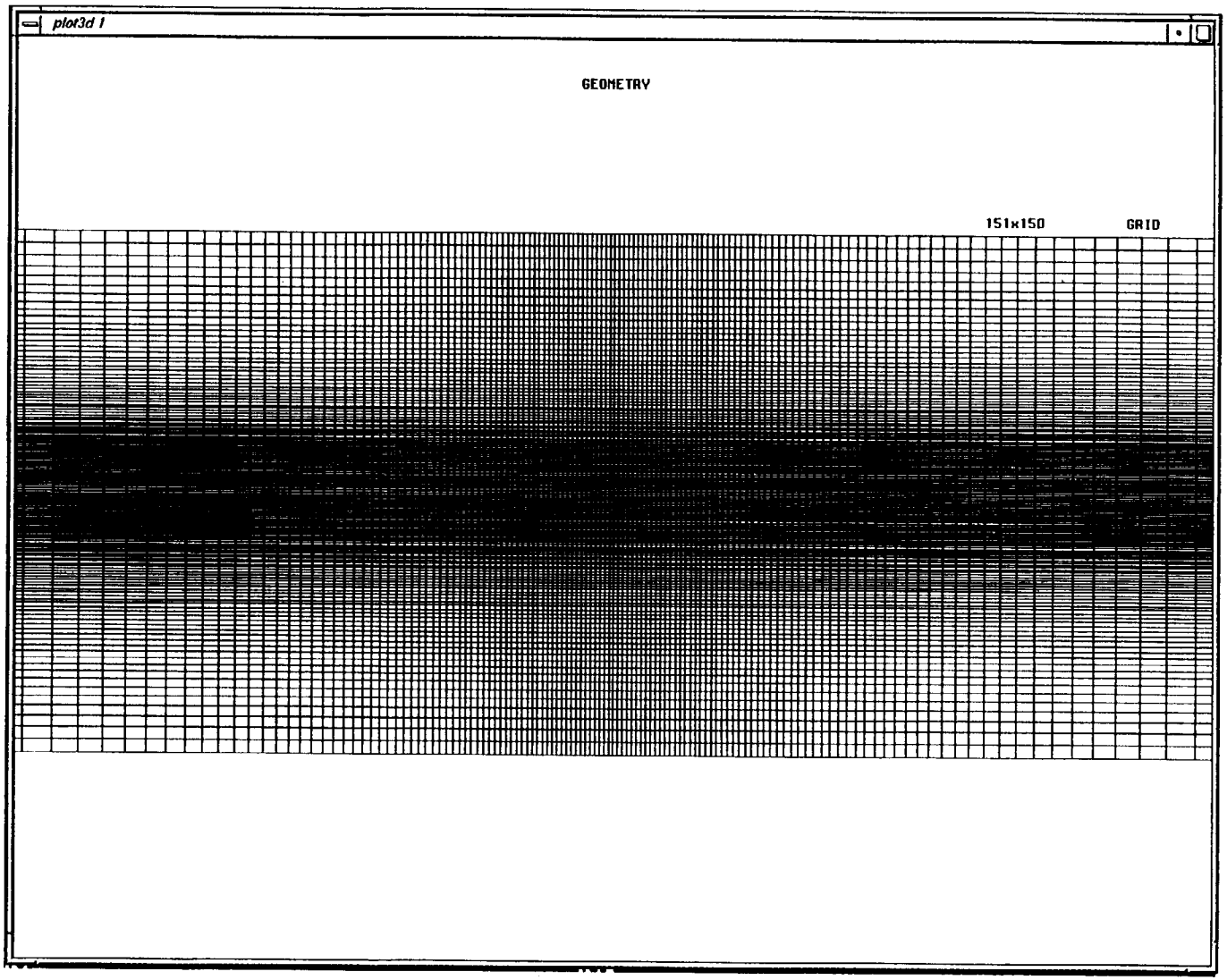

Figure 32: Test section region of tunnel grid.

translated in two-dimensional space until the desired flap gap and overlap are achieved. Finally, the flap is rotated back to a 0° flap angle and the new coordinates of the flap leading edge are determined, along with the translation offsets from the original coordinates of the flap leading edge. The translation offsets and the new coordinates of the flap leading edge are written to an output file for use in setting input parameters in PEGSUS. In PEGSUS, the flap grid is first translated by the translation offsets and then rotated to the desired flap angle about a rotation point defined by the new coordinates of the flap leading edge as computed by GAPME.

In order to imbed the flap grid in the main element grid, the hole boundary of the hole that the flap grid makes in the main element grid must be defined. This is accomplished by using the indirect method of defining a surface to create the hole boundary within PEGSUS. A surface is defined in the flap grid which cuts a hole in the main element grid. The surface was defined as the $j = 70$ grid line, the $i = 15$ grid line, and the $i = 387$ grid line. All the main element grid points which lie within this surface are blanked out. The surface was chosen to provide sufficient grid overlap between the main element grid and the flap grid to use the double fringe method for the interpolation boundary points.

It was also necessary to specify a hole in the flap grid caused by the main element grid in order to properly handle the flap gap region. In this case, the direct method of hole specification was used. Two hole regions were explicitly defined in the flap grid as shown in Figure 33. For a flap deflection angle of 30°, the first was defined as the region i =203 to $i = 204$ and j =120 to $j = 125$. The second was defined as the region $i = 205$ to $i = 217$ and $j = 86$ to $j = 125$. These two holes in the flap grid also allowed the lift enhancing tabs attached to the main element to be contained entirely within the main element grid as shown in Figure 34. The definition of the two holes in the flap grid had to be changed whenever flap deflection angle was changed, but it did not have to be changed for gap changes.

A similar process was followed for imbedding the main element/flap composite grid within the test section grid. A surface in the main element grid which creates a hole in the test section grid was defined. The surface was specified as the $j = 112$ grid line, the $i = 6$ grid line, and the $i = 556$ grid line. This allowed sufficient overlap between the main element grid and the test section grid to use the double fringe method for the interpolation boundary points.

The final composite grid is shown in Figure 35 for an airfoil angle of attack of 0°. Angle of attack was changed by rotating the test section grid in PEGSUS to the desired angle while holding the airfoil grids fixed. A total of 140,095 grid points (including grid points in holes that were blanked out) were used in the composite grid. The composite grid

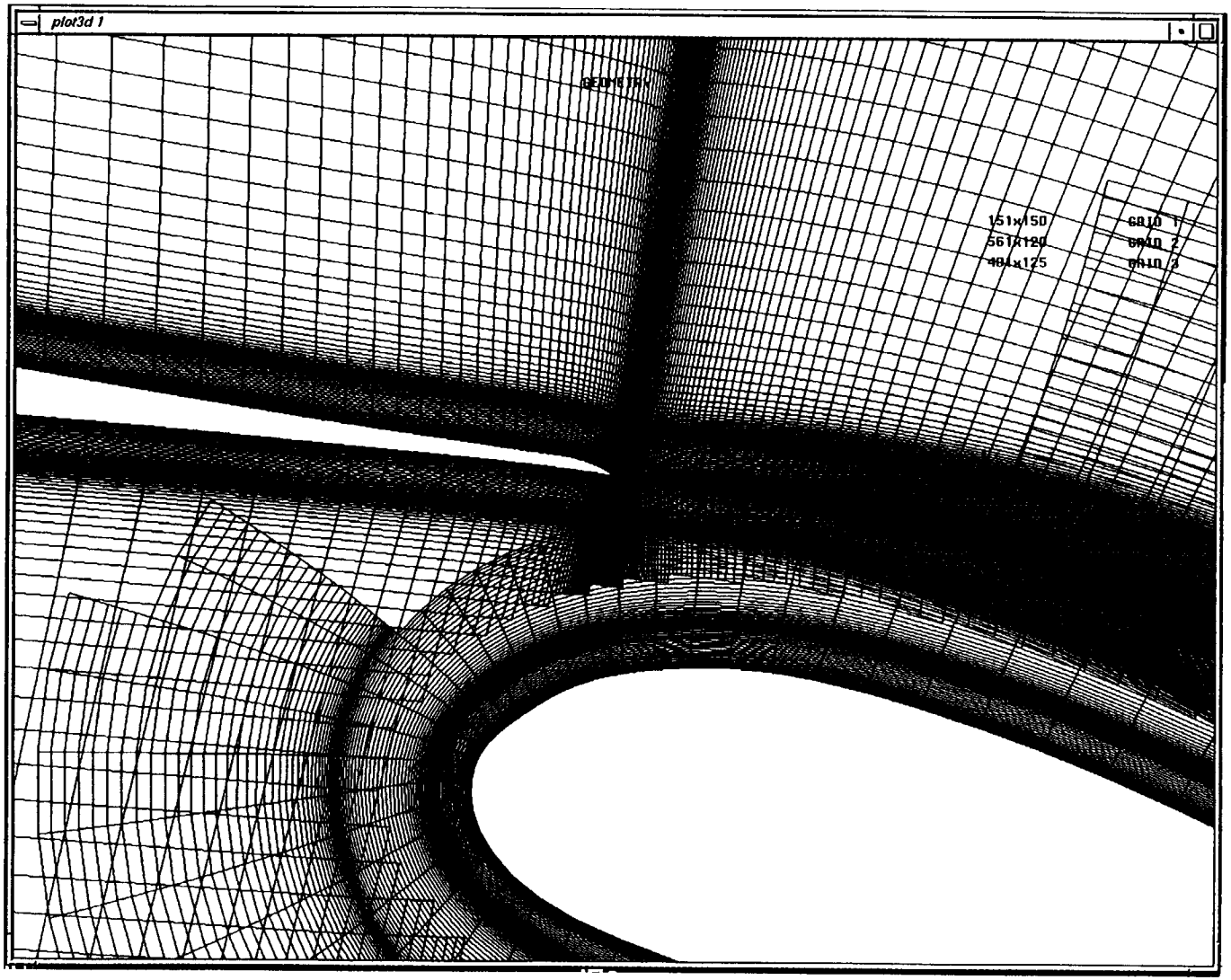

Figure 33: Holes specified in flap grid to accommodate flap gap region.

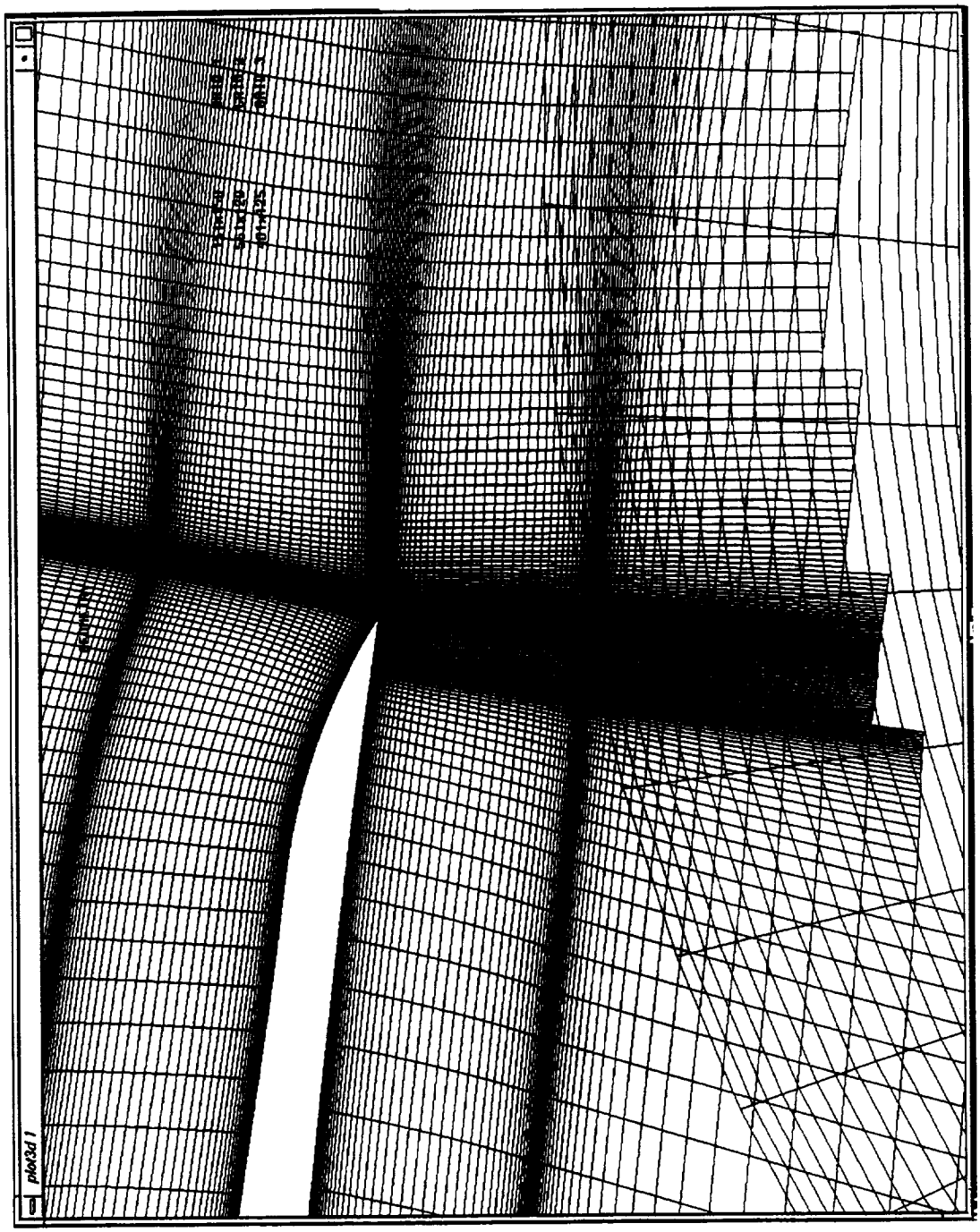

Figure 34: Location of cove tab relative to flap grid.

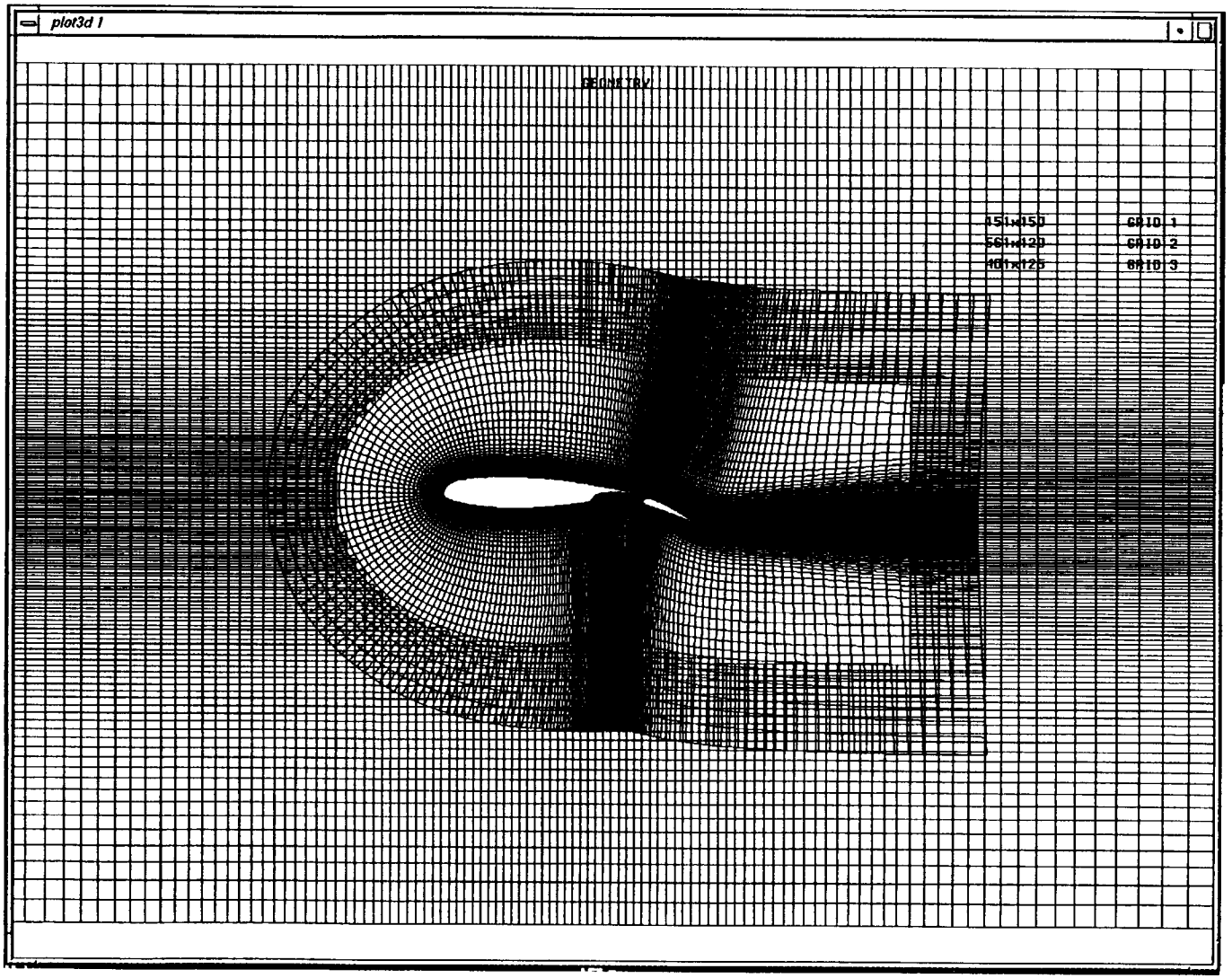

Figure 35: Final chimera composite grid for two-element airfoil in tunnel.

created for this study utilized much finer grid resolution than was used in previous studies [12]. Most of the increased resolution was concentrated in the wake and flap gap regions of the grid. One particular difference between the grid used in this study and those of previous studies was the use of grid spacing fine enough to resolve the boundary layer along all the surfaces of the lift-enhancing tabs. The purpose of the enhanced grid resolution was to try to fulfill one of the key objectives of this research: to develop an understanding of the flow physics associated with lift-enhancing tabs.

Boundary Conditions

All boundary points for a computational grid must be assigned boundary conditions (or initial conditions for some boundary points in unsteady computations) in order for the Navier-Stokes solution algorithm to generate a solution at all field points within the grid. In a composite grid created using the chimera scheme, there are two types of boundary points that must be considered. The first type of boundary points are hole boundary points and outer boundary points of imbedded grids. These boundary points are assigned boundary conditions composed of interpolation stencils and interpolation coefficients computed by a code such as PEGSUS during the composite grid generation process and written to a file which can then be read in by the Navier-Stokes code. The second type of boundary points include surface grid points, wake line points in C grids, and outer boundary points of the composite grid. This type of boundary point must be identified explicitly by the user and assigned some type of boundary condition. This is typically done in a boundary conditions file which is read in by the Navier-Stokes code. In this section the types of boundary conditions applied to the various boundary points of the composite grid will be identified. The specific numerical implementation of the inflow and outflow boundary conditions within INS2D-UP was already covered in Chapter V.

For the grid used in this study, the outer boundary points of the composite grid are the boundary points of the test section grid. The boundary points defined by the grid lines $j = 1$ and $j = 150$ represent the walls of the test section. As mentioned previously, these boundary points were assigned a "slip" boundary condition. This implies the velocity gradient normal to the wall is zero. The pressure at the wall is obtained by forcing the pressure gradient normal to the wall to also be zero. The boundary points defined by the grid line $i = 1$ represent the inflow boundary to the test section. Since the test section walls were modeled as slip walls with no boundary layer, a boundary condition of constant velocity was assumed at the inflow boundary. The pressure at the inflow boundary was determined using the characteristic relations described in Chapter V to transmit pressure information from the interior of the grid to the boundary. The boundary points defined by

the grid line $i = 151$ represent the outflow boundary to the test section. The outflow boundary was assumed to be far enough downstream that the static pressure was constant across the outflow boundary. The velocity at the outflow boundary was determined using a characteristic relation. A number of different inflow and outflow boundary condition combinations were tried to test the sensitivity of the solution to the inflow and outflow boundary conditions. These included constant total pressure at the inflow boundary and extrapolated velocity at the outflow boundary. Use of different inflow and outflow boundary conditions had a negligible effect on the solution.

All surface grid points for the main element and flap were assigned a no-slip boundary condition. For a no-slip boundary condition, the velocity at the surface is set to zero and the pressure at the surface is determined by requiring the pressure gradient normal to the surface to be zero. The surfaces used to define the lift-enhancing tabs were also assigned a no-slip boundary condition. The grid points contained within the surface defining the lift-enhancing tab were identified and given a value of zero in the IBLANK array so that they would be ignored by the Navier-Stokes solver. The boundary conditions for the grid points along the wake lines for the main element and the flap were handled by updating the flow variables at the wake line points using a first order averaging of values from surrounding grid points.

Grid Sensitivity Studies

A great deal of effort went into the development of the standard composite grid used to represent the NACA 63_2-215 ModB two-element airfoil in the Ames 7- by 10-Foot Wind Tunnel for this investigation. Many of the techniques used in the grid generation process were based on work with multi-element airfoil grids done by other researchers [12,39,40,41]. Refinements to the grid generation process were developed on a trial-and -error basis to meet the objectives of the present study. The overall grid generation process has been described in detail above. Once the standard grid was developed, a grid refinement study was conducted to ensure that the solution obtained using the standard grid was grid-independent. A fine grid was developed by doubling the number of grid points in every region in the i direction and every zone in the j direction of the standard grid. The beginning and ending grid point spacings used in every region or zone of the standard grid were preserved in the fine grid. The resulting fine grid had 4 times the number of grid points the standard grid had, for a total of 560,380 grid points.

The solution obtained on the fine grid is compared with the solution obtained on the standard grid in Figure 36. The flap was set to a deflection angle of 27°, a gap of 0.02, and an overlap of 0.015. The angle of attack was 0° and the Reynolds number was set to

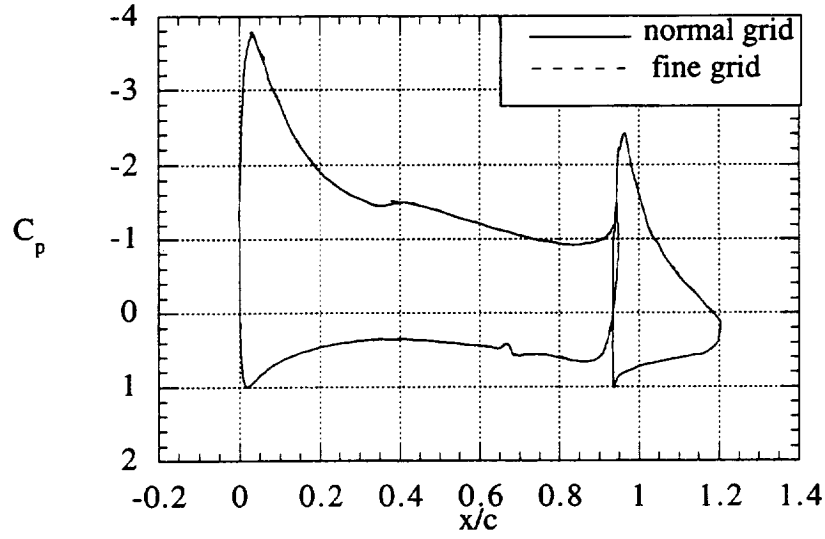

a) Pressure coefficient distribution

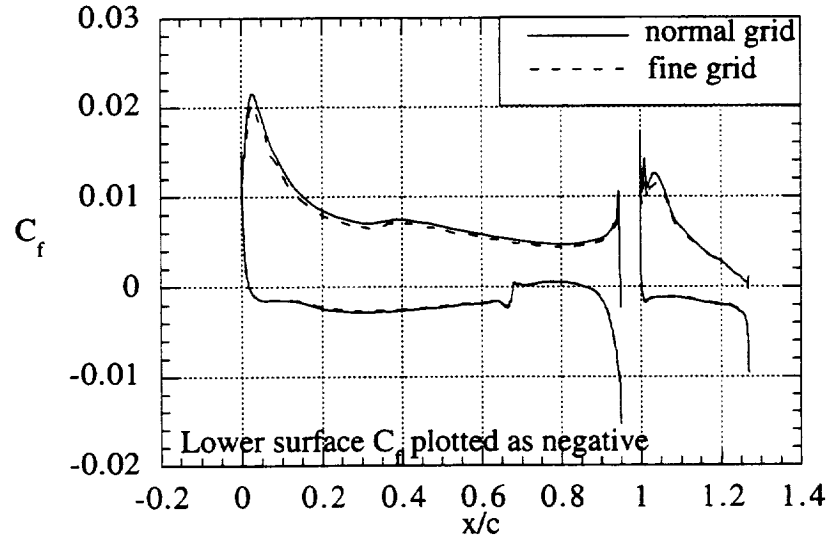

b) Skin friction coefficient distribution

Figure 36: Results of grid sensitivity study. ($\delta_f = 27°$, $z_g/c = 0.02$, $x_{ol}/c = 0.015$, $\alpha = 0°$)

3.5×10^6. The plot of pressure coefficient versus x/c for the two solutions show virtually no difference between the solution obtained using the fine grid and the solution obtained using the standard grid. The integrated force and moment coefficients varied by approximately 0.25%. A slight difference can be seen between the two solutions in the plot of skin friction coefficient versus x/c. The skin friction coefficients from the fine grid solution indicate that the flow separation that happens at the beginning of the cove region occurs at a position $\Delta x/c = 0.005$ further downstream than the results from the standard grid indicate. Based on the favorable comparison of results obtained for the standard and fine grids, the solutions obtained on the standard grid were assumed to be grid-independent.

The only caveat to this assumption is that separation locations can only be resolved to the accuracy of the local grid point spacing at the point of separation. For cases where the separation point occurs in a region of fine grid point spacing, such as near the trailing edges of the main element or flap, the separation point predicted on the fine grid is essentially the same as the separation point predicted on the standard grid. However, if the separation point occurs in a region which typically has coarser grid point spacing, such as at the mid-chord of the main element or flap, there can be a difference of $\Delta x/c = 0.01 - 0.02$ in the separation point location in the standard and fine grids.

CHAPTER VII
RESULTS AND DISCUSSION

As mentioned previously, the overall goal of this research is to develop an understanding of the flow physics associated with lift-enhancing tabs applied to a multi-element airfoil. Computations were performed for a large number of the configurations tested during the experimental phase of this study. The intent of the computations was to supply additional flow field data that could not be obtained during the experiment. The experimental and computational results obtained during this research will be used together to achieve the overall goal stated above.

All of the computations presented in this report were obtained using the INS2D-UP code in the steady-state mode with the Spalart-Allmaras turbulence model. In the computations, the flow was treated as fully turbulent on both the main element and the flap. The artificial compressibility factor was set to $\beta = 100$ and the pseudo-time step size was set to $\Delta\tau = 1.0$. Steady-state solutions were typically achieved in 500 iterations. The maximum residual in the solution was reduced by 8 orders of magnitude and the maximum divergence in the converged solution was on the order of 1×10^{-3} or less. Typical solution times on a Cray C-90 computer were 1.69×10^{-5} seconds/iteration/point for a total execution time of about 1200 seconds.

First, comparisons of the experimental and computational results for baseline configurations of the NACA 63_2-215 ModB two-element airfoil will be presented and differences between the two discussed. Next, a variety of experimental and computational results illustrating the effects of lift-enhancing tabs on the NACA 63_2-215 ModB two-element airfoil will be shown. Again, any differences between the experimental and computational results will be discussed. Finally, a model will be proposed to explain how lift-enhancing tabs function on multi-element airfoils.

Baseline Configurations

The baseline performance of the NACA 63_2-215 ModB two-element airfoil was established for flap deflection angles of $\delta_f = 19°$, 29°, and 39°. For each flap deflection angle, the flap gap was varied from $z_g/c = 0.02$ to $z_g/c = 0.05$ in 0.01 increments. Flap overlap was held constant at $x_{ol}/c = 0.015$. The experimental results for the 19° and the 29° flap deflection angles were qualitatively very similar, while the results for the 39° flap deflection angle were very different. Thus, only results from the 29° and 39° flap deflection angles will be discussed here.

An important observation regarding flap deflection angle was made near the end of the wind-tunnel test. Light scratch marks were discovered on the surface of the auxiliary turntables underneath the trailing edge of the flap. A careful examination revealed that the scratch marks existed at three positions consistent with the position of the flap trailing edge at each of the three flap deflection angles. A clearance of approximately 0.125 inches existed between the flap and the upper and lower auxiliary turntables. This clearance was filled in with a piece of hard foam which had the same cross-sectional shape as the flap. Thus, the scratch marks on the auxiliary turntables were not made by the flap. The aluminum pieces used as lift-enhancing tabs, however, did extend all the way to the auxiliary turntables and they appeared to be the cause of the scratch marks. The scratch marks indicated that the trailing edge of the flap was being displaced under aerodynamic load. The displacement of the flap trailing edge could only be the result of a deformation of the flap airfoil shape under load, a rotation of the flap due to bending of the flap brackets under load, or a combination of the two effects.

An attempt was made to quantify the motion of the flap trailing edge for different flap deflection angles, both with and without lift-enhancing tabs at the flap trailing edge. A piece of white tape was placed on the lower auxiliary turntable beneath the flap trailing edge. A small ink pen cartridge was taped behind the blunt trailing edge of the flap so that the point of the pen cartridge was in contact with the white tape on the lower auxiliary turntable. The dynamic pressure in the wind-tunnel test section was set to standard test conditions for a few minutes and then returned to zero. The motion of the flap trailing edge under aerodynamic load caused the pen cartridge to leave a mark on the white tape which could be accurately measured.

If the motion of the flap trailing edge is assumed to be due solely to rotation of the flap as a result of bending of the flap brackets under load, then the measurements indicate rotations of 1.5° for a flap deflection angle of 19°, 2.0° for a flap deflection angle of 29°, and approximately 3.0° for a flap deflection angle of 39°. In all cases, the flap deflection angle under load was less than the static flap deflection angle. The change in flap deflection angle for a flap angle of 39° was difficult to measure accurately due to unsteadiness in the flow caused by flow separation over the upper surface of the flap. Time did not permit an assessment of the change in flap deflection angle for all combinations of flap deflection angle, flap gap, and lift-enhancing tabs. However, the limited number of cases checked indicated that the dominant factor in determining the change in flap deflection angle was the static flap deflection angle setting. The assumption that the motion of the flap trailing edge was due solely to rotation of the flap was verified after the wind-tunnel test by performing a

finite element analysis of the flap under pressure load. The results of this analysis indicated that the flap deformed by 0.003 inches or less at the trailing edge.

It should be noted that the phenomenon of the flap deflection angle changing from its static value under load is common on all aircraft with high-lift systems. For a large transport aircraft with the high-lift system fully deployed, the change in flap deflection angle can be as high as 5°. This phenomenon is commonly known as flap blowback. In a study of a multi-element high-lift system, flap blowback can make comparing experimental and computational results difficult. The performance of a multi-element airfoil is strongly dependent on the deflection angle of the various elements. If the flap elements in a computational model are not set to the same deflection angle, under aerodynamic load, as the experimental model, poor correlation of experimental and computational data may result.

Figure 37a shows a comparison of the experimental pressure coefficient distribution on the main element and flap with computational results obtained using INS2D-UP. The flap deflection angle used for the computations was the measured static flap deflection angle of 29°. The angle of attack used was 0°, which permitted the differences between the experimental and computational results to be seen more easily. The pressure coefficient distribution on both the main element and the flap is over predicted by INS2D-UP. The difference between the experimental and computational results is more pronounced on the main element. In a multi-element high-lift system, the lift acting on the main element is very sensitive to the amount of lift generated by the flap. Small changes in flap lift can produce substantial changes in main-element lift. Thus small differences between the experimental and computed pressure coefficient distributions on the flap can lead to large differences on the main element. This highlights the importance of matching the experimental flap deflection angle under aerodynamic load in the computational model.

If the flap deflection angle used in the computational model is reduced by 2° to match the experimental flap deflection angle under aerodynamic load, the agreement between the experimental and computational results is much better, as shown in Figure 37b. In this case the experimental and computed pressure coefficients on the flap match very well. The differences between the experimental and computed pressure coefficient distribution on the main element are substantially reduced, with most of the difference occurring in the leading edge region at the suction peak. Based on these results, all computed results presented in this report for configurations with a static flap deflection angle of 29° will utilize a flap deflection angle of 27°.

The situation is not quite as simple for configurations with a static flap deflection angle of 39°. When the flap is deflected to 39°, the flow over the upper surface of the flap

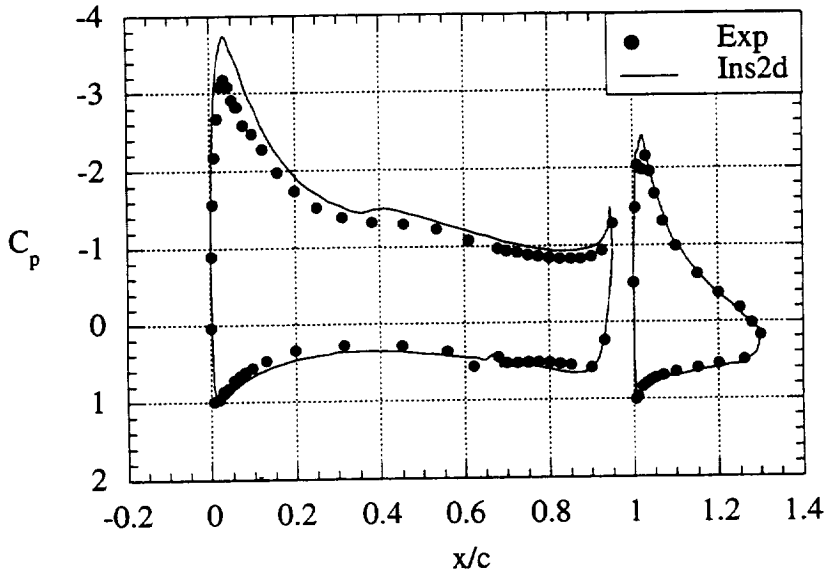

a) INS2D flap angle set to 29°.

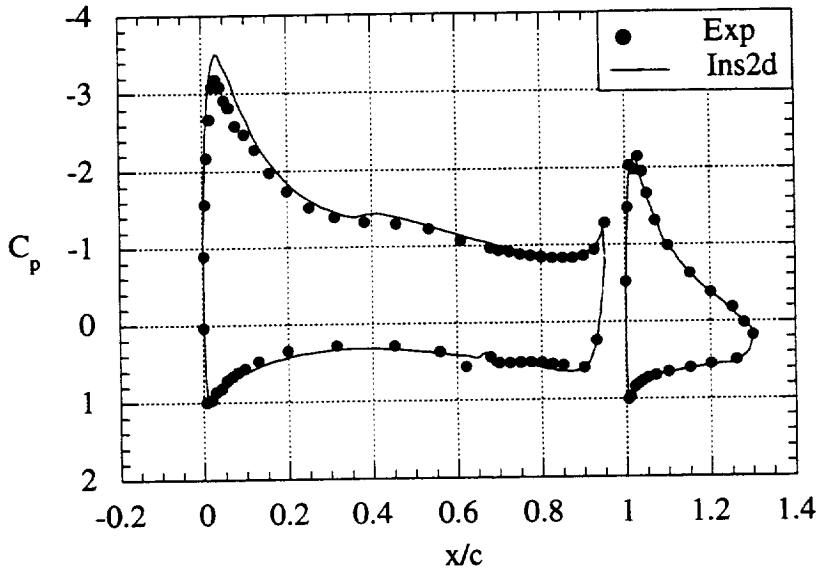

b) INS2D flap angle reduced to 27°.

Figure 37: Comparison of experimental and computed pressure coefficient distributions for baseline configuration ($\delta_f = 29°$, $z_g/c = 0.02$, $x_{ol}/c = 0.015$, $\alpha = 0°$)

begins to separate. For small flap gaps, the region of separated flow is confined to near the trailing edge of the flap. As the flap gap is increased, however, the flow separation point on the flap upper surface moves upstream rapidly. This creates a number of problems

when comparing two-dimensional experimental results to two-dimensional computed results.

The first problem is that when the flow separates on a model such as the one used in this experiment, the flow field is no longer two-dimensional. This is illustrated in Figure 38. Pressure coefficient distributions on the flap are plotted at three different span locations. The spanwise variation in pressure coefficient distribution is evident. The lift acting on the flap is highest at the mid-span and drops off at either end of the flap. Also note that the lift distribution on the flap is not symmetric about the mid-span of the flap. Flow separation on the upper surface of the flap occurs further aft at the mid-span location than it does at the outboard ends of the flap. The three-dimensionality of the flow field causes the lift on the flap to be lower than a strictly two-dimensional flow over the same flap.

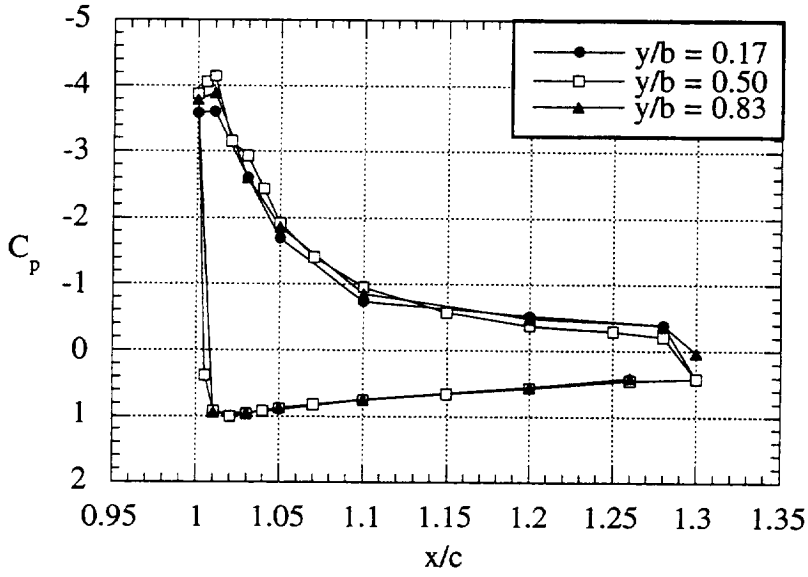

Figure 38: Spanwise variation of pressure coefficient distribution on flap for baseline configuration ($\delta_f = 39°$, $z_g/c = 0.04$, $x_{ol}/c = 0.015$, $\alpha = 0°$).

A second problem is that accurately predicting the point of separation of a flow over a smooth curved surface in an adverse pressure gradient using a Reynolds-Averaged Navier-Stokes code is difficult. Some of the factors affecting the computed separation point are the turbulence model used, whether or not boundary layer transition is modeled, and the spacing of the grid points along the surface in the flow direction. For example, if the grid point spacing on the surface in the vicinity of the flow separation point is 1% of the

airfoil chord, then the computed flow separation point can only be resolved to within 1% of the airfoil chord. Since the lift on the flap is strongly influenced by the location of the flow separation point and the lift on the main element is strongly impacted by the lift on the flap,

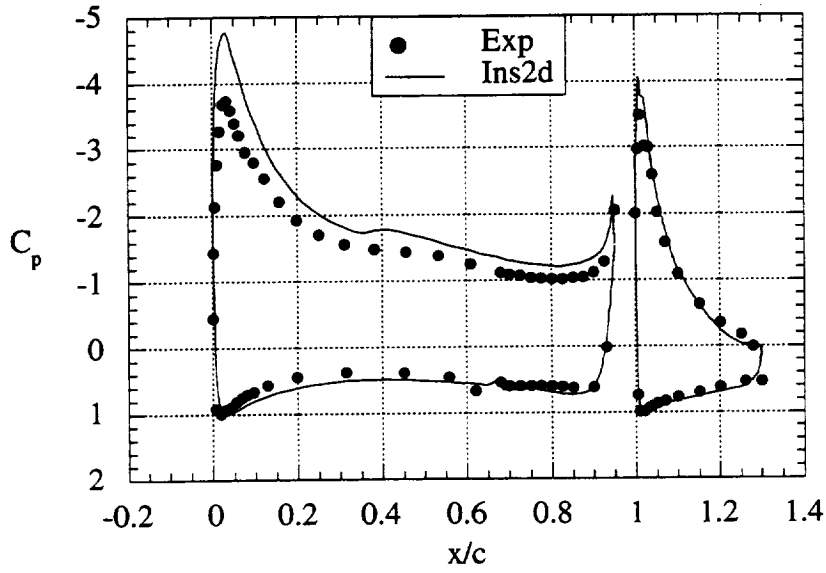

a) INS2D flap angle set to 39°.

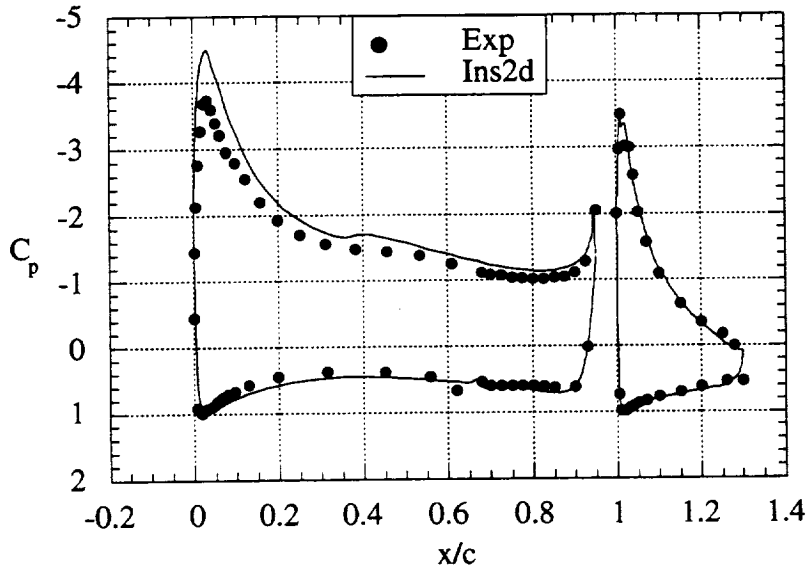

b) INS2D flap angle reduced to 36°.

Figure 39: Comparison of experimental and computed pressure coefficient distributions for baseline configuration ($\delta_f = 39°$, $z_g/c = 0.02$, $x_{ol}/c = 0.015$, $\alpha = 0°$).

small errors in the computed location of the flow separation point can lead to large differences in computed and measured lift on a multi-element airfoil.

Despite these problems, if the same procedure used to set the flap deflection angle in the computational model for a static flap deflection angle of 29° is used for configurations with a 39° static flap deflection angle, reasonable results are obtained. Figure 39 shows a comparison of experimental and computed pressure coefficient distributions on the main element and flap for a configuration with a 39° static flap deflection angle and a flap gap of $z_g/c = 0.02$. The computed results overpredict the pressure coefficient distribution, particularly on the main element. The computed results indicate that the flow has separated on the flap upper surface over the aft 10% of the flap chord, compared to the experimental results which indicate almost no flow separation. When the flap deflection angle is reduced by 3° in the computational model, consistent with the measured change in flap deflection angle under aerodynamic load, the agreement between experimental and computed results improves significantly. The experimental and computed pressure coefficient distributions on the flap agree quite well. The agreement between experimental and computed pressure coefficient distributions on the main element, although improved, is not as good as it was for the configuration with a 29° static flap deflection angle.

When the flap gap for the configuration with a static flap deflection angle of 39° is increased to $z_g/c = 0.04$, some of the problems discussed above become more evident. In this case the flow separates over the upper surface of the flap at approximately the mid-chord of the flap. In Figure 40, the experimental pressure coefficient distribution is compared with the computed pressure coefficient distribution. The flap deflection angle in the computational model is set to 39°. In this case, measured and computed results agree quite well on the main element. The results on the flap, however, indicate a large disagreement in the location of the point of flow separation on the flap upper surface. The computed results predict flow separation on the flap upper surface too early. If the flap deflection angle in the computational model is reduced by 3°, much better agreement is obtained for the comparison of the experimental and computed flap pressure coefficient distributions. The flow separation point on the flap predicted by the computations more closely matches the experimental results. The pressure coefficient distribution on the main element, however, is now over predicted by the computed results. To maintain consistency with the measured changes in flap deflection angle observed in the experiment, all computed results presented in this report for configurations with a static flap deflection angle of 39° will utilize a flap deflection angle of 36°.

An effort was made to identify the source of the remaining difference between the experimental and computed pressure coefficient distributions in Figures 38, 39, and 40. A

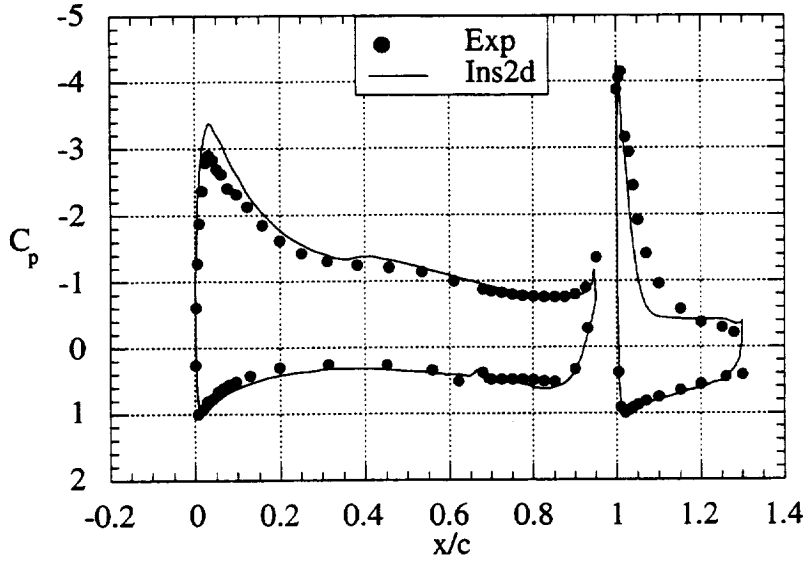

a) INS2D flap angle set at 39°.

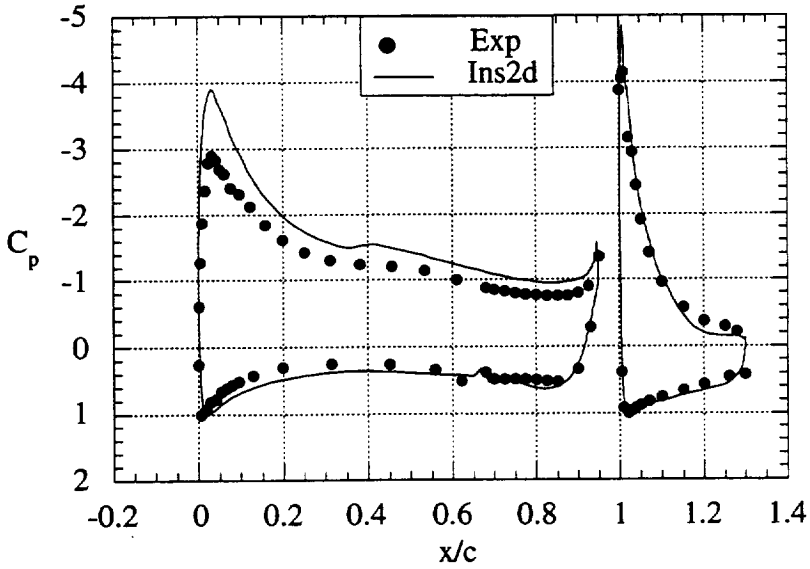

b) INS2D flap angle reduced to 36°.

Figure 40: Comparison of experimental and computed pressure coefficient distributions for baseline configuration ($\delta_f = 39°$, $z_g/c = 0.04$, $x_{ol}/c = 0.015$, $\alpha = 0°$).

close examination of the pressure coefficient distribution in the region of the stagnation point on the main element indicates that the measured and computed stagnation points do not occur at the same location, as illustrated in Figure 41. There are a number of different possible causes for the discrepancy in stagnation point location. The most likely cause is

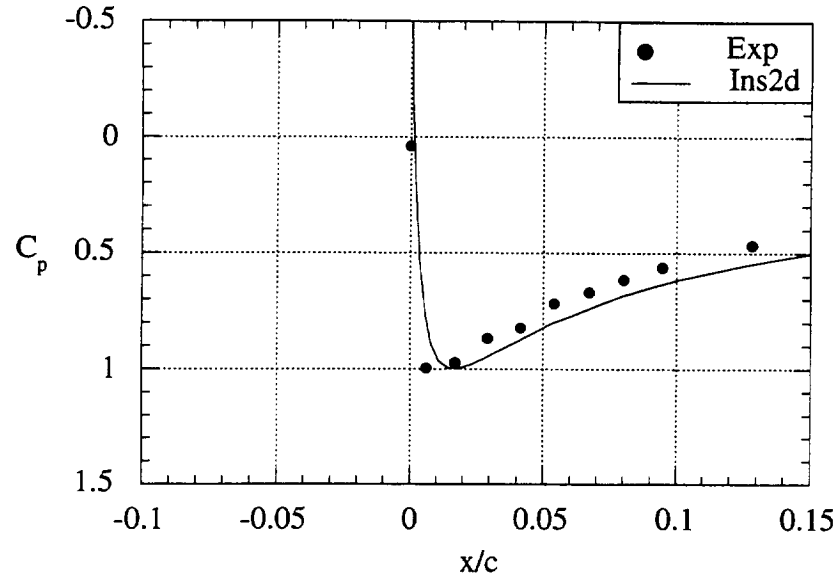

Figure 41: Comparison of experimental and computed pressure coefficient distributions at the leading edge of the main element. ($\delta_f = 29°$, $z_g/c = 0.02$, $x_{ol}/c = 0.015$, $\alpha = 0°$).

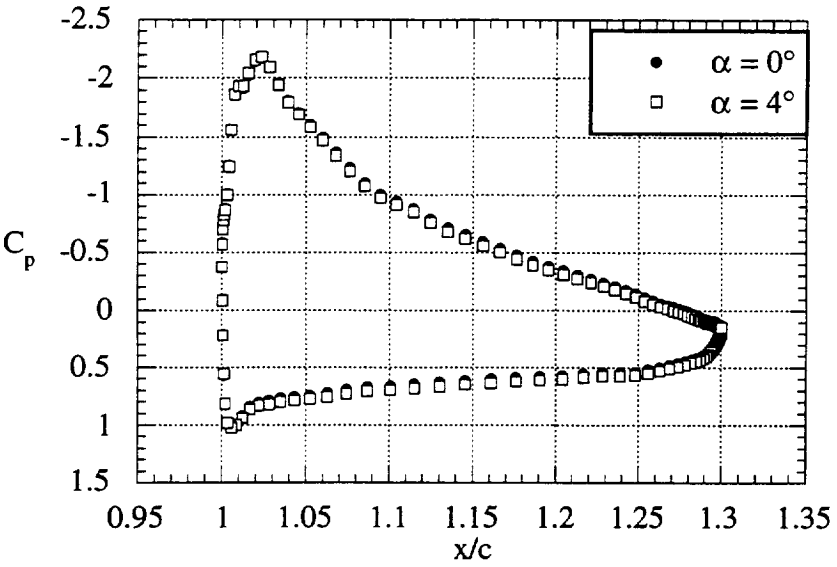

Figure 42: Computed sensitivity of flap pressure distribution to moderate changes in angle of attack for baseline configuration (INS2D $\delta_f = 27°$, $z_g/c = 0.02$, $x_{ol}/c = 0.015$, $\alpha = 0°$).

that the effective angle of attack for the experimental results is lower than it is for the computed results. A difference in effective angle of attack is consistent with the fact that the measured main element pressure coefficient distribution differs from the computed

results, even though the flap pressure coefficient distributions match. The flap pressure coefficient distribution is relatively insensitive to moderate changes in angle of attack as illustrated in Figure 42. The main element pressure coefficient distribution, on the other hand, is very sensitive to angle of attack, particularly near the leading edge where the largest differences between measured and computed results are observed.

The difference in effective angle of attack could be due to flow angularity in the test section, additional flow angularity induced by the image planes, an inadequacy of the slip-wall boundary condition imposed at the outer boundary of the computational grid to simulate the actual test section walls with their boundary layer, or some combination of two or more of these factors. Measurements made by Wadcock [42] in the empty tunnel indicate that yaw angle (which represents angle of attack for the present model installation) varies by $\pm 0.50°$ along a vertical line over the center of rotation of the turntable. This flow angularity could account for some of the difference in effective angle of attack.

The circulation generated by the multi-element airfoil in the test section produces regions of adverse pressure gradient on the side walls of the test section as shown in Figure 43. If the lift, and hence the circulation, of the multi-element airfoil is sufficiently large, it is conceivable that the adverse pressure gradients could cause the side wall boundary layers to separate. If this occurred, it would significantly change the effective angle of attack for the model. Tufts placed on the test section side walls, however, indicated that the side wall boundary layers remained attached.

In order to check the adequacy of the simulation of the test section walls in the computed solution, a second computational grid was created with no test section modeled. The flap grid was completely imbedded in the main element grid, as in the case of the standard grid; however, the outer boundary of the main element grid was located 20 chord lengths from the surface of the main element. The boundary condition established at the main element outer boundary included the influence of a point vortex located at the quarter chord of the main element. The strength of the vortex was set equal to the circulation generated by the multi-element airfoil and was updated at each iteration of the solution. The point vortex was only used to update the boundary conditions at the outer boundary. This new grid simulated the multi-element airfoil in an unbounded free stream flow.

By comparing the solution obtained using the grid with no test section modeled to the solution obtained using the grid with the test section included, an estimate of the effect of the test section walls on the measured force and moment coefficients can be derived. Plots of the computed lift, drag, and pitching moment coefficient, with and without test section walls modeled, are shown in Figure 44. In the case of the lift coefficient, the effect of the presence of the test section walls can be expressed as a change in effective angle of

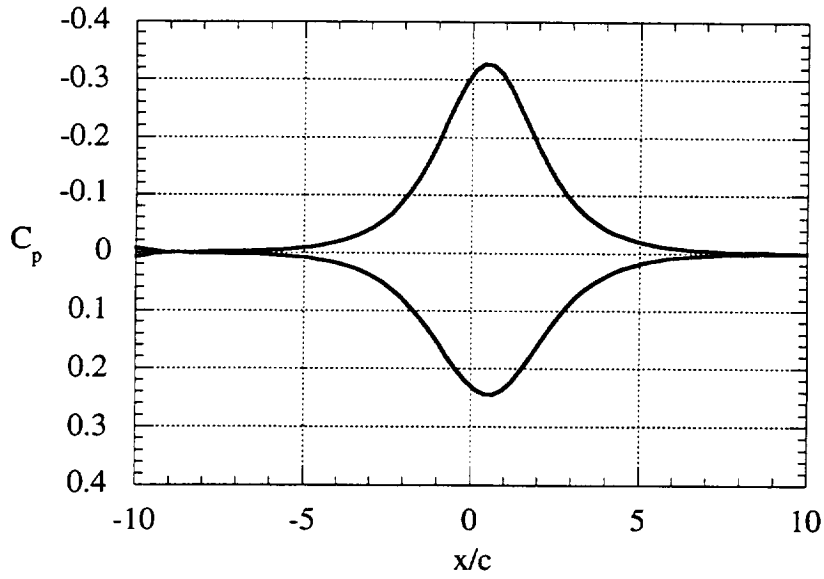

Figure 43: Computed tunnel wall pressure coefficient distribution for the baseline configuration (INS2D $\delta_f = 27°$, $z_g/c = 0.02$, $x_{ol}/c = 0.015$, $\alpha = 8°$).

attack and a change in reference dynamic pressure using the procedure described by Ashby and Harris [43]. The change in dynamic pressure is found by comparing the lift coefficient versus angle of attack curves for the two cases and determining the change in dynamic pressure required to make the two curves parallel. Once the two curves have been made parallel, the change in effective angle of attack is defined as the angle of attack change required to make the two lift coefficient curves coincident. For a baseline configuration with a static flap deflection angle of $\delta_f = 29°$ and a flap gap of $z_g/c = 0.02$, the presence of the test section walls increases the dynamic pressure by 2.5% and increases the angle of attack by 0.2°. If the effect of the presence of the test section walls on the dynamic pressure and angle of attack is computed using traditional methods described by Rae and Pope for two-dimensional testing [18], the dynamic pressure is increased by 1.72% and the angle of attack is increased by 0.093°. These corrections are of the same order as those derived using INS2D-UP results. Thus the computational model is correctly simulating the effect of the presence of the test section walls on the force and moment coefficients of the multi-element airfoil.

The baseline performance of the NACA 63_2-215 ModB two-element airfoil is shown in Figure 45 for a static flap deflection of 29°. Both experimental and computed results for a range of flap gap are shown. The flap deflection angle for the computed results is 27°. The maximum angle of attack used for the computed results is determined by

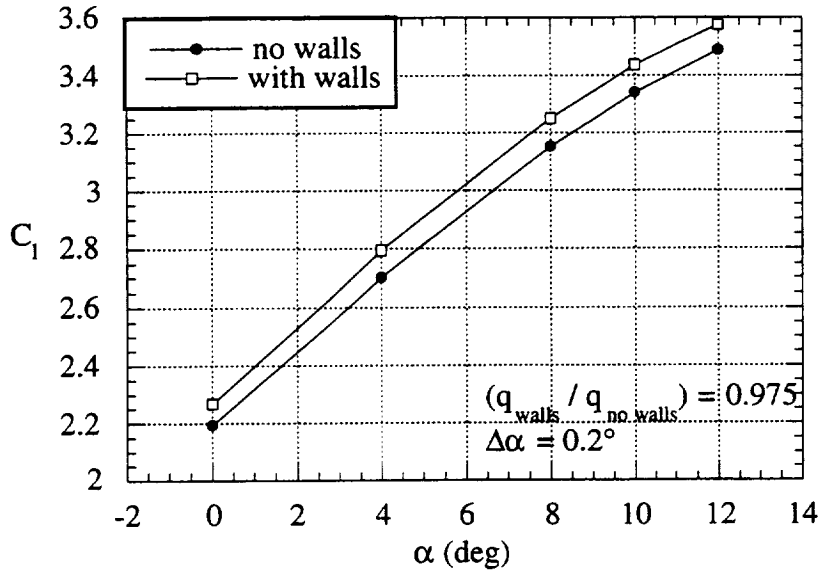

a) Wall interference effects on lift coefficient.

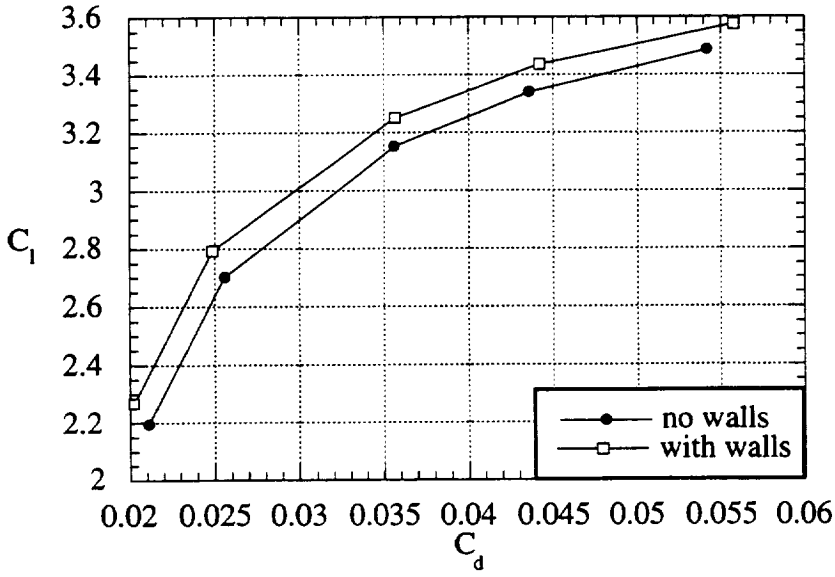

b) Wall interference effects on drag.

Figure 44: Computed wall interference effects on force and moment coefficients for a baseline configuration (INS2D $\delta_f = 27°$, $z_g/c = 0.02$, $x_{ol}/c = 0.015$).

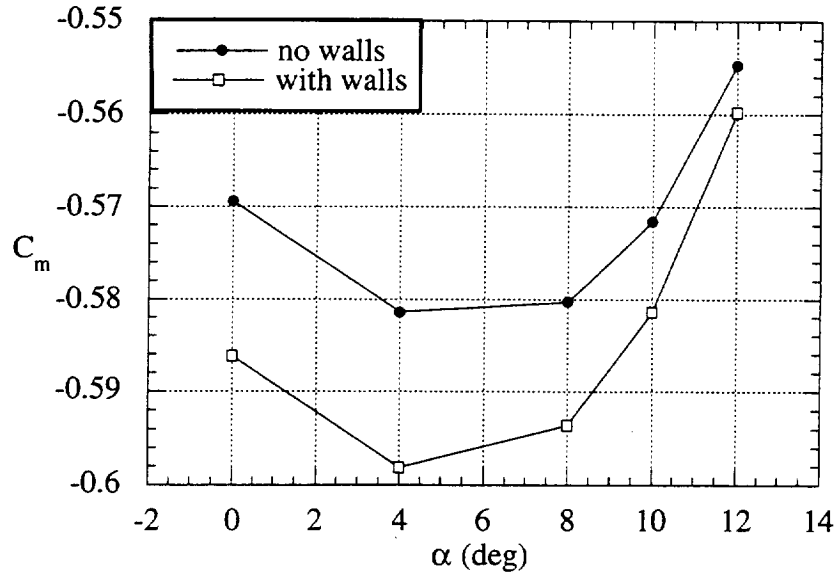

c) Wall intereference effects on pitching moment.

Figure 44 concluded: Computed wall interference effects on force and moment coefficients for a baseline configuration (INS2D $\delta_f = 27°$, $z_g/c = 0.02$, $x_{ol}/c = 0.015$).

the largest angle of attack at which INS2D-UP can converge to a steady-state solution. For angles of attack greater than or equal to the angle of attack for C_{lmax}, the flow field becomes unsteady and INS2D-UP has great difficulty in converging to a steady-state solution. Thus the computed results extend up to an angle of attack which is very near stall.

The experimental lift coefficient versus angle of attack curves exhibit little sensitivity to flap gap. For $z_g/c = 0.04$ or less, the only significant variation in the lift coefficient curves is the value of C_{lmax}. The flap gap that yields the highest C_{lmax} is $z_g/c = 0.04$. For $z_g/c = 0.05$, the entire lift coefficient curve is shifted downward by $\Delta C_l = 0.10$. Tufts on the upper surface of the flap indicated a small amount of flow separation at the trailing edge of the flap for this flap gap setting. The experimental lift coefficient versus drag coefficient is relatively unaffected by changes in flap gap. The maximum change in drag coefficient at a constant lift coefficient is approximately 30 drag counts as flap gap is varied. The experimental pitching moment coefficient curve shifts in the negative direction as flap gap is increased up to a flap gap of $z_g/c = 0.04$. When the flap gap is increased further to $z_g/c = 0.05$, the pitching moment coefficient curve begins to shift back in the positive direction. This change in direction can be attributed to the flow separation over the upper surface of the flap at a flap gap of $z_g/c = 0.05$.

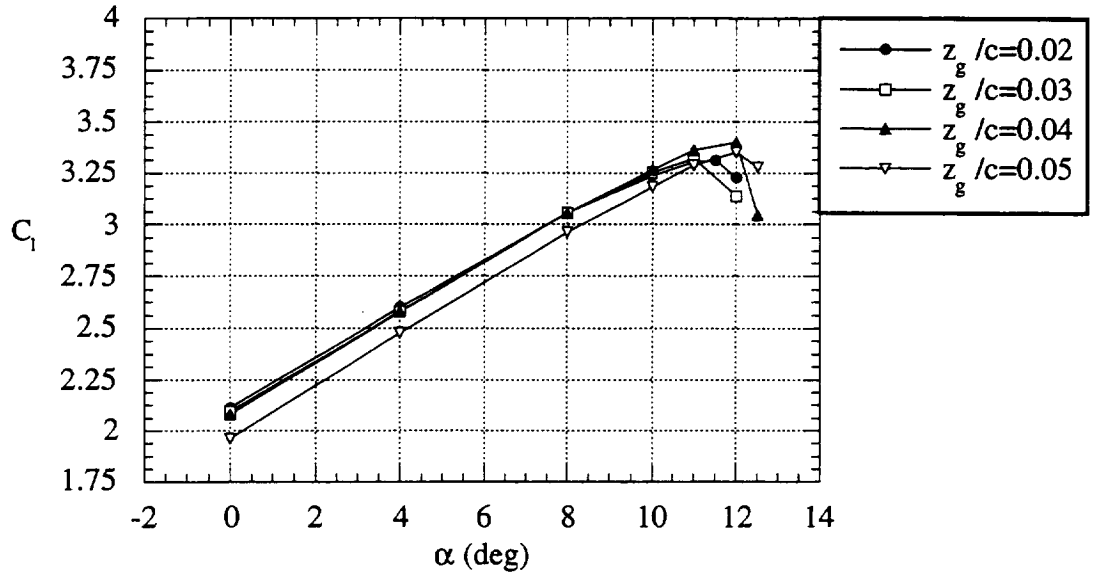

a) Experimental results for lift coefficient.

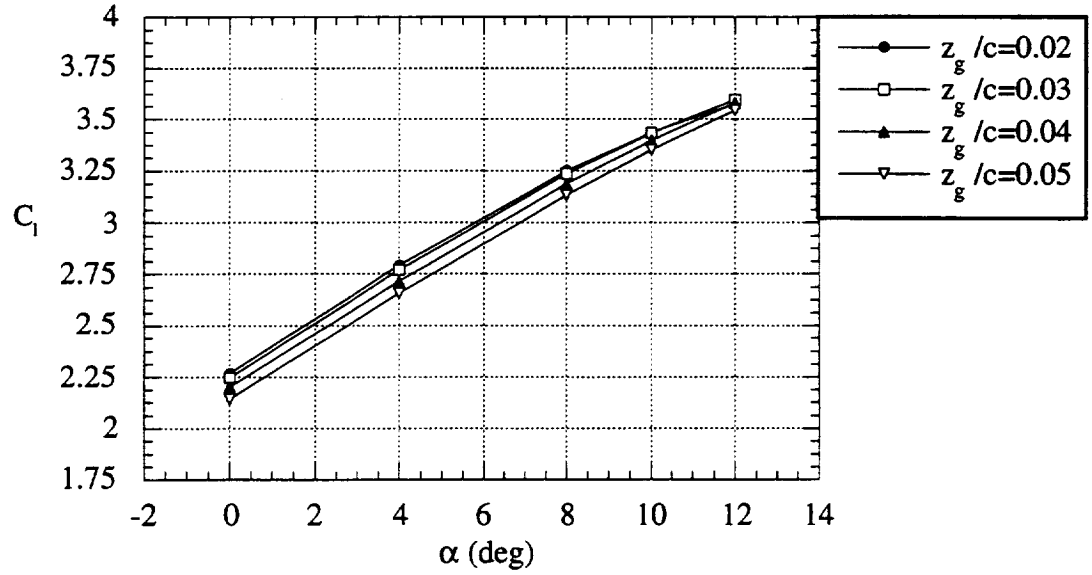

b) Computed results for lift coefficient.

Figure 45: Sensitivity of force and moment coefficients to the size of the flap gap for a baseline configuration ($\delta_f = 29°$, INS2D $\delta_f = 27°$, $z_g/c = 0.02$, $x_{ol}/c = 0.015$).

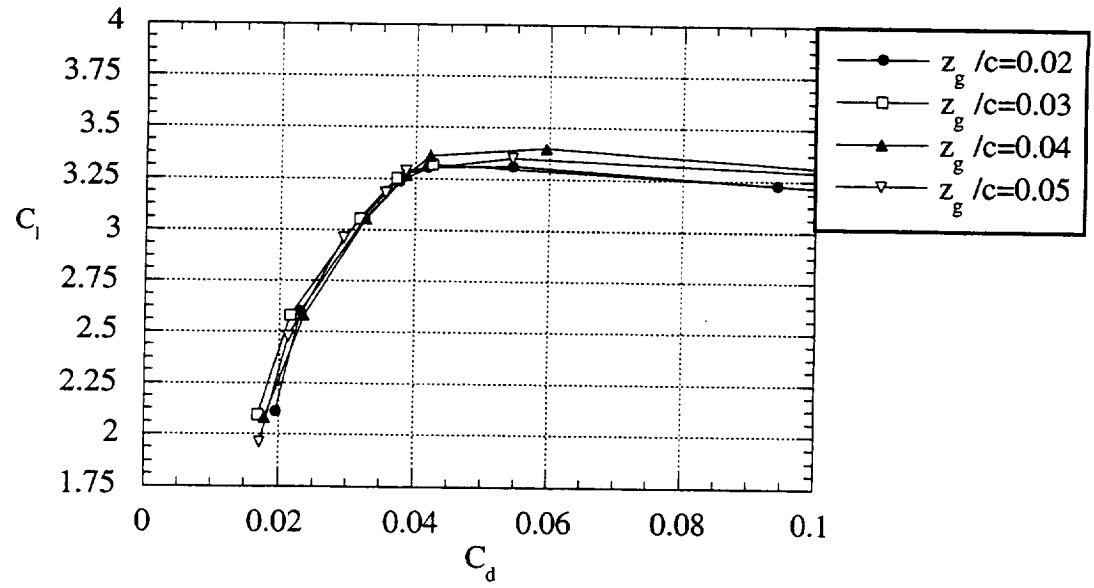

c) Experimental results for drag coefficient.

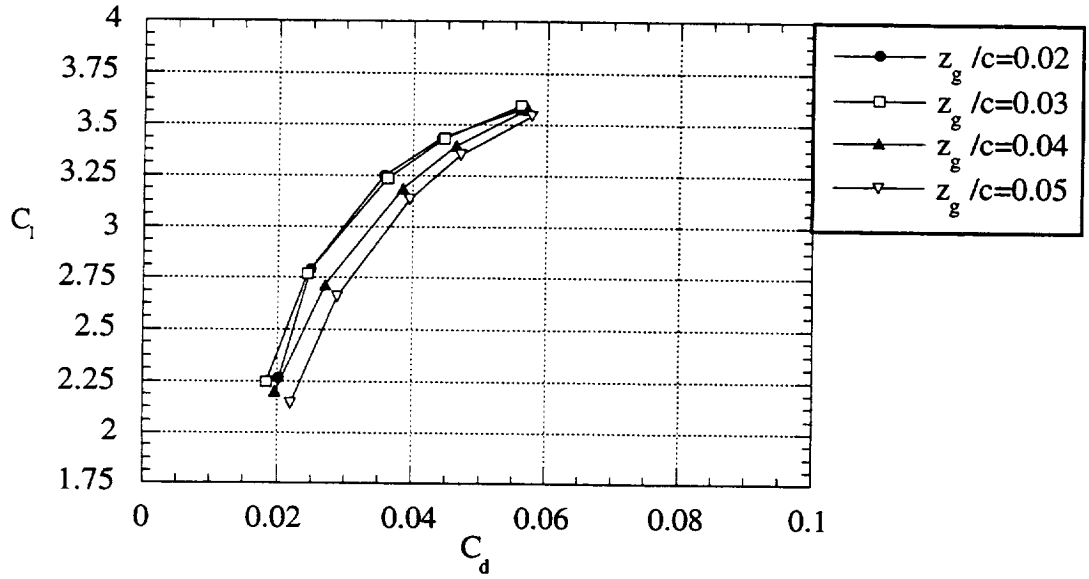

d) Computed results for drag coefficient.

Figure 45 continued: Sensitivity of force and moment coefficients to the size of the flap gap for a baseline configuration ($\delta_f = 29°$, INS2D $\delta_f = 27°$, $z_g/c = 0.02$, $x_{ol}/c = 0.015$).

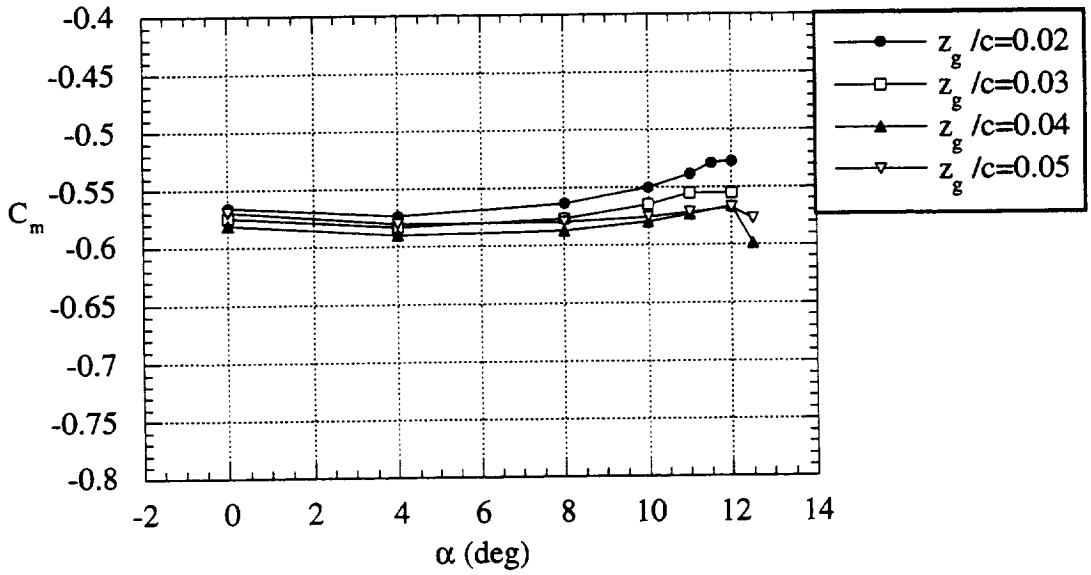

e) Experimental results for pitching moment coefficient.

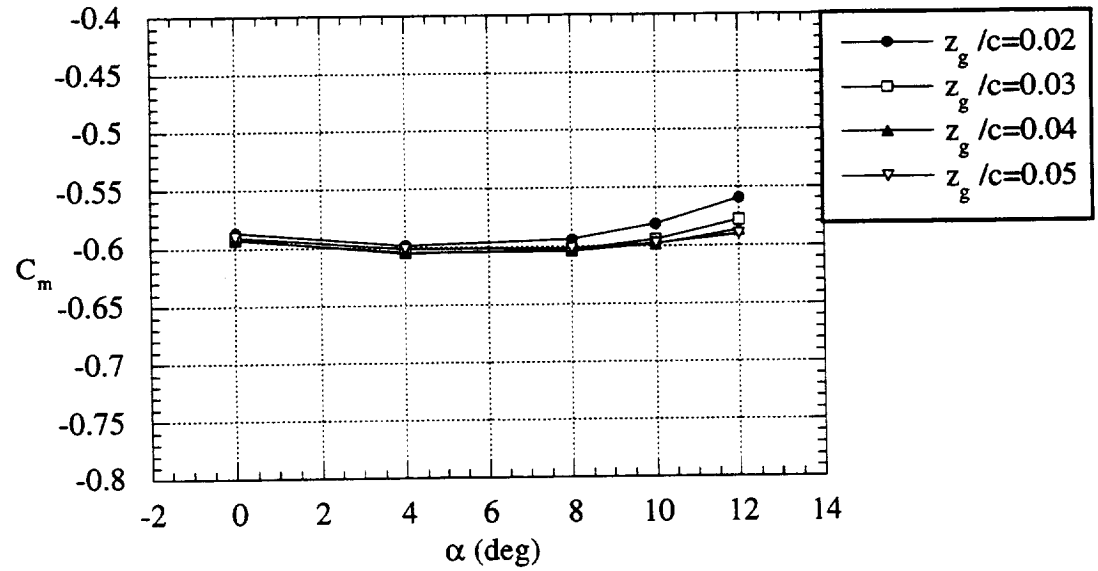

f) Computed results for pitching moment coefficient.

Figure 45 concluded: Sensitivity of force and moment coefficients to the size of the flap gap for a baseline configuration ($\delta_f = 29°$, INS2D $\delta_f = 27°$, $z_g/c = 0.02$, $x_{ol}/c = 0.015$).

The computed results exhibit similar trends to those observed in the experimental results. There is an increased sensitivity to flap gap in the computed results however. The lift coefficient curve begins to shift downward at a flap gap of $z_g/c = 0.04$. Also, all of the computed lift coefficient curves are shifted upward approximately $\Delta C_l = 0.15$ from the corresponding experimental results. The computed lift coefficient versus drag coefficient curves agree quite well with the corresponding experimental curves for flap gaps less than $z_g/c = 0.04$. For flap gaps greater than or equal to $z_g/c = 0.04$, however, the computed drag coefficient begins to increase as flap gap is increased. The computed pitching moment coefficient curves shift in the negative direction as flap gap is increased, but not by as much as the corresponding experimental curves. At a flap gap of $z_g/c = 0.05$, the computed pitching moment coefficient curve begins to shift back in the positive direction, similar to the experimental results. All of the computed pitching moment coefficients are more negative than the corresponding experimental data.

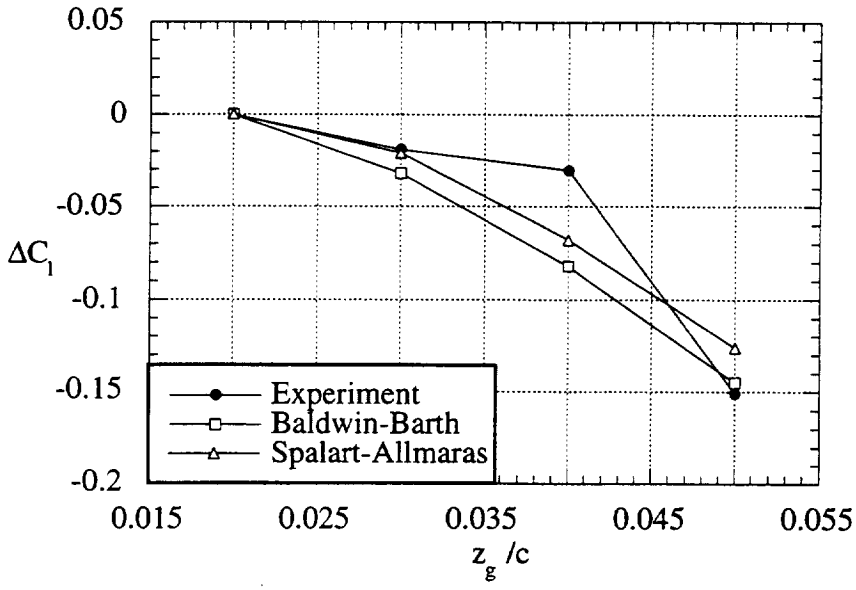

Figure 46: Change in lift coefficient as a function of flap gap for the baseline configuration ($\delta_f = 29°$, INS2D $\delta_f = 27°$, $x_{ol}/c = 0.015$, $\alpha = 0°$).

Because the flow through the flap gap is dominated by viscous effects, it is possible that the turbulence model used in the computations could have a strong impact on the sensitivity of the computed force and moment coefficients to the size of the flap gap. To investigate the effect of the turbulence model on the solution, additional computations were performed using the Baldwin-Barth turbulence model. The computations were performed

for a configuration with a flap deflection angle of 27° (representing a static flap deflection angle of 29°) and an angle of attack of 0°. The flap gap was varied from $z_g/c = 0.02$ to $z_g/c = 0.05$. A plot of the change in lift coefficient versus flap gap is shown in Figure 46. The change in lift coefficient is referenced to the lift coefficient at a flap gap of $z_g/c = 0.02$. As can be seen, the experimental results indicate a small reduction in lift coefficient with increasing gap up to a flap gap of $z_g/c = 0.04$. For larger flap gaps, the lift coefficient begins to decrease rapidly. The computed results using the Spalart-Allmaras and the Baldwin-Barth turbulence models both show a more linear decrease in lift coefficient with increasing flap gap. Both turbulence models overpredict the rate of decrease of lift coefficient as gap is increased for flap gaps less than or equal to $z_g/c = 0.04$. For flap gaps greater than $z_g/c = 0.04$, both turbulence models underpredict the rate of decrease of lift coefficient.

The Baldwin-Barth and Spalart-Allmaras turbulence models are very similar in their formulation. Both are one-equation turbulence models which utilize a transport equation for turbulent viscosity (or turbulent Reynolds number, which is related to turbulent viscosity). The two principal differences between the Baldwin-Barth and the Spalart-Allmaras turbulence models are that the Spalart-Allmaras model has a more sophisticated transition model and the Spalart-Allmaras model includes a non-viscous destruction term that depends on distance to the wall [25]. Since all computations were performed assuming a fully turbulent boundary layer, the differences in the transition model are not the source of the disagreement in results shown in Figure 46. This leaves the non-viscous destruction term in the Spalart-Allmaras model as the source of the differences observed in Figure 46. The non-viscous destruction term is the term involving $c_{w1} f_w$ in equation (19), Chapter IV. The function term f_w is defined by equations (22) through (24) in Chapter IV. The non-viscous destruction term in the Spalart-Allmaras turbulence model was intended to address the "blocking" effect of the wall on the near-wall region of a boundary layer [24]. The inclusion of the non-viscous destruction term in the Spalart-Allmaras turbulence model allows it to match the experimental results more closely than the Baldwin-Barth model. The solution also converges to a steady-state much faster using the Spalart-Allmaras model than it does using the Baldwin-Barth model. For these reasons, the Spalart-Allmaras turbulence model is used for all the computations presented in this report.

The baseline performance of the NACA 63_2-215 ModB two-element airfoil with a static flap deflection of 39° is shown in Figure 47. Both experimental and computed results are shown. The flap deflection angle for the computed results is 36°. Computations were performed for flap gaps of $z_g/c = 0.02$, 0.03, and 0.04. Computed results for a flap gap of $z_g/c = 0.05$ are not included because converged steady-state solutions for the baseline

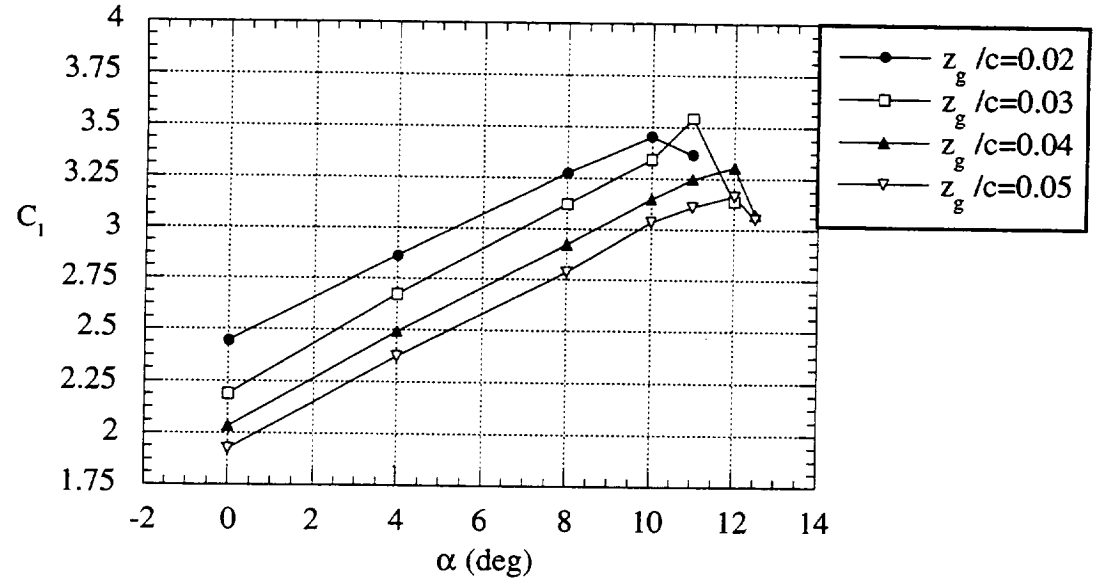

a) Experimental results for lift coefficient

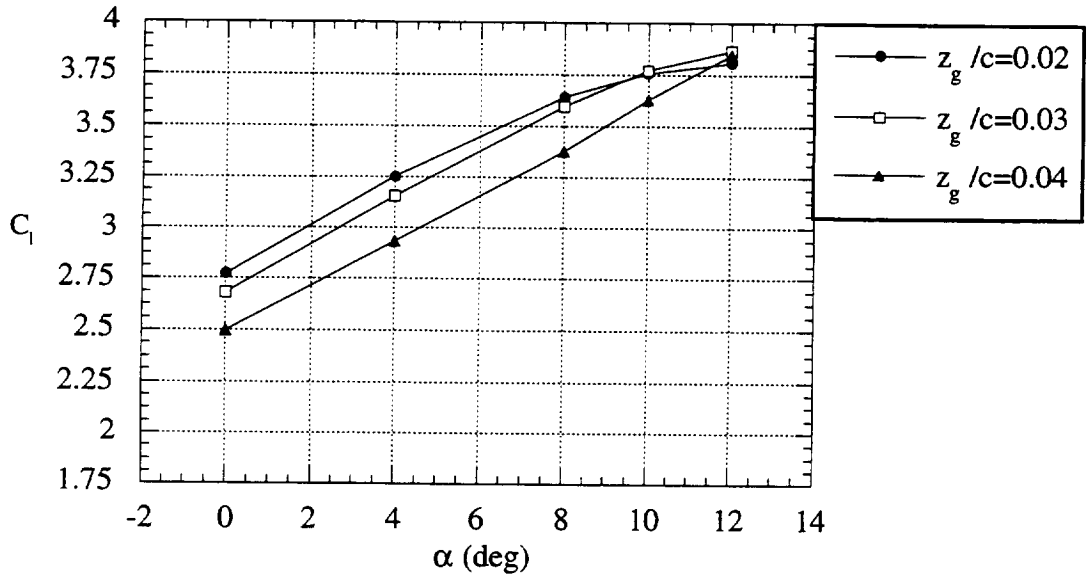

b) Computed results for lift coefficient

Figure 47: Sensitivity of force and moment coefficients to the size of the flap gap for a baseline configuration ($\delta_f = 39°$, INS2D $\delta_f = 36°$, $z_g/c = 0.02$, $x_{ol}/c = 0.015$).

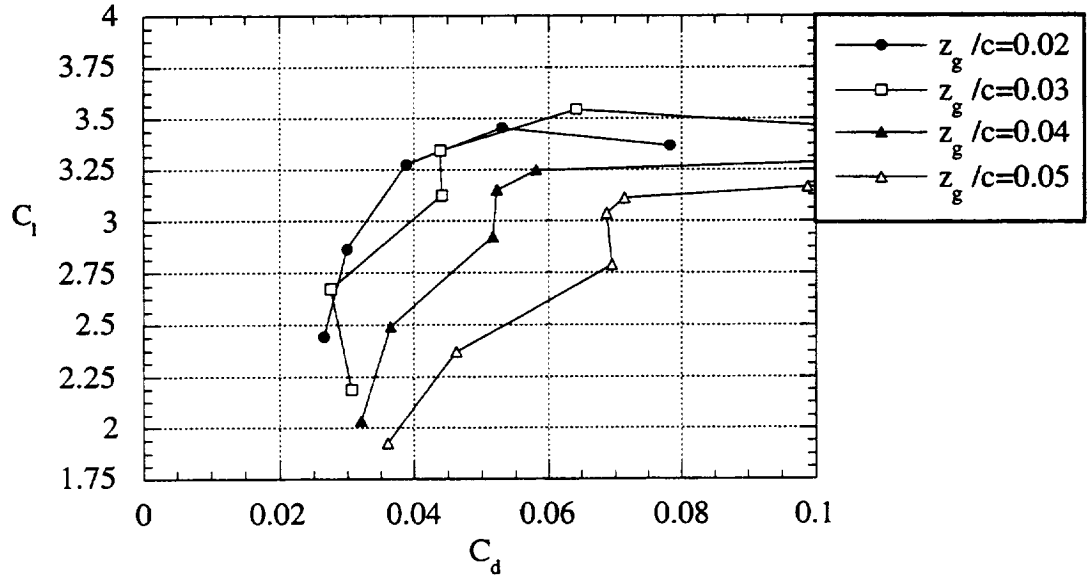

c) Experimental results for drag coefficient

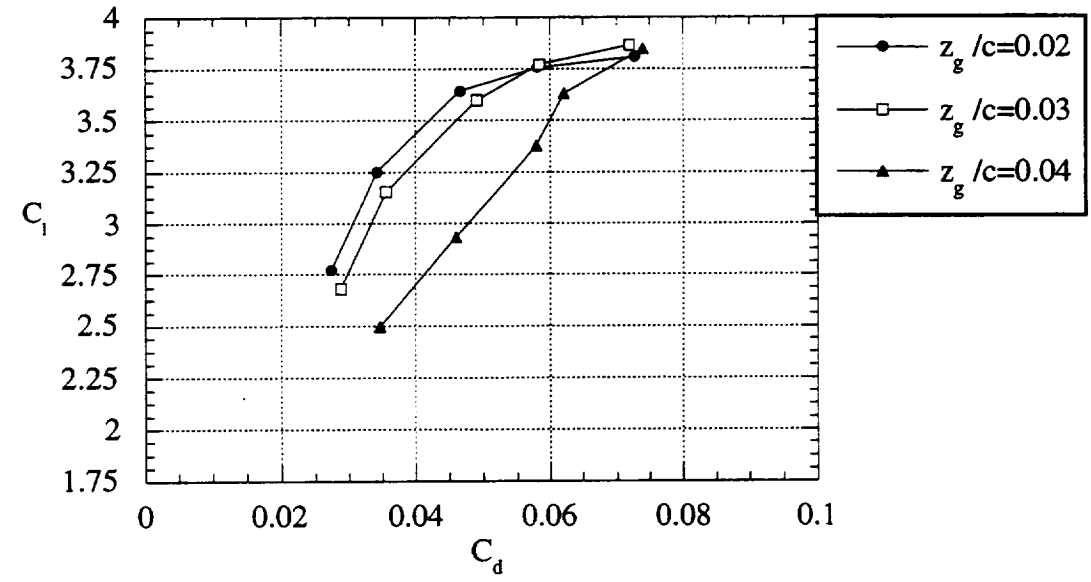

d) Computed results for drag coefficient

Figure 47 continued: Sensitivity of force and moment coefficients to the size of the flap gap for a baseline configuration ($\delta_f = 39°$, INS2D $\delta_f = 36°$, $z_g/c = 0.02$, $x_{ol}/c = 0.015$).

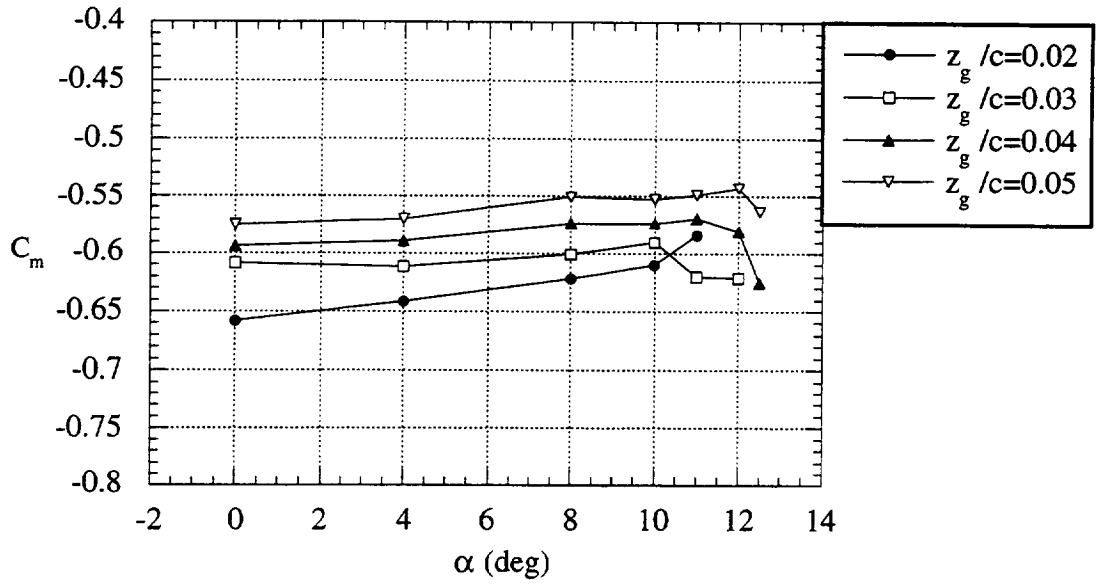

e) Experimental results for pitching moment coefficient

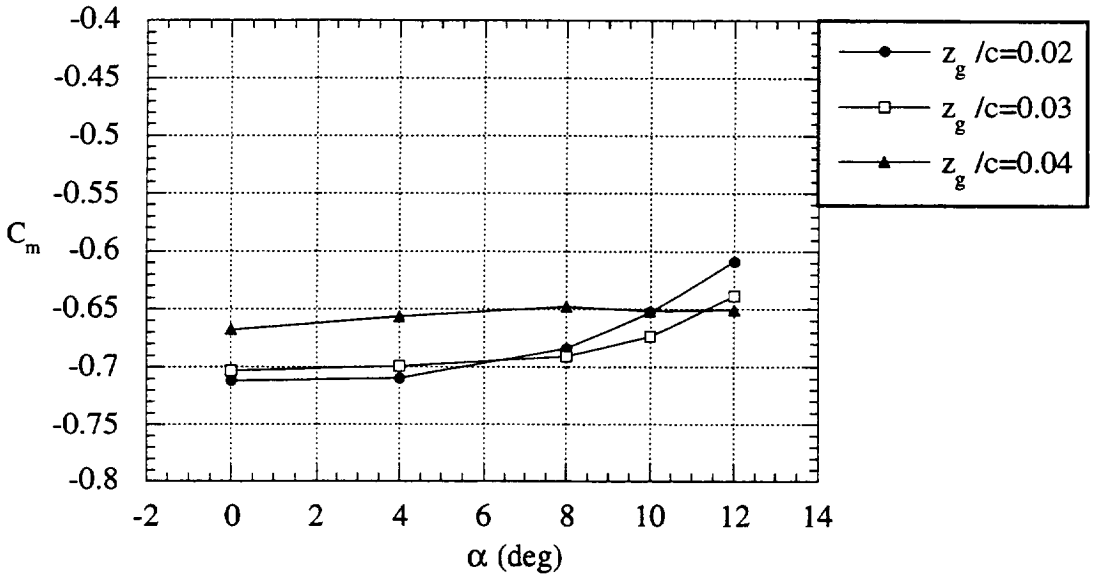

f) Computed results for pitching moment coefficient

Figure 47 concluded: Sensitivity of force and moment coefficients to the size of the flap gap for a baseline configuration ($\delta_f = 39°$, INS2D $\delta_f = 36°$, $z_g/c = 0.02$, $x_{ol}/c = 0.015$).

configuration could not be obtained. This is due to the large region of separated flow over the upper surface of the flap, which creates an unsteady flow field.

The experimental results for lift coefficient show a strong sensitivity to flap gap. At a flap gap of $z_g/c = 0.02$, tufts indicate that the flow over the upper surface of the flap is mostly attached, with just a small region of separated flow over the aft 5% of the flap chord. As the flap gap is increased, the lift coefficient at a given angle of attack decreases rapidly. Tufts on the upper surface of the flap indicated that the separation point moved upstream toward the flap leading edge rapidly as flap gap was increased. As the angle of attack approaches the angle of attack for C_{lmax}, the separation point on the flap upper surface moves aft somewhat for a given flap gap, producing a local increase in lift coefficient. This is particularly evident for a flap gap of $z_g/c = 0.03$. For a two-element airfoil, as angle of attack is increased, the downwash behind the main element is increased, due to the increased lift on the main element. This reduces the effective angle of attack for the flap, reducing the lift on the flap. In particular, the pressure suction peak at the flap leading edge is reduced, which moves the separation point on the flap upper surface aft.

The drag coefficient for a static flap deflection of 39° is very sensitive to flap gap also. As can be seen in Figure 47, the drag coefficient at moderate lift coefficients more than doubles as flap gap is increased from $z_g/c = 0.02$ to $z_g/c = 0.05$. The shift aft of the flow separation point on the flap upper surface at high angles of attack manifests itself as a reduction in drag coefficient at high lift coefficients in the plot of lift coefficient versus drag coefficient. The pitching moment coefficient for this configuration is very sensitive to flap gap as well. As flap gap is increased, the pitching moment coefficient versus angle of attack curve shifts in the positive direction. The slope of the pitching moment coefficient curve is also reduced.

The computational results for this flap deflection angle exhibit the same trends as the experimental data. There is a moderate reduction in lift coefficient as flap gap is increased from $z_g/c = 0.02$ to $z_g/c = 0.03$. The shift in lift coefficient is less than the corresponding shift in experimental lift coefficient for the same gap increase. This is due primarily to the separation point on the upper surface of the flap not moving upstream rapidly enough as gap is increased in the computed results. When the flap gap is increased further to $z_g/c = 0.04$, the reduction in computed lift coefficient is almost double the reduction obtained in going from a flap gap of $z_g/c = 0.02$ to $z_g/c = 0.03$. The computed lift coefficient curves are shifted upward by approximately $\Delta Cl = 0.4$ from the corresponding experimental curves. The computed drag and pitching moment coefficient data also exhibit trends with increasing flap gap that are similar to the experimental data. The principal reason for differences between experimental and computed results at this flap

deflection angle is the inaccuracy in the computed separation point location on the flap upper surface. Some of the reasons for this inaccuracy were cited above.

Lift-Enhancing Tabs on Configurations with Moderate Flap Angle

As mentioned in Chapter III, lift-enhancing tabs of several heights were tested on all the baseline configurations of the NACA 63_2-215 ModB two-element airfoil. Tabs were located at the trailing edges of the main element only, the flap only, and the main element and flap together. Tabs placed at the main element trailing edge will be referred to as cove tabs. Tabs placed at the flap trailing edge will be referred to as flap tabs. Computations were performed for all configurations which included tabs with a height of $z_t/c = 0.005$ and which had static flap deflection angles of 29° and 39°. In addition, computations were performed for a configuration with a static flap deflection angle of 50°, a flap gap of $z_g/c = 0.04$, and a flap overlap of $x_{ol}/c = 0.015$. Both a baseline case and a configuration with a cove tab and a flap tab with heights of $z_t/c = 0.01$ were run.

Figure 48 illustrates the effect of lift-enhancing tabs on the lift, drag, and pitching moment coefficients of the NACA 63_2-215 ModB two-element airfoil. In this case, the static flap deflection angle is 29°, the flap gap is $z_g/c = 0.02$, and the flap overlap is $x_{ol}/c = 0.015$. Both experimental and computed results are shown for a cove tab, a flap tab, and a combination of cove tab and flap tab. All tabs had a height of $z_t/c = 0.005$.

The cove tab has a minimal effect on the total lift coefficient of the two-element airfoil. The slope of the lift coefficient versus angle of attack curve is reduced slightly, with the lift coefficient at an angle of attack of 0° remaining essentially unchanged. The drag coefficient is increased by approximately 75 drag counts at all lift coefficients when a cove tab is added to the airfoil. The pitching moment coefficient curve for the configuration with a cove tab is shifted in the positive direction by $\Delta C_m = 0.03$ compared to the pitching moment coefficient curve for the baseline configuration. The slope of the pitching moment coefficient curve is unaffected by the addition of the cove tab. The computations predict the effects on the force and moment coefficients of adding the cove tab to the baseline configuration quite well. Even though the absolute magnitude of the force and moment coefficients is over predicted by the computations, as discussed above in the section on the baseline configurations, the magnitude of the change in force and moment coefficients due to the addition of the cove tab is predicted accurately for this configuration.

A comparison of the pressure coefficient distribution on the main element and flap for the baseline configuration and the configuration with a cove tab provides insight into how the cove tab affects the two-element airfoil. Experimental and computed pressure coefficient distributions are shown in Figure 49 for both configurations at an angle of attack

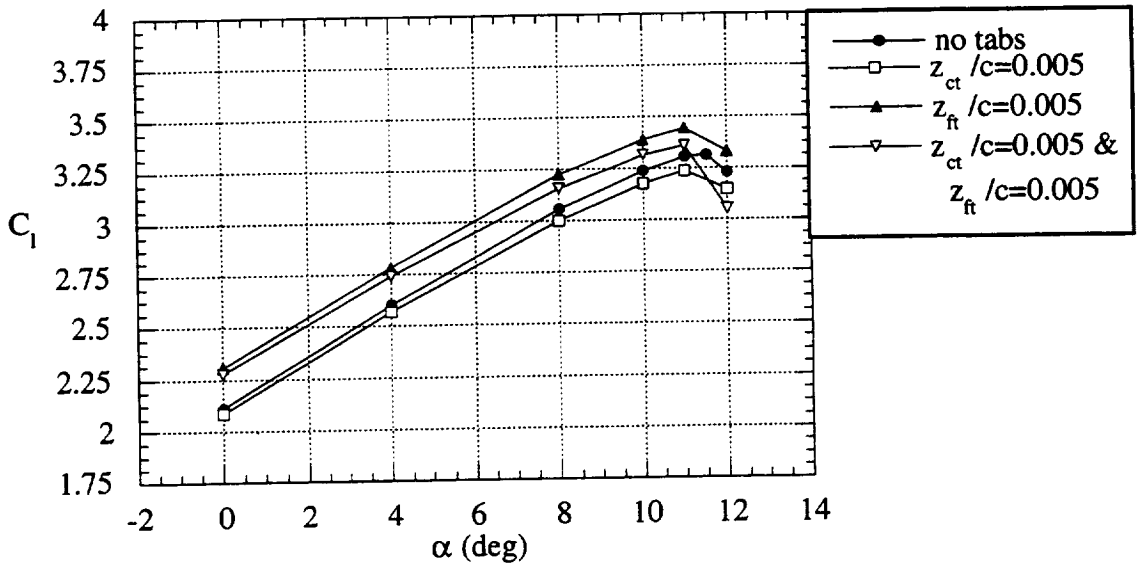

a) Effect of tabs on experimental lift coefficient.

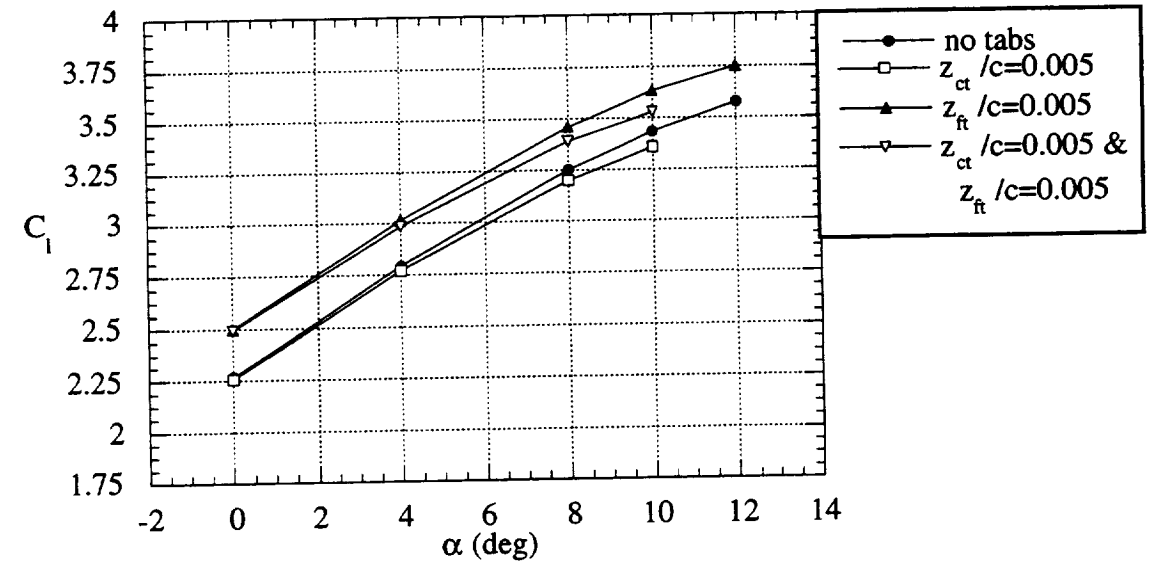

b) Effect of tabs on computed lift coefficient.

Figure 48: Effect of lift-enhancing tabs on the force and moment coefficients of a baseline configuration ($\delta_f = 29°$, INS2D $\delta_f = 27°$, $z_g/c = 0.02$, $x_{ol}/c = 0.015$).

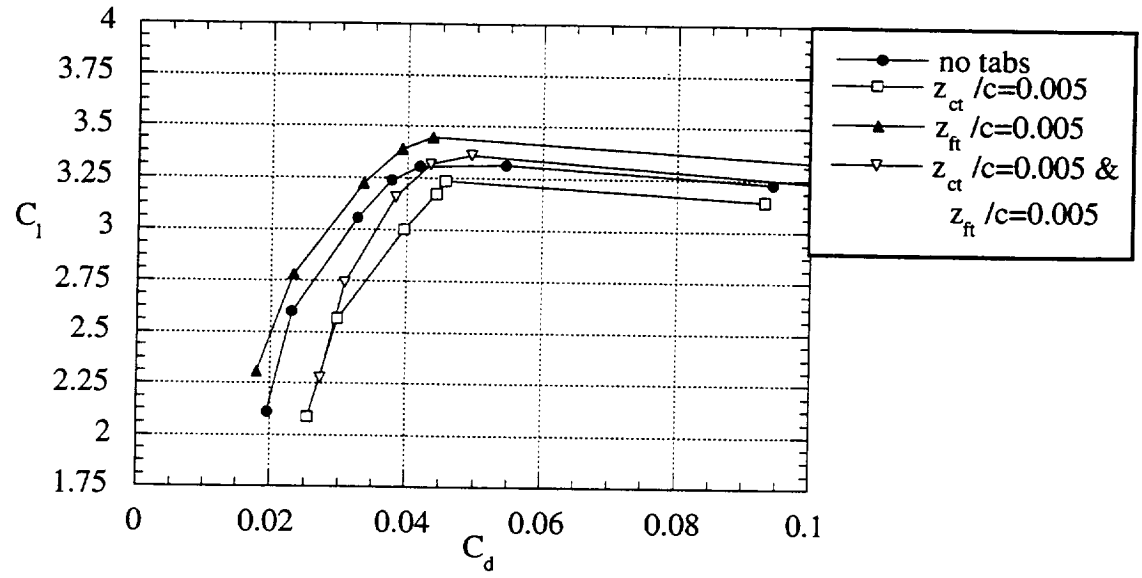

c) Effect of tabs on experimental drag coefficient

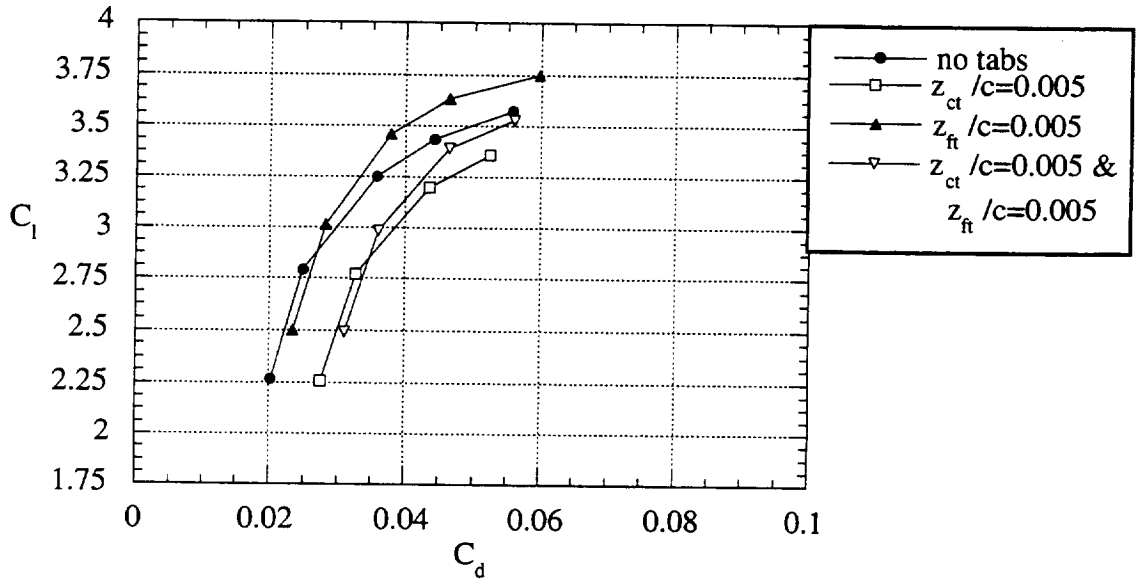

d) Effect of tabs on computed drag coefficient

Figure 48 continued: Effect of lift-enhancing tabs on the force and moment coefficients of a baseline configuration ($\delta_f = 29°$, INS2D $\delta_f = 27°$, $z_g/c = 0.02$, $x_{ol}/c = 0.015$).

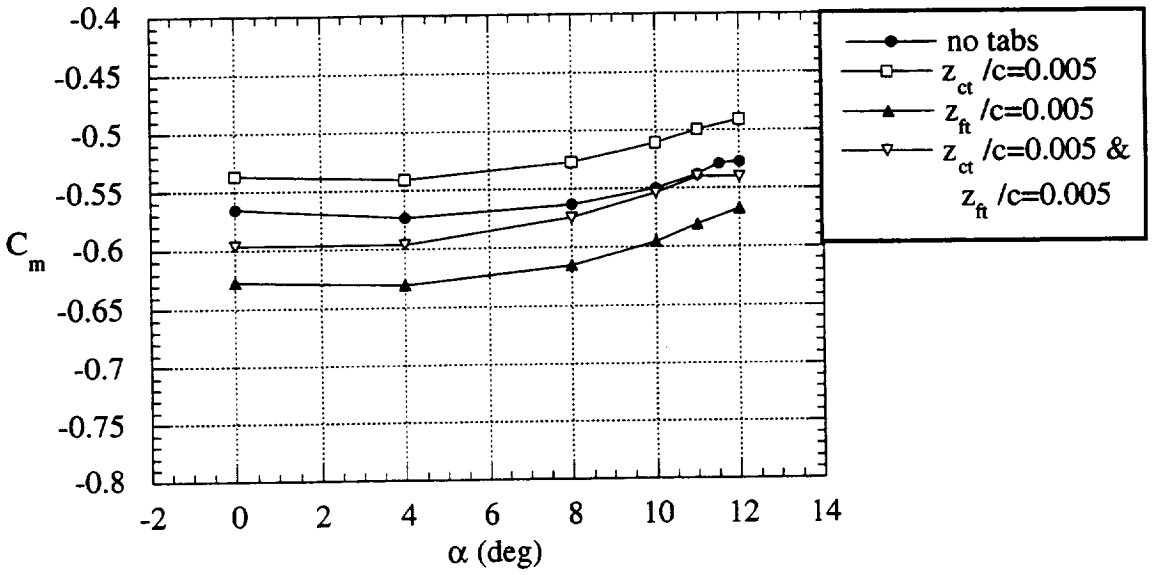

e) Effect of tabs on experimental pitching moment coefficient.

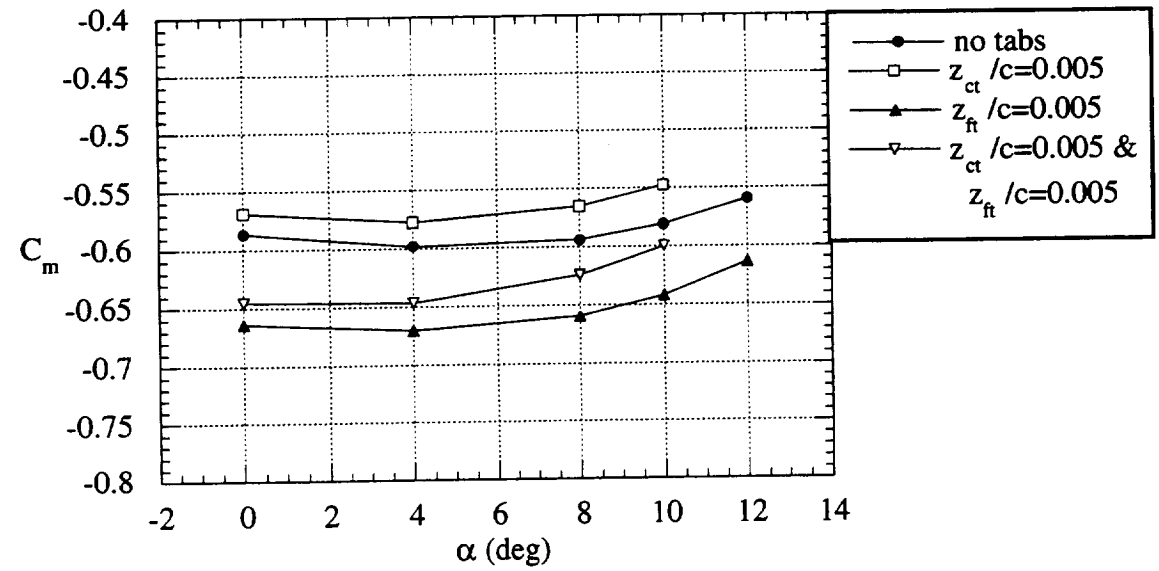

f) Effect of tabs on computed pitching moment coefficient.

Figure 48 concluded: Effect of lift-enhancing tabs on the force and moment coefficients of a baseline configuration ($\delta_f = 29°$, INS2D $\delta_f = 27°$, $z_g/c = 0.02$, $x_{ol}/c = 0.015$).

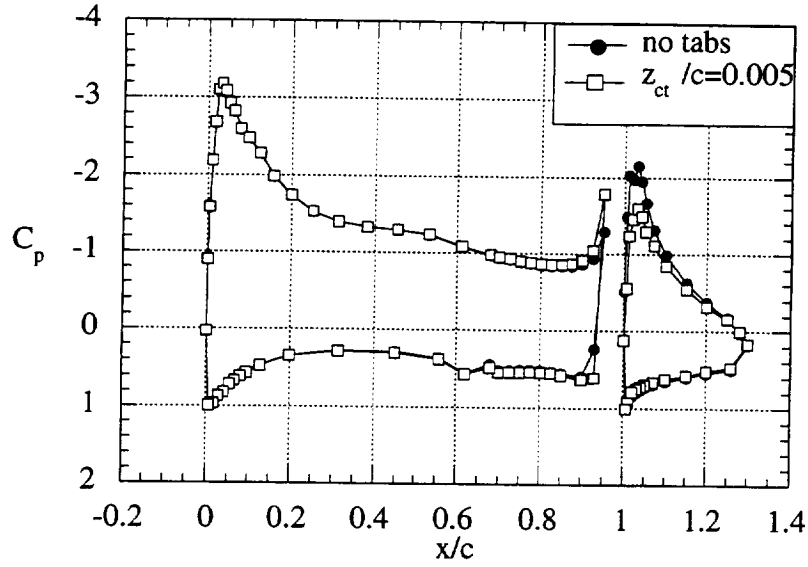

a) Experimental pressure coefficient distribution.

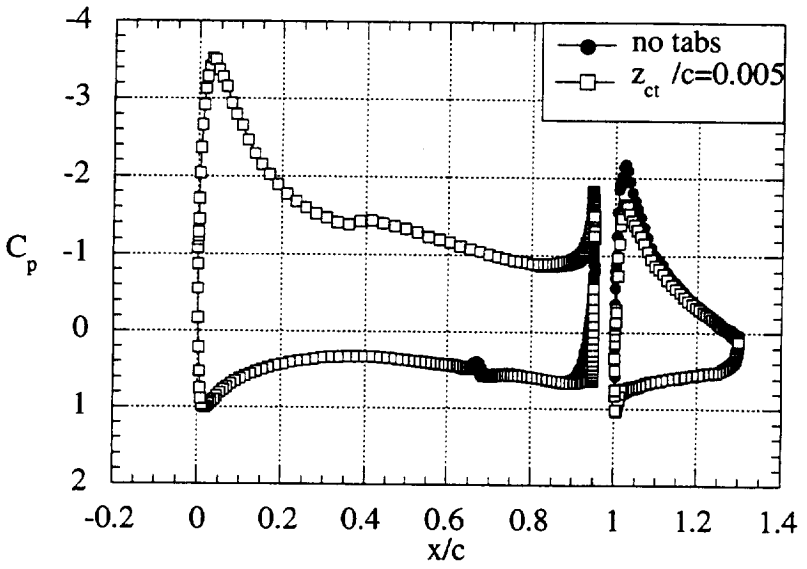

b) Computed pressure coefficient distribution.

Figure 49: Effect of a cove tab on the pressure coefficient distribution of a baseline configuration ($\delta_f = 29°$, INS2D $\delta_f = 27°$, $z_g/c = 0.02$, $x_{ol}/c = 0.015$, $\alpha = 0°$).

of 0°. The cove tab has two main effects on the pressure coefficient distribution. First, the loading on the aft portion of the main element is increased. This effect is primarily confined to the last 5% chord of the main element. The jump in pressure coefficient at the trailing edge of the main element is increased by $\Delta C_p = 0.8$. The second effect is a reduction in the leading edge suction peak on the flap. The suction peak is reduced by $\Delta C_p = 0.6$. This effect is confined to the flap upper surface leading edge region. The pressure coefficients on the flap lower surface and the aft 50% of the upper surface remain essentially unchanged. The computed results indicate changes in the pressure coefficient distribution which agree very well with the experimental results.

The changes in the pressure coefficient distribution can be used to explain the changes observed in the force and moment coefficients due to the addition of the cove tab to the airfoil. The increase in lift coefficient due to the increased loading on the aft portion of the main element is offset by the reduction in lift coefficient on the flap due to the reduction in the suction peak. Apparently, as angle of attack is increased, the reduction in lift coefficient on the flap becomes larger than the increase in lift coefficient on the main element which results in a lower slope of the lift coefficient curve. Reducing the suction peak at the leading edge of the flap while maintaining the pressure coefficient distribution on the remainder of the flap unchanged causes an increase in the pressure drag acting on the flap. The drag is also increased by the base drag acting on the cove tab. This drag can be approximated by multiplying the cove tab area by the jump in pressure coefficient at the trailing edge of the main element. It is unclear whether the changes in pressure coefficient distribution on the main element increase or decrease pressure drag on the main element. The increased negative pressure coefficient on the upper surface will increase pressure drag while the increased positive pressure coefficient on the lower surface will decrease pressure drag. The primary cause for the shift in pitching moment coefficient in the positive direction when a cove tab is added to the configuration is the reduction in the suction peak at the flap leading edge.

Returning to Figure 48, it is evident that adding a flap tab to the baseline configuration produces a significantly different effect than adding a cove tab. The addition of a flap tab produces a substantial increase in lift coefficient at all angles of attack, compared to the lift coefficient at the same angle of attack for the baseline configuration. The lift coefficient curve is shifted upward by $\Delta C_l = 0.2$. The slope of the lift coefficient curve is unaffected by the addition of the flap tab. The maximum lift coefficient is increased by $\Delta C_{lmax} = 0.15$ when a flap tab is added and the angle of attack at which C_{lmax} occurs is reduced by 0.5°. The drag coefficient for the configuration with a flap tab is actually reduced by approximately 30 drag counts at all lift coefficients compared to the

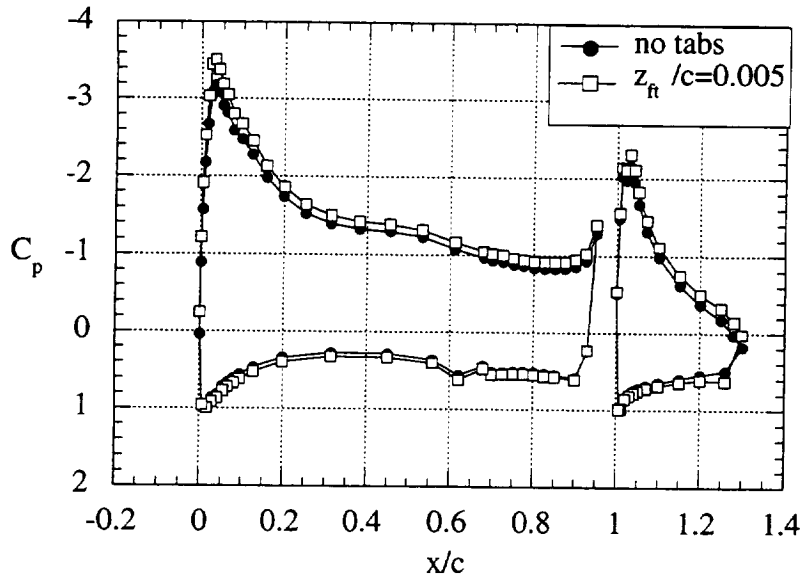

a) Experimental pressure coefficient distribution.

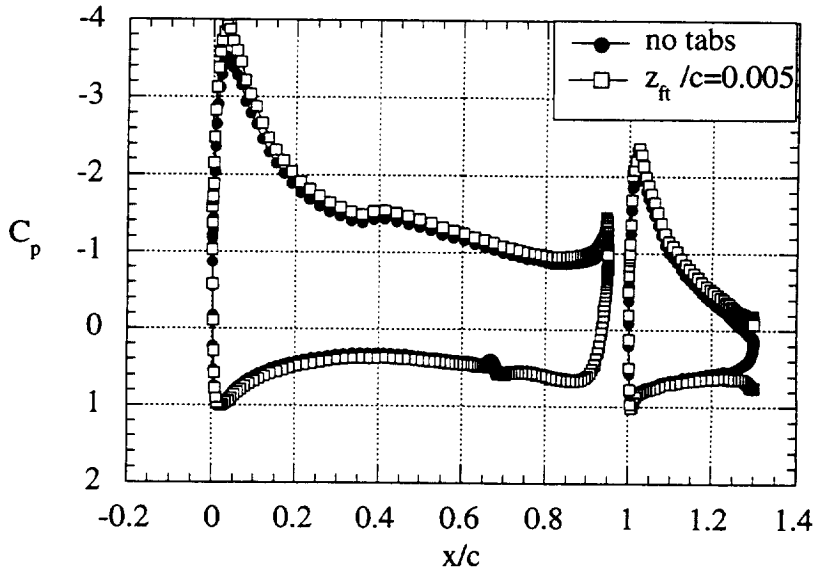

b) Computed pressure coefficient distribution.

Figure 50: Effect of a flap tab on the pressure coefficient distribution of a baseline configuration ($\delta_f = 29°$, INS2D $\delta_f = 27°$, $z_g/c = 0.02$, $x_{ol}/c = 0.015$, $\alpha = 0°$).

results for the baseline airfoil. The pitching moment coefficient curve for the configuration with a flap tab is shifted in the negative direction by $\Delta C_m = 0.07$. Again, the computed results accurately predict the changes in the force and moment coefficients due to the addition of a flap tab to the baseline airfoil.

A comparison of the pressure coefficient distribution on the main element and flap for the baseline airfoil and the configuration with a flap tab is shown in Figure 50 for an angle of attack of 0°. Both experimental and computed results are included. The flap tab produces a markedly different effect on the pressure coefficient distribution on the main element and flap than the cove tab did. The flap tab increases the loading on the aft portion of the flap, much as the cove tab did on the main element. However, the flap tab also increases the overall circulation for the flap, as can be seen by the pressure coefficient distribution on the flap. This creates an increase in lift coefficient on the flap. The circulation for the main element is also increased, leading to a further increase in lift coefficient of the overall airfoil. The increase in circulation about the main element is a direct consequence of the increased lift on the flap. The shift of the pitching moment coefficient curve in the negative direction observed when the flap tab was added to the configuration can also be attributed to the increased lift acting on the flap.

It is more difficult in this case to link changes in the pressure coefficient distribution to the observed changes in drag coefficient when a flap tab is added to the airfoil, since the entire pressure coefficient distribution changes. The magnitude of the pressure coefficient increases fairly uniformly over the whole airfoil (main element and flap), with the exception of the leading edge regions of the main element and flap. The leading edge suction peaks show a larger increase in magnitude than is evident over the rest of the airfoil surface. This may account for the slight reduction in drag coefficient observed when the flap tab is added to the airfoil. Note that, as in the case of the cove tab, the force acting on the flap tab in a direction normal to the tab can be estimated by multiplying the jump in pressure coefficient at the flap trailing edge by the area of the flap tab. In this case, however, only a component of this force acts in the drag direction since the flap is deflected to an angle of 29°.

Returning to Figure 48 a final time, the impact on the force and moment coefficients of adding a cove tab and a flap tab combination to the baseline airfoil can be seen. The changes in the force and moment coefficients of the baseline airfoil appear to be a linear combination of the changes caused by the cove tab and the flap tab individually. The lift coefficient curve is shifted upward by $\Delta C_l = 0.2$, just as the case for the configuration with only a flap tab. However, the slope of the lift coefficient curve is slightly reduced relative to the lift coefficient curves for the baseline and the flap tab only configurations. This is similar to the lift coefficient curve for the configuration with only a cove tab. The drag

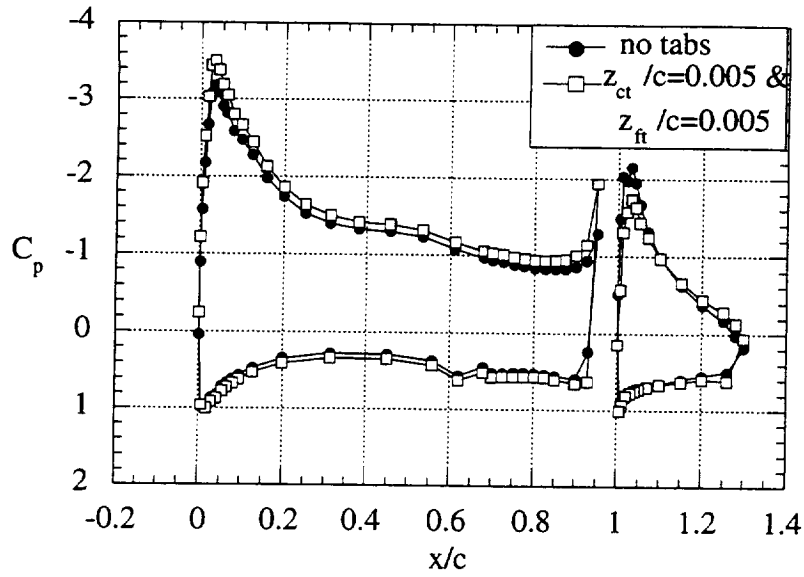

a) Experimental pressure coefficient distribution.

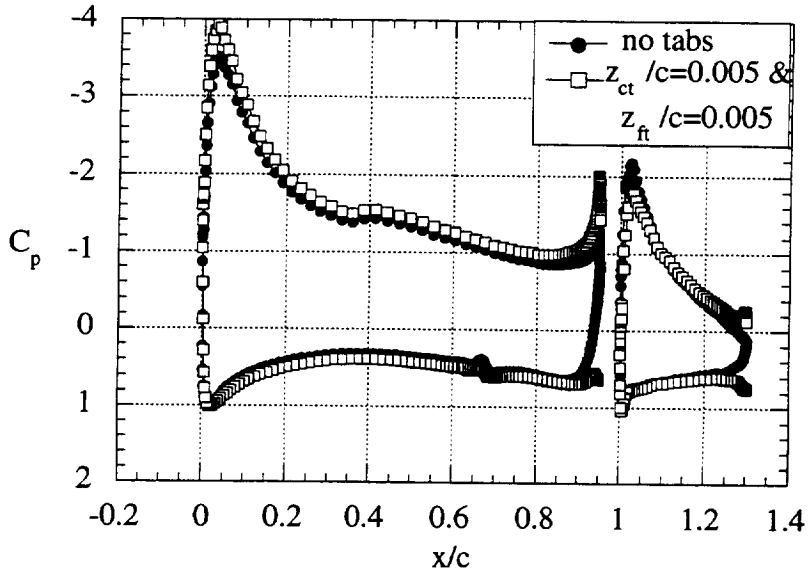

b) Computed pressure coefficient distribution.

Figure 51: Effect of a cove tab and flap tab combination on the pressure coefficient distribution of a baseline configuration ($\delta_f = 29°$, INS2D $\delta_f = 27°$, $z_g/c = 0.02$, $x_{ol}/c = 0.015$, $\alpha = 0°$).

coefficient for the configuration with both cove and flap tabs is slightly less than the drag coefficient for the configuration with just a cove tab at all lift coefficients. The pitching moment coefficient curve is shifted in the negative direction, but the shift is not as great as it is for the configuration with just a flap tab. The shifts in the force and moment coefficient curves predicted by the computed results match the experimental data quite well.

Figure 51 presents a comparison of the pressure coefficient distribution on the main element and flap for the baseline configuration with the distribution for a configuration with both cove and flap tabs of height $z_t/c = 0.005$. The angle of attack is 0° and both experimental and computed results are included. The plots presented in Figure 51 further support the contention that the changes in airfoil performance induced by the combination of a flap tab and a cove tab are just the sum of the changes induced by the individual tabs. Note that the pressure coefficient distributions presented in Figure 51 indicate an increase in circulation on both the flap and the main element, as was the case for the configuration with just a flap tab. In addition, however, the loading on the aft portion of the main element is increased and the suction peak on the flap leading edge is decreased, as was the case for the configuration with just a cove tab. There is general agreement between the experimental and computed results shown in Figure 51.

Having established that the results computed using INS2SD-UP for the various tab configurations exhibit the same trends as the experimental results, the detailed nature of the solution can be used to obtain further information about the flow field which is not available experimentally. Figure 52 shows a computed streamline trace around the cove tab at the trailing edge of the main element. The flap deflection angle for the computed results is 27°, the gap is $z_g/c = 0.02$, and the angle of attack is 0°. The Computational Fluid Dynamics (CFD) post-processing program PLOT3D [44] was used to generate Figure 52. PLOT3D allows sets of streamlines to be started at user-specified grid points within the composite grid. Streamlines can be traced upstream and downstream from the starting point. One of the limitations of PLOT3D is that streamline traces cannot cross wake boundary lines within a C grid. For composite grids, PLOT3D also will not allow streamline traces which start in one grid to cross into another grid. Obtaining adequate streamline definition in a composite grid composed of individual C grids requires sets of streamlines to be started on both sides of the wake boundary lines and within each individual grid. The discontinuities in the streamline traces observed in the wake boundary line region in Figure 52 are a result of the limitations of PLOT3D and not due to any flow phenomena.

The flow field around the cove tab is dominated by three distinct structures. A region of recirculating flow is evident upstream of the tab. Two counter-rotating regions of

Figure 52: Streamline pattern in vicinity of cove tab, computed using INS2D-UP.

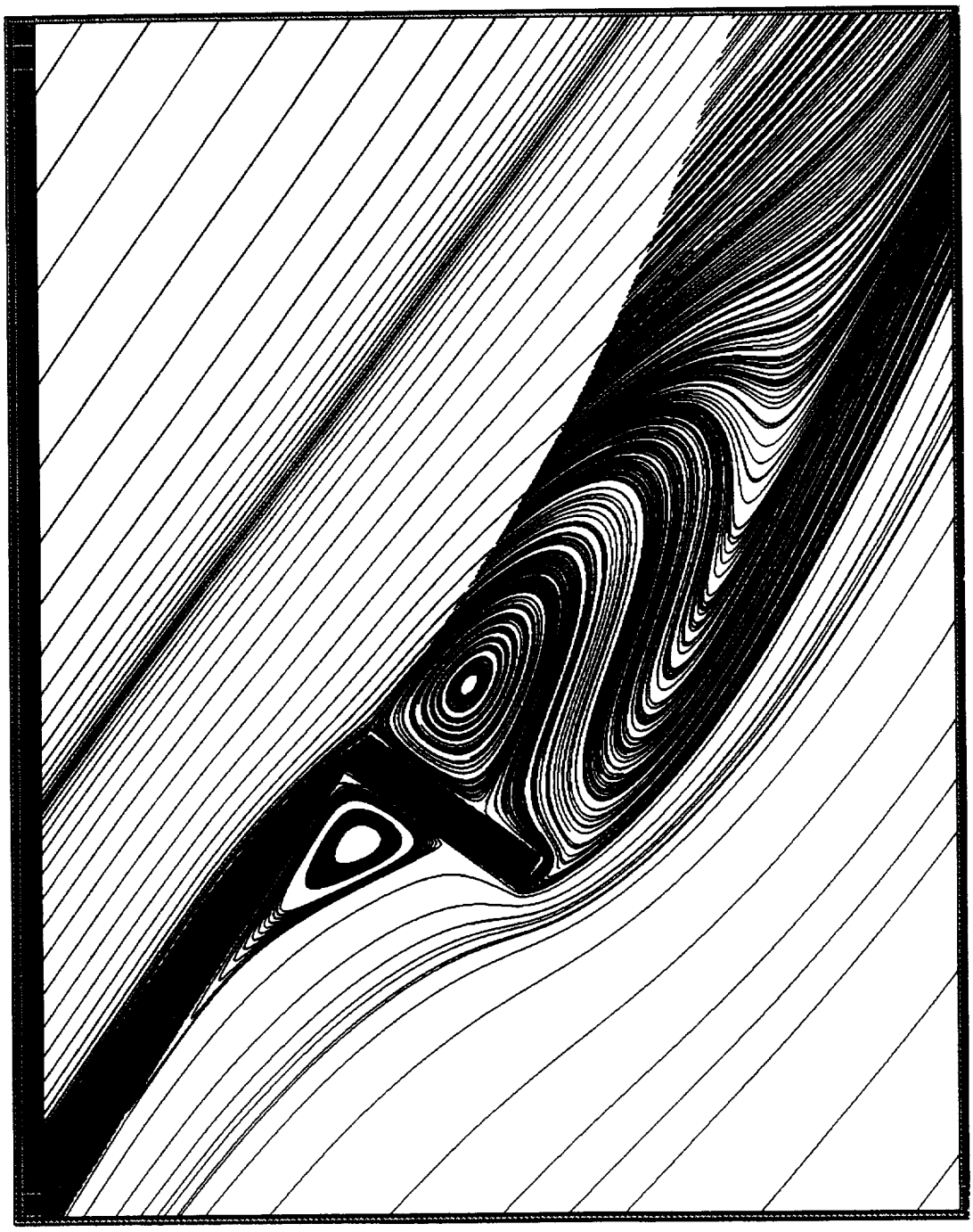

Figure 53: Streamline pattern in vicinity of flap tab, computed using INS2D-UP.

recirculating flow exist aft of the cove tab. The upper recirculation region aft of the tab is the strongest of the three. Note that fluid from the main element upper surface is entrained around the top recirculation region aft of the tab, along the tab aft surface, and upstream along the tip of the tab before reversing direction and going downstream. The flow field indicated by the computed streamlines is consistent with the flow field around a Gurney flap hypothesized by Leibeck [5] and observed at low Reynolds number in a water tunnel by Neuhart and Pendergraft [10].

Streamline traces around a flap tab are shown in Figure 53. Although the streamline pattern for the flap tab is similar to the one for the cove tab, there is one notable exception. There is no closed lower recirculation region aft of the tab as there was behind the cove tab. Fluid from the upper flap surface is entrained around the upper recirculation region aft of the tab, back toward the tab, and then turned back downstream. Apparently, it is the presence of the flap upper surface near the cove tab which turns the flow sufficiently to create the lower recirculation region aft of the cove tab.

If the baseline configuration is changed so that the flap gap is increased to $z_g/c = 0.05$, the effect of the tabs on the force and moment coefficient curves is somewhat different than it was at the smaller flap gap setting, as shown in Figure 54. In this case, adding a cove tab to the configuration produces an upward shift of the lift coefficient curve of $\Delta C_l = 0.1$ relative to the lift coefficient curve for the baseline case. The computed results predict a slightly larger upward shift in lift coefficient of $\Delta C_l = 0.15$ when a cove tab is added to the baseline configuration. The experimental drag coefficient for the configuration with a cove tab increases by as much as 100 drag counts at moderate lift coefficients relative to the baseline configuration. The computed drag coefficient at a given lift coefficient for the configuration with a cove tab, on the other hand, is actually slightly lower than drag coefficient for the corresponding baseline configuration. Note that the magnitude of the computed drag coefficient for this baseline configuration is approximately 50 drag counts higher than the experimental drag coefficient at all lift coefficients. This is probably due to differences between the computed and experimental location of the flow separation point on the flap upper surface near the trailing edge. The experimental pitching moment coefficient is essentially unaffected by the addition of the cove tab. The computed pitching moment coefficient curve is shifted in the negative direction a small amount ($\Delta C_m = 0.01$) when a cove tab is added to the baseline configuration.

Adding a flap tab to the baseline configuration causes an upward shift in the lift coefficient curve of $\Delta C_l = 0.22$ relative to the lift coefficient curve for the baseline configuration. The drag coefficient at a given lift coefficient remains unchanged when a flap tab is added to the baseline configuration. The flap tab shifts the pitching moment

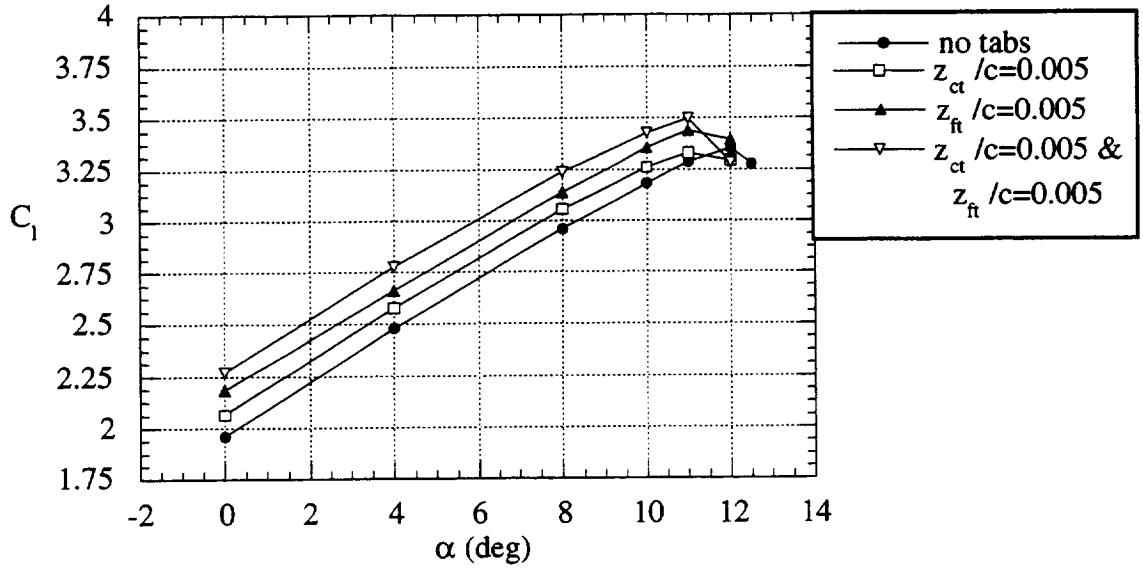

a) Effect of tabs on experimental lift coefficient.

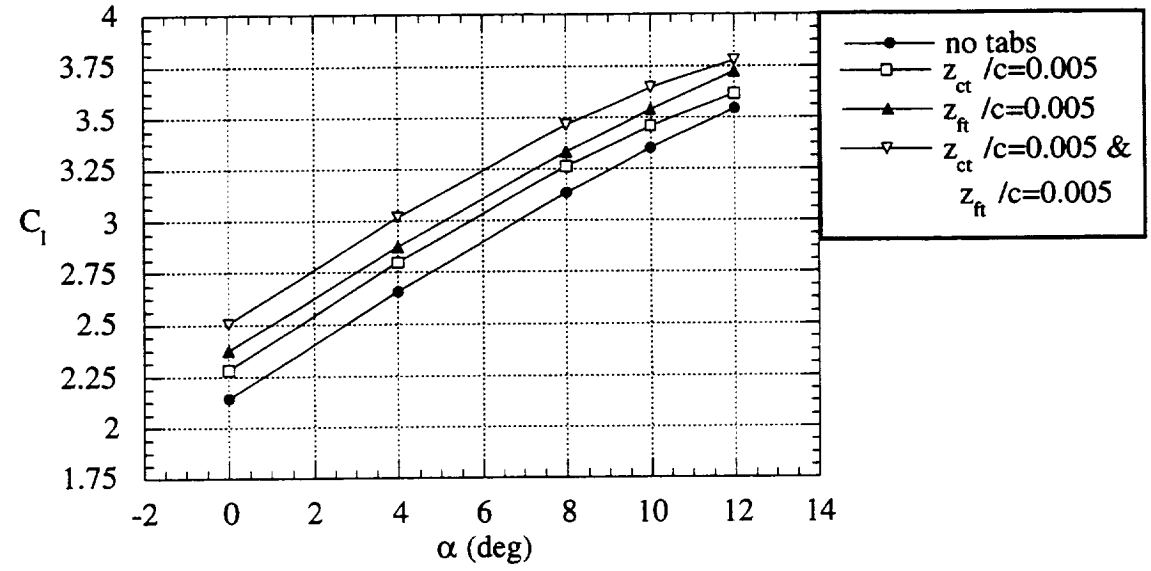

b) Effect of tabs on computed lift coefficient.

Figure 54: Effect of lift-enhancing tabs on the force and moment coefficients of a baseline configuration ($\delta_f = 29°$, INS2D $\delta_f = 27°$, $z_g/c = 0.05$, $x_{ol}/c = 0.015$).

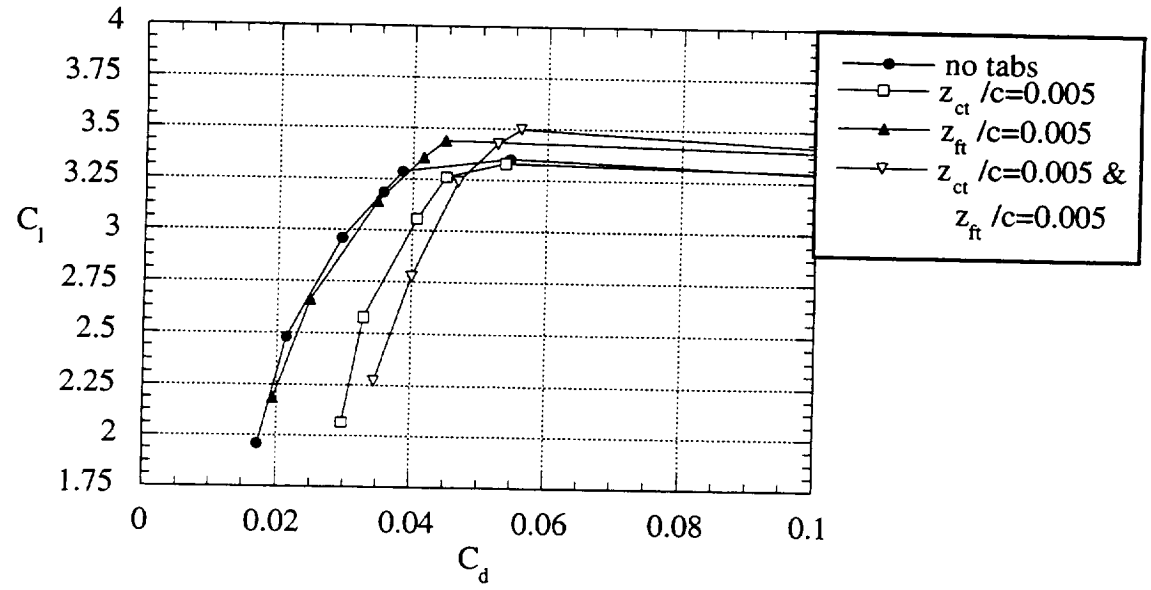

c) Effect of tabs on computed drag coefficient.

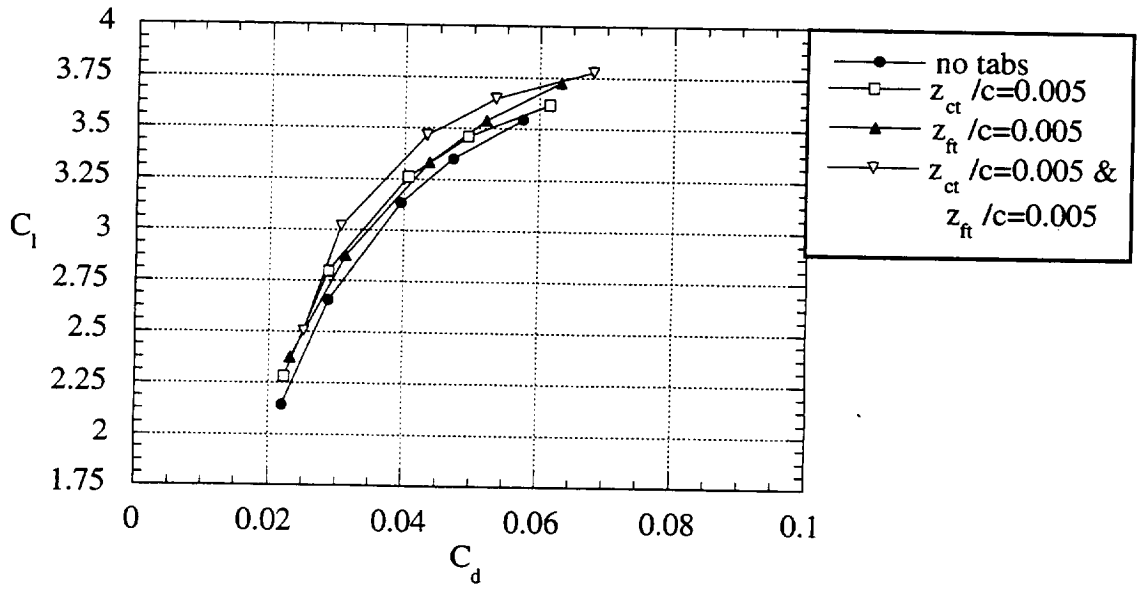

d) Effect of tabs on computed drag coefficient.

Figure 54 continued: Effect of lift-enhancing tabs on the force and moment coefficients of a baseline configuration ($\delta_f = 29°$, INS2D $\delta_f = 27°$, $z_g/c = 0.05$, $x_{ol}/c = 0.015$).

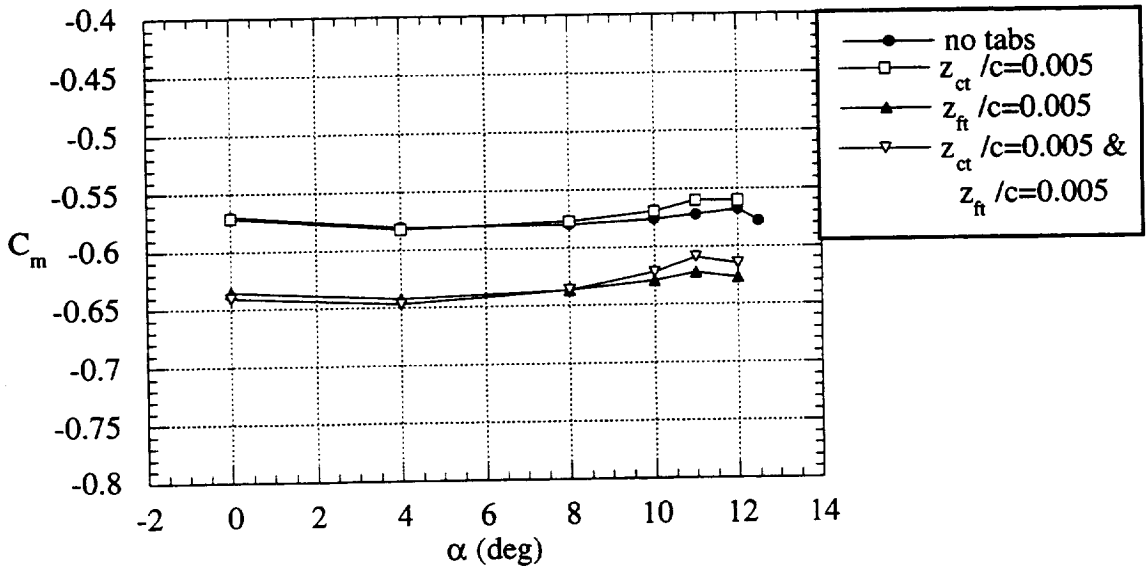

f) Effect of tabs on experimental pitching moment coefficient.

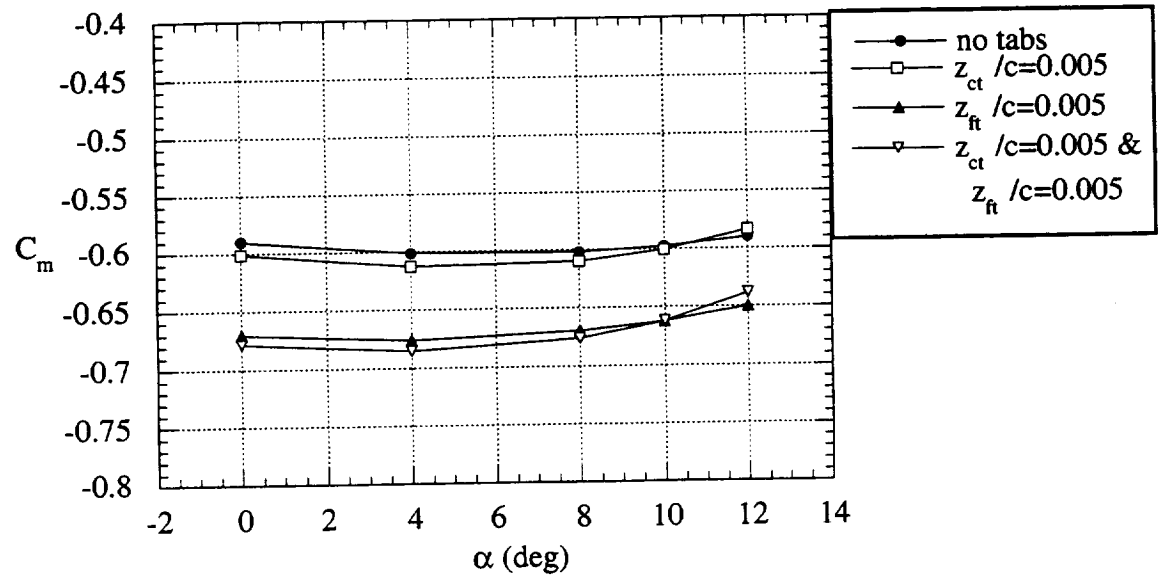

f) Effect of tabs on computed pitching moment coefficient.

Figure 54 concluded: Effect of lift-enhancing tabs on the force and moment coefficients of a baseline configuration ($\delta_f = 29°$, INS2D $\delta_f = 27°$, $z_g/c = 0.05$, $x_{ol}/c = 0.015$).

coefficient curve in the negative direction by $\Delta C_m = 0.07$. The changes in the force and moment coefficients due to the addition of the flap tab are accurately predicted by the computed results.

Adding both a cove tab and a flap tab to the baseline configuration produces the largest upward shift in the lift coefficient curve relative to the baseline case. The magnitude of the shift is $\Delta C_l = 0.30$. This configuration also exhibits the largest drag coefficient increase compared to the baseline case. The drag coefficient is increased by 150 drag counts at moderate lift coefficients. The pitching moment coefficient curve is almost identical to the corresponding curve for the configuration with just a flap tab. The computed results for this configuration predict the changes in lift and pitching moment coefficient well, but the increase in drag coefficient observed in the experimental results is not duplicated in the computed results. This configuration actually has the lowest computed drag coefficient at a given lift coefficient as can be seen in Figure 54.

An examination of the pressure coefficient distribution on the main element and flap for the baseline configuration and the various configurations with tabs provides some additional insight into how the tabs affect the performance of the two-element airfoil when the flap gap is large ($z_g/c = 0.05$). Figure 55 shows a comparison of the pressure coefficient distributions for the baseline case and a configuration with a cove tab. Both the experimental and computed results are included. In general, the addition of a cove tab to the configuration affects the pressure coefficient distribution in a manner similar to that presented in Figure 49 for a flap gap of $z_g/c = 0.02$. The suction peak at the leading edge of the flap is reduced and the loading on the aft portion of the main element is increased. However, the circulation about the main element is also increased for the configuration with a large flap gap when a cove tab is added. This was not observed for the configuration with the small flap gap. It is this increase in circulation about the main element that accounts for the increase in lift coefficient for the configuration with a cove tab relative to the baseline case.

The effect of a flap tab on the pressure coefficient distribution for the configuration with a flap gap of $z_g/c = 0.05$ is illustrated in Figure 56. The changes in the pressure coefficient distribution caused by the addition of the flap tab do not appear to be sensitive to the size of the flap gap, at least over a reasonable range of flap gaps. As in the case of the configuration with a flap gap of $z_g/c = 0.02$, the circulation about the flap and the main element are both increased when a flap tab is added.

Adding both a cove tab and a flap tab to the baseline configuration affects the pressure coefficient distribution as shown in Figure 57. The circulation about the flap is increased and the suction peak at the leading edge is reduced. Comparing with the results

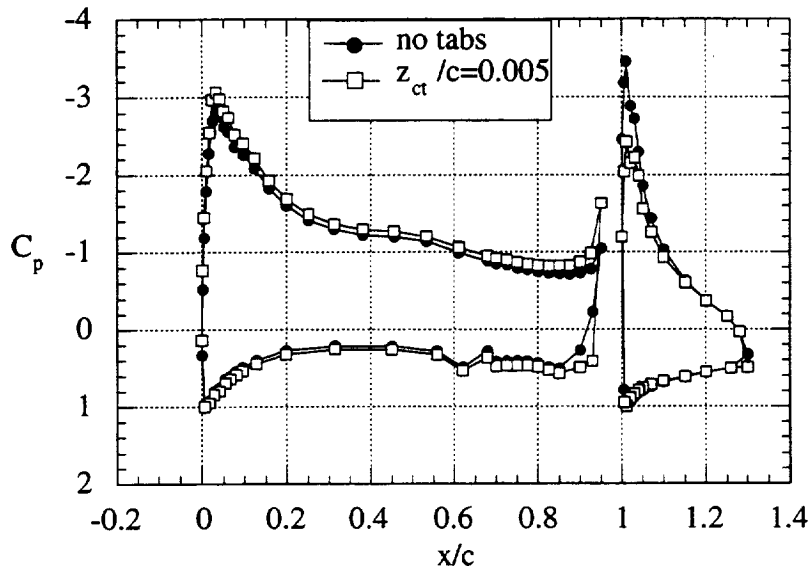

a) Experimental pressure coefficient distribution.

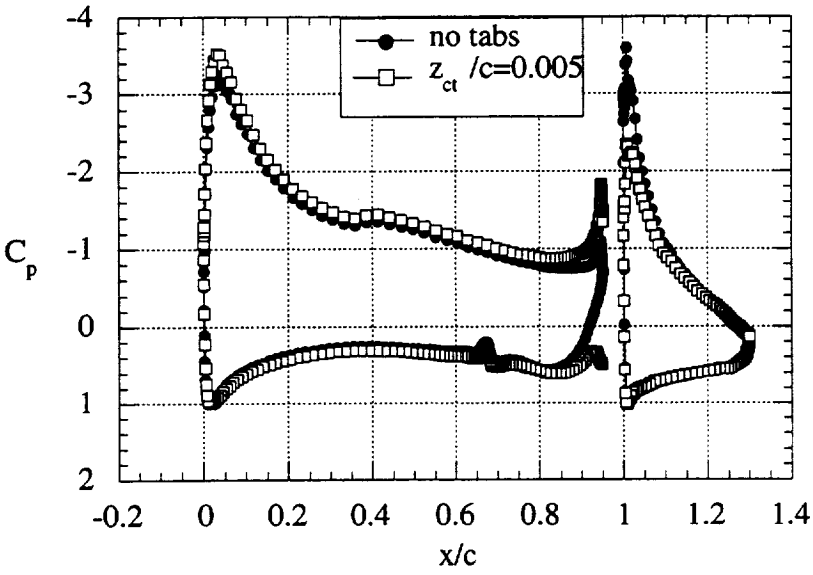

b) Computed pressure coefficient distribution.

Figure 55: Effect of a cove tab on the pressure coefficient distribution of a baseline configuration ($\delta_f = 29°$, INS2D $\delta_f = 27°$, $z_g/c = 0.05$, $x_{ol}/c = 0.015$, $\alpha = 0°$).

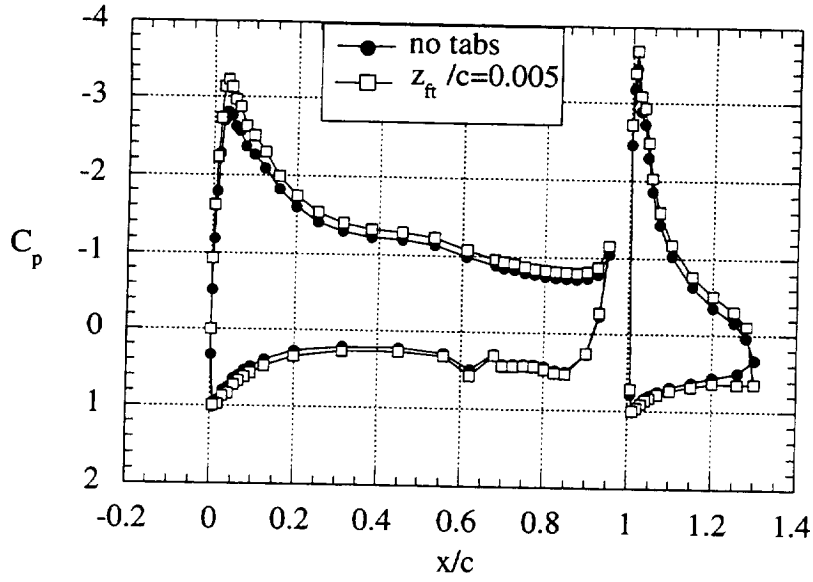

a) Experimental pressure coefficient distribution.

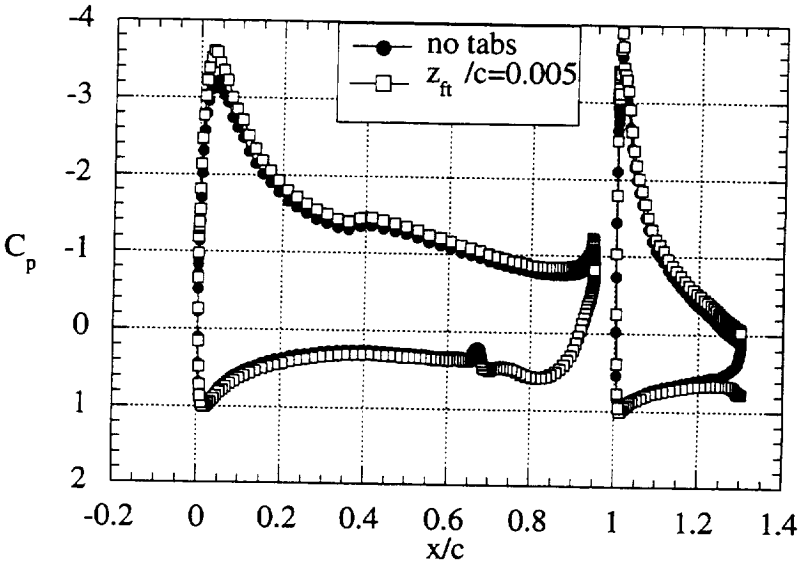

b) Computed pressure coefficient distribution.

Figure 56: Effect of a flap tab on the pressure coefficient distribution of a baseline configuration ($\delta_f = 29°$, INS2D $\delta_f = 27°$, $z_g/c = 0.05$, $x_{ol}/c = 0.015$, $\alpha = 0°$).

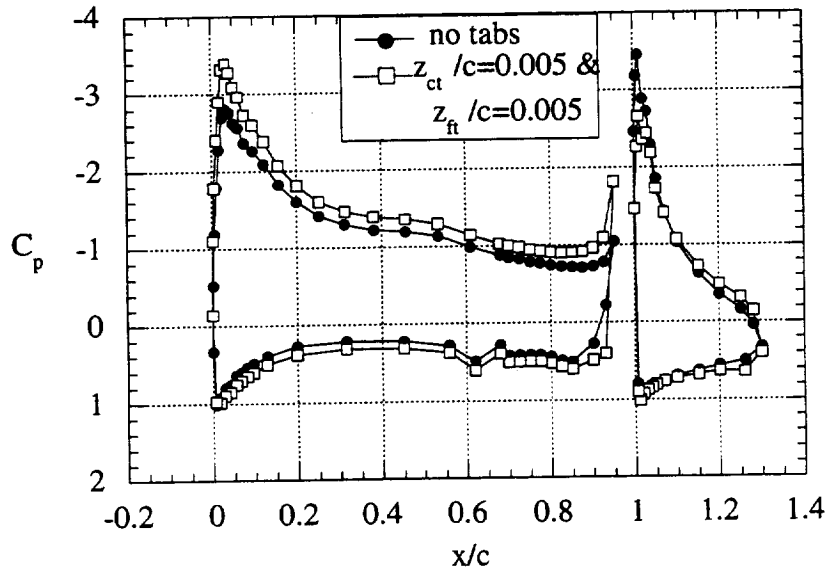

a) Experimental pressure coefficient distribution.

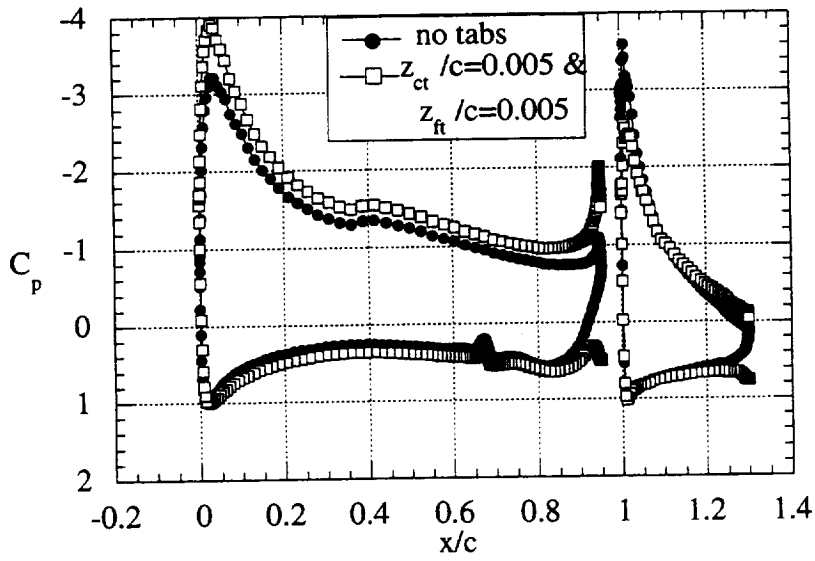

b) Computed pressure coefficient distribution.

Figure 57: Effect of a cove tab and flap tab combination on the pressure coefficient distribution of a baseline configuration ($\delta_f = 29°$, INS2D $\delta_f = 27°$, $z_g/c = 0.05$, $x_{ol}/c = 0.015$, $\alpha = 0°$).

presented in Figure 51 for the same configuration with a flap gap of $z_g/c = 0.02$, the changes in the flap pressure coefficient distribution caused by the tabs do not appear to be very sensitive to the size of the flap gap. The tabs induce a much larger increase in the circulation about the main element for this configuration than was evident at the smaller flap gap. The difference can be attributed primarily to the increase in circulation about the main element caused by the cove tab, as discussed above.

At large flap gaps ($z_g/c = 0.05$) the individual wakes from the flap and the main element can be identified in the total pressure profile of the wake measured with the wake rake at a distance equal to one chord length behind the airfoil. The wake total pressure profiles for the baseline configuration and various configurations with tabs are shown in Figure 58. For this data, the wake rake was held at a fixed position in the tunnel. Since the angle of attack was held constant at 0°, the angular orientation of the wake rake did not have to be changed for any of these configurations. The individual main element and flap

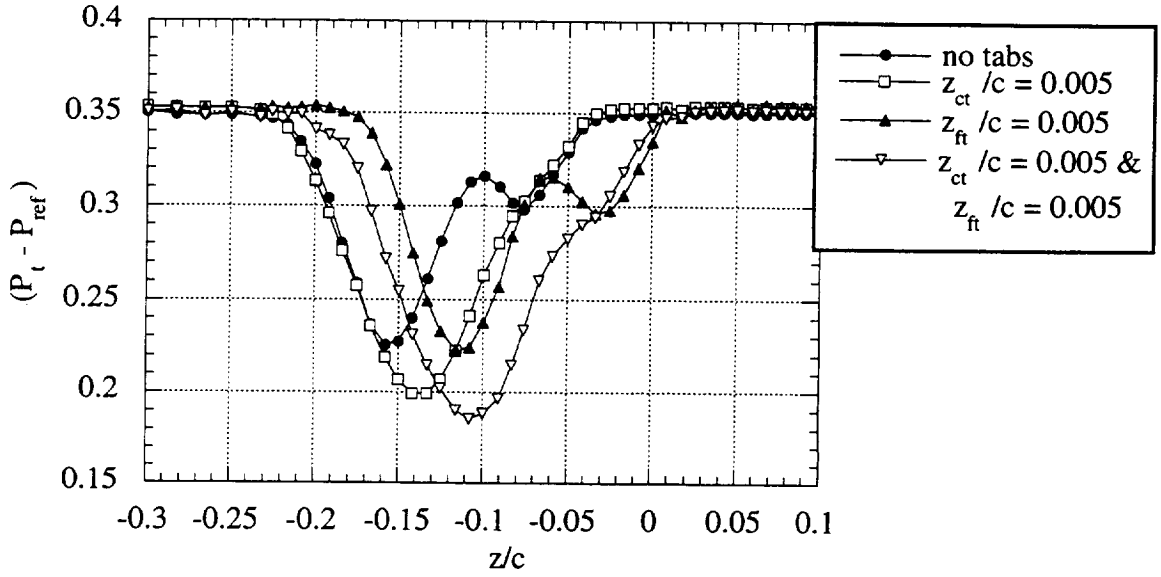

Figure 58: Effect of tabs on the total pressure distribution in the wake 1 chord length aft of the airfoil trailing edge for a baseline configuration ($\delta_f = 29°$, $z_g/c = 0.05$, $x_{ol}/c = 0.015$).

wakes for the baseline configuration are easily identifiable, with the larger total pressure deficit corresponding to the main element wake. The addition of a cove tab to the main element causes the main element wake to thicken substantially. At a distance of one chord length behind the airfoil, the main element and flap wakes have merged. The increased drag caused by the addition of the cove tab is evident in the larger total pressure deficit of

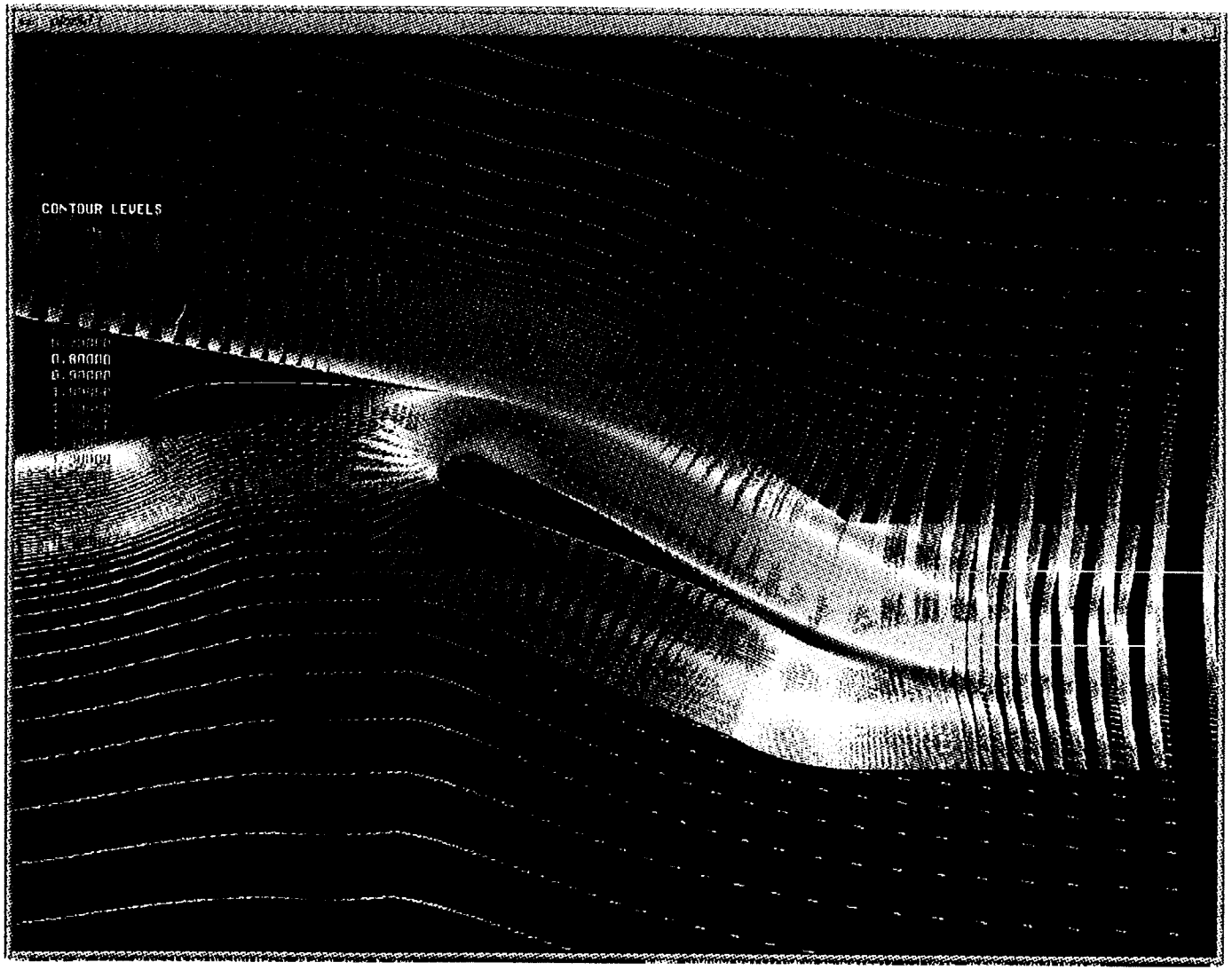

a) Baseline configuration.

Figure 59: Velocity vector plots obtained from INS2D-UP solution ($\delta_f = 27°$, $z_g/c = 0.05$, $x_{ol}/c = 0.015$, $\alpha = 0°$).

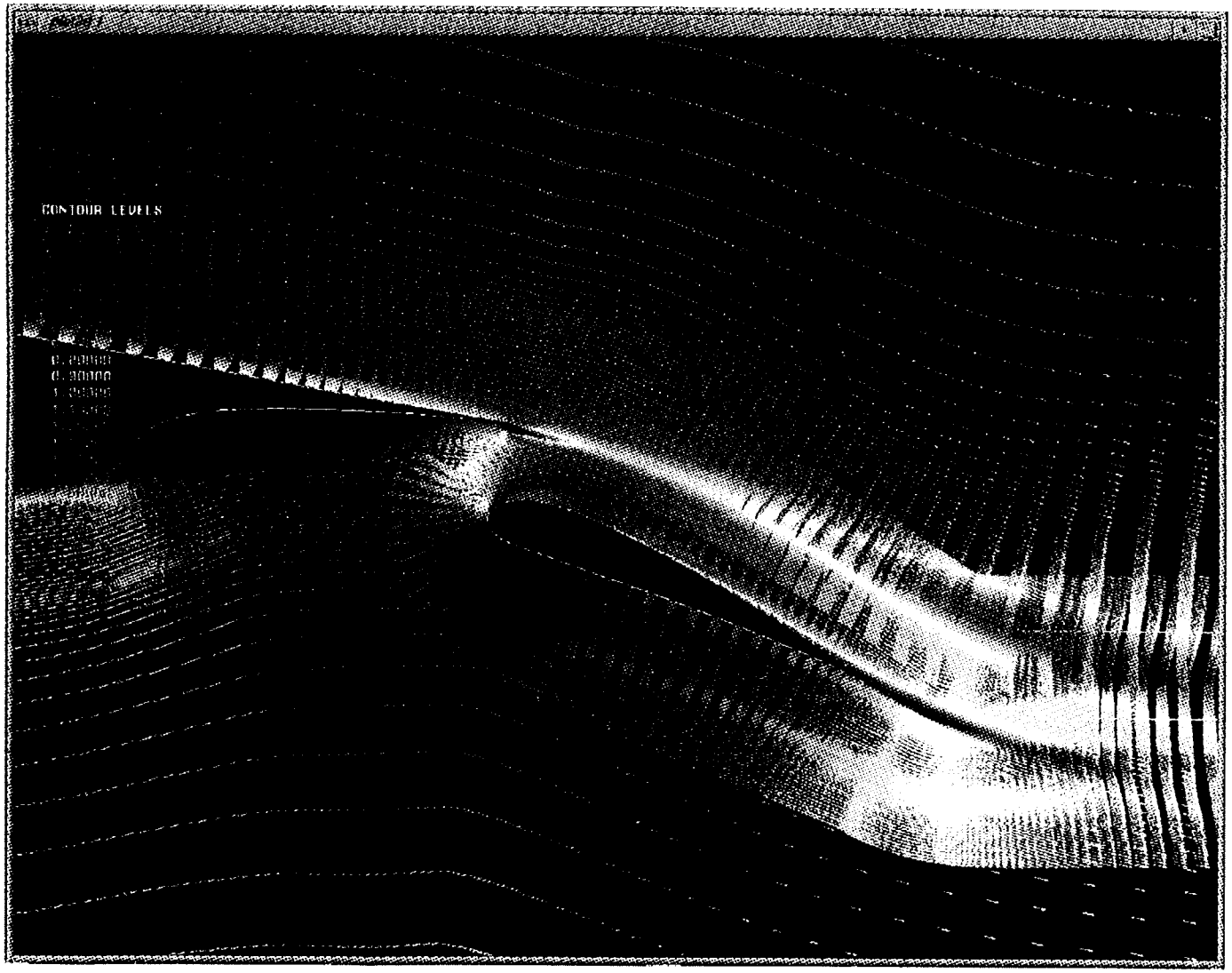

b) Cove tab configuration.

Figure 59, continued: Velocity vector plots obtained from INS2D-UP solution ($\delta_f = 27°$, $z_g/c = 0.05$, $x_{ol}/c = 0.015$, $\alpha = 0°$).

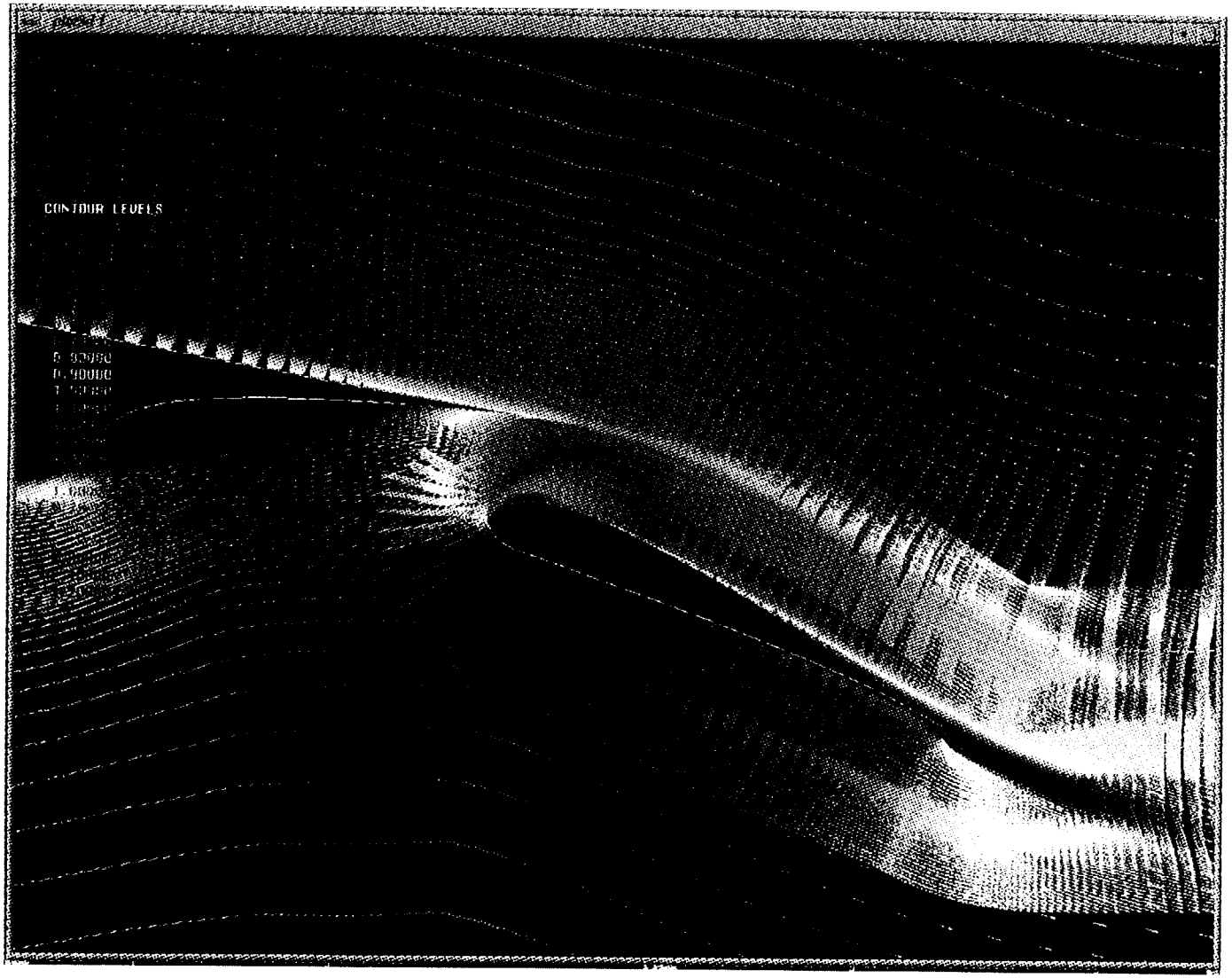

c) Flap tab configuration.

Figure 59, continued: Velocity vector plots obtained from INS2D-UP solution ($\delta_f = 27°$, $z_g/c = 0.05$, $x_{ol}/c = 0.015$, $\alpha = 0°$).

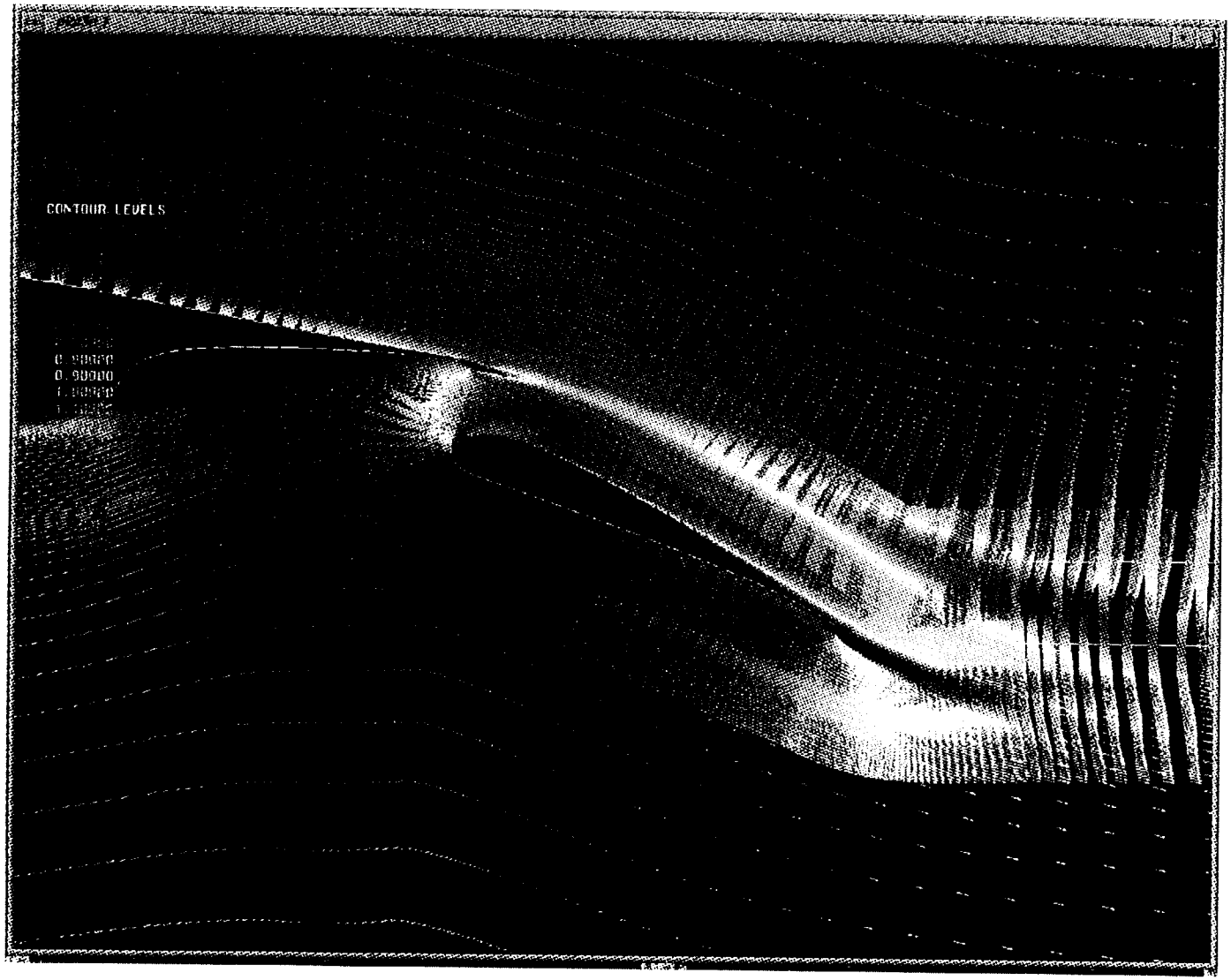

d) Configuration with both a cove tab and a flap tab.

Figure 59, concluded: Velocity vector plots obtained from INS2D-UP solution ($\delta_f = 27°$, $z_g/c = 0.05$, $x_{ol}/c = 0.015$, $\alpha = 0°$).

the wake. The increased circulation about the main element caused by the cove tab can also be inferred from the shift to the right in the peak total pressure deficit of the main element wake. Adding a flap tab to the baseline configuration does not appreciably change the shape of the wake total pressure profile or the magnitude of the peak total pressure deficit in the main element or flap wakes. The individual main element and flap wakes are still visible in the total pressure profile. The wake total pressure profile is shifted to the right, however, indicating an increase in circulation about both the flap and the main element. Adding both a cove tab and a flap tab to the baseline configuration causes a broadening of the main element wake total pressure profile. The main element wake and the flap wake have almost completely merged. This wake profile exhibits the largest shift to the right, indicating this configuration has the largest increase in circulation about the airfoil. This wake profile also has the largest total pressure deficit, indicating that this configuration has the highest drag. All of these observations are consistent with the force and moment data presented above.

The computed results for this baseline configuration and the various associated tab configurations can be used to provide further details on the effect the tabs have on the wakes of the main element and flap. PLOT3D was used to construct velocity vector plots from the computed solutions. The velocity vectors are colored according to the velocity magnitude for each vector. Figure 59 shows velocity vector plots for the baseline configuration and for each of the three tab configurations. In Figure 59a, the wakes from the baseline main element and flap are clearly visible as yellow and orange colored regions that approximately follow the wake boundary lines within each grid. When a cove tab is added to the main element, the wake from the main element becomes much thicker and the velocity magnitude within the wake is lower than it was for the baseline case, as seen in Figure 59b. The main element wake for the cove tab configuration is also turned toward the flap upper surface more, indicating higher circulation on the main element. Adding a flap tab to the baseline configuration produces a similar thickening of the flap wake and a reduction in the velocity magnitude within the wake, as shown in Figure 59c. The wakes of the main element and the flap for a configuration with both a cove tab and a flap tab can be seen in Figure 59d.

Lift-Enhancing Tabs on Configurations with High Flap Angle

All of the lift-enhancing tab results presented to this point have been for a configuration with a static flap deflection angle of 29°. Increasing the flap deflection angle to 39° produces some changes in the way the lift-enhancing tabs affect the performance of the two-element airfoil. A flap deflection angle of 39° produces the highest lift coefficient at

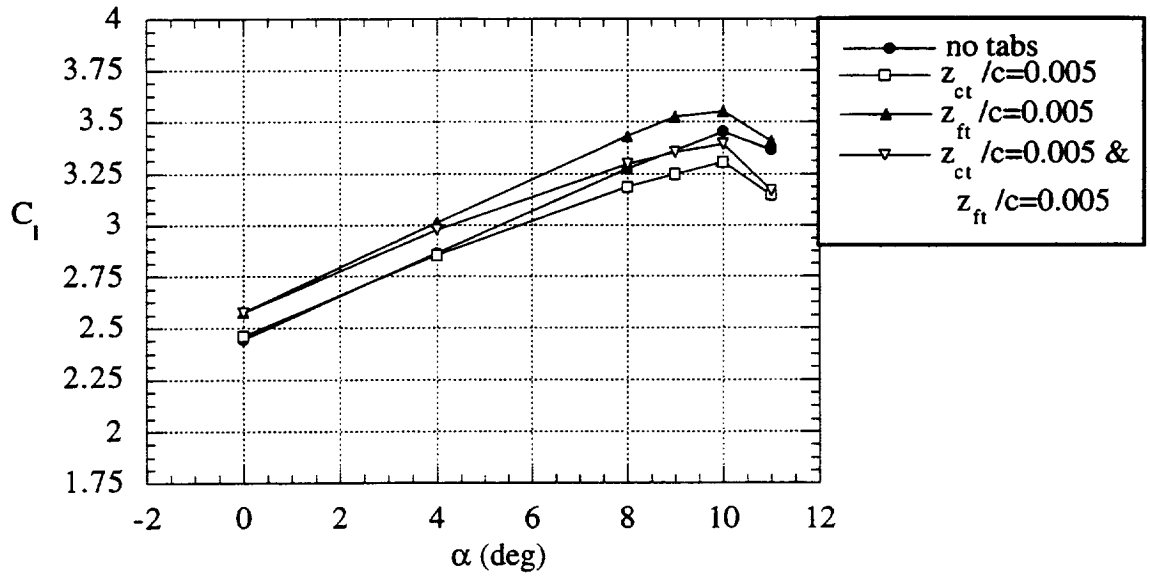

a) Effect of tabs on experimental lift coefficient.

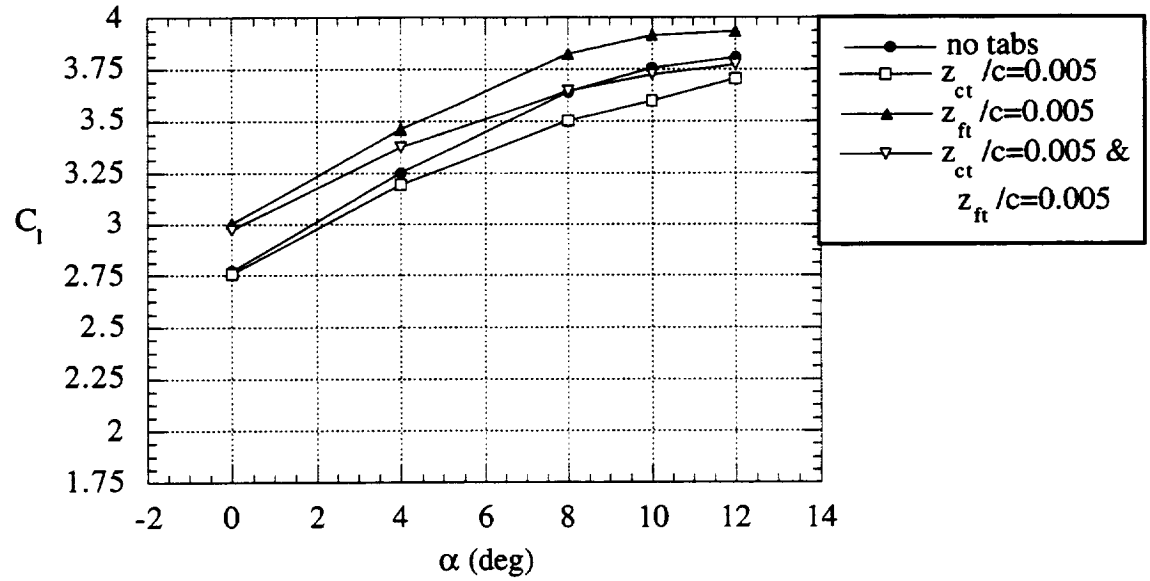

b) Effect of tabs on computed lift coefficient.

Figure 60: Effect of lift-enhancing tabs on the force and moment coefficients of a baseline configuration ($\delta_f = 39°$, INS2D $\delta_f = 36°$, $z_g/c = 0.02$, $x_{ol}/c = 0.015$).

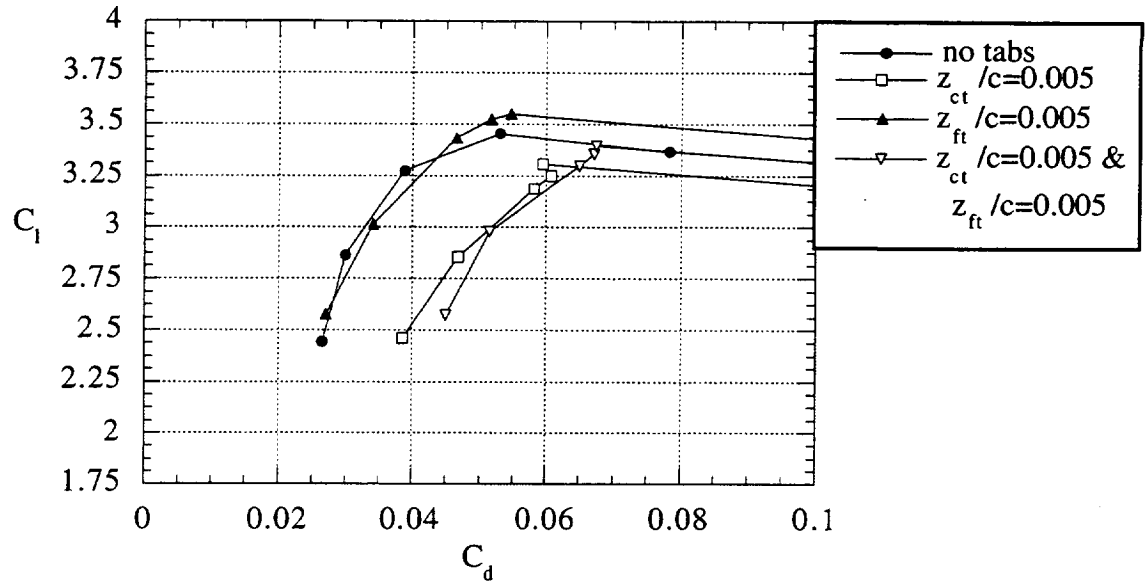

c) Effect of tabs on experimental drag coefficient.

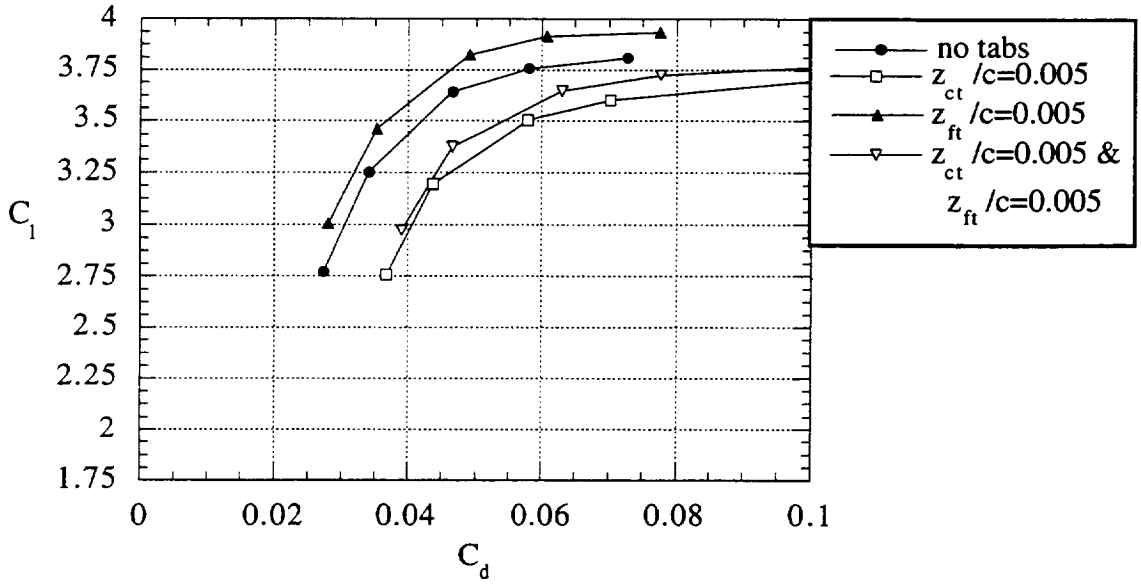

d) Effect of tabs on computed drag coefficient.

Figure 60 continued: Effect of lift-enhancing tabs on the force and moment coefficients of a baseline configuration ($\delta_f = 39°$, INS2D $\delta_f = 36°$, $z_g/c = 0.02$, $x_{ol}/c = 0.015$).

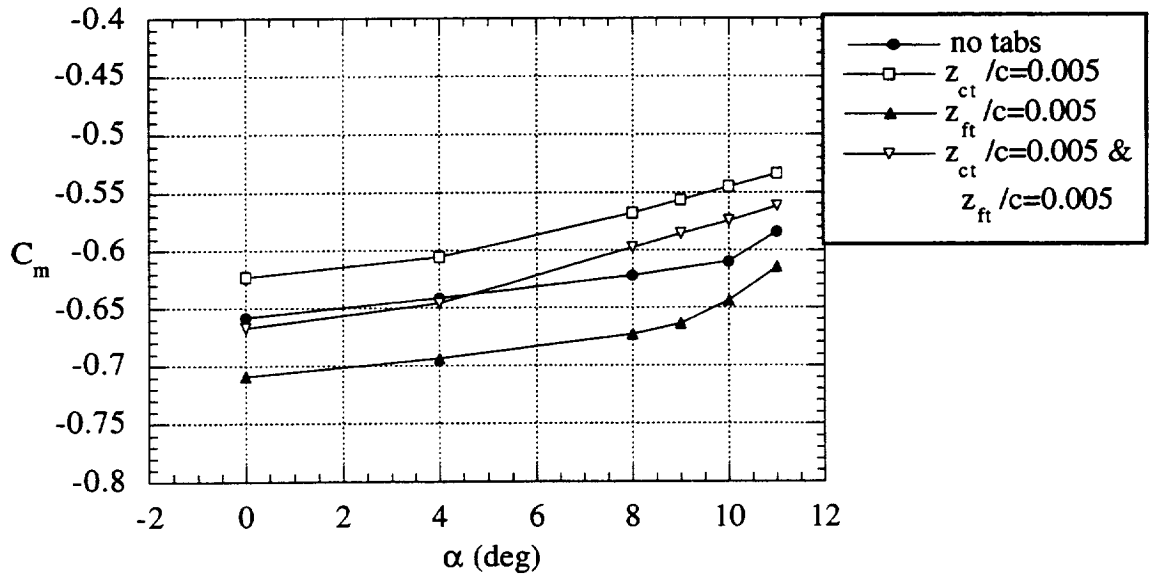

e) Effect of tabs on experimental pitching moment coefficient.

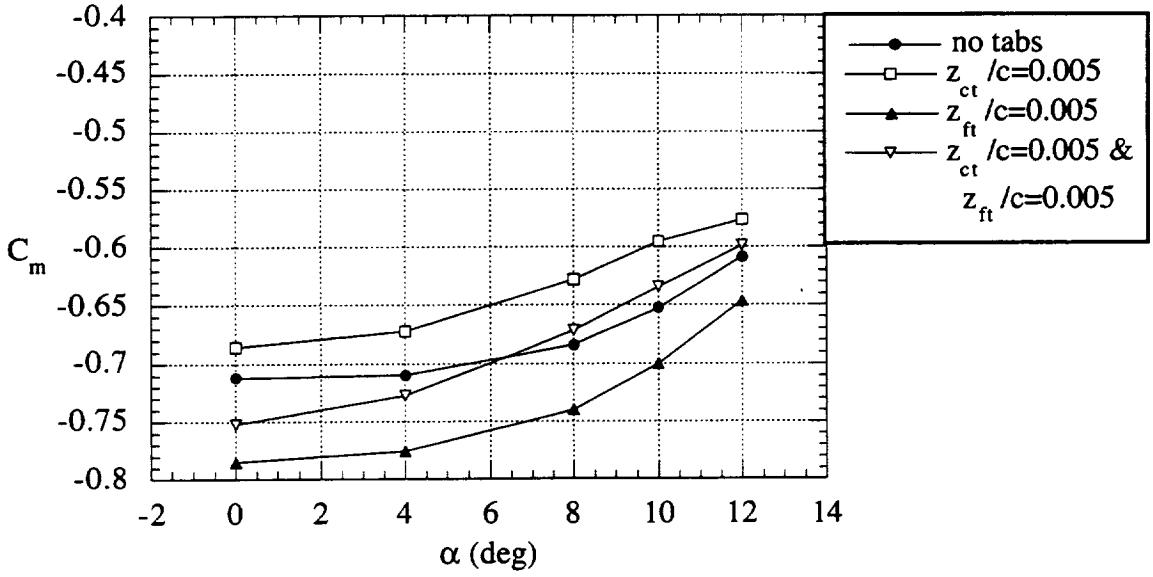

f) Effect of tabs on computed pitching moment coefficient.

Figure 60 concluded: Effect of lift-enhancing tabs on the force and moment coefficients of a baseline configuration ($\delta_f = 39°$, INS2D $\delta_f = 36°$, $z_g/c = 0.02$, $x_{ol}/c = 0.015$).

a given angle of attack for this airfoil. Even at a flap gap of $z_g/c = 0.02$, a small amount of separated flow exists on the upper surface of the flap near the trailing edge. If the flap gap is made larger, the flow separates over much of the flap upper surface and the lift coefficient decreases rapidly at all angles of attack. If the flap deflection angle is made larger, the flow also separates on the upper surface of the flap.

Figure 60 shows the effect of lift-enhancing tabs on the force and moment coefficients of a baseline configuration with a static flap deflection angle of 39° and a flap gap of $z_g/c = 0.02$. Both experimental and computed results are included. The changes produced in the force and moment coefficients of the baseline configuration by the tabs are very similar to those shown in Figure 48 for a static flap deflection angle of 29° and the same flap gap. The addition of a cove tab to the baseline case does not change the lift coefficient at low angles of attack. The slope of the lift coefficient curve is significantly reduced compared to the baseline case as angle of attack is increased. The reduction in slope of the lift coefficient curve is larger for the configuration with a flap deflection angle of 39° than it was for the configuration with a 29° flap deflection angle. The computed results indicate a similar reduction in the slope of the lift coefficient curve as angle of attack is increased. When a flap tab is added to the baseline configuration, the lift coefficient curve is shifted upward by $\Delta C_l = 0.15$. The computed results predict a larger increase in lift coefficient when a flap tab is added to the configuration than was observed experimentally. Adding both a cove tab and a flap tab to the baseline configuration shifts the lift coefficient curve upward by the same amount that adding a flap tab only caused. However, the slope of the lift coefficient curve is reduced as angle of attack is increased, similar to the configuration with only a cove tab. The computed results indicate the same type of changes.

The drag coefficient increases by as much as 180 drag counts when a cove tab is added to the configuration. This increase is much larger than was observed for the configuration with a 29° flap deflection angle. The computed increase in drag coefficient for the cove tab configuration is underpredicted by about 80 drag counts. Adding a flap tab to the baseline configuration does not increase the drag coefficient at a given lift coefficient. The computed drag coefficient for the configuration with a flap tab is actually slightly lower than the baseline case for a given lift coefficient. The configuration with both a cove tab and a flap tab has essentially the same drag coefficient at a given lift coefficient as the configuration with just a cove tab, as indicated by both the experimental and computed results.

The changes in pitching moment coefficient due to the addition of lift-enhancing tabs to the baseline airfoil are very similar to those shown in Figure 48 for the configuration

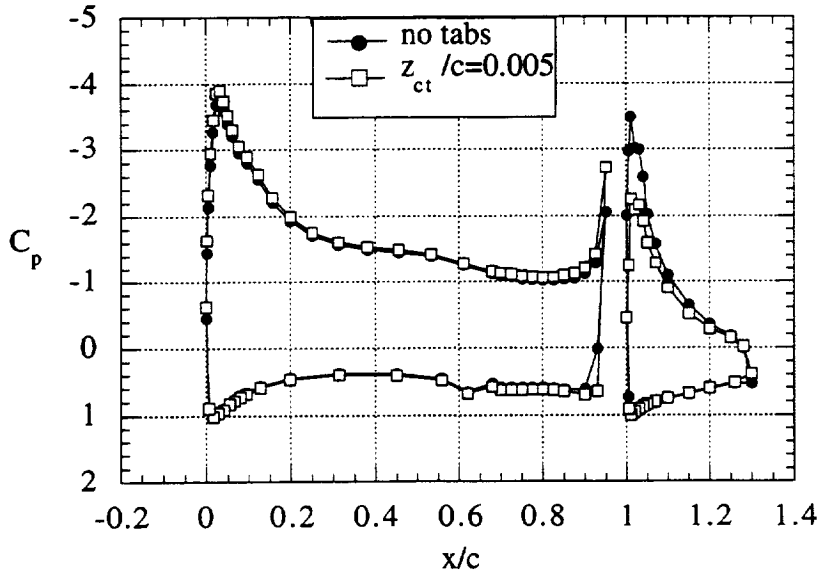

a) Experimental pressure coefficient distribution.

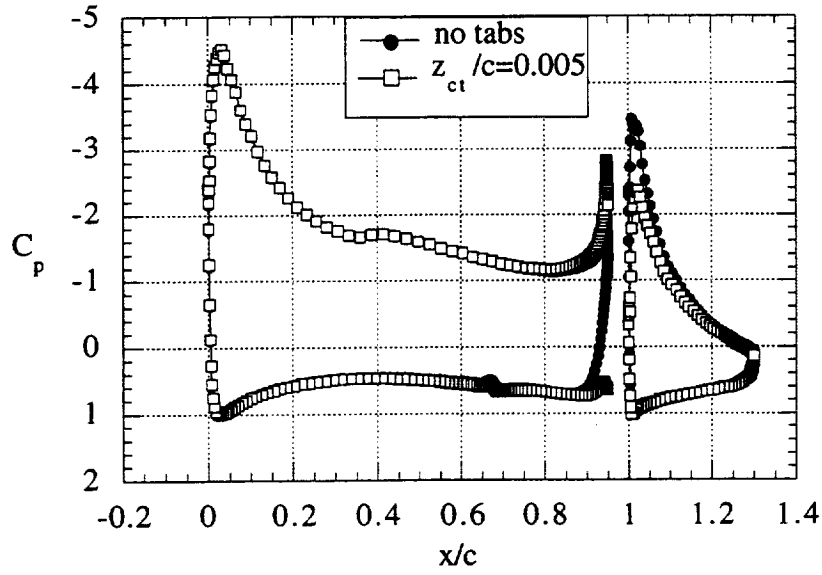

b) Computed pressure coefficient distribution.

Figure 61: Effect of a cove tab on the pressure coefficient distribution of a baseline configuration ($\delta_f = 39°$, INS2D $\delta_f = 36°$, $z_g/c = 0.02$, $x_{ol}/c = 0.015$, $\alpha = 0°$).

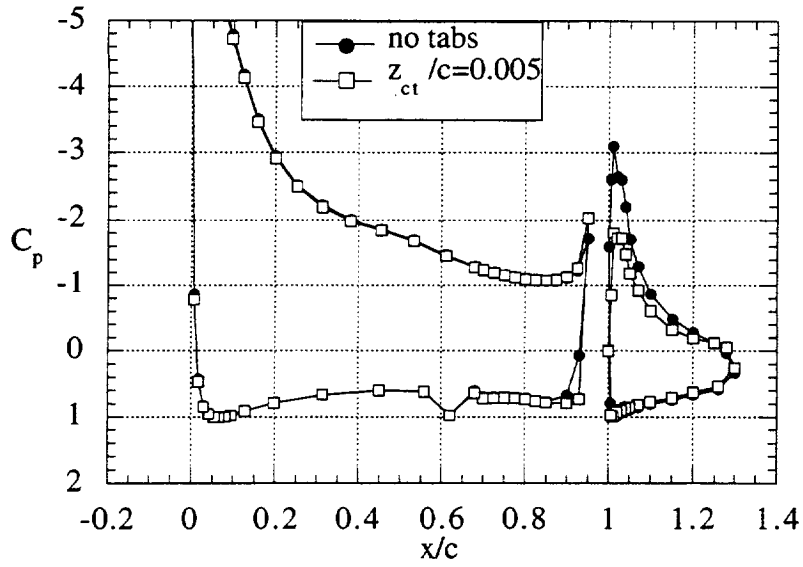

c) Experimental pressure coefficient distribution.

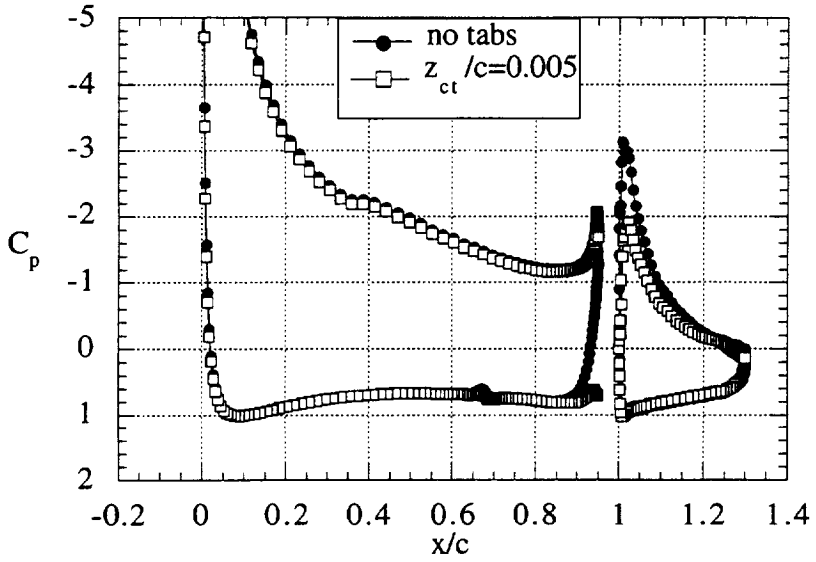

d) Computed pressure coefficient distribution.

Figure 61 concluded: Effect of a cove tab on the pressure coefficient distribution of a baseline configuration ($\delta_f = 39°$, INS2D $\delta_f = 36°$, $z_g/c = 0.02$, $x_{ol}/c = 0.015$, $\alpha = 8°$).

with a 29° flap deflection angle. The addition of a cove tab to the baseline configuration shifts the pitching moment coefficient curve in the positive direction, while adding a flap tab to the baseline configuration shifts the pitching moment coefficient curve in the negative direction. The shift in the pitching moment coefficient curve for the configuration with both a cove tab and a flap tab is approximately a linear combination of the changes caused by the individual tabs. The trends predicted by the computed results match those observed experimentally.

The pressure coefficient distribution on the main element and the flap at two different angles of attack can be used to understand the reduction in the slope of the lift coefficient curve with increasing angle of attack when a cove tab is added to the baseline configuration. Figure 61 shows the pressure coefficient distribution on the main element and the flap for the baseline configuration and a configuration with a cove tab included. Both experimental and computed results are shown for angles of attack of 0° and 8°. The data for an 8° angle of attack is plotted at the same scale as the data for a 0° angle of attack to facilitate comparisons between the two cases. The suction peak at the main element leading edge does not change when a cove tab is added to the baseline configuration, so the fact that the suction peak is clipped in the plot of the results at an angle of attack of 8° does not affect the comparison. The addition of the cove tab to the baseline configuration reduces the suction peak at the leading edge of the flap; however, the decrease is larger at an angle of attack of 8° than it is at an angle of attack of 0°. As mentioned previously, when the angle of attack of the airfoil is increased, the circulation about the main element increases. This causes a larger downwash velocity behind the trailing edge of the main element, which reduces the effective angle of attack of the flap. A consequence of the lower effective angle of attack for the flap is a reduction in the suction peak at the leading edge as angle of attack for the airfoil is increased. The suction peak at the flap leading edge is reduced by $\Delta C_p = 0.4$ for the baseline configuration and by $\Delta C_p = 0.5$ for the configuration with a cove tab. Adding a cove tab to the main element when the flap gap is small accentuates the reduction in the suction peak at the flap leading edge, which leads to a reduction in the slope of the lift coefficient curve as angle of attack is increased.

Increasing the flap gap of the baseline configuration with a 39° flap deflection angle to $z_g/c = 0.04$ causes the flow over a large percentage of the flap upper surface to be separated. This case is clearly a non-optimum baseline configuration, as can be seen by referring back to Figure 47 and looking at the lift coefficient curves for different flap gaps. The presence of a large region of separated flow over the upper surface of the flap greatly affects the effectiveness of the various lift-enhancing tabs, as can be seen in Figure 62. Adding a cove tab to the baseline configuration has a tremendous impact on the lift

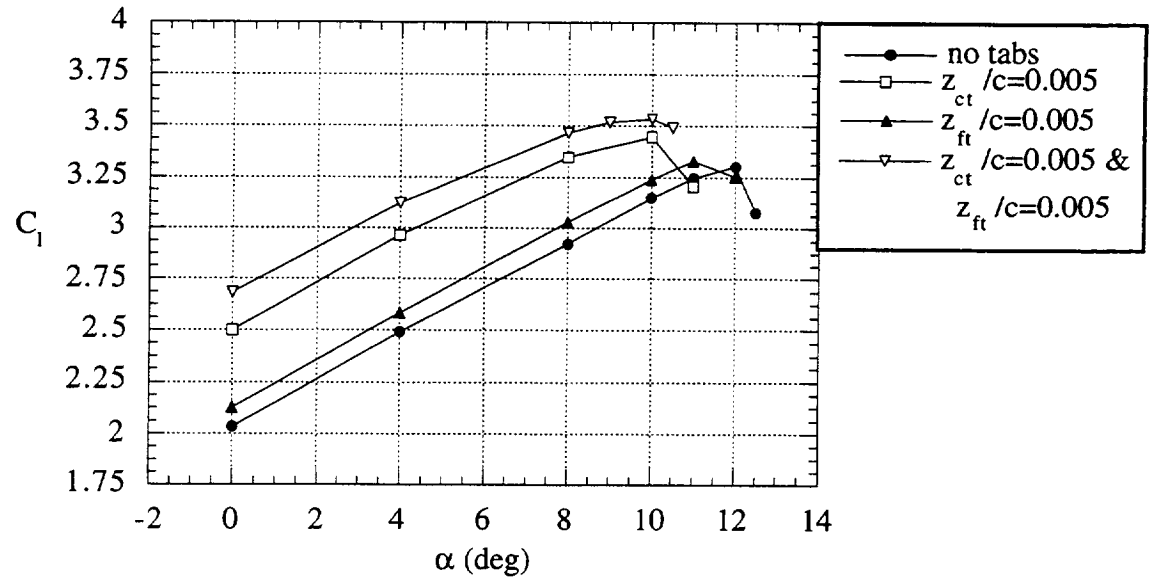

a) Effect of tabs on experimental lift coefficient.

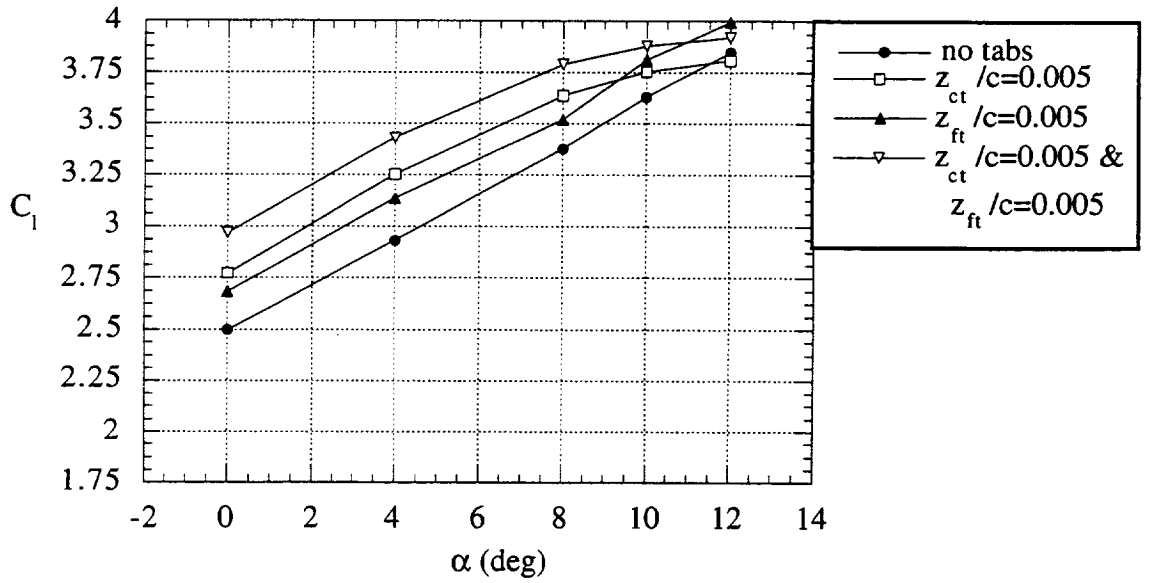

b) Effect of tabs on computed lift coefficient.

Figure 62: Effect of lift-enhancing tabs on the force and moment coefficients of a baseline configuration ($\delta_f = 39°$, INS2D $\delta_f = 36°$, $z_g/c = 0.04$, $x_{ol}/c = 0.015$).

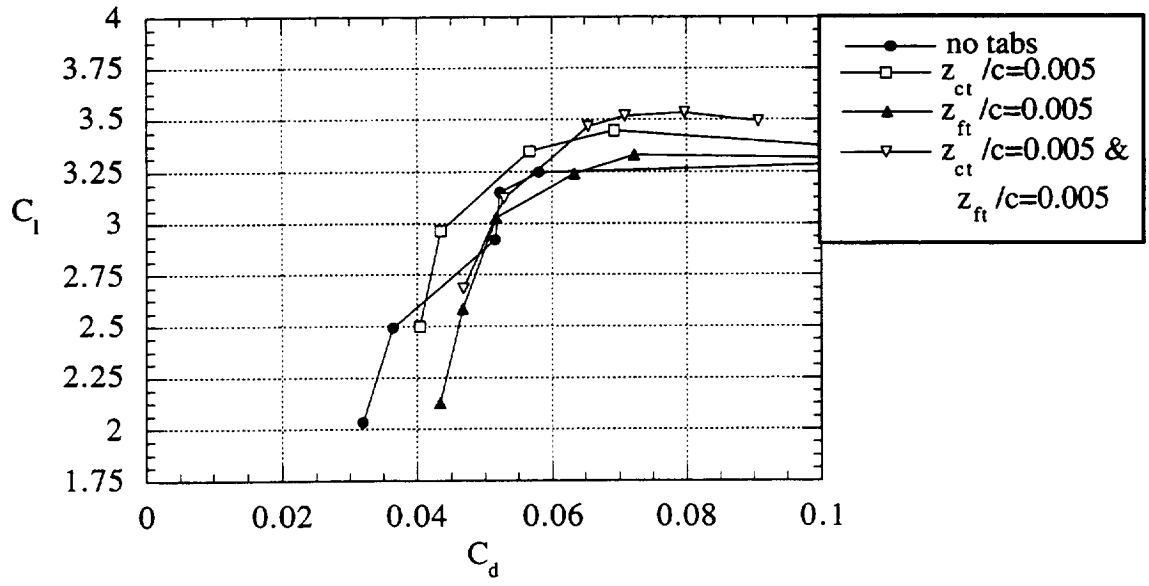

c) Effect of tabs on experimental drag coefficient.

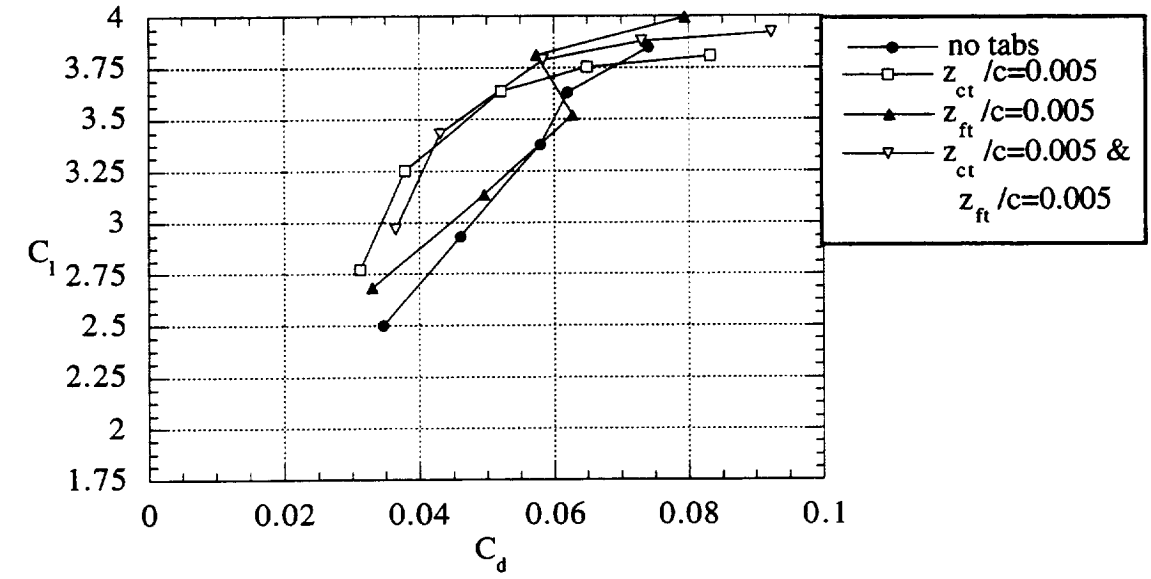

d) Effect of tabs on computed drag coefficient.

Figure 62 continued: Effect of lift-enhancing tabs on the force and moment coefficients of a baseline configuration ($\delta_f = 39°$, INS2D $\delta_f = 36°$, $z_g/c = 0.04$, $x_{ol}/c = 0.015$).

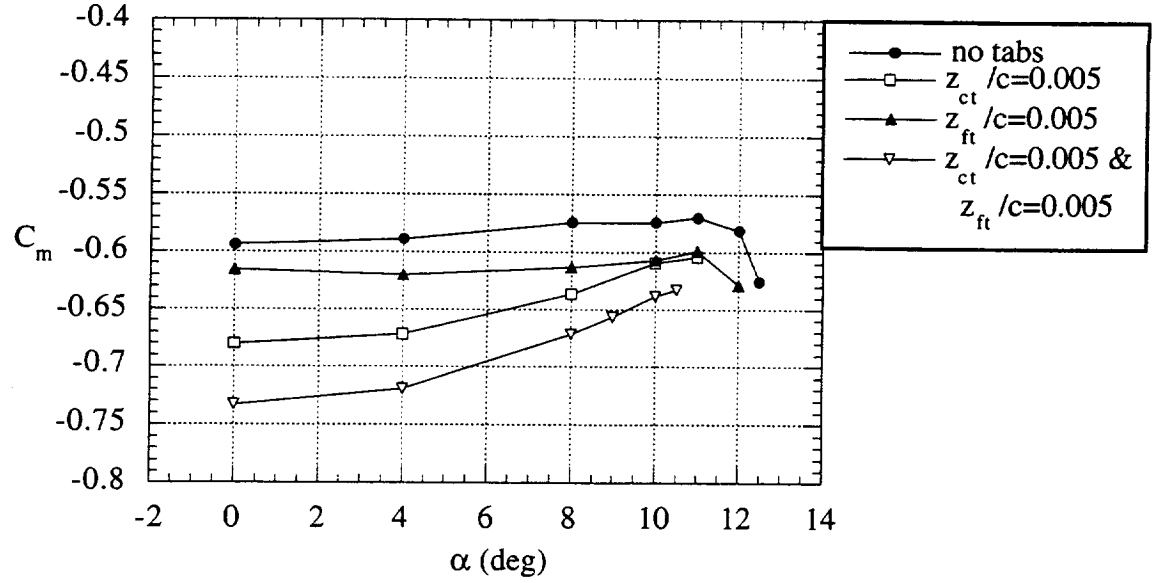

e) Effect of tabs on experimental pitching moment coefficient.

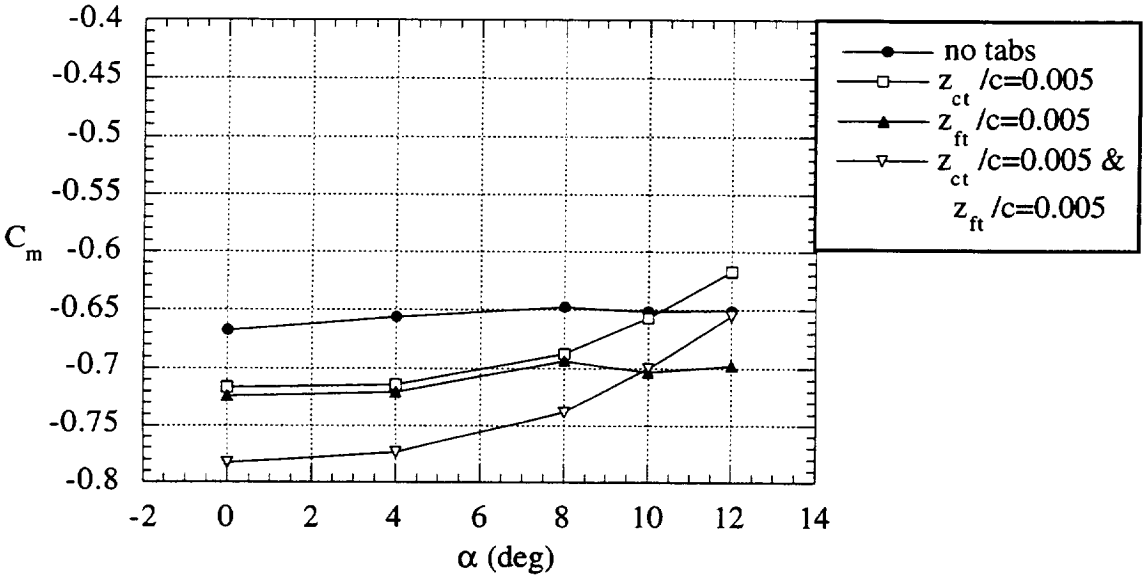

f) Effect of tabs on computed pitching moment coefficient.

Figure 62 concluded: Effect of lift-enhancing tabs on the force and moment coefficients of a baseline configuration ($\delta_f = 39°$, INS2D $\delta_f = 36°$, $z_g/c = 0.04$, $x_{ol}/c = 0.015$).

coefficient curve, shifting it upward by $\Delta C_l = 0.45$. The shift in the lift coefficient curve predicted by the computations is less, with $\Delta C_l = 0.30$. The flap tab is less effective at increasing lift coefficient for this configuration. The addition of a flap tab to the baseline configuration only shifts the lift coefficient curve upward by $\Delta C_l = 0.10$. The computed results for the flap tab configuration are more optimistic, predicting an upward shift of $\Delta C_l = 0.17$. Using a combination of a cove tab and a flap tab on the baseline configuration provides the largest upward shift of the lift coefficient curve. In this case the lift coefficient curve is shifted upward by $\Delta C_l = 0.65$. The computed results predict an upward shift of $\Delta C_l = 0.50$.

The effect of the tabs on the drag coefficient for this configuration is significantly different than what was presented previously for the other configurations. The drag coefficient for the configuration with a cove tab is lower by as much as 75 drag counts compared to the drag coefficient for the baseline configuration at the same lift coefficient. The computed results indicate an even larger reduction in drag coefficient when a cove tab is added to the baseline configuration. Adding a flap tab to the baseline case actually increases the drag coefficient by as much as 100 drag counts at moderate lift coefficients and has little effect on drag coefficient at high lift coefficients. The computed results indicate either a drag coefficient reduction or no change for all lift coefficients. The configuration with the combination of a cove tab and flap tab has the same drag coefficient as the baseline case when the two configurations are at the same lift coefficient. The computed results predict a drag coefficient for this case which is lower than that for the baseline configuration.

The effect on the pitching moment coefficient curve of adding a cove tab to the baseline configuration is a large shift of $\Delta C_m = 0.08$ in the negative direction. The slope of the pitching moment coefficient curve is also increased when a cove tab is added. The addition of a flap tab to the baseline case produces a smaller shift of $\Delta C_m = 0.02$ in the negative direction and the slope is not affected. The largest shift, $\Delta C_m = 0.13$, in the negative direction occurs for the configuration with both a cove tab and a flap tab. The slope of the pitching moment coefficient curve for this case is increased, similar to the configuration with just a cove tab. The computed results indicate similar trends, with the exception that the shift in the negative direction of the pitching moment coefficient curve for the configuration with only a flap tab is slightly greater than it is for the cove tab configuration instead of less, as observed experimentally.

To begin to explain the effects of the lift-enhancing tabs on the force and moment coefficient curves for this baseline configuration, the pressure coefficient distribution for the baseline case and the various tab configurations are compared. Figure 63 shows a

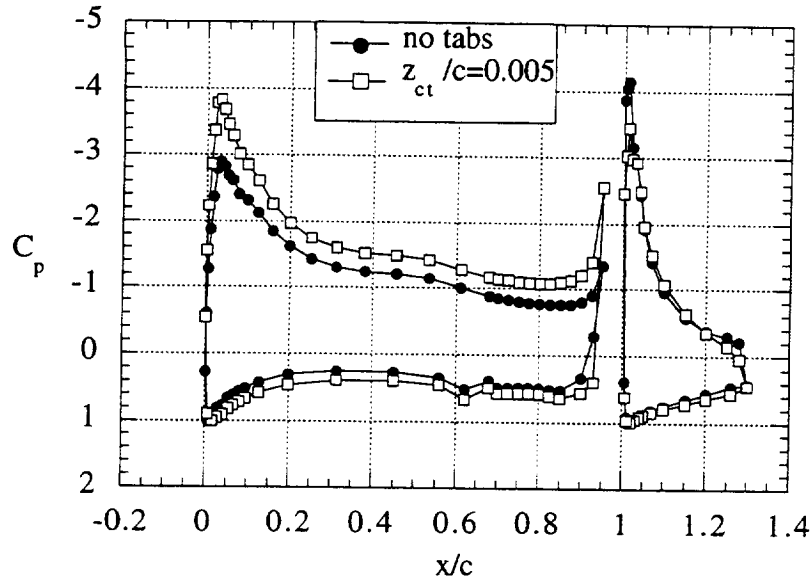

a) Experimental pressure coefficient distribution.

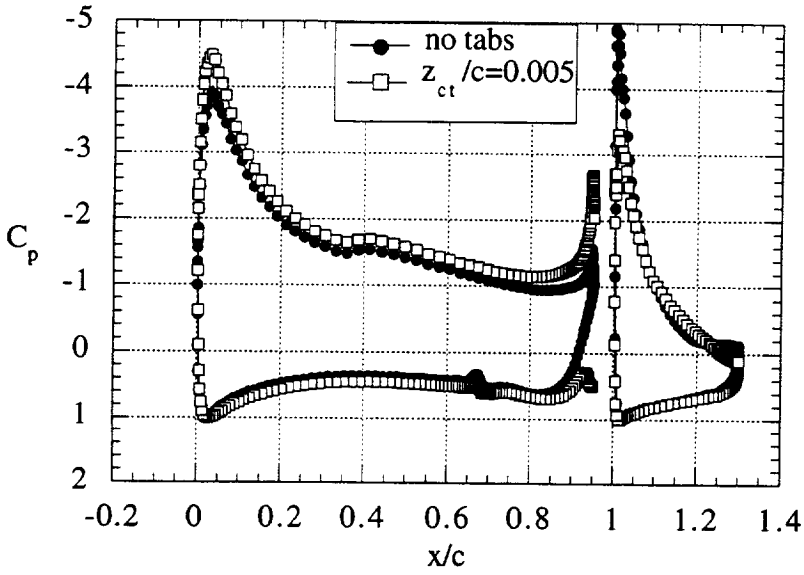

b) Computed pressure coefficient distribution .

Figure 63: Effect of a cove tab on the pressure coefficient distribution of a baseline configuration ($\delta_f = 39°$, INS2D $\delta_f = 36°$, $z_g/c = 0.04$, $x_{ol}/c = 0.015$, $\alpha = 0°$).

comparison of the experimental and computed pressure coefficient distributions on the main element and flap for the baseline case and a cove tab configuration. The angle of attack for the data is 0°. The reduction of the suction peak at the flap leading edge, characteristic of cove tab configurations, is evident. This reduction in suction peak appears to eliminate a region of separated flow on the upper surface of the flap that exists for the baseline configuration. The region of near constant pressure coefficient over the aft 30% of the flap upper surface, which is characteristic of a region of separated flow, is eliminated when a cove tab is added to the configuration. This change is easier to see in the computed results than it is in the experimental data. The reduction of the leading edge suction peak decreases the adverse pressure gradient which the turbulent boundary layer must traverse between the leading and trailing edges of the flap. The smaller adverse pressure gradient allows the boundary layer to remain attached, rather than separating. Note that the reduction in the leading edge suction peak on the flap is much greater in the computed results than it is in the experimental results. This is probably due to differences in the experimental and computed flow separation locations on the baseline configuration. The magnitude of the suction peak on the flap leading edge for the cove tab configuration is well predicted by the computed results. Computed streamlines over the flap for the baseline and cove tab configurations, illustrated in Figures 64a and 64b respectively, show graphically how the cove tab eliminates the separated flow over the flap upper surface.

Returning to Figure 63, it is evident that the majority of the increase in lift coefficient caused by adding a cove tab to the configuration is due to the increase in circulation about the main element. The computed results predict less of an increase in circulation about the main element when the cove tab is added. Again, this can be attributed to differences in the experimental and computed flow separation locations for the baseline configuration. Part of the large increase in circulation about the main element is due to the fact that the cove tab is more effective at increasing the circulation about the main element when the flap gap is large, as was seen earlier (see Figure 54). In addition, the elimination of the flow separation over the flap upper surface also increases the circulation about the main element. The amount of circulation that the flap induces on the main element, for a given flap angle and position, is a function of both the total lift or circulation acting on the flap and the distribution of the lift on the flap. Flow separation on the flap upper surface can change the total lift acting on the flap, the distribution of lift on the flap, or both. The total lift acting on the flap is generally reduced and the center of lift on the flap moves aft when large regions of separated flow exist over the flap upper surface. The effective shape of the flap becomes a bluff body comprised of the actual flap plus the recirculation bubble in the separated flow region. These changes reduce the effectiveness of the flap. Adding a

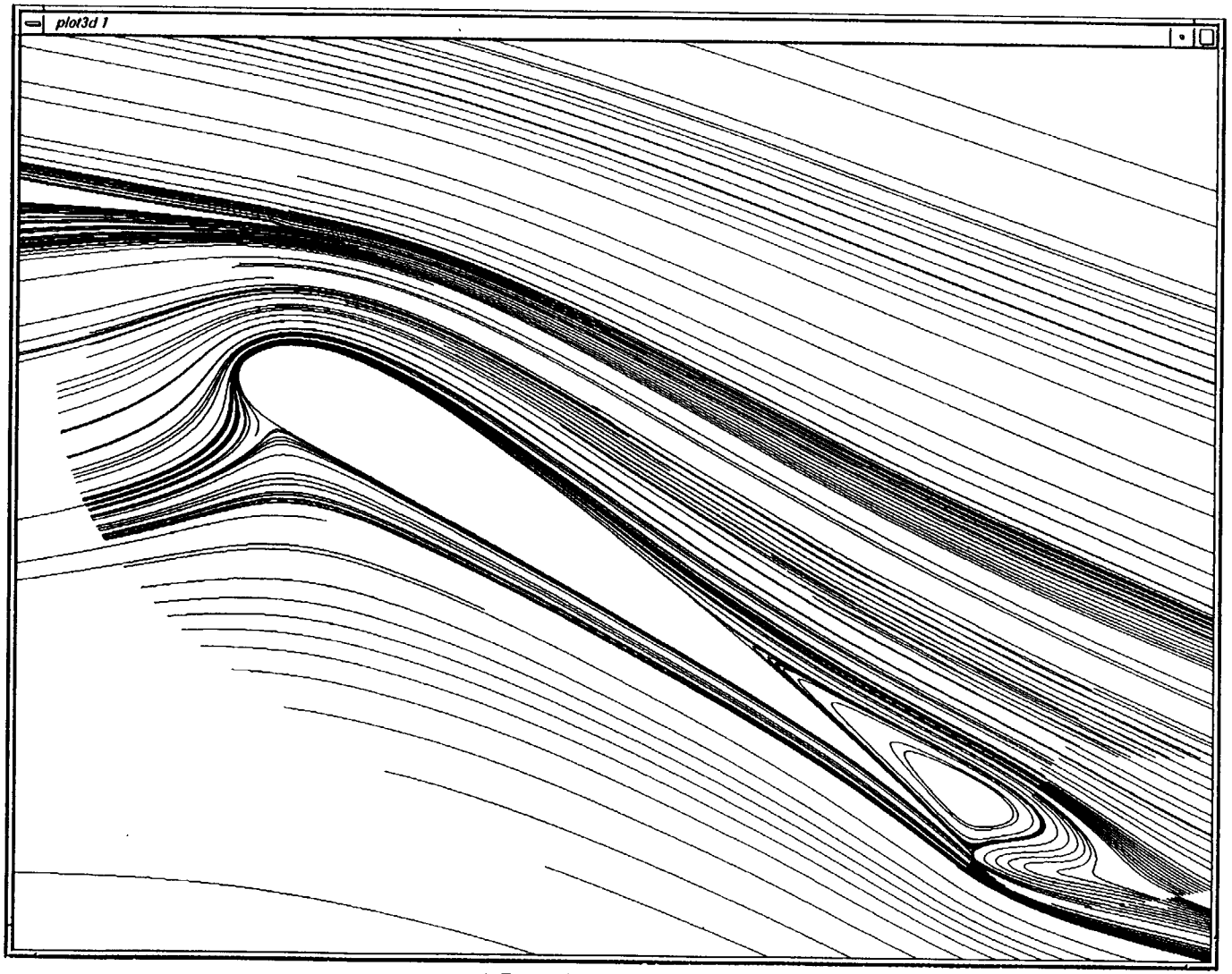

a) Baseline configuration.

Figure 64: Streamline pattern around flap for a configuration with a 39° flap deflection angle, as computed using INS2D-UP.

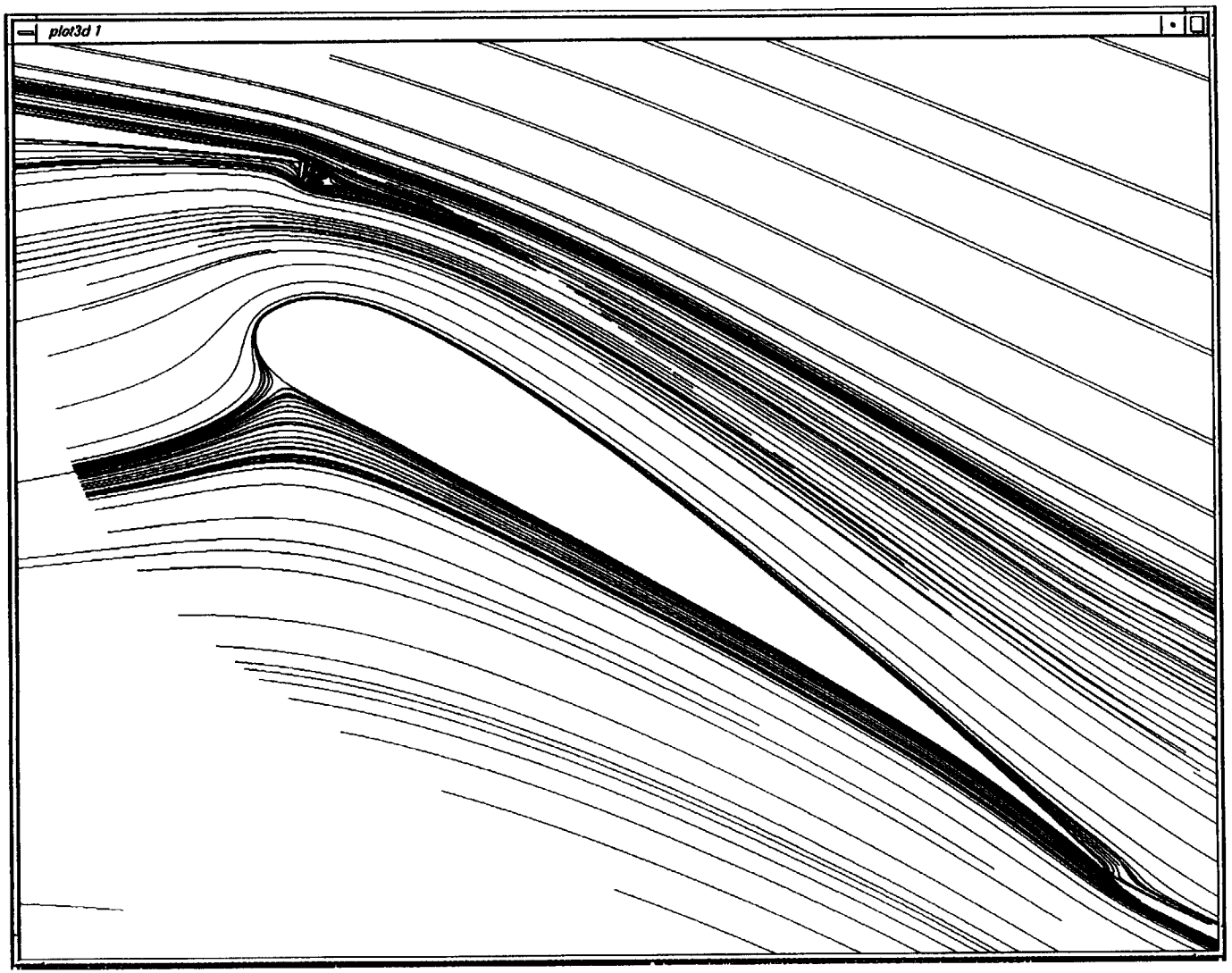

b) Configuration with cove tab.

Figure 64, concluded: Streamline pattern around flap for a configuration with a 39° flap deflection angle, as computed using INS2D-UP.

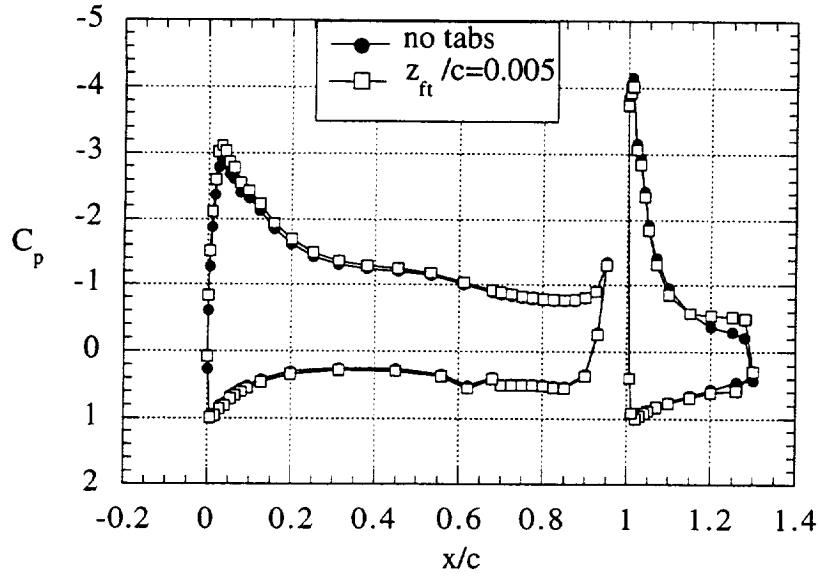

a) Experimental pressure coefficient distribution at $\alpha = 0°$.

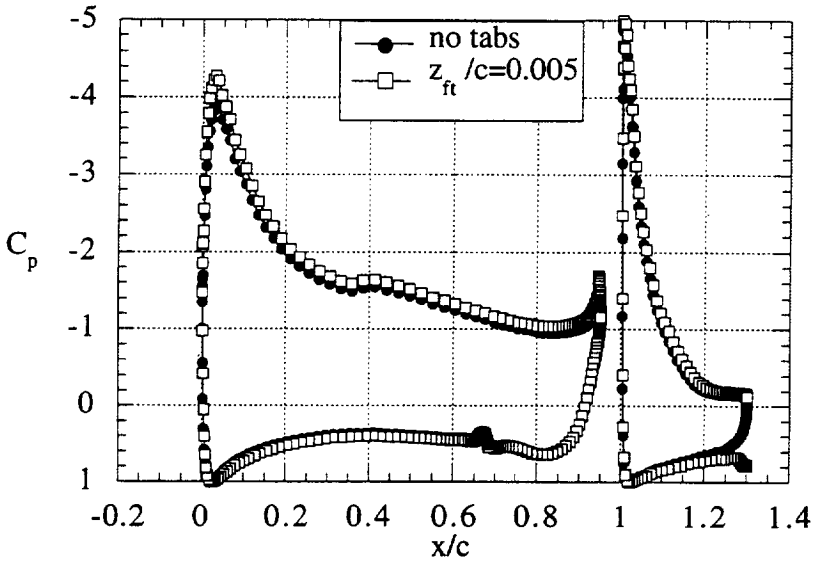

b) Computed pressure coefficient distribution at $\alpha = 0°$.

Figure 65: Effect of a flap tab on the pressure coefficient distribution of a baseline configuration ($\delta_f = 39°$, INS2D $\delta_f = 36°$, $z_g/c = 0.04$, $x_{ol}/c = 0.015$, $\alpha = 0°$).

cove tab to the configuration can eliminate the flow separation over the flap upper surface and improve the performance of the flap. The elimination of the separated flow region over the flap also accounts for the reduction in drag observed in Figure 62 for the cove tab configuration.

Figure 65 shows a comparison of the pressure coefficient distributions on the main element and flap for the baseline case and a flap tab configuration. Both experimental and computed results are presented. Looking at the experimental pressure coefficient distribution on the flap, it appears that the flap tab causes the separated flow region that exists for the baseline configuration to become worse. This observation is consistent with the increase in drag coefficient seen in Figure 62 for the flap tab configuration at moderate lift coefficients. There is an increase in the loading on the aft portion of the flap and the circulation about the flap is increased slightly. The circulation about the main element is also increased slightly when the flap tab is added to the configuration. Insufficient experimental data is available to ascertain why the separated flow region over the flap grew worse when the flap tab was added. The computed results indicate a small increase in the circulation about both the main element and the flap. The separated flow region over the flap is reduced slightly when a flap tab is added, according to the computed data. This is consistent with the reduction in the computed drag coefficient seen in Figure 62 for the flap tab configuration.

A comparison of the pressure coefficient distributions for the baseline case and the configuration with both a cove tab and a flap tab is shown in Figure 66. The angle of attack is 0° and both experimental and computed results are included. The suction peak at the flap leading edge is reduced and the region of separated flow over the flap upper surface, present in the baseline case, is eliminated. The loading on the aft portion of the flap is increased, as is the overall circulation of the flap. The elimination of the separated flow and the increase in the circulation about the flap combine to create a large increase in circulation about the main element. The majority of the increase in lift coefficient of the airfoil, which occurs when the cove tab and flap tab are added to the configuration, is due to the increase in circulation about the main element. The computed results indicate the same types of trends as the experimental data. The increase in circulation about the main element resulting from the addition of the tabs is less than was observed experimentally. This is due primarily to the difference in experimental and computed flow separation locations on the flap upper surface for the baseline configuration. The computed separation location appears to occur further aft on the flap than the experimental data indicates.

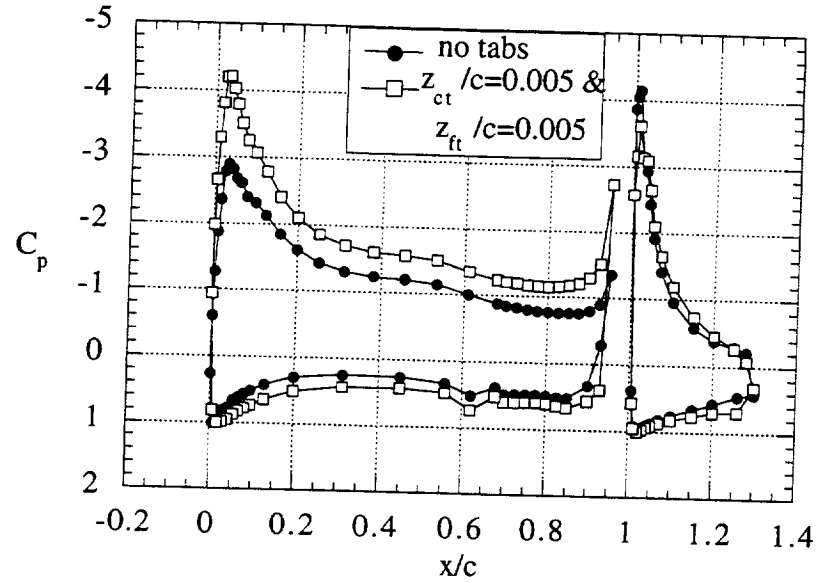

a) Experimental pressure coefficient distribution.

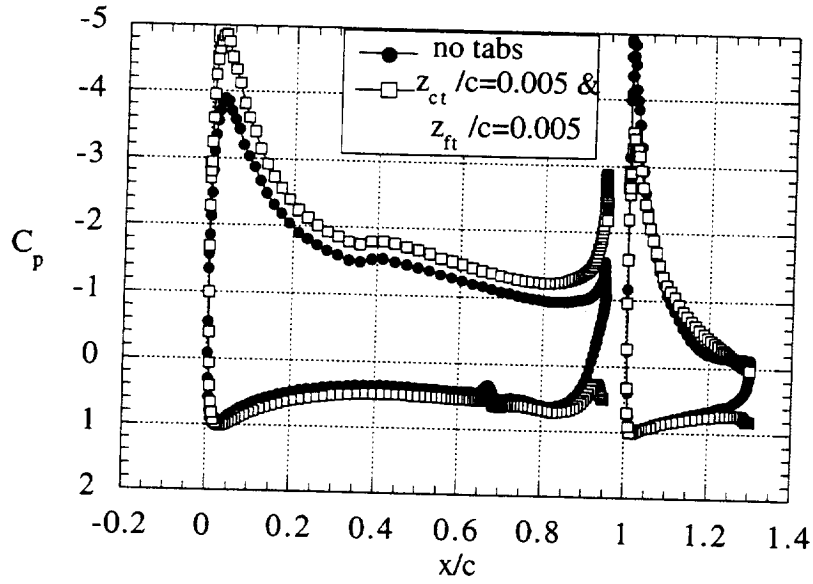

b) Computed pressure coefficient distribution.

Figure 66: Effect of a cove tab and flap tab combination on the pressure coefficient distribution of a baseline configuration ($\delta_f = 39°$, INS2D $\delta_f = 36°$, $x_g/c = 0.04$, $x_{ol}/c = 0.015$, $\alpha = 0°$).

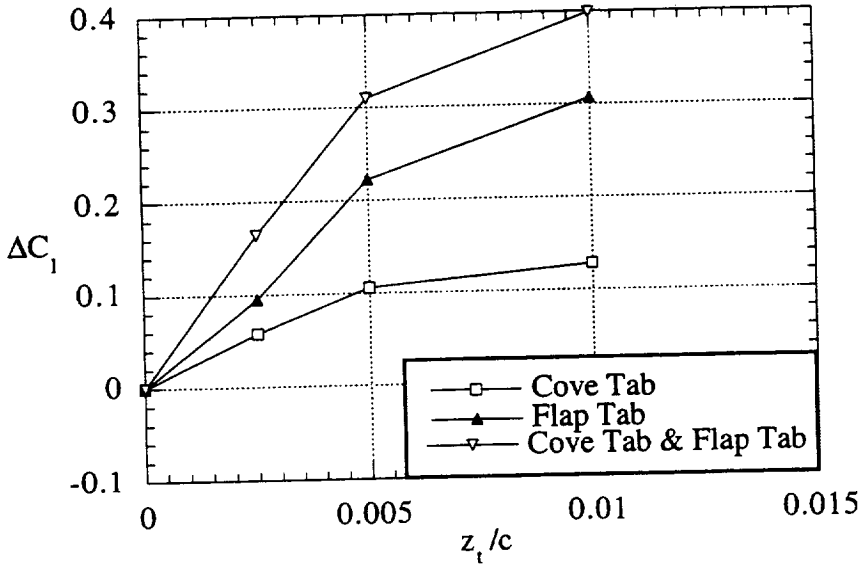

a) $\delta_f = 29°$, $z_g/c = 0.05$.

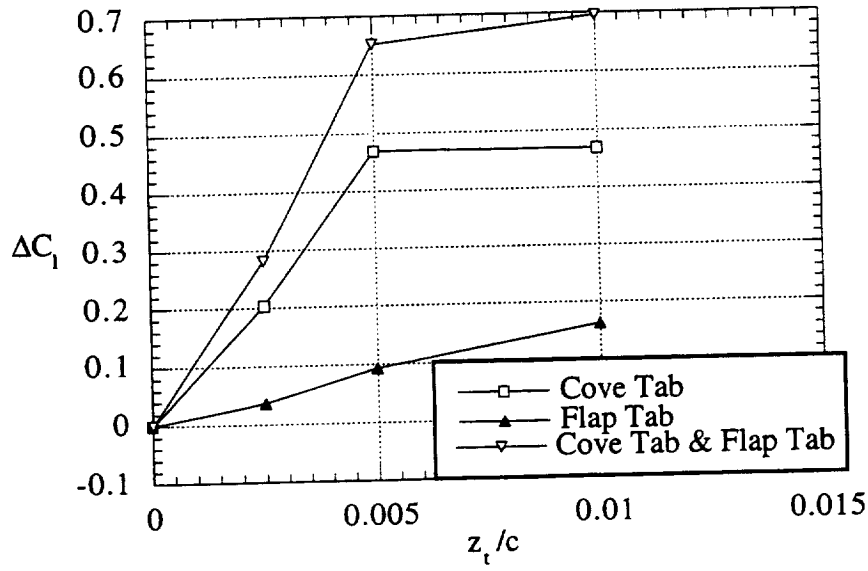

b) $\delta_f = 39°$, $z_g/c = 0.04$.

Figure 67: Effect of tab height on lift coefficient increment for two different flap deflection angles.

Overall Performance of Lift-Enhancing Tabs

All the results presented to this point have been for tabs with a height of $zt/c = 0.005$. Figure 67 shows the effect of varying tab height on the change in lift coefficient relative to the baseline case for configurations with flap deflection angles of 29° and 39°. Experimental results for three different tab configurations are presented at an angle of attack of 0°. The three configurations are cove tab only, flap tab only, and cove tab and flap tab together. It should be noted again that for configurations with a cove tab and a flap tab, the tabs were of the same height. Computations were not performed for tab heights other than $zt/c = 0.005$; hence, computed results are not included in Figure 67. For configurations with a flap deflection angle of 29°, all three tab configurations produce a nonlinear increase in lift coefficient as tab height is increased. The increase in lift coefficient caused by the cove tab appears to be reaching an asymptotic value of $\Delta C_l = 0.13$ at a tab height of $z_{ct}/c = 0.01$. The change in lift coefficient for configurations with a flap tab only and a combination of cove tab and flap tab is still rising at a tab height of $z_t/c = 0.01$. The configuration with a combination of cove tab and flap tab produces the largest increases in lift coefficient, with a $\Delta C_l = 0.4$ at a tab height of $z_t/c = 0.01$.

For configurations with a flap deflection angle of 39° and a flap gap of $z_g/c = 0.04$, the flap tab is the least effective configuration for increasing the lift coefficient. The flap tab produces a nearly linear increase in lift coefficient with increasing tab height. At a flap tab height of $z_{ft}/c = 0.01$ the change in lift coefficient is $\Delta C_l = 0.17$. By contrast, on a configuration with a flap deflection angle of 29°, the flap tab produces a change in lift coefficient of $\Delta C_l = 0.31$ for a flap tab height of $z_{ft}/c = 0.01$. The reason for the reduced performance of the flap tab at a flap deflection angle of 39° is the presence of a separated flow region over the flap upper surface. The cove tab, on the other hand, produces large increases in lift coefficient for this configuration. The increase in lift coefficient caused by the cove tab has reached an asymptotic value of $\Delta C_l = 0.47$ at a cove tab height of $z_{ct}/c = 0.005$. Again, the configuration with a combination of cove tab and flap tab produces the largest increase in lift coefficient at a given tab height. The change in lift coefficient appears to be reaching an asymptotic value of $\Delta C_l = 0.70$ at a tab height of $z_t/c = 0.01$. It is possible that if the cove tab height were held constant at $z_{ct}/c = 0.005$ while the flap tab height was increased, further increases in lift coefficient could be obtained; however, this was not investigated.

An interesting benefit of using cove tabs on a multi-element airfoil is that they reduce the sensitivity of the lift of the multi-element airfoil to the size of the flap gap. This is illustrated in Figure 68. Lift coefficient for a configuration with a cove tab is plotted as a function of angle of attack for several different flap gap sizes. A plot of the lift coefficient

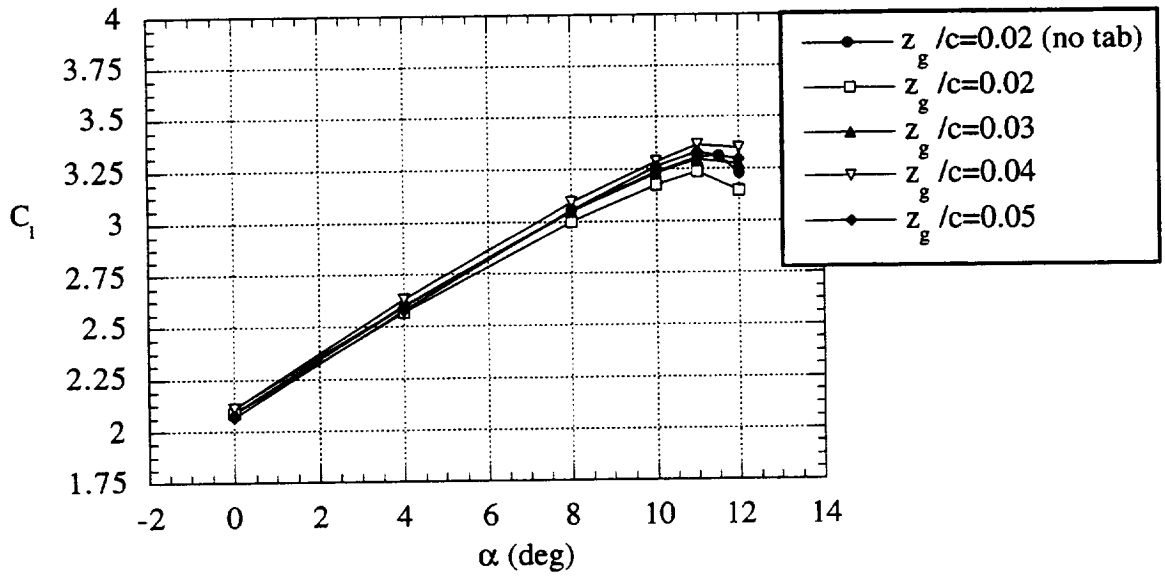

a) $\delta_f = 29°$, $z_{ct}/c = 0.005$.

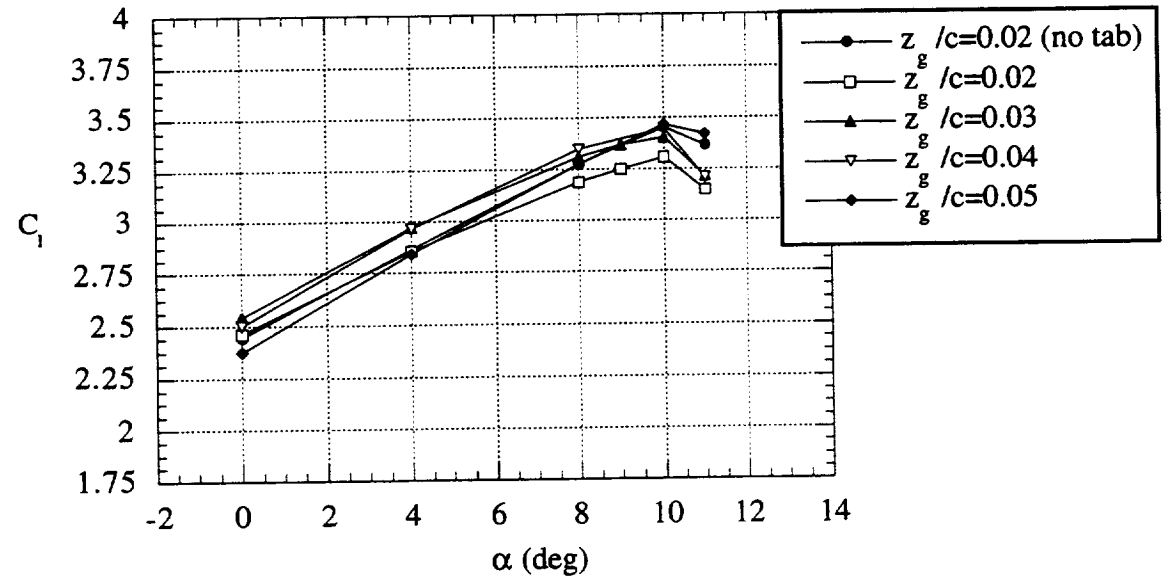

a) $\delta_f = 39°$, $z_{ct}/c = 0.005$.

Figure 68: Effect of flap gap variations on configurations with a cove tab.

curve for the baseline configuration is included for reference. Results are shown for both a configuration with a 29° flap deflection angle and a configuration with a 39° flap deflection angle. All of the data presented in Figure 68 are experimental results. At both flap deflection angles, the lift coefficient curves for the configurations with a cove tab are coincident with or shifted upward slightly from the reference baseline lift coefficient curve. The only exception to this is the cove tab configuration with a flap gap of $z_g/c = 0.02$. For this configuration the lift coefficient curve is coincident with the baseline lift coefficient curve at low angles of attack. The slope of the lift coefficient curve for this configuration, however, is less than that of the baseline curve, leading to lower lift coefficients than the baseline case at higher angles of attack. Comparing Figure 68 with the experimental results shown in Figures 45 and 47, it is evident that adding a cove tab to the baseline configuration has reduced the sensitivity to flap gap. This is particularly true for the configuration with a 39° flap deflection angle. The lift coefficient for the baseline configuration drops off rapidly as the flap gap is increased (Figure 47) due to flow separation over the upper surface of the flap. Adding a cove tab to the configuration eliminates the flow separation, as shown previously, and greatly reduces the sensitivity to the size of the flap gap.

Performance of the baseline configuration that produced the highest lift coefficients was compared with performance of the three tab configurations (cove tab only, flap tab only, and cove tab and flap tab combination) which produced the highest lift coefficients. Only the experimental data is considered in this comparison since the computed results for a flap deflection angle of 39° did not consistently predict the separation location on the flap upper surface accurately. Figure 69a shows the comparison of the lift coefficient versus angle of attack curves for the various configurations. The configuration with a cove tab of height $z_{ct}/c = 0.005$ has a lift coefficient curve that is shifted up by $\Delta C_l = 0.11$ relative to the baseline configuration lift coefficient curve. The configuration with a flap tab of height $z_{ft}/c = 0.005$ has a lift coefficient curve that is shifted up by $\Delta C_l = 0.16$ relative to the baseline configuration lift coefficient curve. The configuration with a combination of a cove tab and flap tab has the best performance of the four configurations. The lift coefficient curve for this configuration is shifted up by $\Delta C_l = 0.27$ relative to the baseline configuration lift coefficient curve. This represents an 11% increase in lift coefficient at 0° angle of attack. C_{lmax} occurs at the same angle of attack for all of the configurations. C_{lmax} for the configuration with a cove tab of height $z_{ct}/c = 0.005$ is the same as for the baseline configuration. C_{lmax} for the other two configurations is increased by 0.09 relative to the baseline configuration.

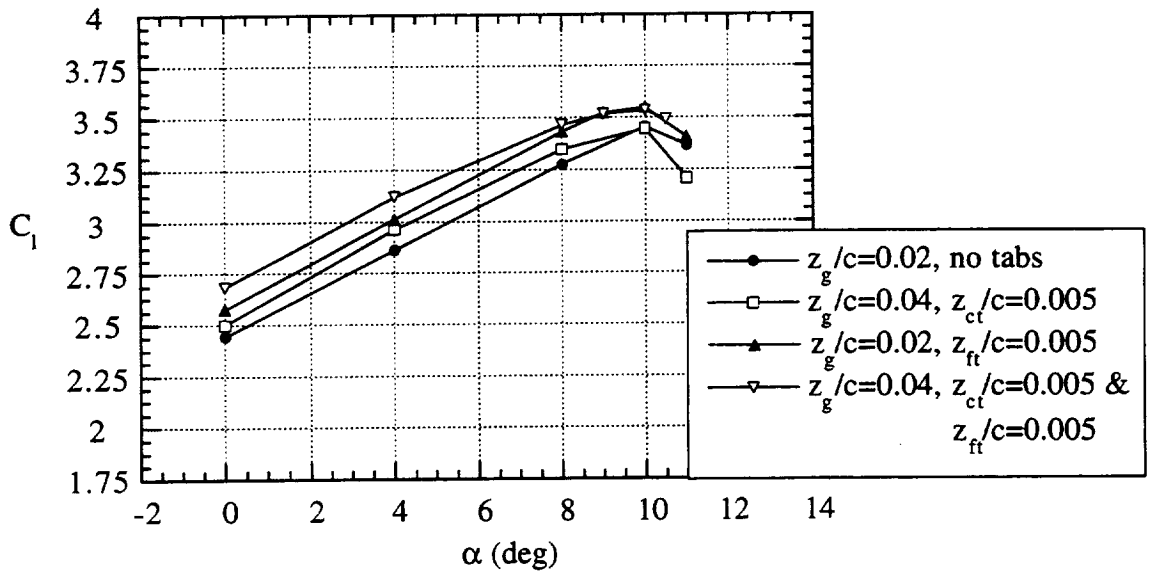

a) Lift coefficient.

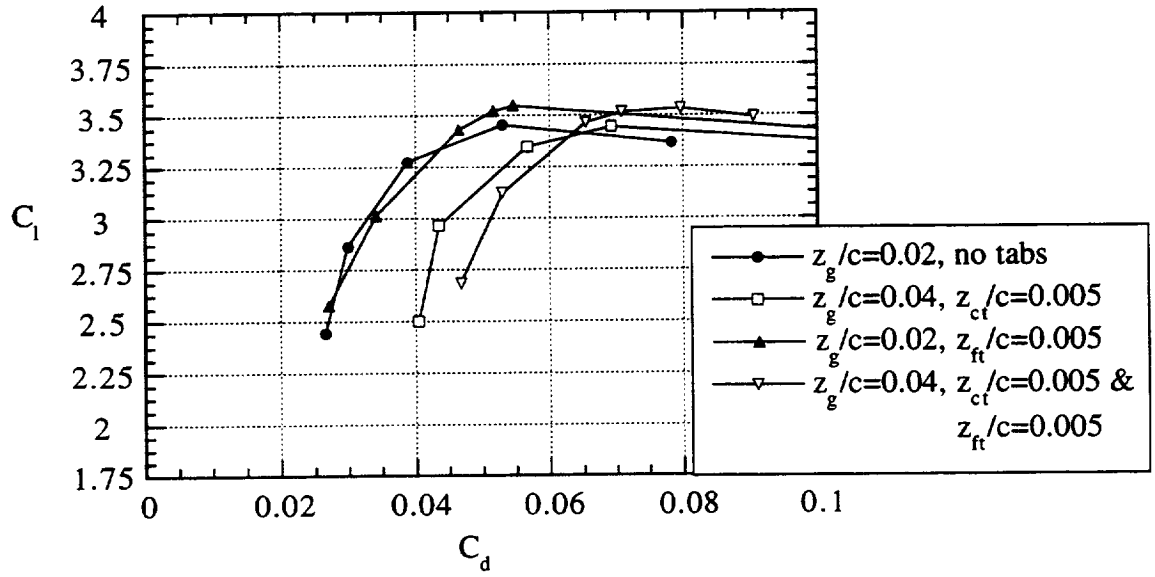

b) Drag coefficient.

Figure 69: Comparison of the force and moment coefficients for the optimum tab configurations with those for the optimum baseline configuration. (δ_f = 39°, x_{ol}/c = 0.015)

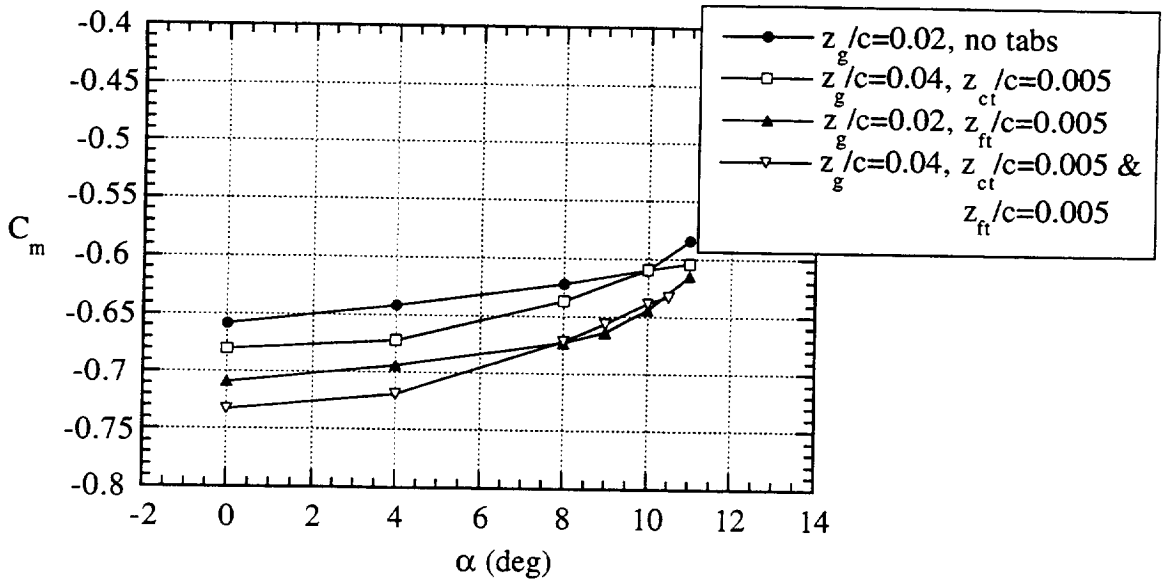

c) Pitching moment coefficient.

Figure 69 concluded: Comparison of the force and moment coefficients for the optimum tab configurations with those for the optimum baseline configuration.
($\delta_f = 39°$, $x_{ol}/c = 0.015$)

Figure 69b shows the comparison of the lift coefficient versus the drag coefficient curves for the various configurations. The flap tab configuration has essentially the same drag as the baseline configuration at a given lift coefficient. The drag coefficient for the cove tab configuration is greater than that for the baseline configuration by as much as 130 drag counts at the same lift coefficient. The drag coefficient for the configuration with both a cove tab and a flap tab is nearly double the drag coefficient of the baseline configuration at the same lift coefficient.

The pitching moment coefficient versus angle of attack curves for the various configurations are compared in Figure 69c. The configuration with a cove tab has a pitching moment coefficient curve that is shifted in the negative direction by $\Delta C_m = 0.02$ relative to the baseline pitching moment coefficient curve. The pitching moment coefficient curve of the configuration with a flap tab is shifted in the negative direction by $\Delta C_m = 0.05$ relative to the baseline pitching moment coefficient curve. The configuration with both a cove tab and a flap tab has a pitching moment coefficient curve that is shifted in the negative direction by $\Delta C_m = 0.07$ relative to the baseline pitching moment coefficient curve. All three configurations with tabs have pitching moment coefficient curves with a larger

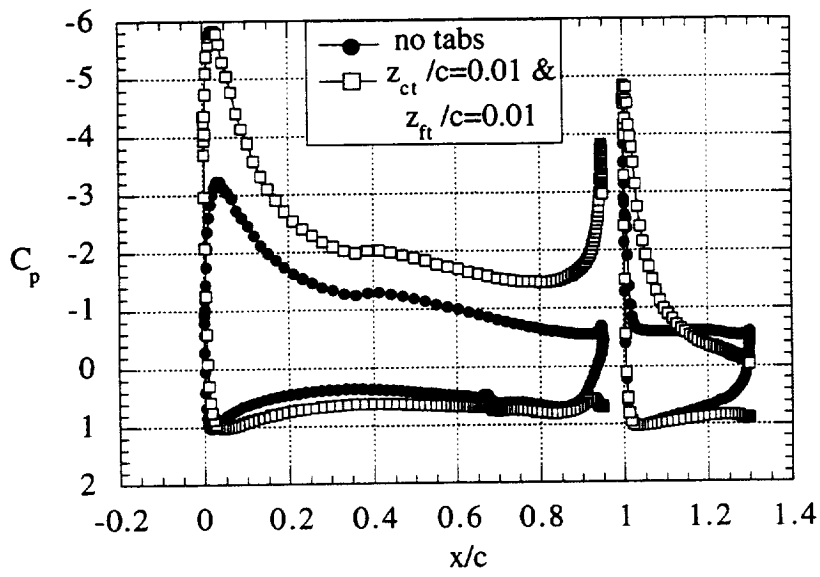

Figure 70: Effect of a cove tab and flap tab combination on the pressure coefficient distribution of a baseline configuration with a large flap deflection angle ($\delta_f = 50°$, $x_g/c = 0.04$, $x_{ol}/c = 0.015$).

positive slope as angle of attack increases, compared to the baseline pitching moment coefficient curve.

The results shown in Figure 64 suggest that the maximum flap deflection angle for a multi-element airfoil can be increased by adding a cove tab to the configuration. The maximum flap deflection angle is normally defined as the largest angle at which a flap gap can be found that keeps the flow over the upper surface of the flap attached. To investigate whether or not a cove tab will permit a larger maximum flap deflection angle, the flow over a configuration with a 50° flap deflection angle was computed using INS2D-UP. This flap deflection angle is about 10° larger than the maximum flap deflection angle for the baseline configuration. The flap gap was set at $z_g/c = 0.04$ since results presented earlier indicate that cove tabs function more efficiently at a larger flap gap. The angle of attack for the computation was 0°. Computed results were obtained for both a baseline configuration and a configuration with both a cove tab and a flap tab. The height of the tabs was $z_t/c = 0.01$. The flap tab was included since Figure 69 indicates that a configuration with both a cove tab and a flap tab produces the largest increase in lift coefficient relative to the best baseline configuration.

The computed pressure coefficient distributions for the baseline and tab configurations are shown in Figure 70. The pressure coefficient distribution on the flap of

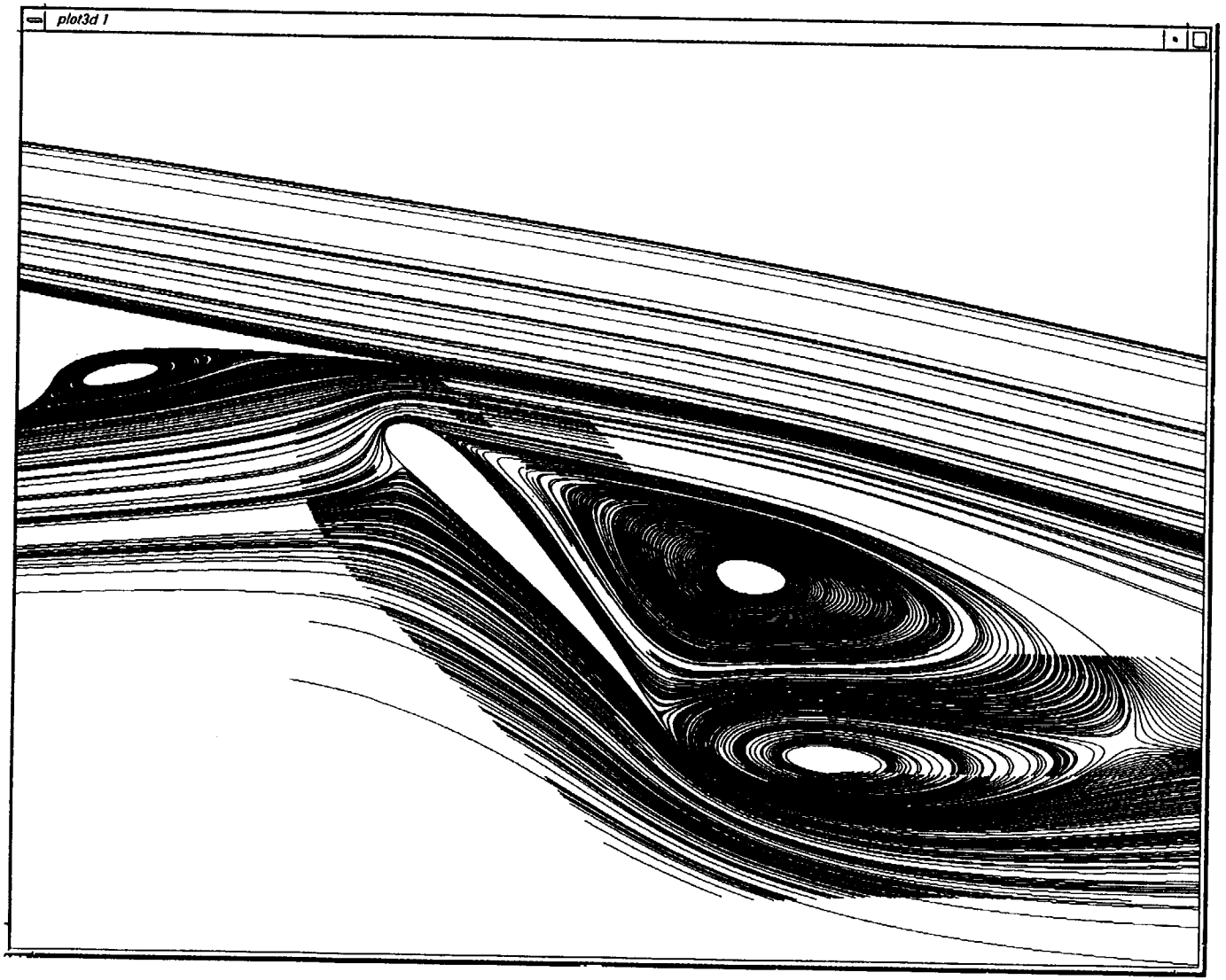

a) Baseline configuration.

Figure 71: Streamline pattern around flap for a configuration with a 50° flap deflection angle, as computed using INS2D-UP.

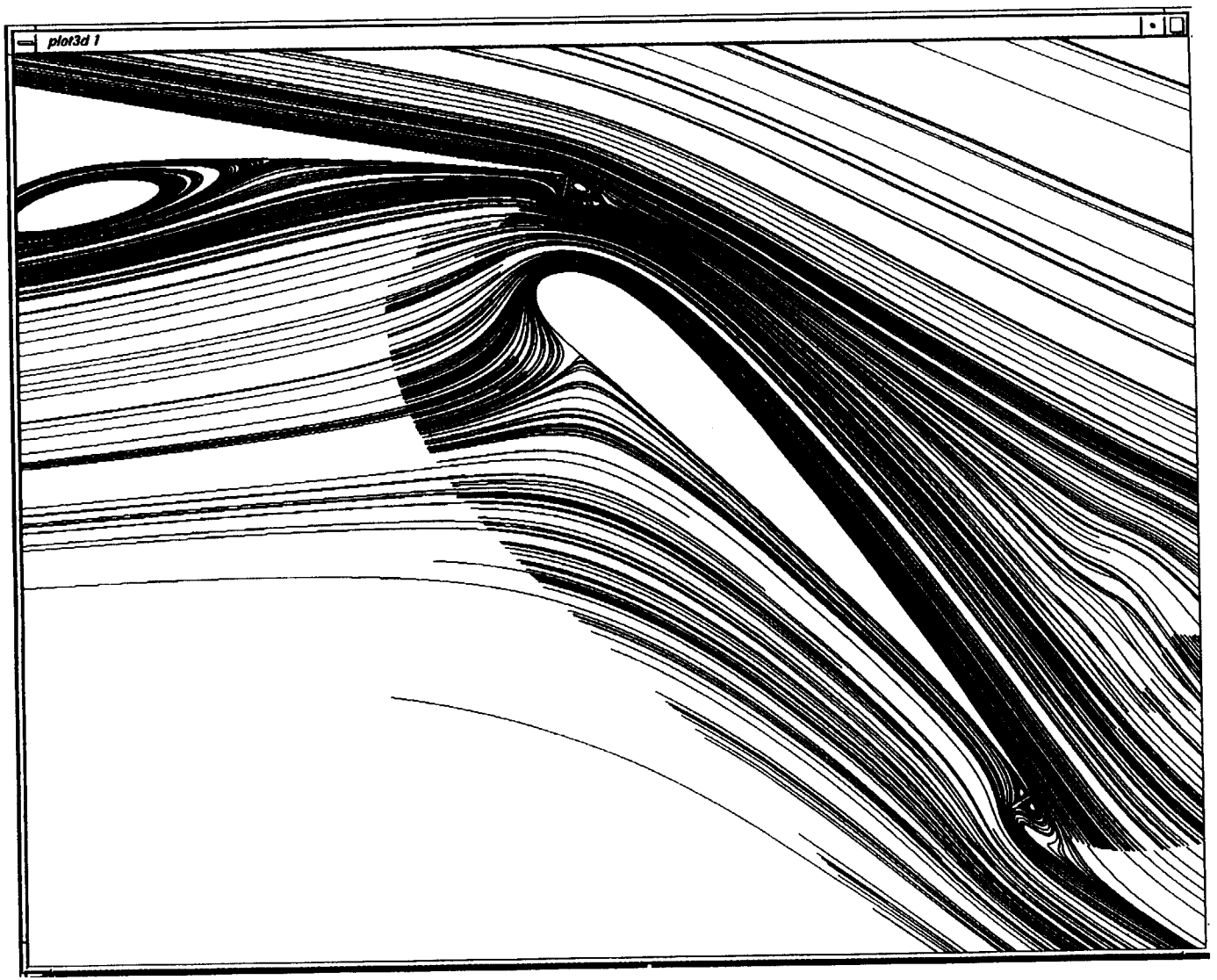

b) Configuration with cove tab and flap tab.

Figure 71, concluded: Streamline pattern around flap for a configuration with a 50° flap deflection angle, as computed using INS2D-UP.

the baseline configuration indicates that separated flow exists over the entire upper surface of the flap. When the cove tab and flap tab are added to the configuration, the separated flow is eliminated, increasing the lift on the flap, which in turn produces a tremendous increase in lift on the main element. The lift coefficient for the baseline configuration is $C_l = 2.050$. The lift coefficient for the configuration with tabs is increased to $C_l = 3.328$. By comparison, the highest computed lift coefficient obtained for a configuration with tabs and a 39° flap deflection angle at an angle of attack of 0° was 2.98 (see Figure 62). The drag coefficient is reduced from $C_d = 0.1335$ to $C_d = 0.0855$ when tabs are added to the configuration. The reduction in drag is a result of the elimination of the separated flow over the flap.

The computed streamlines shown in Figure 71 provide a graphic illustration of how lift-enhancing tabs affect the flow for a configuration with a very large flap deflection angle. The streamlines for the baseline configuration, shown in Figure 71a, confirm the existence of a large region of separated flow over the upper surface of the flap. When the lift-enhancing tabs are added to the configuration, the separated flow region is eliminated, as shown in Figure 71b. Note that there is a local distortion of the streamlines in the wake of the main element near the flap trailing edge in Figure 71b. As the main element wake traverses the adverse pressure gradient over the upper surface of the flap, the velocity deficit in the wake gets very large, forcing the velocity at the center of the wake to be nearly zero. This causes the streamlines above the flap near the flap trailing edge to "wander" slightly due to the extremely small components of velocity. The flow never actually reverses, however, as was predicted by the computations of Carrannanto [12] (see Figure 7). The results shown in Figures 70 and 71 indicate that lift-enhancing tabs can be used to increase the maximum flap deflection angle of a multi-element airfoil.

Qualitative Model for Lift-Enhancing Tabs

A great deal of experimental and computed data has been presented illustrating the effect of lift-enhancing tabs on a multi-element airfoil. A simple analytic model will now be developed which will provide a mathematical basis for understanding how lift-enhancing tabs affect a multi-element airfoil. The goal in developing this model is to gain insight into what parameters are important in determining the performance of the tabs. The model should be kept as simple as possible, yet it should capture all the dominant effects of the tabs on the airfoil. No attempt is being made to create a model which accurately predicts the actual performance of tabs on any multi-element airfoil at any condition. It has already been shown that even a full two-dimensional Reynolds-averaged incompressible Navier-Stokes code has difficulties in accurately predicting the performance of tabs on a

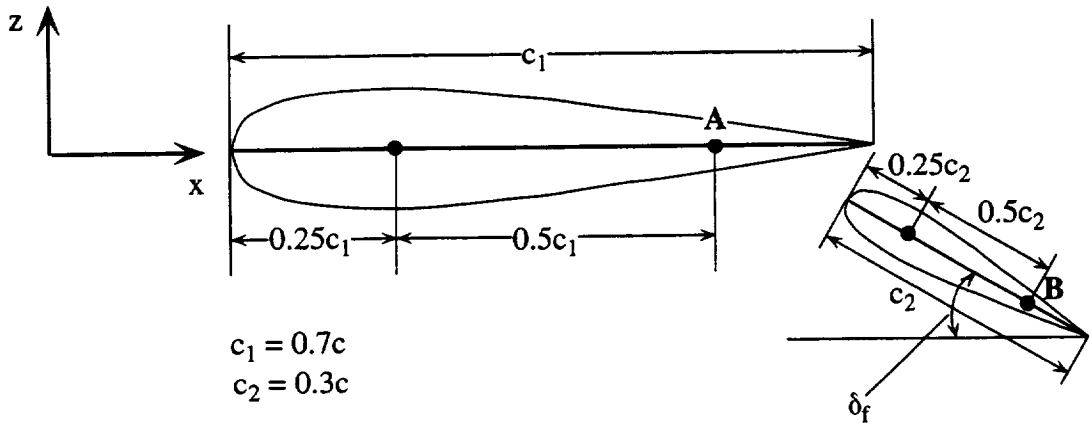

a) Dimensions for model of two-element airfoil.

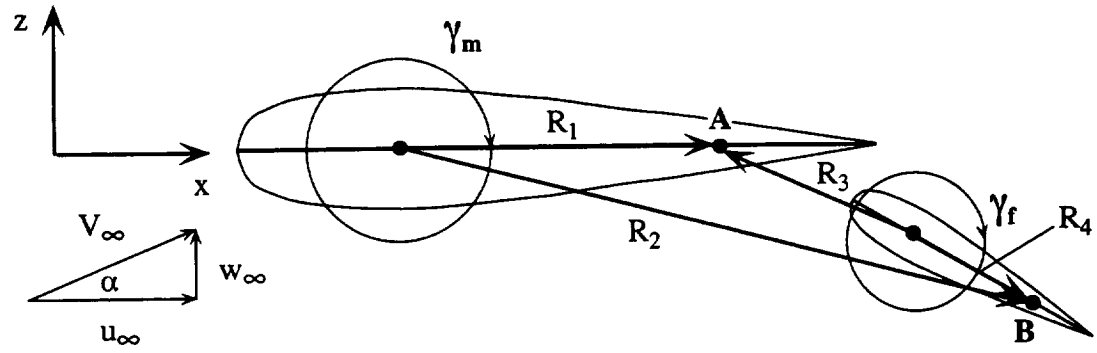

b) Nomenclature for point vortices representing main element and flap.

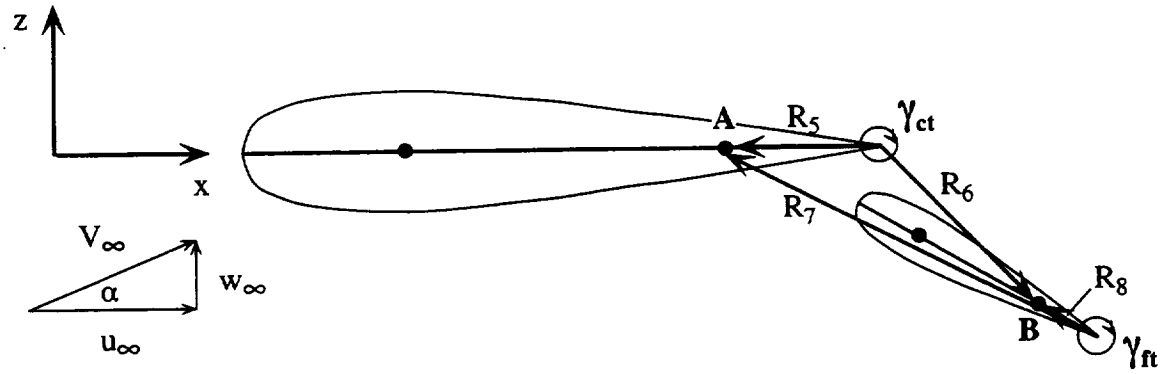

c) Nomenclature for point vortices representing cove tab and flap tab.

Figure 72: Simplified model for qualitatively assessing influence of lift-enhancing tabs on a multi-element airfoil.

multi-element airfoil in some cases, such as when large regions of separated flow exist over the flap. However, using tools such as a two-dimensional Navier-Stokes code in conjunction with simple models to determine how tabs function and what parameters affect their performance will give designers a better understanding of how to best incorporate lift-enhancing tabs into multi-element design.

The simple analytic model proposed as a vehicle for understanding how lift-enhancing tabs affect the performance of a multi-element airfoil is shown in Figure 72. The two-element airfoil is represented by two symmetric airfoils. The main element has a chord length of c_1 and the flap has a chord length of c_2. The flap airfoil is deflected to a flap deflection angle δ_f relative to the main element. The flow over this two-element airfoil is assumed to be potential flow. This means all viscous effects are neglected. The flow is also assumed to be incompressible and two-dimensional. The two-element airfoil is at an angle of attack α, as shown in Figure 72b. The lift of the main element is represented by a point vortex of strength γ_m located at the quarter chord location on the airfoil. Similarly, the lift of the flap is represented by a point vortex of strength γ_f located at the quarter chord of the flap. The cove tab and flap tab are represented by point vortices with strength γ_{ct} and γ_{ft} located at the trailing edges of the main element and flap respectively. The direction of rotation of each vortex is as shown in Figure 72c. Both a cove tab and a flap tab will be included in the derivation of the model. The tabs can then be easily removed from the model, either individually or together, by setting the strengths of the vortices representing the tabs equal to zero.

Boundary conditions are established requiring the flow normal to the chord line be zero at the 3/4 chord location denoted by points **A** and **B** on the main element and flap respectively. It should be noted that the location of points **A** and **B** are chosen so that the lift curve slope for the two-element airfoil is equal to the theoretical value of 2π predicted by thin airfoil theory when the strengths of the point vortices representing the lift-enhancing tabs are set to zero. The location of points **A** and **B** may need to be shifted when γ_{ct} and γ_{ft} are not zero to maintain the proper theoretical lift curve slope; however, for the present application, this was not done. Using the 3/4 chord location on the main element and flap for points **A** and **B** respectively is adequate for qualitatively studying the effect of lift-enhancing tabs on a two-element airfoil.

To apply the boundary condition, the velocity induced by each point vortex at points **A** and **B** must be computed. This requires the position vectors between each point vortex and the points **A** and **B** to be defined, as shown in Figures 72b and 72c. Using the coordinate system shown in Figure 72, the position vectors can be defined as follows.

$$\vec{R}_1 = \mathbf{0.5}c_1\,\hat{i}$$

$$\vec{R}_2 = R_2\left(\frac{R_{2x}}{R_2}\hat{i} + \frac{R_{2z}}{R_2}\hat{k}\right)$$

$$\vec{R}_3 = R_3\left(\frac{R_{3x}}{R_3}\hat{i} + \frac{R_{3z}}{R_3}\hat{k}\right)$$

$$\vec{R}_4 = \mathbf{0.5}c_2\left(\mathbf{cos}(\delta_f)\,\hat{i} - \mathbf{sin}(\delta_f)\,\hat{k}\right)$$

$$\vec{R}_5 = -\mathbf{0.25}c_1\,\hat{i}$$

$$\vec{R}_6 = R_6\left(\frac{R_{6x}}{R_6}\hat{i} + \frac{R_{6z}}{R_6}\hat{k}\right) \qquad (85)$$

$$\vec{R}_7 = R_7\left(\frac{R_{7x}}{R_7}\hat{i} + \frac{R_{7z}}{R_7}\hat{k}\right)$$

$$\vec{R}_8 = \mathbf{0.25}c_2\left(-\mathbf{cos}(\delta_f)\,\hat{i} + \mathbf{sin}(\delta_f)\,\hat{k}\right)$$

Note that position vectors $\mathbf{R}_1$, $\mathbf{R}_4$, $\mathbf{R}_5$, and $\mathbf{R}_8$ are fixed by the airfoil geometry and the choice of location for the point vortices and the points **A** and **B**. The position vectors $\mathbf{R}_2$, $\mathbf{R}_3$, $\mathbf{R}_6$, and $\mathbf{R}_7$ are dependent on the flap deflection angle, gap, and overlap. The position vectors given in equation (85) are expressed as a magnitude multiplying a unit vector. This is done to facilitate the velocity computations.

Next the velocity induced at points **A** and **B** by each of the point vortices must be computed. A point vortex induces only a tangential component of velocity. The radial component of velocity is always zero. The tangential component of velocity induced by a point vortex of strength γ at a point that is a distance R from the vortex is given by the following equation.

$$u_\theta = \frac{\gamma}{2\pi R} \qquad (86)$$

Using equation (86) together with the position vectors defined in equation (85), the velocity induced by each point vortex at points **A** and **B** is given by the following set of equations.

$$\vec{V}_1 = -\frac{\gamma_m}{\pi c_1}\hat{k}$$

$$\vec{V}_2 = \frac{\gamma_m}{2\pi R_2}\left(\frac{R_{2z}}{R_2}\hat{i} - \frac{R_{2x}}{R_2}\hat{k}\right)$$

$$\vec{V}_3 = \frac{\gamma_f}{2\pi R_3}\left(\frac{R_{3z}}{R_3}\hat{i} - \frac{R_{3x}}{R_3}\hat{k}\right)$$

$$\vec{V}_4 = -\frac{\gamma_f}{\pi c_2}\left(\sin(\delta_f)\hat{i} + \cos(\delta_f)\hat{k}\right)$$

$$\vec{V}_5 = \frac{2\gamma_{ct}}{\pi c_1}\hat{k}$$

$$\vec{V}_6 = \frac{\gamma_{ct}}{2\pi R_6}\left(\frac{R_{6z}}{R_6}\hat{i} - \frac{R_{6x}}{R_6}\hat{k}\right)$$

$$\vec{V}_7 = \frac{\gamma_{ft}}{2\pi R_7}\left(\frac{R_{7z}}{R_7}\hat{i} - \frac{R_{7x}}{R_7}\hat{k}\right) \qquad (87)$$

$$\vec{V}_8 = \frac{2\gamma_{ft}}{\pi c_2}\left(\sin(\delta_f)\hat{i} + \cos(\delta_f)\hat{k}\right)$$

With the velocity induced at points **A** and **B** by all the point vortices defined by equation set (87), the boundary condition can now be applied at **A** and **B**. Note that velocities $\mathbf{V}_1$, $\mathbf{V}_3$, $\mathbf{V}_5$, and $\mathbf{V}_7$ apply to point **A** and velocities $\mathbf{V}_2$, $\mathbf{V}_4$, $\mathbf{V}_6$, and $\mathbf{V}_8$ apply to point **B**. The component of each velocity normal to the chord line associated with points **A** and **B** must sum to zero. The free stream velocity must be included in the summation as well. Performing the summation at point **A** yields the following equation.

$$w_\infty - \frac{\gamma_m}{\pi c_1} - \frac{\gamma_f}{2\pi R_3}\left(\frac{R_{3x}}{R_3}\right) + \frac{2\gamma_{ct}}{\pi c_1} - \frac{\gamma_{ft}}{2\pi R_7}\left(\frac{R_{7x}}{R_7}\right) = 0 \qquad (88)$$

This equation can be rearranged to give an expression for the strength γ_m of the point vortex representing the lift of the main element as follows.

$$\gamma_m = 2\gamma_{ct} + \pi c_1\left\{w_\infty - \frac{\gamma_f}{2\pi R_3}\left(\frac{R_{3x}}{R_3}\right) - \frac{\gamma_{ft}}{2\pi R_7}\left(\frac{R_{7x}}{R_7}\right)\right\} \qquad (89)$$

Performing the summation at point **B** yields the equation given below.

$$\left[u_\infty + \frac{\gamma_m}{2\pi R_2}\left(\frac{R_{2z}}{R_2}\right) - \frac{\gamma_f}{\pi c_2}\sin(\delta_f) + \frac{\gamma_{ct}}{2\pi R_6}\left(\frac{R_{6z}}{R_6}\right) + \frac{2\gamma_{ft}}{\pi c_2}\sin(\delta_f)\right]\sin(\delta_f) + \left[w_\infty - \frac{\gamma_m}{2\pi R_2}\left(\frac{R_{2x}}{R_2}\right) - \frac{\gamma_f}{\pi c_2}\cos(\delta_f) - \frac{\gamma_{ct}}{2\pi R_6}\left(\frac{R_{6x}}{R_6}\right) + \frac{2\gamma_{ft}}{\pi c_2}\cos(\delta_f)\right]\cos(\delta_f) = 0 \tag{90}$$

Equation (90) can also be rearranged to give an expression for the strength γ_f of the point vortex representing the lift of the flap as shown in equation (91) below.

$$\gamma_f = 2\gamma_{ft} + \pi c_2 \left\{ \begin{array}{l} \left(u_\infty \sin(\delta_f) + w_\infty \cos(\delta_f)\right) - \frac{\gamma_m}{2\pi R_2}\left(\frac{R_{2x}}{R_2}\cos(-\delta_f) + \frac{R_{2z}}{R_2}\sin(-\delta_f)\right) \\ -\frac{\gamma_{ct}}{2\pi R_6}\left(\frac{R_{6x}}{R_6}\cos(-\delta_f) + \frac{R_{6z}}{R_6}\sin(-\delta_f)\right) \end{array} \right\} \tag{91}$$

Equations (89) and (91) represent two equations for the two unknown vortex strengths γ_m and γ_f. The vortex strengths γ_{ct} and γ_{ft} which represent the cove tab and the flap tab are assumed to be known from some other source, such as an empirical correlation derived from the experimental data. If there is no cove tab or flap tab, the corresponding vortex strength is simply zero. The remainder of the variables in equations (89) and (91) are known from the geometry of the model. Equations (89) and (91) could be solved explicitly for the unknown vortex strengths γ_m and γ_f in terms of known quantities; however, it is more instructive to leave them in their present form in order to study how changing different parameters affects the circulation, and hence the lift, of each element.

Taking the partial derivative of equations (89) and (91) with respect to each of the vortex strengths yields a set of sensitivity relationships for γ_m and γ_f. From equation (89) the following relations are obtained

$$\frac{\partial \gamma_m}{\partial \gamma_f} = -\frac{c_1}{2R_3}\left(\frac{R_{3x}}{R_3}\right) > 0 \tag{92}$$

$$\frac{\partial \gamma_m}{\partial \gamma_{ct}} = 2 > 0 \tag{93}$$

$$\frac{\partial \gamma_m}{\partial \gamma_{ft}} = -\frac{c_1}{2R_7}\left(\frac{R_{7x}}{R_7}\right) > 0 \tag{94}$$

Similarly, taking the partial derivatives of equation (91) with respect to each of the vortex strengths yields

$$\frac{\partial \gamma_f}{\partial \gamma_m} = -\frac{c_2}{2R_2}\left(\frac{R_{2x}}{R_2}\cos(-\delta_f) + \frac{R_{2z}}{R_2}\sin(-\delta_f)\right) < 0 \tag{95}$$

$$\frac{\partial \gamma_f}{\partial \gamma_{ct}} = -\frac{c_2}{2R_6}\left(\frac{R_{6x}}{R_6}\cos(-\delta_f) + \frac{R_{6z}}{R_6}\sin(-\delta_f)\right) < 0 \tag{96}$$

$$\frac{\partial \gamma_f}{\partial \gamma_{ft}} = 2 > 0 \tag{97}$$

Taking partial derivatives of equations (89) and (91) with respect to some of the other variables in those equations would provide additional sensitivity relationships for parameters such as angle of attack, flap deflection angle, and flap gap. The present emphasis, however, is on understanding how lift-enhancing tabs affect the performance of a multi-element airfoil. Note that for a given configuration, all of the quantities on the right hand side of equations (92) through (97) are fixed. Thus the magnitudes of the partial derivatives are known once a configuration is selected.

Examining the sensitivity relationships given by equations (92) through (94), it is evident that increases in the vortex strengths γ_f ,γ_{ct} , and γ_{ft} all increase the vortex strength γ_m. On the other hand, equations (95) and (96) indicate that increases in γ_m and γ_{ct} cause a decrease in the vortex strength γ_f. Only an increase in γ_{ft} can cause an increase in the vortex strength γ_f, as indicated by equation (97). This information can be used to develop insight into how lift-enhancing tabs affect the performance of a multi-element airfoil.

The easiest case to examine is the one in which a flap tab is added to the baseline configuration. Adding a flap tab increases the strength of the flap vortex γ_f and the main element vortex γ_m as predicted by equations (97) and (94). The increase in γ_f also contributes to the increase in the vortex strength γ_m, as predicted by equation (92). On the other hand, the increase in γ_m contributes to a decrease in the vortex strength γ_f, as predicted by equation (95). Since all the experimental and computed results presented in this report indicate that adding a flap tab to a two-element airfoil causes a net increase in the lift of both the main element and the flap, the reduction in vortex strength γ_f predicted by equation (95) must be less in magnitude than the increase in vortex strength γ_f predicted by equation (97).

The effect of adding a cove tab to the baseline configuration is a little more difficult to analyze. Equation (93) indicates that the vortex strength γ_m will be increased by adding a cove tab. The vortex strength γ_f, on the other hand, will be reduced by the cove tab and by the increase in γ_m as shown in equations (96) and (95). The reduction in strength of γ_f causes a reduction in γ_m as indicated by equation (92). For configurations where no flow separation occurs on the upper surface of the flap, the experimental and computed results presented earlier in this report indicate that the lift of the main element increases and the lift of the flap decreases when a cove tab is added. The net lift of the two-element airfoil remains essentially unchanged. This implies that the increase in γ_m and the decrease in γ_f predicted by the sensitivity relationships must approximately balance each other.

The use of point vortices to represent lift-enhancing tabs is useful not only for predicting the effect of the tabs on the overall lift of the various elements in a multi-element airfoil, but also for predicting the local changes in pressure distribution on the elements caused by the tabs. Adding a point vortex to the trailing edge of the main element or flap with the direction of rotation of the vortex as indicated in Figure 72c will cause an increase in the velocity on the upper surface and a decrease in velocity on the lower surface in the vicinity of the trailing edge. The pressure coefficients on the upper surface become more negative and on the lower surface they become more positive as a result, leading to an increase in loading on the aft portion of the airfoil. The point vortex which represents a cove tab induces a velocity which retards the flow through the flap gap. This leads to a lower suction peak on the flap leading edge. The changes in local pressure coefficient distribution caused by the point vortices used to represent tabs are consistent with the changes observed experimentally.

The model described above captures the dominant effects of lift-enhancing tabs on a multi-element airfoil. The model is simple enough that analytic expressions for a set of sensitivity relationships can be derived which provide a mathematical basis for understanding how lift-enhancing tabs work. The accuracy of the model can be increased by increasing the number of point vortices used to represent each element of the airfoil. Note, however, that all the point vortices are distributed along the chord line of each element. The thickness of each element is not being modeled and detailed surface pressure coefficient distributions cannot be obtained from this model. To obtain surface pressure coefficient distributions, a potential flow panel method can be used to represent the actual surface of each element. The surface of each element is discretized into a set of panels and singularities of unknown strength are distributed on the panels. The singularities can be sources, doublets, vortices, or some combination of these. Appropriate boundary conditions are applied (i.e. flow normal to each panel must be zero), resulting in a linear

system of equations which must be solved for the unknown singularity strengths. Reference [45] provides an excellent description of a wide variety of both two-dimensional and three-dimensional panel methods.

To further demonstrate that using a point vortex at the trailing edge of an airfoil element to represent a lift-enhancing tab is a reasonable model, a simple two-dimensional potential flow panel code was written. The code, called PMARC2D, is based on the three-dimensional panel code PMARC [35]. The airfoil surface is discretized into a set of N panels and constant strength distributions of sources and doublets are applied to each panel. The strengths of the sources, σ_j, are determined from a boundary condition requiring the flow normal to each panel to be zero, as shown in equation (98).

$$\sigma_j = \vec{n}_j \bullet \vec{V}_\infty \tag{98}$$

Thus the source strengths are known for a given airfoil geometry and free stream velocity vector. The strengths of the doublets, μ_j, are determined by requiring the potential inside the airfoil element to be equal to the free stream potential. This results in the following system of linear equations to be solved for the unknown doublet strengths.

$$\sum_{i=1}^{N}\sum_{j=1}^{N} C_{ij}\mu_j = -\sum_{i=1}^{N}\sum_{j=1}^{N} B_{ij}\sigma_j \tag{99}$$

The terms C_{ij} and B_{ij} are influence coefficients. They represent the potential induced at the center of panel i by a unit strength doublet or source distribution respectively on panel j. The influence coefficients depend only on the geometry of the discretized airfoil surface and thus are also known for a given airfoil geometry. Once equation (99) is solved for the unknown doublet strengths, the tangential component of velocity on the airfoil surface is obtained by differentiating the doublet distribution and the normal component of velocity on the airfoil surface is given by the source strengths.

For the airfoil to carry lift, a wake panel with a constant strength doublet distribution on it must be attached to the airfoil trailing edge to enforce the Kutta condition. The Kutta condition, in the context of this potential flow model, requires the velocity at the sharp trailing edge of the airfoil to be finite and to leave the airfoil surface tangent to the bisector of the trailing edge angle. The strength of the doublet distribution on the wake panel which satisfies this condition is given by

$$\mu_w = \mu_u - \mu_l \tag{100}$$

where μ_u is the doublet strength on the upper surface panel at the trailing edge and μ_l is the doublet strength on the lower surface panel at the trailing edge. Equation (100) can be incorporated into equation (99) by adding or subtracting the wake panel influence coefficients, C_{iw}, to the corresponding surface panel influence coefficients, C_{iu} and C_{il}, respectively in equation (99).

A point vortex can be easily added to the trailing edge of the airfoil to represent a lift-enhancing tab by noting that a panel with a constant strength doublet distribution μ_j on it is equivalent to two point vortices with strength μ_j and opposite sign located at the edges of the panel. Thus a point vortex of strength γ_{tab} can be added to the airfoil trailing edge by increasing the doublet strength on the wake panel by $\mu_{tab} = \gamma_{tab}$. Equation (100) then becomes

$$\mu_w = \mu_u - \mu_l + \mu_{tab} \tag{101}$$

Equation (101) is incorporated into equation (99) in the same manner as was done for equation (100). The extra term μ_{tab} is a known quantity (user-specified), so the product $C_{iw}\,\mu_{tab}$ can be moved to the right hand side of equation (99). Adding the point vortex to the airfoil trailing edge by increasing the doublet strength on the wake panel by $\mu_{tab} = \gamma_{tab}$ modifies the Kutta condition to simulate the effect of the lift-enhancing tab on the airfoil.

PMARC2D was used to model the NACA 63_2-215 ModB two-element airfoil that was used throughout this research. The upper and lower surfaces of the main element were each represented with 50 equally-spaced panels. The flap upper and lower surfaces were each represented with 25 equally-spaced panels. The configuration chosen for this illustration was one with a flap deflection angle of 27°, a flap gap of $z_g/c = 0.05$, a flap overlap of $x_{ol}/c = 0.015$, and an angle of attack of 0°. The four cases which were run included the baseline configuration, a cove tab configuration, a flap tab configuration, and a configuration with both a cove tab and a flap tab. The strengths of the point vortices used to represent the tabs were determined on a trial and error basis. The strength of the point vortex used to model the flap tab was chosen so that the computed results matched the experimentally observed jump in pressure coefficient at the flap trailing edge. The strength of the point vortex used to simulate the cove tab was chosen so that the computed results best matched both the experimentally observed jump in the pressure coefficient at the trailing edge of the main element and the reduction in the flap leading edge suction peak. The vortex strengths γ_{ct} and γ_{ft}, determined for the cove tab configuration and the flap tab configuration respectively, were used together for the configuration with both a cove tab and a flap tab.

The results of the PMARC2D computations are shown in Figure 73. The pressure coefficient distribution for each of the tab configurations is compared with the baseline configuration. In Figure 73a, the effect of the cove tab on the baseline pressure coefficient distribution can be seen. The circulation of the main element is increased slightly and the loading at the trailing edge of the main element is also increased. The suction peak at the flap leading edge has been reduced as well. Comparing Figure 73a with the experimental results shown in Figure 55, it is evident that the changes to the baseline pressure distribution caused by adding a cove tab are well predicted by PMARC2D. Note that the pressure coefficient distribution in the cove region of the main element is not accurately predicted by PMARC2D. Since PMARC2D is a potential flow code, it cannot predict the separated flow region that exists in the cove on the main element.

The effect of the flap tab on the baseline pressure coefficient distribution is shown in Figure 73b. The circulation of both the main element and the flap is increased when the flap tab is added to the baseline configuration. The loading at the trailing edge of the flap is increased as well. Comparing Figure 73b to the experimental results in Figure 56, it can be seen that the PMARC2D model does a good job of predicting the changes to the baseline pressure coefficient distribution caused by the addition of the flap tab. A similar comparison of the PMARC2D results for the configuration with both a cove tab and a flap tab, shown in Figure 73c, to the experimental results shown in Figure 57 indicates that PMARC2D also handles this case well.

Both the simple analytic model developed earlier and the PMARC2D results just presented indicate that many of the flow field changes caused by adding lift-enhancing tabs to a multi-element airfoil can be explained using potential flow models. The primary way that viscous effects interact with the performance of lift-enhancing tabs is through the separation of the boundary layer on the upper surface of the flap. It has been shown that adding a cove tab to a multi-element airfoil can move the flow separation point on the flap upper surface further aft or eliminate the flow separation entirely. The mechanism by which a cove tab accomplishes this effect is the reduction of the flap leading edge suction peak. This reduces the adverse pressure gradient for the boundary layer on the flap upper surface, permitting it to remain attached longer. Conceptually, it is possible to couple a potential flow code such as PMARC2D with an integral boundary layer scheme to produce a code which could predict boundary layer separation locations, thus obtaining a more complete model for analyzing lift-enhancing tabs on a multi-element airfoil. However, the economy of using INS2D-UP to perform these type of computations would seem to make

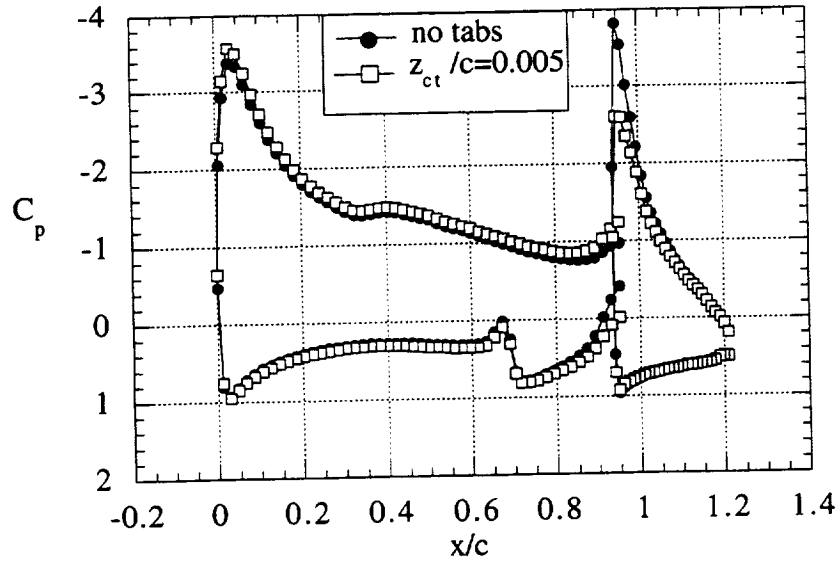

a) Effect of a cove tab on the baseline pressure distribution.

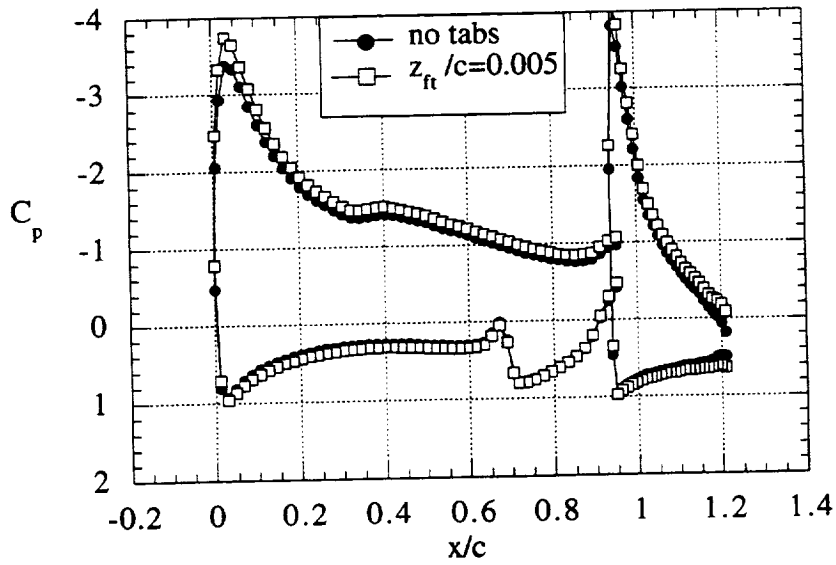

b) Effect of a flap tab on the baseline pressure distribution.

Figure 73: Potential flow code PMARC2D predictions of the effect of lift-enhancing tabs on the pressure coefficient distribution of a baseline configuration ($\delta_f = 27°$, $x_g/c = 0.05$, $x_{ol}/c = 0.015$, $\alpha = 0°$).

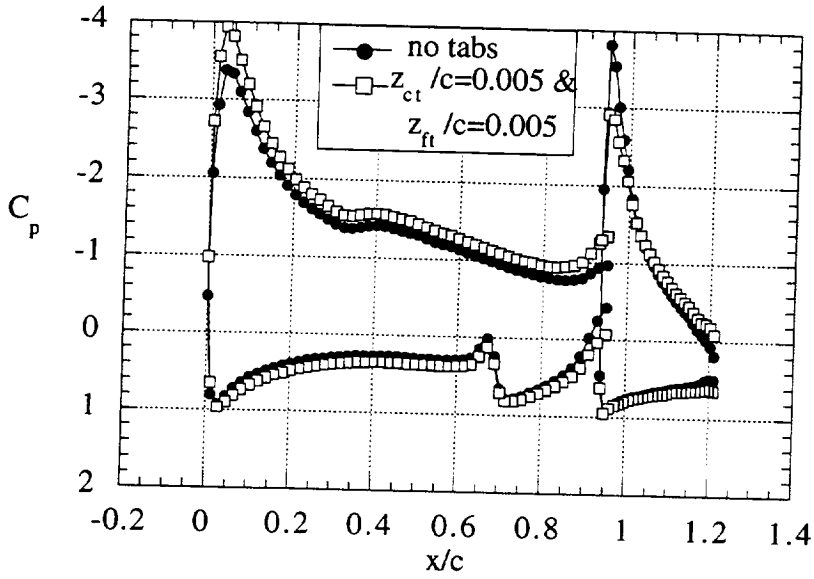

c) Effect of both a cove tab and a flap tab on the baseline pressure distribution.

Figure 73 concluded: Potential flow code PMARC2D predictions of the effect of lift-enhancing tabs on the pressure coefficient distribution of a baseline configuration ($\delta_f = 27°$, $x_g/c = 0.05$, $x_{ol}/c = 0.015$, $\alpha = 0°$).

such a step unwarranted. Development of a potential flow method coupled with a boundary layer scheme for analyzing three-dimensional applications of lift-enhancing tabs would make more sense, since three-dimensional Navier-Stokes computations are very time-consuming to perform.

CHAPTER VIII
CONCLUSIONS

An experimental and computational investigation of the effects of lift-enhancing tabs on a multi-element airfoil has been conducted. The goal of the study was to develop an understanding of the flow physics associated with lift-enhancing tabs on a multi-element airfoil. The experimental work was conducted in the NASA Ames 7- by 10-Foot Wind Tunnel. A NACA 63_2-215 ModB airfoil with a 30% chord fowler flap was used as the model for the test. Parameters varied in the test include flap deflection angle, flap gap, tab height, and the airfoil element to which the tab was attached. Flap angle was varied from 19° to 39° in 10° increments. Flap gap was varied from $z_g/c = 0.02$ to 0.05 in 0.01 increments. Tab heights of $z_t/c = 0.0025$, 0.005, and 0.01 were tested. The tabs were mounted to the main element trailing edge (cove tab), the flap trailing edge (flap tab), and to both elements simultaneously. All of the testing was conducted at a Reynolds number of 3.5×10^6.

The computational database was generated using the two-dimensional, incompressible, Reynolds-Averaged Navier-Stokes code INS2D-UP. A chimera composite structured grid was created which represented the NACA 63_2-215 ModB two-element airfoil in the 7- by 10-Foot Wind Tunnel. Time was spent refining the grid to capture all of the dominant flow field features, particularly in the region near the trailing edge of each element and in the wakes. Grid spacing normal to all surfaces of the airfoil, including the lift-enhancing tabs, was set to 1×10^{-5} to resolve the details of the boundary layers. Grid sensitivity studies showed that solutions obtained on the standard grid were grid independent. All of the computed results were obtained by running INS2D-UP in the steady-state mode. The Spalart-Allmaras turbulence model was used and the flow was assumed to be fully-turbulent. Computed results were obtained for all experimental configurations with flap deflection angles of 29° and 39° and tab heights of $z_t/c = 0.005$, as well as the corresponding baseline cases (with no tabs). The average computation time for each case was approximately 1200 seconds on a Cray C-90 computer.

Initial comparisons between the experimental and computed results produced poor agreement, with the computed results overpredicting the airfoil lift coefficient by a large margin. Much of the discrepancy between the experimental and computed results was traced to changes in the flap deflection angle under load in the experiment. The flap deflection angle in the experiment was reduced by 2° to 3° under aerodynamic load, depending on the initial flap deflection angle setting. The amount of change in flap deflection angle was found to be primarily a function of the initial static flap deflection

angle. When the change in flap deflection angle under aerodynamic load was taken into account in the computations, much better agreement between computed and experimental results was achieved, particularly for cases where no flow separation existed on the flap upper surface. It was more difficult to achieve good correlation between experimental and computed results for configurations where significant flow separation existed over the flap upper surface. This was due primarily to inaccuracies in the computed separation location. Overall, however, the computed results predicted all of the trends observed in the experimental data quite well. The computational database was used to supplement the experimental data and provide additional details about the flow field.

The effect of cove tabs on multi-element airfoil performance is dependent on flap angle. For baseline configurations with moderate flap deflection angles, the flow over the upper surface of the flap is fully attached and adding a cove tab produces only a small increase in lift coefficient. The lift coefficient of the main element increases, but the increase is offset by a decrease in the lift coefficient of the flap. As the flap gap is increased, the increment in lift coefficient on the main element becomes larger than the reduction in lift coefficient of the flap, resulting in a net increase in lift for the airfoil. Drag is increased significantly relative to the baseline configuration when a cove tab is added. For baseline configurations with large flap deflection angles, the flow over much of the upper surface of the flap is separated and adding a cove tab produces a significant increase in lift coefficient relative to the baseline configuration. In this case, the cove tab reduces or eliminates the flow separation over the upper surface of the flap by reducing the flap leading edge suction peak. This reduces the adverse pressure gradient that the boundary layer on the flap upper surface must traverse, allowing it to remain attached longer. The elimination of the separated flow over the flap leads to a large increase in lift and a significant reduction in drag.

The effect of flap tabs on multi-element airfoil performance is not dependent on flap angle. Adding a flap tab to a baseline configuration significantly increases the lift coefficient, regardless of whether the flow over the upper surface of the flap is attached or separated. The lift coefficient increases on both the main element and the flap when a flap tab is added to the configuration. Drag coefficient at a given lift coefficient does not increase when a flap tab is added to the baseline configuration. The drag coefficients for the configurations with flap tabs were typically within 10 drag counts of the drag coefficients for the baseline configuration at the same lift coefficient.

The cove and flap tabs can be used in combination to achieve lift coefficients that are significantly higher than is possible with any baseline configuration at a given angle of attack. The combination of a cove tab of height $z_{ct}/c = 0.005$ and flap tab of height

$z_{ft}/c = 0.005$ on a configuration with a 39° flap angle and a flap gap of $z_g/c = 0.04$ produced an 11% increase in lift coefficient at 0° angle of attack compared to the highest lift coefficient achieved with a baseline configuration at that angle of attack. C_{lmax} was increased by 3% compared to the highest C_{lmax} for a baseline configuration. Computed results indicate that the maximum flap deflection angle can be extended by as much as 10° without any flow separation over the flap by adding a cove tab and flap tab combination to the airfoil. Sensitivity of the mult-element airfoil lift coefficient to the flap gap size is also greatly reduced when a cove tab is added to the configuration.

A simple analytic model for lift-enhancing tabs on a two-element airfoil was developed to provide a more detailed understanding of how lift-enhancing tabs work. The model assumes the effect of lift-enhancing tabs on the performance of a multi-element airfoil can be described using potential flow. The lift-enhancing tabs are represented by point vortices located at the trailing edges of the airfoil elements. The lift of each airfoil element is modeled with a point vortex located at the quarter chord location of the element. Mathematical expressions were then developed for the sensitivity of the lift of one element to the lift of the other and to the presence of lift-enhancing tabs. These sensitivity relationships provide a mathematical basis for explaining the effects of lift-enhancing tabs on multi-element airfoils. The trends predicted by the sensitivity relationships are in good agreement with those observed in the experimental and computational databases. The potential flow model with the tabs represented by point vortices captures all of the dominant effects of lift-enhancing tabs on the pressure coefficient distributions of each element, for cases with no flow separation. This was demonstrated by using a two-dimensional potential flow panel method to represent the two-element airfoil and point vortices at the element trailing edges to represent the lift-enhancing tabs. The predicted changes in pressure coefficient distribution due to the addition of tabs to the configuration are in close agreement with experimental results.

This research shows that lift-enhancing tabs provide a powerful means of increasing the high-lift performance of a multi-element airfoil. The most likely application for lift-enhancing tabs on a commercial transport would be in the approach and landing configurations, when the high-lift system is typically fully deployed to achieve the maximum lift coefficient at a given angle of attack. The high lift system becomes the limiting factor in the performance of the aircraft at this condition. The increase in performance afforded by lift-enhancing tabs for this configuration would allow approach speed or angle of attack to be reduced or maximum landing weight to be increased. Alternatively, lift-enhancing tabs may allow the number of trailing-edge flap elements to be reduced without degradation in the performance of the high-lift system, leading to lighter,

mechanically simpler flap actuation systems. Use of lift-enhancing tabs could also have implications for things like landing gear size and thrust-reverser performance requirements.

In the take-off configuration, the high-lift system is only partially deployed. As demonstrated by the present study, the cove tab is not useful for configurations where the flow over the flap upper surface is fully attached. It has been shown that a flap tab can substantially increase the lift of a multi-element airfoil, even at the moderate flap deflection angles associated with a take-off configuration. However, the increase in lift provided by a flap tab could also be achieved by increasing the flap deflection angle. It is not clear from the present study whether using a flap tab would be more effective than increasing the flap deflection angle.

Aircraft manufacturers such as Boeing often modify the design of an aircraft that has been in production for a while to create a growth version that provides increased cargo or passenger capacity or increased range. Lift-enhancing tabs would be useful as an inexpensive means of providing the increased high-lift performance sometimes necessary for growth versions of an aircraft without changing the existing high-lift system. Lift-enhancing tabs can also be used to restore performance which is lost due to the presence of flap track fairings and other hardware necessary to deploy the flap system. For general aviation aircraft, lift-enhancing tabs provide an inexpensive means of increasing the performance of existing high-lift systems which are not always highly-optimized.

Further work remains to fully define the impact of lift-enhancing tabs on high-lift systems. The impact of three-dimensional effects, such as wing sweep, on the effectiveness of lift-enhancing tabs needs to be investigated. The two-dimensional Navier-Stokes code INS2D-UP has been demonstrated to be an effective tool for analyzing lift-enhancing tabs on multi-element airfoils. Full three-dimensional Navier-Stokes solutions for a typical transport aircraft high-lift system with lift-enhancing tabs, however, are expensive and time-consuming to obtain. The development of a three-dimensional potential flow method coupled with a boundary layer scheme and tabs represented by vortex elements would be an attractive alternative for analyzing such problems. An empirical or analytic expression relating tab height to the strength of the vortex used to represent the tab remains to be defined. Tabs augment the number of parameters available to work with in high-lift system design and change some of the constraints, such as maximum flap deflection angle, governing the high-lift optimization process. Optimization studies need to be performed on multi-element airfoil configurations with lift-enhancing tabs to determine new high-lift system performance boundaries.

REFERENCES

1 Meredith, P. T., "Viscous Phenomena Affecting High-Lift Systems And Suggestions For Future CFD Development," AGARD CP-515, Paper No. 19, October, 1992.

2 Smith, A. M. O., "High-Lift Aerodynamics," J. Aircraft, Vol 12, No. 6, June 1975, pp. 501-530.

3 Storms, B. and Jang, C., "Lift Enhancement of an Airfoil Using a Gurney Flap and Vortex Generators," J. Aircraft, Vol. 31, No. 3, May 1994, pp. 542-547.

4 Valarezo, W. O., Dominik, C. J., McGhee, R. J., Goodman, W. L., and Paschal, K. B., "Multi-Element Airfoil Optimization for Maximum Lift at High Reynolds Numbers," AIAA Paper 91-3332, AIAA 9th Applied Aerodynamics Conference, Baltimore, MD., September 23-25, 1991.

5 Liebeck, R. H., "Design of Subsonic Airfoils for High Lift," J. Aircraft, Vol 15, No 9, Sept. 1978, pp. 547-561.

6 Katz, J. and Largman, R., "Effect of 90 Degree Flap on the Aerodynamics of a Two-Element Airfoil," Journal of Fluids Engineering, Vol. 111, Mar. 1989, pp. 93-94.

7 Roesch, P. and Vuillet, A., "New Designs for Improved Aerodynamic Stability on Recent Aerospatiale Helicopters," Vertica, Vol. 6, 1982, pp. 145-164.

8 Storms, B. and Ross, J., "An Experimental Study of Lift-Enhancing Tabs on a Two-Element Airfoil," AIAA Paper 941868, AIAA 12th Applied Aerodynamics Conference, Colorado Springs, CO., June 20-22, 1994.

9 Ross, J., Storms, B., and Carrannanto, P., "Lift-Enhancing Tabs on Multi-Element Airfoils," AIAA Paper 933504, AIAA 11th Applied Aerodynamics Conference, Monterey, CA., August 9-11, 1993.

10 Neuhart, D.H., and Pendergraft Jr., O.C., "A Water Tunnel Study of Gurney Flaps," NASA TM 4071, 1988.

11 Jang, C., Ross, J., and Cummings, R., "Computational Evaluation of an Airfoil with a Gurney Flap," AIAA Paper 922708, AIAA 10th Applied Aerodynamics Conference, Palo Alto, CA, June 22-24, 1992.

12 Carrannanto, P., Storms, B., Ross, J., and Cummings, R., "Navier-Stokes Analysis of Lift-Enhancing Tabs on Multi-Element Airfoils," AIAA Paper 940050, 32nd Aerospace Sciences Meeting and Exhibit, Reno, NV., January 10-13, 1994.

13 Ashby, D., "Experimental Investigation of Lift-Enhancing Tabs on a Two-Element Airfoil," SAE Paper 951975, SAE Aerotech '95, Los Angeles, CA, September 18-21, 1995.

14 Hicks, R., and Schairer, E., "Effects of Upper Surface Modification on the Aerodynamic Characteristics of the NACA 63_2215 Airfoil Section," NASA TM 78503, January, 1979.

15 Takahashi, T. and Ross, J., "On the Development of an Efficient Wake Survey System," SAE Paper 951990, SAE Aerotech '95, Los Angeles, CA, September 18-21, 1995.

16 Zilliac, G., "Modelling, Calibration, and Error Analysis of Seven-Hole Pressure Probes," Experiments in Fluids, Vol. 14, 1993, pp. 104-120.

17 Tolhurst, W., "The Fundamentals of Measuring Dynamic Pressure and Velocity in the Ames 40- by 80-Foot Wind Tunnel," National Full-Scale Aerodynamics Complex Documentation Archives, December, 1987.

18 Rae, W., and Pope, A., Low-Speed Wind Tunnel Testing, 2nd edition, John Wiley & Sons, New York, New York, 1984.

19 Schlichting, H., Boundary Layer Theory, 7th edition, McGraw-Hill, New York, New York, 1979.

20 Rogers, S., Wiltberger, N., and Kwak, D., "Efficient Simulation of Incompressible Viscous Flow Over Single and Multi-Element Airfoils," AIAA Paper No. 92-0405, 30th Aerospace Sciences Meeting & Exhibit, Reno, NV., January 6-9, 1992.

21 Rogers, S., "Progress in High-Lift Aerodynamic Calculations," AIAA Paper No. 93-0194, 31st Aerospace Sciences Meeting & Exhibit, Reno, NV., January 11-14, 1993.

22 Dominik, C., "Application of the Incompressible Navier-Stokes Equations to High-Lift Flows," AIAA Paper No. 94-1872, 12th Applied Aerodynamics Conference, Colorado Springs, CO., June 20-23, 1994.

23 Anderson, D. A., Tannehill, J. C., and Pletcher, R. H., Computational Fluid Mechanics and Heat Transfer, Hemisphere Publishing Corporation, New York, New York, 1984.

24 Spalart, P. R. and Allmaras, S. R., "A One-Equation Turbulence Model for Aerodynamic Flows," AIAA Paper No. 92-0439, 30th Aerospace Sciences Meeting & Exhibit, Reno, NV., January 6-9, 1992.

25 Rogers, S. E., Menter, F. R., Durbin, P. A., and Mansour, N. N., "A Comparison of Turbulence Models in Computing Multi-Element Airfoil Flows," AIAA Paper No. 94-0291, 32nd Aerospace Sciences Meeting & Exhibit, Reno, NV., January 10-13, 1994.

26 Baldwin, B. S. and Barth, T. J., "A One-Equation Turbulent Transport Model for High Reynolds Wall Bounded Flows," AIAA Paper 91-0160, 29th Aerospace Sciences Meeting & Exhibit, Reno, NV., January 7-10, 1991.

27 Thomas, P. and Lombard, C., "Geometric Conservation Law and Its Application to Flow Computations on Moving Grids," AIAA Journal, Vol. 17, No. 10, 1979, pp. 1030-1037.

28 Rogers, S., Chang, J., and Kwak, D., "A Diagonal Algorithm for the Method of Pseudocompressibility," Journal of Computational Physics, Vol. 73, 1987, pp. 364-379.

29 Rogers, S. and Kwak, D., "An Upwind-Differencing Scheme for the Incompressible Navier-Stokes Equations," NASA TM 101051, Nov. 1988.

30 Rogers, S. and Kwak, D., "Upwind Differencing Scheme for the Time-Accurate Incompressible Navier-Stokes equations," AIAA Journal, Vol. 28, No. 2, February 1990.

31 Rogers, S., "Numerical Solution of the Incompressible Navier-Stokes Equations," NASA TM 102199, Nov. 1990.

32 Chorin, A., "A Numerical Method for Solving Incompressible Viscous Flow Problems," Journal of Computational Physics, Vol. 2, 1967, pp. 12-16.

33 Rogers, S. E., "A Comparison of Implicit Schemes for the Incompressible Navier-Stokes Equations With Artificial Compressibility," AIAA Paper No. 95-0567, 33rd Aerospace Sciences Meeting and Exhibit, Reno, NV., January 9-12, 1995.

34 Benek, J. A., Buning, P. G., and Steger, J. L., "A 3-D Chimera Grid Embedding Technique," AIAA Paper No. 85-1523, AIAA 7th Computational Fluid Dynamics Conference, Cincinnati, OH., July 15-17, 1985.

35 Ashby, D. L., Dudley, M. R., Iguchi, S. K., Browne, L., and Katz, J., "Potential Flow Theory and Operation Guide for the Panel Code PMARC," NASA TM 102851, January, 1991.

36 Vinokur, M., "On One-dimensional Stretching Functions for Finite Difference Calculations," NASA CR 3313, October, 1980.

37 Chan, W. M., Chui, I. T., and Buning, P. G., "User's Manual for the HYPGEN Hyperbolic Grid Generator and the HGUI Graphical User Interface," NASA TM 108791, October, 1993.

38 Suhs, N. E., and Tramel R. W., "PEGSUS 4.0 User's Manual," AEDC-TR-91-8, November, 1991.

39 Cao, H., Kusunose, K., Spalart, P., Ishimitsu, K., Rogers, S., and McGhee, R., "Study of Wind Tunnel Wall Interference for Multi-Element Airfoils Using a Navier-Stokes Code," AIAA Paper No. 94-1933, 12th AIAA Applied Aerodynamics Conference, Colorado Springs, CO., June 20-22, 1994.

40 Jasper, D., Agrawal, S., and Robinson, B., "Navier-Stokes Calculations on Multi-Element Airfoils Using a Chimera-Based Solver," AGARD CP-515, Paper No. 8, September, 1993.

41 Mathias, D., "Navier-Stokes Analysis of Flow About a Flap Edge," Master's Thesis, California Polytechnic State University, San Luis Obispo, CA., June, 1994.

42 Wadcock, A., "The NASA Ames 7ft. x 10ft. Wind Tunnel – Present Flow Quality and Recommendations for Improvement," Final Report for Contract NAS2-11945, Analytical Methods Inc., July, 1987.

43 Ashby, D. and Harris, S., "Computation of Wind Tunnel Wall Effects for Complex Models Using a Low-Order Panel Method," NASA TM 104019, Feb. 1994.

44 Walatka, P., Buning, P., Pierce, L., and Elson, P., "Plot3d User's Manual," NASA TM 101067, July, 1992.

45 Katz, J. and Plotkin, A., Low-Speed Aerodynamics From Wing Theory to Panel Methods, McGraw-Hill, New York, New York, 1991.

APPENDIX A

Table 2

Main Element and Flap Coordinates

main x/c	main z/c	flap x/c	flap z/c
0.9500	0.0049	1.0000	-0.0020
0.9490	0.0050	0.9990	-0.0019
0.9400	0.0062	0.9950	-0.0015
0.9200	0.0081	0.9900	-0.0010
0.9000	0.0099	0.9800	-0.0004
0.8500	0.0128	0.9600	0.0001
0.8200	0.0137	0.9400	-0.0003
0.8000	0.0140	0.9250	-0.0013
0.7700	0.0133	0.9000	-0.0033
0.7500	0.0120	0.8750	-0.0058
0.7350	0.0094	0.8500	-0.0086
0.7300	0.0080	0.8250	-0.0117
0.7250	0.0066	0.8000	-0.0150
0.7200	0.0050	0.7700	-0.0192
0.7100	-0.0006	0.7500	-0.0218
0.7090	-0.0012	0.7250	-0.0254
0.7080	-0.0020	0.7200	-0.0259
0.7070	-0.0030	0.7160	-0.0261
0.7030	-0.0076	0.7140	-0.0260
0.7012	-0.0116	0.7120	-0.0258
0.6950	-0.0197	0.7080	-0.0249
0.6900	-0.0250	0.7060	-0.0240
0.6850	-0.0280	0.7050	-0.0235
0.6800	-0.0310	0.7040	-0.0228
0.6750	-0.0330	0.7030	-0.0220
0.6500	-0.0368	0.7020	-0.0210
0.6250	-0.0404	0.7010	-0.0192
0.6000	-0.0438	0.7005	-0.0178
0.5750	-0.0470	0.7000	-0.0160
0.5500	-0.0501	0.7005	-0.0135
0.5250	-0.0530	0.7012	-0.0116
0.5000	-0.0556	0.7020	-0.0098
0.4750	-0.0580	0.7040	-0.0065
0.4500	-0.0601	0.7070	-0.0030
0.4250	-0.0618	0.7100	-0.0006
0.4000	-0.0632	0.7200	0.0050
0.3750	-0.0641	0.7300	0.0080
0.3500	-0.0647	0.7350	0.0094

Table 2 Continued

Main Element and Flap Coordinates

main x/c	main z/c	flap x/c	flap z/c
0.3250	-0.0648	0.7600	0.0128
0.3000	-0.0645	0.7900	0.0138
0.2750	-0.0637	0.8100	0.0139
0.2500	-0.0625	0.8200	0.0137
0.2250	-0.0609	0.8400	0.0131
0.2000	-0.0588	0.8600	0.0122
0.1750	-0.0562	0.8800	0.0110
0.1500	-0.0531	0.9200	0.0081
0.1250	-0.0494	0.9400	0.0062
0.1000	-0.0450	0.9600	0.0039
0.0900	-0.0430	0.9800	0.0016
0.0800	-0.0408	0.9850	0.0010
0.0700	-0.0384	0.9900	0.0003
0.0600	-0.0357	0.9925	0.0000
0.0500	-0.0328	0.9950	-0.0004
0.0400	-0.0294	0.9990	-0.0009
0.0300	-0.0256	1.0000	-0.0010
0.0200	-0.0211		
0.0100	-0.0150		
0.0050	-0.0104		
0.0040	-0.0093		
0.0030	-0.0079		
0.0020	-0.0063		
0.0010	-0.0042		
0.0008	-0.0037		
0.0000	0.0000		
0.0008	0.0075		
0.0010	0.0085		
0.0020	0.0125		
0.0030	0.0156		
0.0040	0.0182		
0.0050	0.0205		
0.0100	0.0293		
0.0200	0.0408		
0.0300	0.0489		
0.0400	0.0550		
0.0500	0.0599		
0.0600	0.0640		
0.0700	0.0673		
0.0800	0.0702		

Table 2 Concluded

Main Element and Flap Coordinates

main x/c	main z/c	flap x/c	flap z/c
0.0900	0.0727		
0.1000	0.0748		
0.1250	0.0788		
0.1500	0.0816		
0.1750	0.0835		
0.2000	0.0847		
0.2250	0.0855		
0.2500	0.0859		
0.2750	0.0860		
0.3000	0.0859		
0.3250	0.0856		
0.3500	0.0853		
0.3750	0.0852		
0.4000	0.0845		
0.4250	0.0835		
0.4500	0.0819		
0.4750	0.0800		
0.5000	0.0777		
0.5250	0.0750		
0.5500	0.0720		
0.5750	0.0688		
0.6000	0.0653		
0.6250	0.0615		
0.6500	0.0576		
0.6750	0.0534		
0.7000	0.0491		
0.7250	0.0447		
0.7500	0.0402		
0.7750	0.0357		
0.8000	0.0311		
0.8250	0.0266		
0.8500	0.0222		
0.8750	0.0179		
0.9000	0.0137		
0.9250	0.0098		
0.9350	0.0084		
0.9400	0.0076		
0.9425	0.0073		
0.9450	0.0069		
0.9490	0.0063		
0.9500	0.0062		

APPENDIX B

Table 3

Main Element and Flap Pressure Tap Locations (center of span)

Index	Main		Flap	
m	x/c	z/c	xf0/c	zf0/c
0	0.95	0.0049	1.000	-0.0020
1	0.93	0.006809	0.960	0.0001
2	0.9	0.0099	0.900	-0.0033
3	0.85	0.0128	0.850	-0.0086
4	0.825	0.01372	0.800	-0.0150
5	0.8	0.014	0.770	-0.0192
6	0.775	0.01319	0.750	-0.0218
7	0.75	0.012	0.740	-0.0234
8	0.725	0.0066	0.730	-0.0249
9	0.7	-0.01394	0.720	-0.0259
10	0.67933	-0.03096	0.710	-0.0254
11	0.6204	-0.041	0.705	-0.0235
12	0.558	-0.0491	0.700	-0.0160
13	0.4499	-0.0601	0.705	-0.0051
14	0.3138	-0.0647	0.710	-0.0006
15	0.198	-0.0586	0.720	0.0050
16	0.1283	-0.0499	0.730	0.0080
17	0.0946	-0.044	0.740	0.0101
18	0.08	-0.0408	0.750	0.0114
19	0.067	-0.0376	0.770	0.0131
20	0.0541	-0.0341	0.800	0.0138
21	0.0414	-0.0299	0.850	0.0126
22	0.0289	-0.0252	0.900	0.0094
23	0.0169	-0.0194	0.950	0.0050
24	0.0061	-0.0115	0.980	0.0016
25	0	0	1.000	-0.0020
26	0.0014	0.0102		
27	0.0047	0.0199		
28	0.0097	0.0289		
29	0.0162	0.0369		
30	0.0236	0.044		
31	0.0318	0.0501		
32	0.0407	0.0554		
33	0.05	0.0598		
34	0.0611	0.0644		
35	0.0762	0.0691		
36	0.0964	0.0741		

Table 3 Concluded

Main Element and Flap Pressure Tap Locations (center of span)

Index	Main		Flap	
m	x/c	z/c	xf0/c	zf0/c
37	0.1229	0.0785		
38	0.1568	0.0822		
39	0.1992	0.0847		
40	0.2508	0.0859		
41	0.3116	0.0858		
42	0.3805	0.0849		
43	0.4555	0.0816		
44	0.5333	0.074		
45	0.6102	0.0638		
46	0.67933	0.05255		
47	0.7	0.0491		
48	0.725	0.0447		
49	0.75	0.0402		
50	0.775	0.0357		
51	0.8	0.0311		
52	0.825	0.0266		
53	0.85	0.0222		
54	0.875	0.0179		
55	0.9	0.0137		
56	0.925	0.0098		
57	0.95	0.0049		